UNIVERSIDAD DE LA LAGUNA
Departamento de Astrofísica

Universidad de La Laguna

Large-Amplitude Oscillations in Erupting and Quiescent Solar Prominences

A dissertation submitted by
Valeriia Liakh
as a requirement for the degree of
Doctor of Philosophy in Astrophysics
by University of La Laguna

INSTITUTO Đ ASTROFÍSICA Đ CANARIAS
San Cristóbal de La Laguna, Tenerife, Spain
November 2021

A mis padres, hermano por su apoyo incondicional.
A mi abuelo, que siempre está en mi corazón.
Esta tesis es tan mía como vuestra.

Acknowledgements/Agradecimientos

I am grateful for the financial support received from Instituto de Astrofísica de Canarias via an Astrophysicist Resident fellowship. I would like to thank my supervisors, Manuel Luna and Elena Khomenko for all the time they have shared with me during these four years of thesis and also continuing guidance and support. I thankfully acknowledge the technical expertise and assistance provided by the Spanish Supercomputing Network (Red Española de Supercomputación), as well as the computer resources used: the LaPalma Supercomputer, located at the Instituto de Astrofísica de Canarias. I also acknowledge the computer resources at MareNostrum4 and the technical support provided by Barcelona Supercomputing Center (RES-AECT-2020-1-0012 and RES-AECT-2020-2-0010). I am grateful for the support from ISSI www.issibern.ch to team 413 and team 431 on "Large-Amplitude Oscillations as a Probe of Quiescent and Erupting Solar Prominences" led by M. Luna. I would like to acknowledge the participants of those meetings Judith Karpen, Rony Keppens, José Luis Ballester, Michael Ruderman, Holly Gilbert, Jaume Terradas, Yuhong Fan, Yu-Hao Zhou, Peng-Fei Chen, Bojan Vrŝnak, Andreu Adrover-González for the very useful discussions.

Resumen

En esta tesis, nos centramos en estudiar las propiedades de las oscilaciones de gran amplitud (LAO, por sus siglas en inglés) utilizando los modelos realistas de protuberancias y la activación de dichos movimientos por perturbaciones externas. Las LAO implican movimientos con amplitudes de la velocidad superiores a $20\,\mathrm{km\,s^{-1}}$, y grandes porciones del filamento se mueven en fase, lo que indica una fuerte conexión con la estructura del campo magnético del filamento. Dichos movimientos son provocados por eventos energéticos solares como erupciones, chorros y erupciones distantes o cercanas. La motivación de este trabajo proviene de los estudios recientes que han demostrado que las LAO son muy comunes en protuberancias y abren una nueva ventana para estudiar la estructura de protuberancias mediante una técnica conocida como sismología de protuberancias, que combina observaciones y modelado teórico de las LAO. Este estudio se basa en simulaciones numéricas dependientes del tiempo realizadas con el código magnetohidrodinámico (MHD, de sus siglas en inglés) MANCHA3D.

En la primera parte de este trabajo, realizamos simulaciones numéricas 2.5D de las LAO usando un modelo de cuerda de flujo magnético formado a partir de una configuración de arcada cizallada usando movimientos convergentes en los puntos de los pies. Cargamos artificialmente la masa de protuberancia en las depresiones magnéticas de la cuerda de flujo, y luego aplicamos perturbaciones horizontales y verticales para excitar los diferentes modos de oscilación. La perturbación horizontal excita las oscilaciones longitudinales de gran amplitud (LALOs por sus siglas en inglés) junto con las oscilaciones verticales de pequeña amplitud causadas por la reacción inversa del campo magnético. El período de las oscilaciones longitudinales disminuye al disminuir el radio de curvatura de las líneas del campo magnético de acuerdo con el modelo de péndulo. La perturbación vertical desencadena las LAO verticales del plasma de protuberancia y las oscilaciones simétricas a lo largo del campo magnético. Estos movimientos son causados por la compresión y rarefacción del plasma. Las LAO verticales están muy sincronizados en las diferentes regiones de protuberancia, y su período se mantiene constante con la altura. Esto sugiere que el modo vertical corresponde al modo normal global de la estructura de protuberancia. El análisis del diagrama de tiempo-distancia de la velocidad transversal revela la presencia de ondas magnetoacústicas rápidas emitidas desde la región de la protuberancia. Esto nos hace sugerir que la fuga de ondas puede ser responsable de la amortiguación de las LAO verticales en este experimento. Hemos comparado las propiedades de los modos de las oscilaciones longitudinales y transversales en los modelos de protuberancia con los diferentes ángulos de cizalladura de la estructura magnética y los contrastes de densidad de protuberancia. Hemos encontrado que solo la variación del ángulo de cizalladura afecta ligeramente el período de los LALO. Esto está asociado con la variación del radio de curvatura en la proyección 2D en estos modelos. El período de las oscilaciones verticales depende ligeramente de la densidad debido al efecto de la inercia de la protuberancia. También hemos estudiado la excitación de las LAO en la protuberancia modelada como una cuerda de flujo por una perturbación externa. Este experimento muestra que la onda del evento energético perturba fuertemente la estructura del campo magnético de la cuerda de flujo. La masa de protuberancia sigue esos cambios en la configuración del campo magnético y se mueve desde la posición de equilibrio debido al movimiento del campo magnético. Esta fuerte perturbación de la cuerda produce el movimiento del plasma de la protuberancia, pero no hay un frente de onda directo desde la ubicación de la perturbación que alcance la masa de protuberancia. La perturbación externa agita la cuerda de flujo y excita las oscilaciones en ambas polarizaciones. Sus propiedades son una mezcla de las puramente horizontales y verticales. Para el experimento con perturbación horizontal, realizamos estudios de convergencia y encontramos que el amortiguamiento de la oscilación es principalmente numérico pero puede reducirse aumentando la resolución espacial. Esto motiva nuestro próximo experimento numérico.

En la segunda parte del trabajo, hemos estudiado la influencia de la resolución espacial en experimentos numéricos de las LALO. Realizamos simulaciones numéricas dependientes del tiempo de las LALO utilizando la configuración magnética 2D con la masa de protuberancia cargada en sus depresiónes magnéticas. Excitamos las LALOs perturbando la masa de protuberancia a lo largo del campo magnético. Realizamos los experimentos con cuatro valores de resolución espacial: 240, 120, 60 y 30 km. Hemos estudiado las propiedades de las LALO en las diferentes regiones de protuberancia. En las regiones de protuberancia inferior y central, obtenemos que los LALO están fuertemente amortiguados incluso usando simulaciones de alta resolución. Comparando el tiempo de amortiguamiento en los diferentes experimentos, encontramos que aumenta significativamente cuando aumentamos gradualmente una resolución espacial. Sin embargo, la diferencia entre los experimentos con resolución espacial 30 y 60 km es relativamente pequeña. Esto sugiere que una mejora adicional de la resolución espacial no afecta el tiempo de amortiguamiento. Esto también indica que hay un mecanismo físico responsable de la atenuación en esta región de la protuberancia en lugar de una disipación numérica. En la región superior de la protuberancia, los movimientos del plasma se amplifican sorprendentemente en la primera fase durante los primeros 130 minutos y decaen lentamente en la segunda fase. La amplificación se vuelve aún más eficiente con el incremento de la resolución espacial. Para comprender mejor el motivo del fuerte amortiguamiento en la parte inferior y la amplificación en la parte superior, hemos analizado la evolución temporal de las diferentes contribuciones de la energía. El análisis revela que una parte de la energía se emite en la corona circundante debido a la fuga de ondas. El diagrama de tiempo-distancia de la velocidad transversal confirma la existencia de ondas que se propagan hacia arriba. La fuerza de Lorentz en la parte superior de la protuberancia actúa de manera opuesta que en la parte inferior. Realiza un trabajo positivo durante la etapa inicial de oscilaciones y puede ser responsable de la aceleración del plasma. Además, hemos analizado la integral de tiempo del flujo de Poynting entrante en las regiones superior e inferior de la protuberancia. El análisis revela que una parte significativa del flujo magnético que sale de la región inferior se transfiere a la parte superior. Concluimos que la fuerte atenuación de las oscilaciones en la región inferior es causada parcialmente por la fuga de ondas y de la energía y la transferencia de impulso a través de las líneas de campo desde la parte inferior a la región superior de la protuberancia. Además, los experimentos de alta resolución son cruciales al estudiar los períodos y el mecanismo de amortiguación de las LALO. El período concuerda bien con el modelo de péndulo solo cuando se usa una resolución espacial suficientemente alta. Los resultados sugieren que la difusión numérica en simulaciones con resolución espacial insuficiente puede ocultar importantes mecanismos físicos, como la amplificación de las oscilaciones.

En la última parte de esta tesis, hemos estudiado la excitación de las LAO por perturbaciones externas considerando tanto las configuraciones magnéticas de cuerda de flujo como de arcada cizallada. Además, consideramos dos tipos diferentes de perturbaciones externas. El primer tipo está asociado con un evento eruptivo cerca de la protuberancia tipo cuerda de flujo. El segundo tipo implica el uso de la perturbación artificial ubicada a cierta distancia de la protuberancia modelada como dos cuerdas de flujo o la arcada cizallada que contiene la protuberancia. En los primeros experimentos con erupción como la perturbación externa, obtenemos que no produce las LAO en la protuberancia ubicada en su vecindad. Sin embargo, la erupción produce cambios en la configuración de la protuberancia y también desencadena oscilaciones de pequeña amplitud (SAO, por sus siglas en inglés). Durante la erupción, se forma una capa de corriente alargada detrás de la cuerda de flujo en erupción. Las flujos de entrada en la reconexión producen cambios en el campo magnético de la protuberancia. Además, la capa de corriente se vuelve inestable y comienzan a formarse islas magnéticas en ella. Estos plasmoides se forman moviéndose hacia arriba o abajo. Los plasmoides que se propagan hacia abajo causan perturbaciones en el campo de velocidad cuando chocan con los bucles llamados “post-reconnection”. Esta pertur-

bación de velocidad se propaga en los alrededores y entra en la cuerda magnética provocando la perturbación de la protuberancia. El análisis de los movimientos oscilatorios del plasma de la protuberancia en la cuerda muestra que solo se excitan las SAO amplitud debido a la erupción cercana y la inestabilidad de los plasmoides. Los movimientos tienen un carácter complejo mostrando una mezcla de modos longitudinales y transversales con períodos largos y cortos. Los experimentos con una perturbación artificial distante muestran que la onda de este evento energético podría propagarse a través del campo magnético, alcanzando protuberancias cercanas y lejanas. El estudio de los movimientos revela la excitación de las LAO transversales y SAO longitudinales en ambas protuberancias. Las propiedades de las oscilaciones, como la amplitud, el período y el comportamiento de amortiguación, son similares en ambas cuerdas magnéticas. En la región superior de las cuerdas magnéticas, la amplitud de las SAO longitudinales aumenta gradualmente durante los primeros minutos después de la perturbación por el frente de onda. En este experimento, el frente de onda produce la inclinación del campo magnético de la cuerda magnética. Posteriormente el campo magnético recupera la configuración inicial. El plasma de la protuberancia sigue el movimiento de la cuerda de flujo, aumentando la amplitud de la oscilación longitudinal. También hemos estudiado la activación externa de las LAO en un modelo de arcada cizallada. El análisis muestra que aunque el vector normal del frente de onda es paralelo al eje de la configuración magnética, esta perturbación no excita a las LALOs. Cuando el frente de onda se acerca a la protuberancia, empuja el plasma denso hacia abajo. Por lo tanto, la onda desencadena las LAO verticales y movimientos de compresión y rarefacción a lo largo del campo magnético.

Abstract

In this thesis, we focus on studying the properties of the large-amplitude prominence oscillations (LAOs) using the realistic prominence models and the triggering of such motions by external perturbations. LAOs involve motions with the velocity amplitudes above $20\,\mathrm{km\,s^{-1}}$, and large portions of the filament move in phase, indicating a strong connection with the magnetic field structure of the filament. Such motions are triggered by solar energetic events such as distant or nearby flares, jets, and eruptions. The motivation of this work comes from the recent studies that have shown that LAOs are very common in prominences and open a new window to study the prominence structure by means of a technique known as prominence seismology, which combines observations and theoretical modeling of LAOs. This study is based on time-dependent numerical simulations performed with the magnetohydrodynamic (MHD) code MANCHA3D.

In the first part of this work, we perform 2.5D numerical simulations of LAOs using a magnetic flux rope model formed from a sheared arcade configuration using converging motions at the foot points. We artificially load the prominence mass in the magnetic dips of the flux rope, and then we apply horizontal and vertical perturbations to excite the different oscillation modes. Horizontal triggering excites the large-amplitude longitudinal oscillations (LALOs) together with the small-amplitude vertical oscillations caused by the back-reaction of the magnetic field. The period of the longitudinal oscillations decreases with decreasing of the radius of curvature of the magnetic field lines, in agreement with the pendulum model. Vertical perturbation triggers the vertical LAOs of the prominence plasma and the symmetric oscillations along the magnetic field. These latter motions are caused by compression and rarefaction of the plasma. The vertical LAOs are very synchronized in the different prominence regions, and their period remains constant with height. This suggests that the vertical mode corresponds to the global normal mode of the prominence structure. Analysis of the time-distance diagram of the transverse velocity reveals the presence of the fast magnetoacoustic waves emitted from the prominence region. This makes us suggest that wave leakage can be responsible for the damping of the vertical LAOs in this experiment. We have compared the properties of the modes of the longitudinal and transverse oscillations in the prominence models with the different shear angles of the magnetic structure and the prominence density contrasts. We have found that only the variation of the shear angle slightly affects the period of the LALOs. This is associated with the variation of the radii curvature in the 2D projection in these models. The period of the vertical oscillations slightly depends on the density due to the effect of the prominence inertia. We have also studied the excitation of the LAOs in the flux rope prominence by an external perturbation. This experiment shows that the wave from the energetic event strongly perturbs the flux rope magnetic field structure. The prominence mass follows those changes in the magnetic field configuration and moves from the equilibrium position due to the motion of the magnetic field. This strong perturbation of the rope produces the motion of the prominence plasma, but there is no direct wave front from the energetic event reaching the prominence mass. The external disturbance perturbs the flux rope exciting oscillations of both polarizations. Their properties are a mixture of those excited by purely horizontal and vertical excitation. For the experiment with horizontal triggering, we perform convergence studies, and we find that the damping of the oscillation is mainly numerical, but the numerical effects can be reduced by increasing the spatial resolution. This motivates the numerical experiments presented in the following.

In the second part of the work, we have studied the influence of spatial resolution on numerical experiments of LALOs. We perform time-dependent numerical simulations of LALOs using the 2D magnetic configuration with the prominence mass loaded at its dips. We trigger LALOs by perturbing the prominence mass along the magnetic field. We perform the experiments with

four values of spatial resolution: 240, 120, 60, and 30 km. We have studied the properties of LALOs in the different prominence regions. At the bottom and central prominence regions, we obtain that LALOs are strongly damped even using the high-resolution simulations. Comparing the damping time in the different experiments, we find that it increases significantly when we gradually increase a spatial resolution. However, the difference between the experiments with spatial resolution 30 and 60 km is relatively small. This suggests that a further improvement of the spatial resolution should not significantly affect the damping time. This also indicates that some physical mechanism might be responsible for the attenuation in this prominence region rather than the numerical dissipation. At the top prominence region, the plasma motions are surprisingly amplified in the first phase, during 130 minutes, and slowly decay in the second phase. The amplification becomes even more efficient with the improvement of the spatial resolution. In order to understand further the reason for the strong damping at the bottom and the amplification at the top, we have analyzed the temporal evolution of the different energy contributions. The analysis reveals that a portion of the energy is emitted in the surrounding corona due to wave leakage. The time distance diagram of the transverse velocity confirms the existence of waves propagating upward. The Lorentz force acts in an opposite way at the upper prominence region than at the bottom. It does positive work during the initial stage of oscillations and can be responsible for the acceleration of the plasma. We have analyzed the time-integral of the incoming Poynting flux at the top and bottom prominence regions. The analysis reveals that a significant portion of the magnetic flux that leaves the bottom region is transferred to the top. We conclude that the strong attenuation of the oscillations at the bottom region is caused partially by the wave leakage and the energy and momentum transfer across the field lines from the bottom to the top prominence regions. We conclude that the high-resolution experiments are crucial when studying the periods and the damping mechanism of LALOs. The period agrees well with the pendulum model only when using a sufficiently high spatial resolution. The results suggest that numerical diffusion in simulations with insufficient spatial resolution can hide important physical effects, such as the amplification of the oscillations.

In the last part of this thesis, we have studied the excitation of LAOs by external perturbations considering both the flux rope and dipped arcade magnetic configurations. We consider two different types of external disturbances. The first type is associated with an eruptive event near the flux rope prominence. The second type implies using an artificial perturbation located at a certain distance from two flux rope prominences or the dipped arcade containing the prominence. In the first experiment, when the eruption acts as an external perturbation, we obtain that this eruption does not produce LAOs in the prominence located in its vicinity. However, the eruption produces changes in the magnetic configuration of the prominence and triggers the small-amplitude oscillations (SAOs). During the eruption, an elongated current sheet is formed behind the erupting flux rope. The reconnection inflows also affect the prominence magnetic field. In addition, the current sheet becomes unstable, and magnetic islands start to form in it. After these plasmoids are formed, they move upward or downward. Those plasmoids that propagate downward cause perturbations in the velocity field by colliding with the post-reconnection loops. This velocity perturbation propagates in the surroundings and enters the flux rope causing the disturbance of the prominence mass. The analysis of the oscillatory motions of the prominence plasma in the flux rope shows that only SAOs are excited due to the nearby eruption and the plasmoid instability. The motions have a complex character showing a mixture of longitudinal and transverse oscillations with short and long periods.

Another series of experiments with a distant artificial perturbation shows that the wave created by such an energetic event can propagate across the magnetic field, reaching both the closer and further flux rope prominences. The study of the motions reveals the excitation of the transverse LAOs and longitudinal SAOs in both prominences. The properties of the oscillations,

such as amplitudes, periods, and damping times, are similar in both flux ropes. In the upper region of the flux ropes, the amplitude of the longitudinal SAOs gradually increases during the first minutes after the wave front propagation. In this experiment, the wave front produces the inclination of the magnetic field of the flux rope. Later the magnetic field recovers its initial configuration. The prominence plasma follows the motion of the flux rope, increasing the amplitude of the longitudinal oscillation.

Finally, we have studied the external triggering of LAOs in a dipped arcade model. The analysis shows that even though the normal vector of the wave front is parallel to the spine of the magnetic configuration, this perturbation does not excite LALOs. When the wave front approaches the prominence, it pushes the dense plasma down. Therefore, the wave triggers the vertical LAOs and motions due to compression and rarefaction along the magnetic field.

Contents

1

Introduction

The dynamics of solar prominences have been actively studied in recent decades. Of particular interest is the investigation of solar prominences oscillations. Due to the complex structure of solar prominences and the lack of information on the magnetic field and plasma properties from the direct measurements, researchers were forced to look for new approaches to study these objects. Interpretation of oscillations in terms of MHD waves opens a new window for the study of prominences. In particular, the large-amplitude oscillations (LAOs), which have a global nature, allow us to extract information about the large-scale structure and properties of solar prominences, relating the oscillatory periods and damping times to different parameters of the plasma and magnetic field configuration using theoretical modeling. This technique is called *prominence seismology*. Furthermore, the LAOs are often triggered by an external perturbation associated with a wave that comes from an energetic event, such as a solar flare, an eruptive event, or an activity of a nearby jet. This makes it possible to study the propagation, interaction, and impact of these energetic disturbances on the prominence structure.

1.1 Solar prominences

Solar prominences, also called filaments, are clouds of cold and dense plasma suspended in the solar corona. The early solar astronomers observed these mysterious "red flames" during the solar eclipses making drawings of these structures (see more in Tandberg-Hanssen 1995). The first reported observation of a prominence is by Vassenius (1773) who noticed their red color and temporal evolution, which explains the given name, "red flames". During this early phase, it was speculated that the prominences were part of the lunar atmosphere or mountains of the Sun. The drawings of the prominence structures during the solar eclipses helped to establish their solar origin. A big step in the study of these solar objects was done with the invention of photography. The photography allowed to obtain permanent records of the prominences, and, as a consequence, many prominence properties were extracted from these observations, such as shape, altitude, and emissivity. The subsequent advances in the prominence observations were achieved with the spectrographic methods. The spectrographic prominence observations during the solar eclipse in 1868 confirmed the gaseous nature of the prominences by detecting the two lines of hydrogen, two lines of sodium, and one unknown spectral line. Janssen (1868) and Lockyer (1868) realized that the unknown line did not match any known element and postulated the existence of a new one. Since the element had been found in the Sun, it was named Helium. Later, this element was also found on the Earth (Palmieri 1881; Ramsay 1895). Using a narrow slit for spectroscopy and a wide slit for monochromatic imaging, different aspects associated with prominences were investigated, such as eruptions, correlation of the number of prominences with

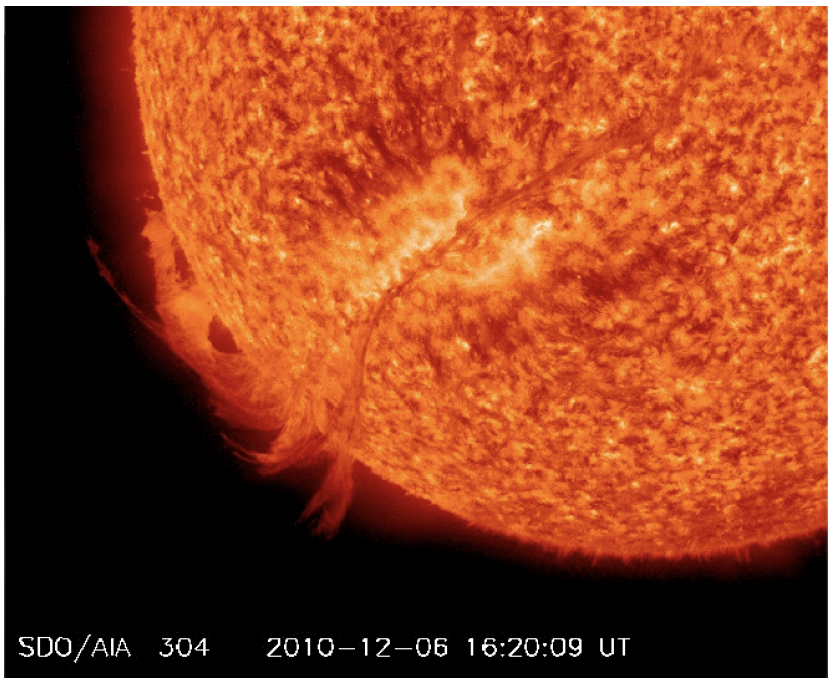

Figure 1.1: Erupting prominence-filament as seen by AIA/SDO in the He II line at 30.4 nm.

the solar activity, and even the prominence "fine structure", called prominence threads. From the width of the spectral line, the prominence temperature was estimated for the first time. With the invention of the spectroheliograph (Hale & Ellerman 1903), using Hα and H and K lines of ionized calcium, it was found that the dark structures on the disk are the same as off-limb prominences. These dark structures were called filaments. Since then, the terminology is the following: an object is called filament when seen on the disk as a dark structure (absorption in lines like Hα) and seen above the limb as a bright structure we call it prominence. In this thesis work, the terms filament and prominence are equivalent in the whole text. The prominence-filament structure example is shown in Figure 1.1. This figure shows that the bright and dark regions of the prominence depend on its position. The dark ones are seen absorbing chromospheric light, while the bright ones are illuminated by the chromospheric light in contrast with the corona in the background. Using the K3 and H spectroheliograms, D'Azambuja & D'Azambuja (1948) studied the law of rotation of filaments as a function of latitude and provided the proof of the solar differential rotation. The invention of the coronograph by Bernard Lyot in 1930 (Lyot 1936) allowed the observers the study of the corona and prominences at any time, even in the absence of eclipses. The coronographs remain an important instrument for solar corona observations. The physical conditions in prominences have been further studied with polarimetry. This allowed obtaining magnetograms that record the location, polarity, and intensity of the solar magnetic fields. Using this technique, Babcock & Babcock (1955) found that prominences are above the neutral line, separating positive and negative polarities. Based on the Zeeman splitting effect, Zirin & Severny (1961) obtained the magnetic field strength

of 200 G in the active region prominences. The Hanlé effect has also been used to estimate weaker magnetic fields in the quiescent prominences using polarimetric observations (Leroy et al. 1977; Sahal-Brechot et al. 1977). The space missions allowed to make another step in our understanding of the nature of solar prominences. For instance, Solar and Heliospheric Observatory (SOHO), Solar Dynamics observatory with AIA telescope, and HINODE with Solar Optical telescope obtained observations of many spectacular Coronal Mass Ejections (mostly associated with the prominence eruptions), demonstrated the dynamics of the different types of prominences.

The first classification of solar prominences was proposed by Secchi (1875) who divided them into steady and active. Since then, there have been proposed different prominence classifications depending on their shape, relative position, origin, or eruptive activity (see more in Vial & Engvold 2015). Nowadays, prominences are mainly classified depending on their relative position to an active region (AR). There are three types: quiescent, intermediate, and active region prominences. Active region prominences are always located in an AR. In contrast, the quiescent type is placed far from any AR in a quiet region. Intermediate prominences have an intermediate position with one end close or inside an AR and the other in a quiet region. Quiescent prominences are usually long-lived, with lifetimes ranging from several days up to several weeks. In contrast, active region prominences have shorter lifetimes and can erupt or disappear several hours after their formation. Active region prominences have a stronger magnetic field up to several hundred Gauss (Kuckein et al. 2009; Guo et al. 2010), and are located at the lower heights of about 20 Mm, while quiescent prominences have a magnetic field strength of $3-45$ G (Leroy 1989; Paletou et al. 2001) and can reach the height of up to 100 Mm. It is an open question to explain how the plasma with chromospheric properties can reach those heights. Intermediate prominences have a combination of characteristics of both active region and quiescent types. The other dimensions of the filaments, such as length and thickness, usually range within $60-600$ Mm and $3-10$ Mm, respectively, although the quiescent prominences are usually longer than the active region prominences.

Typically, a prominences structure consists of a spine, barbs, and extreme ends (see review by Mackay et al. 2010). The spine is the main axis of the prominence body and can be clearly distinguished when seen in absorption on the disk. The barbs are the prominence structural elements that deviate from the prominence spine, forming an angle. It has been suggested that these lateral extensions are plasma in the dips induced by a minor polarity with respect to the dominant polarity (Aulanier & Demoulin 1998). The high-resolution observations of quiescent filaments showed that all three structural components consist of small-scale thread-like components. The threads have a width of ~ 200 km and represent the prominence "fine structure". The orientation of the threads is co-aligned with the local magnetic field (Lin et al. 2005a,b, 2008a,b). Lin et al. (2005a) pointed out that in most cases, the magnetic flux tube is only partially filled with the prominence plasma while the length of the field lines usually significantly exceeds the length of the threads. These structural units are essential for studying the properties of the local magnetic fields because the motions of the threads reflect the topology of the magnetic field.

Filaments or prominences are always observed above the polarity-inversion line (PIL) (Babcock & Babcock 1955). This line lies where the radial component of the magnetic field changes the sign. The filaments are embedded in the filament channels, the regions in the chromosphere surrounding the PIL, which magnetic field is mostly horizontal and the axial component at both sides of the channel has the same direction (Foukal 1971b,a; Martin et al. 1992). It is believed that the magnetic field in the filament channel is a part of the larger structure extended high in the corona. Indeed, direct measurement of the magnetic field in the filaments showed that it is mostly horizontal, having an angle of $15-40$ degrees with the filament spine (Leroy 1989;

Paletou & Aulanier 2003; Collados et al. 2003). Another evidence has been found studying the overlying magnetic field. For instance, the axial component of the magnetic arcades overlying the prominence structure has the same direction as the corresponding component of the magnetic field of the prominence channel (Saito & Hyder 1968; Saito & Tandberg-Hanssen 1973). Using polarimetric observations, Lites (2005) showed that the filament channels include concave magnetic field lines. This may indicate the existence of the concave up lines in the magnetic field of the filament as well.

The measured properties of the prominence plasma vary in different observations. The number density derived from spectropolarimetric observations ranges between $n = 10^{10} - 10^{11}\,\mathrm{cm}^{-3}$ (Hirayama 1985; Parenti & Vial 2007). The temperature of the quiescent prominence core is close to the chromospheric conditions, $6000 - 10000$ K (Stellmacher et al. 2003; Parenti et al. 2005). This suggests that the prominence plasma is approximately 100-times denser and cooler than the surrounding solar corona. Spectroscopic observations showed the emission of the lines of higher temperatures at the filament edges. This region, appearing in emission, has been called prominence-corona transition region (PCTR; see Labrosse et al. 2010).

1.2 Theoretical models of prominence structure

The vertical extent of the prominence usually lies in the range of $15 - 100$ Mm with no signs of strong vertical stratification of the plasma. This dimension exceeds by two orders of magnitude the pressure scale height of the prominence plasma. In this situation, the gas pressure gradient cannot support such tall structures. The most important questions that arise are: how these heavy structures are supported against gravity and what is the origin of their mass. It is generally accepted that the support of the prominences is due to their magnetic fields. However, there are still many unknowns about the magnetic field structure. Apart from giving support, the magnetic field isolates the cold prominence mass from the million-degree solar corona. Similarly, several models have been proposed to explain the origin of the prominence mass. In the following, we discuss the models suggested to explain both aspects.

1.2.1 Magnetic field modelling

The observations described above suggest that the filament magnetic field is nonpotential, with a strong axial component mostly aligned with the filament axis. The resulting structure is a sheared magnetic field. Additionally, the magnetic field must have a dipped region to provide support to the cold prominence mass against gravity. These constraints have to be satisfied by theoretical models of the magnetic configuration.

One of the early models is the one by Kippenhahn & Schlüter (1957) who proposed a magnetic structure containing dips. In this model, the cold prominence plasma weight is balanced by the magnetic tension in the dips. The magnetic field structure is non-force-free. The magnetic tension on the dips is exactly equal to the weight of the prominence. Thus the curvature of the dips depends on the mass of the prominence. In the absence of prominence, the field is completely straight and horizontal. In this sense, the prominence mass deforms or bends the field lines generating the dips. This model has a normal polarity field. This means that the polarity of the field at the prominence is the same as the photospheric field. However, in most of the observations, the polarity is inverse. Kuperus & Raadu (1974) proposed an alternative model where the magnetic structure has the inverse polarity and contains the dips even in the absence of the prominence plasma. In this model, it is assumed that the cool prominence plasma weight is small compared to the magnetic tension or the magnetic pressure gradient force. The presence of the prominence produces a small perturbation of the magnetic structure with no

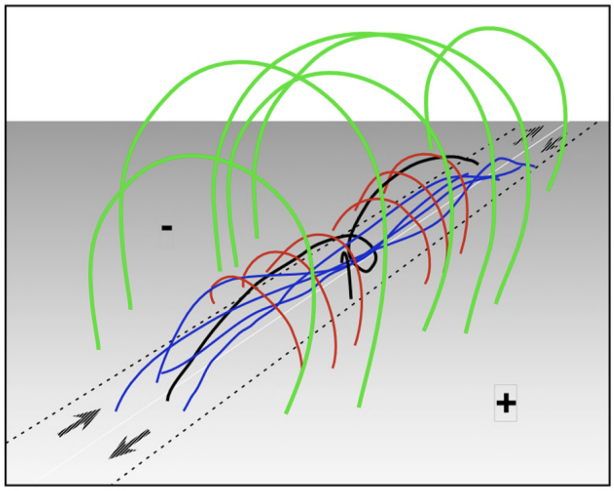

Figure 1.2: Filament magnetic structure represented by a sheared arcade. The white line denotes the PIL; the signs denote the dominant polarity at the each side of the PIL; the arrows show direction of the shearing motion. Color lines denote different types of the field lines formed from a bipole by the shearing motions. Adapted from Mackay et al. (2010).

significant deformations.

In contrast to Kippenhahn & Schlüter (1957), in many of the recent works on prominence modeling, it is assumed that the magnetic field structure of the filament channel is independent of the evolution of the plasma and is not largely modified by the presence of the prominence. This assumption is based on the fact that the time scales of the evolution of the magnetic field are much longer than the time scales associated with the plasma flows in noneruptive prominences (Gaizauskas et al. 1997, 2001; Wang & Muglach 2007). There is still a debate regarding the structure of the filament channel. However, the proposed models can be roughly divided into the sheared arcade and the flux rope. In the former, the structure consists of a sheared arcade over the PIL (Antiochos et al. 1994; DeVore & Antiochos 2000; Aulanier & Schmieder 2002; DeVore et al. 2005). In the latter, a flux rope lies horizontally above the PIL (Kuperus & Raadu 1974; Pneuman 1983; van Ballegooijen & Martens 1989; Priest et al. 1989; Rust & Kumar 1994; Aulanier & Demoulin 1998; Chae et al. 2001; Gibson & Fan 2006). In both groups of models, the resulting structure contains twisted field lines. Observations show that the field around the prominence is likely weakly twisted. In this regard, the set of field lines that supports the prominence is similar in both models.

Sheared arcade structure is formed from an initial simple bipolar magnetic structure by imposing a shearing motion along the PIL. (Antiochos et al. 1994; DeVore & Antiochos 2000; Aulanier & Schmieder 2002; DeVore et al. 2005). The field lines move in the opposite directions at each side of the PIL, increasing the shear and the axial component. During this process, the magnetic field lines become elongated and even can reconnect. The newly formed magnetic configuration includes different types of field lines as shown in Figure 1.2. However, not all the field lines are suitable for hosting the prominence material (Luna et al. 2012a). The green and red lines are not capable of hosting stable prominence due to the absence of the dipped region. However, they can host the short-lived threads that are draining back to the chromosphere. This

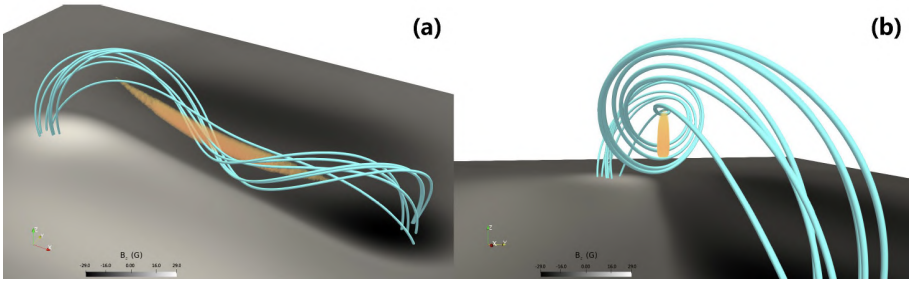

Figure 1.3: Different perspectives of a flux rope prominence model and magnetic field lines in 3D, when the equilibrium after the mass loading is reached. The yellow isosurfaces denote the prominence mass with the density contrast 20 with respect to the corona. The blue lines represent the selected magnetic field lines. Adapted from Zhou et al. (2018).

phenomenon has been called coronal rain (Müller et al. 2003, 2005). The black lines have only one twist and, consequently, one dip where the prominence plasma can reside. The blue lines can be considered as the most suitable for the support of the longer threads. In particular, only these long field lines are suitable for forming the long condensations in the evaporation-condensation model described below.

A flux rope model is a model that consists of a twisted magnetic structure with a strong axial component. The bottom helical part of a flux rope can host the prominence mass (see Figure 1.3). Prominence models are constrained to be in magnetostatic equilibrium with their surroundings. The flux rope equilibrium is achieved with the help of the coronal arcades overlying the flux rope. These coronal arcades provide the magnetic tension force needed to hold the flux rope at the low corona. The flux rope models can be divided into two groups according to the mechanisms of the flux rope formation. The first type of model explains the formation of a twisted flux rope via surface processes. The second type of model considers the flux rope forming below the surface due to subsurface motions and rising to the photosphere and above. The observations by Gaizauskas et al. (1997, 2001) and Wang & Muglach (2007) indicate that the quiescent and intermediate filaments are formed due to the reconfiguration of the coronal magnetic field by the surface motions. The observations by Lites & Low (1997) and Okamoto et al. (2009) reveal that the active region filaments are formed due to the flux rope emergence, dragging cool, and dense photospheric plasma into the corona.

Surface models of the flux rope formation follow the hints from the observations (Hindman et al. 2006) about the existence of the strong shear motions at the surface below the filament. Surface mechanisms can also include differential rotation and converging flows onto the PIL. Observations by Gaizauskas et al. (1997, 2001) showed that surface motions play a critical role in forming the filament channel and the filament. The main idea of surface models is to form a flux rope structure using different types of surface motions or their combinations. van Ballegooijen & Martens (1989) considered a flux rope formation using the shearing and converging motions (Fig 1.4). The authors applied the shearing motions followed by the convergence in the direction to the PIL at the base of the bipole. Due to the shearing motions, the foot points move in opposite directions, and the distance between them increases. This process increases the shear and the axial component of the magnetic field. The authors then applied the converging motions in the direction to the PIL. These motions bring the foot points from the different sides together. When the field lines approach each other at the PIL, they may reconnect, producing a long axial

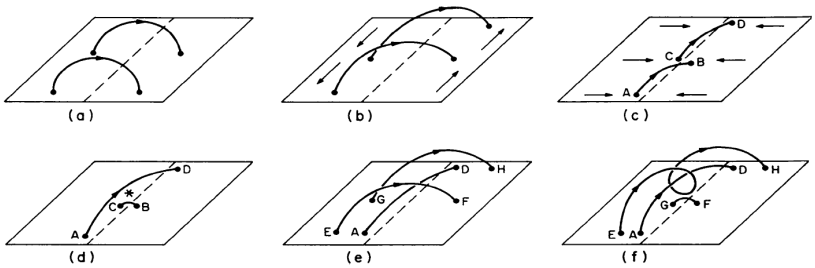

Figure 1.4: Illustration of the mechanism of the flux rope formation via shearing and converging surface motions proposed by van Ballegooijen and Martens. Adapted from van Ballegooijen & Martens (1989).

field line with a twist and a small post-reconnection loop remaining under this field line. This process can be repeated many times, creating a twisted flux rope that includes the dipped region for the filament support. There were different variations of the van Ballegoojien and Martens model. Based on this approach, Martens & Zwaan (2001) considered the flux rope formation by the interaction of two bipoles. The models mentioned above use the surface motions to form the flux rope structures. However, it has to be noted that these processes involve higher velocities of the shearing and convergence motions than actually observed in the photosphere. More realistic surface velocities would imply longer time scales of the flux rope formation.

The subsurface models consider that the flux rope is formed by the subsurface motions, and it rises to the corona due to the magnetic buoyancy, carrying the chromospheric material in the dips (Rust & Kumar 1994). Such models have been widely studied in numerical simulations. Moreno-Insertis (2004), Archontis et al. (2004); Archontis (2008); Murray et al. (2006); Galsgaard et al. (2007) showed that the flux rope axis cannot rise through the photosphere when only using the magnetic buoyancy. This suggests that the dipped structure cannot appear in the corona due to the rising of the flux rope. However, the upper part of the flux rope can emerge in the corona. Therefore, the flux rope in the corona can be formed by reconfiguring the emerged magnetic structure. Many authors followed the above approach to form the rising flux rope structures (see, e.g., Manchester et al. 2004; Magara 2006; Archontis & Török 2008; Fan 2009). Fan (2009) showed a possible scenario of the formation of the flux rope from an emerged U-loop due to the shearing and rotational motions at the base of the structure in the photosphere in the 3D MHD simulations (Fig 1.5). This experiment demonstrates that the formed magnetic structure is able to reach coronal heights.

There have been many attempts to reproduce realistic magnetic flux ropes by extrapolating the magnetic field obtained from the photospheric magnetograms to the corona. Extrapolations using linear magnetohydrostatic and linear force-free models produce a helical flux rope, and the plasma is assumed to reside in the dipped region. Nonlinear force-free field (NLFFF) models allow one to obtain a more complete picture and model not only the flux rope but also its surrounding. Several authors developed NLFFF models by extrapolating the observed photospheric magnetic fields (Régnier et al. 2002; Régnier & Amari 2004; Régnier & Canfield 2006; Régnier & Priest 2007; Canou et al. 2009). van Ballegooijen (2004) proposed the alternate technique to build NLFFF. Their approach involves inserting a flux rope into a potential field. The magnetic field then evolves to an equilibrium state after a magnetofrictional relaxation. As a consequence, van Ballegooijen (2004) obtained an NLFFF model that includes the flux rope and

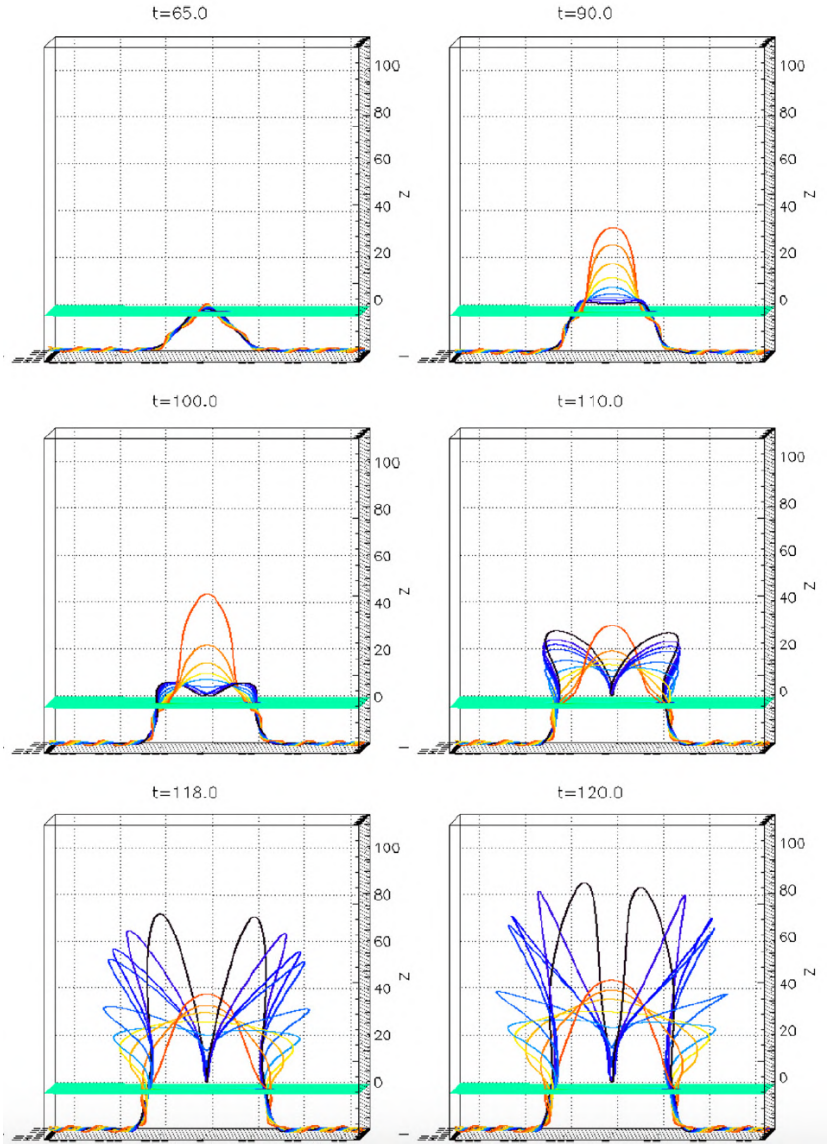

Figure 1.5: Temporal evolution of the tracked magnetic field lines in a 3D model of the flux rope formation. The upper part of the highly twisted flux rope rises from the photosphere and becomes twisted due to the shearing and rotational motions at the foot points at the photosphere. The different colors are used to follow the evolution of the different field lines. Adapted from Fan (2009).

its surrounding. Models based on extrapolations allowed some authors to estimate the magnetic twist and investigate the flux rope stability (Su et al. 2009).

1.2.2 Models for the prominence plasma

As we have discussed before, the prominence density is a hundred times larger than that of the ambient corona, and it is extended up to the heights of 100 Mm, having an enormous mass. Several decades ago, the researchers realized that this large prominence mass must come from the chromosphere rather than the corona. The reason is that the chemical composition of prominences is similar to the chromosphere (Vial & Engvold 2015), and a huge portion of the coronal material would be required to create a prominence. Several mechanisms have been proposed to explain how the chromospheric plasma is converted into prominence above the corona. All the models of the prominence mass formation can be roughly divided into three groups: injection, levitation, and evaporation-condensation models.

Injection models explain the loading of the cold plasma into the corona due to an upward force associated with the magnetic reconnection in the chromosphere (Wang 1999; Chae 2001). This reconnection can happen, for example, between minor-polarity intrusions and the main-polarity filament magnetic field (Litvinenko 2000; Wang 2001; Chae et al. 2005). The reconnection produces unidirectional flows of the mass inside the flux tube. In order to explain the counterstreaming motions, it is assumed that the reconnection happens at both sides of the PIL. The injection model is supported by observations that show strong jetting throughout the chromospheric network (see, e.g. De Pontieu et al. 2007). However, on the one hand, this model can hardly explain the frequency of the appearance of the prominence mass in the corona and the predominantly horizontal mass flows. On the other hand, it is unclear if the reconnection at the chromosphere can produce the flows of the material reaching the height of typical quiescent filaments. Nevertheless, the injection models can be suitable to explain mass loading in active region prominences.

According to the levitation model, the plasma in filaments is assumed to be lifted by the magnetic field that rises from the convective zone. This model is, therefore, directly related to the subsurface models of the magnetic field formation described in Section 1.2.1. Two possibilities for transporting plasma into the corona are considered in a frame of the levitation model. The first one assumes that a twisted flux rope emerges in the corona and brings cold material in the dipped regions. The second one uses reconnection or flux cancellation after the magnetic field emergence as a main reason for lifting the mass (van Ballegooijen & Martens 1989; Priest et al. 1996; Oliver et al. 1999; Litvinenko & Martin 1999; Galsgaard & Longbottom 1999; Litvinenko & Wheatland 2005; Welsch et al. 2005). The numerical simulations showed that the latter mechanism could indeed deliver the cold plasma. However, the density contrast of the lifted mass with respect to the corona is only 20 %, which is too low for a typical prominence (Galsgaard & Longbottom 1999). The simulations also showed that the U-loops could not break through the photosphere and bring the plasma high in the corona. This makes it difficult for the levitation models to explain the mass appearance of the intermediate and quiescent filaments (Fan 2001; Archontis et al. 2004; Manchester et al. 2004; Mackay & van Ballegooijen 2006; Galsgaard et al. 2007; Archontis & Török 2008). Yet another scenario can be considered for the levitation model, i.e., the reconfiguration of the emerged magnetic fields could lead to the flux rope formation and rising it high into the corona, dragging cool plasma in the dips. In a recent work based on high-resolution 2.5D simulations, Jenkins & Keppens (2021) studied the levitation-condensation scenario of the prominence formation, where a coronal flux rope forms and eventually builds up in-situ condensations.

The evaporation-condensation models consist of the evaporation of the chromospheric plasma

that flows along the field lines and the subsequent condensation of this plasma in the dips of the filament channel. The plasma evaporates due to the coronal heating near the foot points (Aschwanden et al. 2001; Winebarger et al. 2002) If the loop length is larger than the critical length, defined by the properties of thermal conduction and the heating and cooling processes, the plasma starts to cool down, reaching the distance where the heating is negligible, and thermal conduction cannot compensate for the cooling. The plasma continues cooling down until it condenses and the thermal equilibrium is recovered. The length of the field lines of the quiescent filaments significantly exceeds the length of an ordinary loop. This indicates that the evaporation-condensation model is the most plausible for the quiescent and intermediate filament formation. However, this model cannot explain the mass formation in active region filaments because the length of their magnetic field lines is too short to let the thermal instability develop. The numerical simulations explored the main properties of the dynamics and evolution of the condensations (Antiochos et al. 1999, 2000; Karpen et al. 2001, 2003, 2005, 2006; Karpen & Antiochos 2008; Xia et al. 2011, 2012a; Luna et al. 2012c; Xia et al. 2012b; Xia & Keppens 2016). Varying the properties of the heating process at the base, the authors demonstrated the possibility of the repetitive cycles of condensation formation and counterstreaming motions. The estimates for the speed of the flow, the lifetimes, and the sizes of the condensations show good agreement with observations of the quiescent filaments. A more detailed description of the theoretical models of prominence formations can be found in the review by Mackay et al. (2010).

1.3 Prominence oscillations

Observations reveal that solar prominences are highly dynamic with many kinds of motions, including ubiquitous oscillations and waves. The first evidence for prominence oscillations goes back to the first part of the 20th century (Dyson 1930; Newton 1935; Bruzek 1951; Dodson 1949; Moreton & Ramsey 1960; Ramsey & Smith 1965, 1966; Hyder 1966). In these early works, the observed filaments were called "winking filaments". The authors found that the filament appeared and disappeared from the Hα filter images. This blinking is associated with the line-of-sight (LOS) velocity that produces the Doppler shifts of the spectral line in and out of the line center pass-band filter. Observations were performed with the narrow-band Hα filters with a spectral width of 0.5Å indicating that the LOS oscillation velocity of the winking filaments should be larger than $23\,\mathrm{km\,s^{-1}}$. Moreton & Ramsey (1960) found evidence that the triggering of the oscillation is related to a wave emanating from flares that shake the prominence. Later on, with the development of spectroscopic techniques, oscillations with velocity amplitudes much smaller than those of the winking filaments were found. The detected velocities range from the noise level of $0.1\,\mathrm{km\,s^{-1}}$ up to $10\,\mathrm{km\,s^{-1}}$.The first observation of this kind of oscillation is by Harvey (1969). Since then, a large number of observations have been obtained (see reviews by Tripathi et al. 2009; Arregui et al. 2018).

There have been several attempts to classify the oscillations according to their observable properties such as period, amplitude, the direction of oscillation (i.e., polarization), or triggering type (e.g. Tsubaki 1988; Vrsnak 1993). However, the classification happened to be not very straightforward since one event can be classified as belonging to multiple oscillation types. Oliver (1999) and Oliver & Ballester (2002) proposed a classification based on the velocity amplitude. The oscillations were roughly divided into small-amplitude oscillations (SAOs) with velocities up to $2-3\,\mathrm{km\,s^{-1}}$ and large-amplitude oscillations (LAOs) with a velocity equal to or larger than $20\,\mathrm{km\,s^{-1}}$. This classification was done to distinguish SAOs from winking filaments, which are LAOs.

In recent decades, a large number of oscillation events have been observed, with many of the oscillations having intermediate amplitudes between a few $\mathrm{km\,s^{-1}}$ and up to $20\,\mathrm{km\,s^{-1}}$.

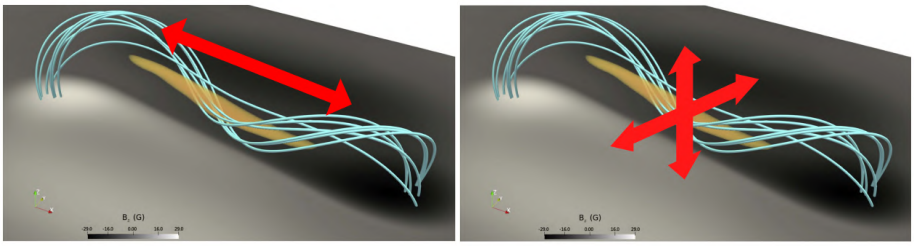

Figure 1.6: Same as Figure 1.3 but showing different polarizations of the oscillations. The arrows show the direction of motion. Left panel: longitudinal motions; right panel: transverse oscillations including vertical and horizontal polarizations

Nowadays, the classification according to the velocity amplitude remains, but its interpretation has changed. According to the modern classification scheme, the LAOs have amplitudes larger than 10 km s^{-1}, a typical value of the sound speed in the prominence plasma, while the SAOs have amplitudes below that value. Exceeding the local sound speed, the LAOs could be nonlinear, while the SAOs would be linear. LAOs are often triggered by external perturbations such as Moreton and EIT (EUV) waves (Eto et al. 2002; Okamoto et al. 2004; Gilbert et al. 2008; Asai et al. 2012; Liu et al. 2012, 2013; Shen et al. 2014a; Xue et al. 2014; Takahashi et al. 2015; Zhang & Ji 2018) or nearby activity such as jets, flares, subflares (Jing et al. 2003, 2006; Vršnak et al. 2007; Li & Zhang 2012a). A large portion of the filament oscillates, reflecting the global characteristics of the plasma and the magnetic field structure. In contrast, SAOs are, in general, not related to the flare activity or any energetic disturbance, and only a small part of the prominence is involved in the motion (see review by Arregui et al. 2018).

Large-amplitude oscillations are additionally classified according to the polarization of the oscillatory motions. Large-amplitude longitudinal oscillations (LALOs) are motions parallel to the magnetic field, whereas transverse LAOs are perpendicular to the magnetic field. Also, transverse oscillations can be vertically or horizontally polarized. A sketch of the different polarizations is shown in Figure 1.6. This figure illustrates a flux rope prominence model by Zhou et al. (2018) showing the filament channel field lines and the cold mass at the dipped part of those lines. The arrows indicate the longitudinal (left panel) and both transverse vertical and horizontal oscillations (right panel).

1.4 Observations of LAOs

Large-amplitude oscillations are very spectacular phenomena that increasingly attract the attention of solar observers. In this section, the main results of the observations of LAOs with different polarizations are described. The first systematic investigation of the prominence oscillations in the "winking filaments" has been done by Ramsey & Smith (1965, 1966) and, later on, by Hyder (1966). From Hα spectrograms, Ramsey & Smith (1966) deduced that the same filament excited by the different triggers oscillated with the same period. This indicates that the filaments have their proper characteristic periods of oscillations. The above idea has been taken as a basis for the prominence seismology. This technique allows deriving the magnetic field and plasma properties from the oscillatory characteristics. More recently, with the development of new telescopes and instruments, the number of reported LAOs and the quality of the observations have increased.

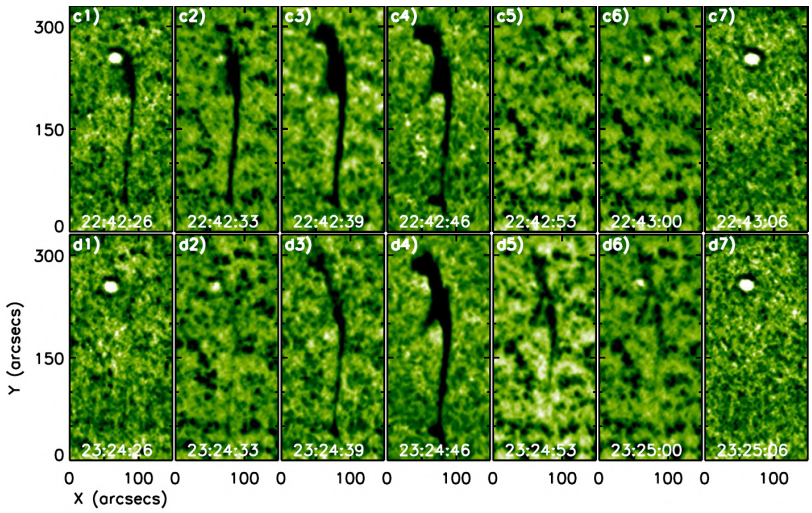

Figure 1.7: Hα images showing oscillating (winking) filament. From left to right: monochromatic images at -1.2, -0.8, -0.5, 0.0, +0.5, +0.8, and +1.2 Å from Hα line center and nearly the same moment of time. The sequence of images at the bottom row is taken at a later time than the one at the top row. Adapted from Shen et al. (2014a).

In the following, we briefly describe some examples of the LAOs observations of the transverse and longitudinal polarizations. A very interesting observation was reported by Shen et al. (2014a). The EUV disturbance after the X2.1 flare propagated in the corona as an upward dome-like wave and a surface wave. The authors found the temporal and spatial consistency between the arrival of the surface wave and the start of the filament oscillations. The author suggested that the filament oscillations were triggered by the surface wave from the energetic event. The four successive winking filaments were excited one by one according to the distance to the energetic event. These filaments showed a clear pattern of oscillations. The authors fitted the Doppler signal to a damped sinusoidal function and obtained the periods in the range of $11-22$ minutes, Doppler velocities of $6-14\,\mathrm{km\,s^{-1}}$, and damping times of $25-60$ minutes. Each triggered filament showed its own period of oscillations, although the exciter was the same EUV wave. Furthermore, not all the filaments responded to the perturbation. One of the unperturbed filaments was located very close to the energetic event. It is unclear why some of the filaments showed oscillatory motions while the others seemed to be unperturbed. Figure 1.7 shows the time sequence of line-center Hα images of one of the winking filaments. In each row, the panels show monochromatic filament images at the same wavelengths but at two consequent moments of time. In the panels (c1)-(c3), we see that the filament becomes more visible and its contrast increases, while in the panel (c4), we see its disappearance indicating a shift from the line-center to the line-wing due to the Doppler effect. In the panels following (c4), the filament is invisible. In panels, (d1)-(d7) filament appears again and then gradually becomes invisible due to the Doppler shift.

The first LALOs event was reported by Jing et al. (2003). Later, in Jing et al. (2006) the authors described several additional observations. An example from the latter work is shown in Figure 1.8. In this case, the authors have not found any apparent association with any flare.

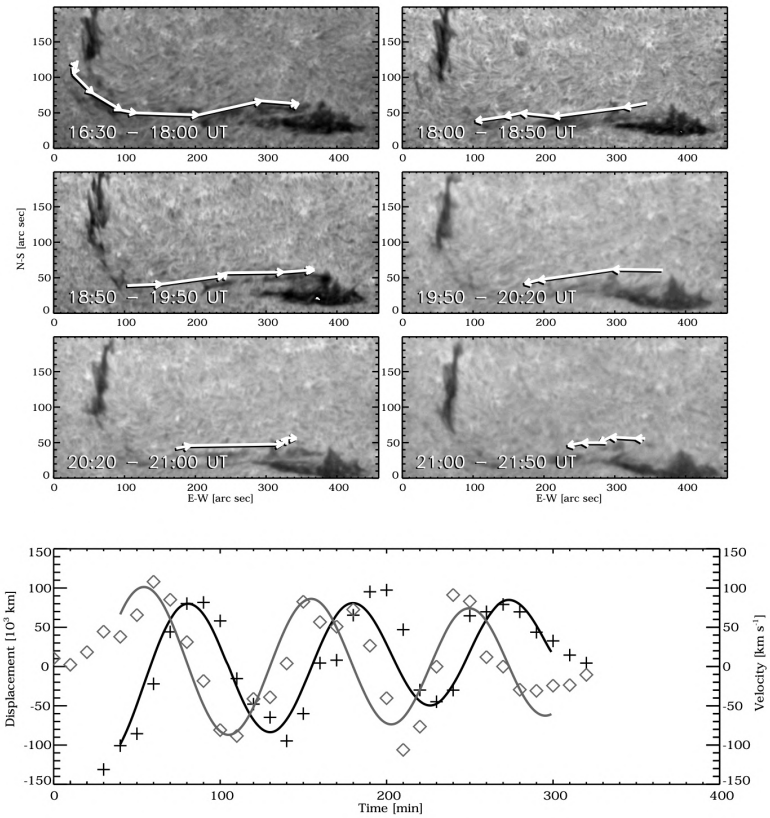

Figure 1.8: Upper three rows of images: filament observed at the Big Bear Solar Observatory. The while arrows over the images indicate the mass front motion during three oscillation cycles. Bottom panel: the measured positions and the derived velocities of the mass front are indicated by cross and diamond symbols, respectively. The signals were fitted by damped harmonic functions (solid lines). Adapted from Jing et al. (2006).

The arrows in Figure 1.8 show the direction of plasma motions. It is noticeable that the plasma moves along the magnetic field. The periodic motion started from the southern end of the short filament and traveled westward along the filament. The bottom panel of Figure 1.8 shows the displacement and velocity as a function of time and the best fit to the damped harmonic function (solid line). This figure shows that the oscillations initially had a very large amplitude and then started to decay. The oscillation period is around 100 minutes, the maximum displacement is 100 Mm, and the maximum velocity amplitude is 100 km s^{-1}. Additionally, the authors detected the motions from both sides in the shortest filaments, indicating so-called counterstreaming motions. In the same paper, Jing et al. (2006) described two more events of the LALOs. These events were observed to be triggered by flare activity located close to one end of the filament axis.

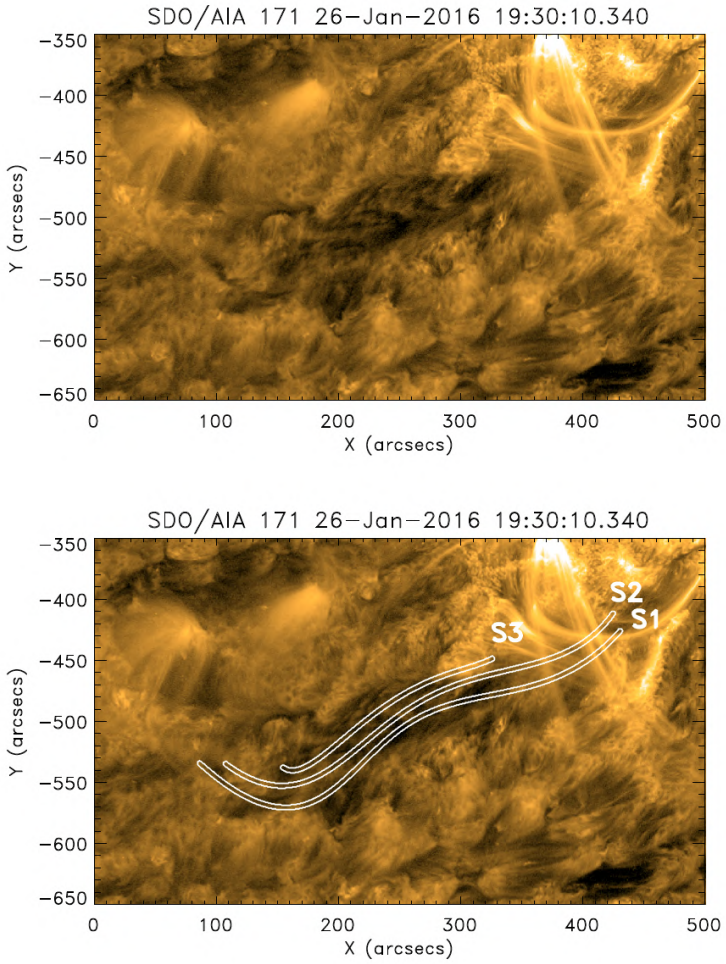

Figure 1.9: Top panel: filament channel observed in 171 Å band by the Atmospheric Imaging Assembly telescope (AIA). At the center of the image, the central portion of the filament appears in absorption. Bottom panel: the same image over-plotted with the three artificial slits used to study the oscillatory motion. Adapted from Luna et al. (2017).

Luna et al. (2014) used 36 artificial slits placed at different angles to study the LALO events. The authors showed that the time-distance diagram strongly depends on the angle, indicating the need to choose the slit position in the most optimal way. Luna et al. (2017) applied a similar approach but using curved artificial slits. Figure 1.9 shows the AIA filament observations and the three selected positions of the curved artificial slits, and Figure 1.10 shows the time-distance diagram taken at the slit 1. The red curve shows the best fit for this oscillation that allows

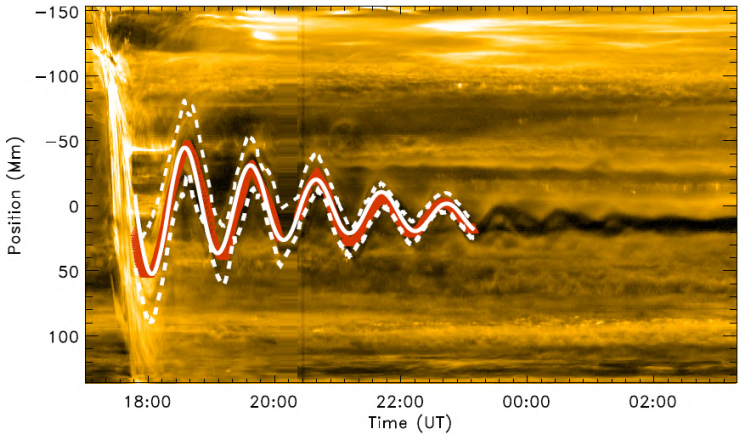

Figure 1.10: Time-distance diagram of the longitudinal filament oscillations observed in 171 Å AIA band, obtained from the slit 1 in Figure 1.9. The red line denotes the best-fit by damped sinusoidal function. The dashed white lines indicate the region of uncertainty. Adapted from Luna et al. (2017).

estimating the magnitude, period, and damping time. The curved slits have also been used by Luna et al. (2018) for the detection of prominence oscillations in GONG observations.

1.4.1 Transverse oscillations: periods and damping times

Transverse oscillations usually have short periods below one hour and damping times equal to $1-4$ oscillatory periods. However, the transverse oscillations with a longer period exceeding one hour have also been reported by many authors (Isobe & Tripathi 2006; Isobe et al. 2007; Pintér et al. 2008; Hershaw et al. 2011; Pant et al. 2015). The transverse oscillations of both vertical (Ramsey & Smith 1965, 1966; Eto et al. 2002; Okamoto et al. 2004; Gilbert et al. 2008; Zhang & Ji 2018) and horizontal polarizations (Isobe & Tripathi 2006; Hershaw et al. 2011; Liu et al. 2012; Gosain & Foullon 2012; Xue et al. 2014) have been observed. For the vertical oscillations, Eto et al. (2002) obtained a period of 15 minutes. The observations by Shen et al. (2014a) gave the period and damping time of the vertical oscillations in the range of $11-22$ minutes and $25-60$ minutes, respectively. More recently, Zhang & Ji (2018) reported from SMART and AIA/SDO observations the vertical oscillations with similar oscillatory properties, with periods and damping times of $29-37$ minutes and of $26-78$ minutes. Gosain & Foullon (2012) interpreted the horizontal LAOs in terms of the global kink modes and defined the period and damping time equal to 28 minutes and 44 minutes. Similarly, Xue et al. (2014) obtained 20 minutes and 99 minutes for the period and damping time, respectively. Many authors described oscillations as simply transverse, not defining horizontal or vertical polarization because it was impossible to detect the polarization precisely. For the transverse oscillations, Okamoto et al. (2004), Gilbert et al. (2008), Liu et al. (2012), and Liu et al. (2013) found the period to be around of 30 minutes. Shen et al. (2017) obtained a shorter period of 15 minutes and the damping time of 60 minutes. It is also complicated and not always possible to distinguish between the transverse and longitudinal modes (Pant et al. 2015, 2016; Chen et al. 2017). For instance, in the first

catalog of the LAOs based on several months of the Global Oscillation Network Group (GONG) Hα data near the maximum of the solar cycle 24, Luna et al. (2018) classified oscillations as transverse if the angle between the direction of plasma motion and the filament spine was larger than 40 degrees. This catalog provided a large number of oscillatory events and statistics of the characterization of LAOs. For the transverse oscillations, it was found that the period varies in the range of $30-80$ minutes, and the damping time is equal to several oscillatory periods, indicating strong damping. More recently, Zhang (2020) observed the short-period transverse oscillations of $437-475$ seconds with the ratio of the damping time to the period, in the range of $2.4-3.6$. Summarizing all above, the periods and damping times of the transverse oscillation can vary in the different observations. The common characteristic is that the period is usually below one hour, and the amplitude strongly decreases after several oscillatory periods.

1.4.2 Transverse oscillations: global and noncollective motions

Hershaw et al. (2011) reported horizontal prominence oscillations observed with SOHO/EIT telescope. They measured periods of oscillations in two legs at different heights and found the range of periods of $86-101$ minutes in one leg and $92-104$ minutes in the other leg. Furthermore, the velocity amplitude had different values in both legs, of $50\,\mathrm{km\,s^{-1}}$ and $33\,\mathrm{km\,s^{-1}}$, respectively. The differences in the oscillatory characteristics make the authors suggest that the prominence could be composed of the individual oscillating threads. Liu et al. (2012) reported horizontal oscillations and detected three oscillating threads. From the best fit, the oscillatory parameters had similar values suggesting the global transverse oscillations. Gosain & Foullon (2012) reanalyzed the observations by Liu et al. (2012) and showed the coherent motions in the first phase, but, later on, the motions became noncollective. Gosain & Foullon (2012) suggested that the noncollective behavior could be associated with the inhomogeneous prominence structure. In contrast, the observations by Shen et al. (2014b) revealed the global prominence oscillations in the vertical direction.

1.4.3 Longitudinal oscillations: periods and damping times

Since the first observations of LALOs by Jing et al. (2003, 2006), the number of the reported events has increased (e.g., Zhang et al. 2012; Li & Zhang 2012a; Luna et al. 2014). These LALOs are characterized by a period of the order of one hour (see, e.g., Jing et al. 2003, 2006; Vršnak et al. 2007; Shen et al. 2014b; Zhang et al. 2017, 2020); the direction of these motions coincides with the direction of the magnetic field, forming an angle of approximately $10-30$ degrees with respect to the filament spine (Luna et al. 2014; Hanaoka & Sakurai 2017; Luna et al. 2018). This value of the angle is in agreement with the direct magnetic field measurements (e.g., Leroy et al. 1983, 1984; Casini et al. 2003). Observations show that the LALOs are usually strongly damped (Bi et al. 2014; Zhang et al. 2017; Luna et al. 2017; Zhang et al. 2020). The GONG catalog of LAOs by Luna et al. (2018) provided a statistical study of the oscillatory characteristics of these motions. The distribution of the damping time per period peaks at $\tau/P = 1.25$. The authors confirmed that the damping rates depend nonlinearly on the oscillation velocity. There is no unique explanation for this strong decay and nonlinear dependence on the amplitude. In order to explain the observed damping, various candidates for the damping mechanism have been proposed, as we will explain in Section 1.6.

1.4.4 Longitudinal oscillations: threads oscillations

Li & Zhang (2012a) reported the observations of LALOs associated with the different prominence threads. The motions of the threads could be distinguished since their oscillatory periods were

different. The authors suggest that the periods of the prominence threads reflect the physical conditions of the field line and the environment where the prominence thread resides. Therefore, studying the dynamics of the threads is important for understanding the physics of the prominences. Luna et al. (2014) reported another example of the LALOs associated with the prominence threads. The authors pointed out that the motions become unsynchronized after several cycles, and the layers move out of phase, indicating different periods and, consequently, different conditions across the prominence. These out-of-phase thread motions have been often associated with counterstreaming flows in the filaments (Lin et al. 2005a).

1.5 LAOs triggering

LAOs should have a huge amount of energy due to the combination of a large mass and large velocities involved. Thus, it is intriguing how the disturbances in prominences can transport and accumulate such an amount of energy. Most of the LAOs events have been associated with energetic disturbances. However, the detailed mechanism of how these oscillations are excited is not well known. The first evidence of such kind of perturbation was by Moreton & Ramsey (1960) who discovered the existence of waves emanating from flares or coronal mass ejections (CME) that propagate in the solar atmosphere with huge velocities of $500 - 1500\,\mathrm{km\,s^{-1}}$.

More recently, the Extreme ultraviolet Imaging Telescope (EIT) aboard the Solar and Heliospheric Observatory (SOHO) discovered another wave-like phenomenon in the solar corona, which is now called EIT or EUV waves (Moses et al. 1997; Thompson et al. 1998). These waves are associated with flares or coronal mass ejections (CMEs) and propagate at speeds of $200 - 300\,\mathrm{km\,s^{-1}}$. It has been suggested that the EIT or EUV wave could be a coronal manifestation of the Moreton wave (see, e.g., Thompson et al. 1998). However, other authors have proposed a different interpretation (see, e.g., Chen et al. 2002). The front of the EIT wave shows a dome-like propagation. According to the wave interpretation, an MHD wave propagates from an energetic event and can excite LAOs reaching the filaments. Since this wave propagates in an environment where the phase speed increases with height, the wave front appears inclined, and its normal vector points to the solar surface. When reaching the filament, the Moreton wave inclines it and pushes it down, and, as a consequence, the vertical oscillations are established.

The evidence for the LAOs excitation in filaments by Moreton, EIT or EUV waves have been shown in many observations (Eto et al. 2002; Okamoto et al. 2004; Gilbert et al. 2008; Asai et al. 2012; Liu et al. 2013; Shen et al. 2014a; Xue et al. 2014; Takahashi et al. 2015; Shen et al. 2017). There has been observed a simultaneous excitation of the different polarizations by the same waves from energetic events. Gilbert et al. (2008) described an experiment in which the filament oscillations excited by Moreton wave had a mixed behavior, showing different polarizations. Asai et al. (2012) used SMART observations and EUV with AIA in Hα of the same prominence excited by EUV and Moreton waves. Hα observations suggested the longitudinal oscillations with the amplitude of $50\,\mathrm{km\,s^{-1}}$ and the period of 15 minutes. The EUV observations gave evidence of the transverse oscillations. The corresponding amplitude was equal to $30\,\mathrm{km\,s^{-1}}$, and the period varied in the range of $12 - 16$ minutes.

An interesting example of the LAOs excitation was reported by Shen et al. (2014b). A shock wave, associated with a powerful flare, excited the transverse oscillations in the filament and the prominence and the longitudinal oscillations in another filament. The authors proposed a scenario when the LAOs polarization depends on the angle between the normal vector of the arriving wave front and the filament spine. More recent observations of the presence of the different polarizations have been reported by Pant et al. (2016); Wang et al. (2016); Zhang et al. (2017). Oscillations in different directions in different filament threads have been reported by Mazumder et al. (2020).

All observations mentioned above demonstrate that the excitation of LAOs is a complex process, where two polarizations can be excited separately, or oscillations can appear coupled. The excitation of the longitudinal oscillations is often related to the magnetic activity in the filament vicinity, such as magnetic reconnection resulting in jets, nearby flares, CME, failed eruptions, or surges (Jing et al. 2003, 2006; Isobe & Tripathi 2006; Isobe et al. 2007; Vršnak et al. 2007; Zhang et al. 2012; Li & Zhang 2012b; Luna et al. 2014; Zhang et al. 2017; Luna et al. 2017; Zhang et al. 2020). Figure 1.10 shows an example of the time-distance diagram of the LALOs perturbed by two nearby eruptions (Luna et al. 2017). As we can see from this figure, the triggers excite the LALOs with a huge amplitude around 100 Mm. Summarizing all observations above, it seems that waves are mostly responsible for the excitation of the transverse LAOs, and the magnetic activity in the vicinity is more often associated with LALOs. However, in many cases, the driver triggers LAOs of a mixture of different polarizations.

Observations showed that in some cases LAOs are present in the pre-erupting phase of the prominence and during its slow rise (Isobe & Tripathi 2006; Isobe et al. 2007; Chen et al. 2008; Pintér et al. 2008; Bocchialini et al. 2011; Li & Zhang 2012b; Bi et al. 2014; Joshi et al. 2016; Zheng et al. 2017). In these cases, there is no identified external agent exciting the oscillations. Some authors suggest that LAOs can be a precursor of prominence eruptions. Isobe et al. (2007) showed that LAOs are present during the slow-rise eruption stage. This indicates that during the slow rise, the filament has to be in a state of nonlinear equilibrium in order to allow for the presence of oscillations. It is worth highlighting the observational work by Bi et al. (2014). They showed that the period of LALOs increases during the slow rise, revealing mass drainage or decrease of the magnetic twist. Many observations demonstrated that the presence of LAOs in the filament before eruption is a common feature and can be used as a diagnostic tool for prominence stability.

1.6 Theoretical aspects of LAOs

After several decades of observations, an important amount of information about prominence oscillations has been accumulated. Several models have been proposed to explain different aspects of oscillations, but many of these aspects remain unexplained. Firstly, modeling tries to explain the physics of the restoring forces for each of the polarization of LAOs. The knowledge of physics can be used to derive relations between the observed periods and the parameters of the prominence. Secondly, observations showed that different types of LAOs usually have a short attenuation time, indicating an effective damping mechanism. Finally, it is important to understand which driver can perturb such large prominence structures and excite their global oscillations. In order to explain these aspects of LAOs, many analytical and numerical models have been developed. In this section, we describe such models and their main findings.

1.6.1 Models for transverse LAOs

Several analytical and numerical works have been done, providing new insights on the nature of transverse LAOs. The complexity of theoretical studies has increased with time, from simple harmonic oscillator modeling to 1D numerical modeling and sophisticated 2D, 2.5D, and 3D simulations.

The first attempts to explain the periods of transverse LAOs have been made by Hyder (1966) and Kleczek & Kuperus (1969). The authors interpreted the transverse oscillations in terms of a very simple model of a harmonic oscillator where the prominence is modeled as an elastic membrane being the magnetic tension the restoring force. Joarder & Roberts (1992a,b) and Oliver et al. (1993) studied the normal modes of the prominence longitudinal and

transverse oscillations using a slab model. They found a large variety of normal modes with different periodicities. Terradas et al. (2013) studied numerically the oscillations of a prominence embedded in a 2D dipped magnetic configuration. They showed that the Lorentz force is the restoring force for the transverse oscillations with a larger contribution of the magnetic tension. 2D numerical simulations by Luna et al. (2016b), Zhang et al. (2019) and Jelínek et al. (2020) reproduced observed transverse oscillation periods of a few minutes. Additionally, Terradas et al. (2013) and Luna et al. (2016b) found that the vertical period remains constant with height, indicating the global nature of the oscillations. Terradas et al. (2013) suggested that the vertical period has a simple dependence on the plasma and magnetic field properties. The period increases with the prominence density and decreases with the length of the field line. The relation between the vertical period and the thermodynamic and magnetic properties of the global prominence structure is valuable for prominence seismology.

In a different line of works, the transverse oscillations have been studied using Kuperus & Raadu like framework (see Kuperus & Raadu 1974). In their model, the filament is represented by a line current or by a cylinder, and it is stabilized and tied to the chromosphere by overlaying magnetic arcades. Kuperus & Raadu (1974) gave an expression for the vertical oscillations of a prominence (see their Equation (6)). Their model allows for the study of vertical and horizontal oscillations. Schutgens & Tóth (1999) performed MHD simulations using Kuperus & Raadu model. The prominence was represented by a current-carrying cylinder. It was shown the existence of the decoupled modes of oscillations of different polarizations. Kolotkov et al. (2016) studied the linear oscillations in the same framework of a current-like prominence model. Periods of the vertical and horizontal oscillations and the stability of the structure to different oscillations as a function of its parameters were investigated. This study was extended later to a weakly nonlinear case (Kolotkov et al. 2018). It has been demonstrated that the horizontal and vertical oscillations are strongly coupled, and this coupling is more efficient for larger amplitudes.

Recently, oscillations in 3D prominence models have been considered in several numerical studies. Terradas et al. (2016) studied oscillations in a 3D configuration based on Titov & Démoulin (1999) flux rope structure with an inserted prominence mass. It was shown that the period of the vertical oscillations does not depend on the flux rope twist. Zhou et al. (2018) formed a 3D prominence field using the method of van Ballegooijen & Martens (1989). As in Terradas et al. (2016), the authors loaded the prominence mass in the dips of the resulting field configuration (see Figure 1.3). Oscillations of the different polarizations were studied. It was shown that horizontal and vertical polarizations have periods of around 10 and 14 minutes, respectively. Both polarizations fit very well the predictions from the 2D slab model by Díaz et al. (2001). The work by Zhou et al. (2018) confirmed the magnetic nature of the transverse oscillations and the Lorentz force as a main restoring force. In the same vein, Adrover-González & Terradas (2020) considered the transverse LAOs in a 3D sheared configuration and studied the dependence of the period on the prominence width and density contrast and the magnetic field strength in the dips.

1.6.2 Models for longitudinal LAOs (LALOs)

Several candidates have also been proposed to explain LALOs. The first attempt has been made by Vršnak et al. (2007). It was proposed that the observed LALOs in a flux rope prominence were triggered by the injection of the poloidal magnetic flux. The authors modeled the prominence as a harmonic oscillator with the magnetic pressure gradient as a restoring force. They derived the period as a function of the filament length and the Alfvén speed of the poloidal field.

Later, Luna & Karpen (2012) proposed the so-called pendulum model where the main restoring force is the solar gravity projected along the magnetic field. This model was confirmed by

the results of the numerical simulations by Luna et al. (2012c). Since the motion is along the magnetic field, it was demonstrated that the Lorentz force has no contribution to the restoring force. Of the two remaining forces, the gravity projected along the dip and the gas pressure gradient, the former was seen to be dominant in the simulations by Luna et al. (2012c). The LALOs period was shown to depend only on the radius of curvature of the magnetic field line where the prominence plasma resides (Luna et al. 2012c; Zhang et al. 2012). In subsequent work, Luna et al. (2012a) studied the oscillation modes in a single flux tube analytically, with a plasma thread located at its dipped part and with hot coronal regions outside. The aim was to investigate how the geometry of the magnetic flux tube affects longitudinal oscillations. The authors have found the normal modes of the system and showed that the longitudinal oscillations are strongly influenced by the curvature of the magnetic field lines in the cold plasma regions, while the geometry of the hot regions has very little influence. It was found that longitudinal oscillations combine a pendulum oscillation and a slow-mode oscillation (Luna et al. 2012a; Zhang et al. 2012). Under the prominence conditions, the pendulum contribution dominates. The contribution of the slow modes is more significant when the magnetic field lines are very shallow.

Using the 2D prominence model, Terradas et al. (2013) confirmed that the gas pressure gradient contributes to the restoring force of the longitudinal oscillations, in addition to the gravity projected along the magnetic field. However, their results seem to contradict the pendulum model because the oscillation period in their simulations does not follow the dependence on the curvature of the field lines suggested by the pendulum model. The reason for such behavior is very shallow dips in the prominence model used. The study of Terradas et al. (2013) was followed by a numerical work by Luna et al. (2016b) where it was convincingly demonstrated the agreement between the oscillation period in the simulations and the pendulum model. Luna et al. (2016b) concluded that, under the prominence conditions, the main restoring force of LALOs is the projected gravity with only a small contribution of the gas pressure gradient. This conclusion has been confirmed in the recent 2D and 3D studies (Zhou et al. 2018; Zhang et al. 2019; Adrover-González & Terradas 2020; Fan 2020; Luna & Moreno-Insertis 2021).

1.6.3 Damping of LAOs

Observations show that LAOs of the different polarizations damp quickly (see, e.g., the catalog by Luna et al. 2018). The physical mechanisms responsible for this strong attenuation are unclear, and several candidates have been proposed. Regarding the transverse oscillations, Kleczek & Kuperus (1969) proposed the emission of the acoustic waves as a damping mechanism in their model. Using the line current filament model, Schutgens & Tóth (1999) explained damping of vertical oscillations by the emission of the fast magnetoacoustic waves. More recently, Zhang et al. (2019) have shown the wave leakage to be the main damping mechanism of the transverse oscillations in their 2D simulations. The resonant absorption has been proposed as an alternative damping mechanism. The resonant absorption is associated with the kinetic energy transfer of the transverse oscillations into the Alfvén continuum at the prominence-corona transition region. Using the 3D numerical simulations, Terradas et al. (2016) showed that resonant absorption indeed efficiently attenuates vertical oscillations. The recent work by Adrover-González & Terradas (2020) confirmed that resonant absorption is the dominant damping mechanism for transverse oscillations in the 3D configurations.

Several dissipation mechanisms, such as radiative losses and thermal conduction, have been invoked to explain the LALOs attenuation by Zhang et al. (2012) and Zhang et al. (2019). These authors pointed out the importance of the inclusion of the nonadiabatic effects into the consideration. Nevertheless, by using numerical simulations, these authors obtained that

nonadiabatic effects alone are not enough to explain the observed attenuation (see also Zhang et al. 2020). Zhang et al. (2019) found that in a situation of a relatively weak magnetic field, wave leakage is also important for LALOs damping. The motion of the prominence mass produces perturbations to the field structure that emanate in the form of MHD waves.

Luna & Karpen (2012) and Zhang et al. (2013) suggested an alternative mechanism for the LALOs attenuation related to the loss or gain of the prominence mass. Luna & Karpen (2012) proposed that damping is associated to mass accretion of the prominence threads (see also Ruderman & Luna 2016). In contrast, Zhang et al. (2013) considered that the damping is associated with mass drainage. Therefore, either prominence mass accretion or drainage can result in decreasing the velocity amplitude of the prominence oscillations.

1.6.4 Models for triggering of LAOs

As mentioned before, the triggering of LAOs has been attributed to energetic events such as Moreton, EIT, nearby subflares, jets, and the eruption of a filament. The triggering of LAOs has been much less studied theoretically than the restoring forces and the damping mechanisms. However, some ideas have been proposed. Shen et al. (2014b) observed that LAOs are excited in several filaments by the same EUV wave and proposed that, depending on the direction between the arrival of the wave and the filament spine, the shock wave could excite longitudinal or transverse oscillations. The plausible wave-prominence (or wave-filament) interaction process is represented in Figure 1.11. When the vector normal to the wave front is transverse with respect to the filament spine at the moment of the wave arrival, oscillations of horizontal or vertical polarization can be excited (Figures 1.11(a) and 1.11(c)). Longitudinal oscillations can be triggered when the vector normal to the front points in the direction parallel to the filament spine (Figures 1.11(b) and 1.11(d)). However, as shown by observations by Shen et al. (2014a), this explanation seems insufficient since some filaments remain unperturbed, despite being located at a close distance from a flare.

Propagation of Moreton and EIT (EUV) waves and their interaction with prominences were studied in many numerical works (see, e.g., Chen et al. 2002, 2005; Vršnak et al. 2016; Chen et al. 2016; Piantschitsch et al. 2017; Afanasyev & Zhukov 2018; Mei et al. 2020). Chen et al. (2002, 2005) performed a numerical study of an erupting flux rope and discussed a possible origin of the Moreton and EIT(EUV) waves. Their numerical experiments showed a piston-like shock straddling the flux rope, whose skirt sweeps the solar surface and propagates with a velocity of more than $700\,\mathrm{km\,s^{-1}}$. It was suggested that the skirt of the shock wave corresponds to the coronal Moreton wave. Another wave-like phenomenon, propagating with a smaller velocity of around $200\,\mathrm{km\,s^{-1}}$, was found in these simulations. The authors associated this phenomenon with an EIT wave formed by successive stretching and opening of the field lines covering the erupting flux rope. The region of the enhanced density was observed in front of this wave, while its inner boundary coincides with a dimming region.

The interaction of Moreton and EUV waves with the surroundings magnetic arcades and coronal holes has been extensively studied as well (Vršnak et al. 2016; Chen et al. 2016; Piantschitsch et al. 2017; Afanasyev & Zhukov 2018; Mei et al. 2020). Chen et al. (2016) studied the interaction between a fast-mode wave and an isolated magnetic flux system by means of numerical simulations. They showed that when the wave impacts the magnetic structure and reaches the region of plasma-β close to unity, part of the fast-mode wave is converted to the slow mode. This slow wave continues to stay trapped inside the magnetic loops and finally forms a stationary front. Chen et al. (2016) suggested that a EUV wave can also be produced by a fast-mode wave when the latter reaches the region where plasma-β is equal to unity, and some part of it converts into a slow mode that forms a stationary front. Although these numerical

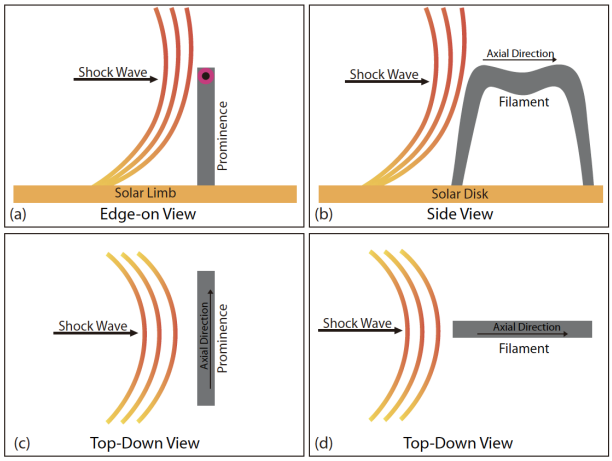

Figure 1.11: Cartoon demonstration of the wave–prominence and wave–filament interaction processes (Shen et al. 2014b).

simulations gave essential information about the waves associated with the energetic events, they did not show the interaction of the wave with prominence mass and excitations of LAOs.

Another way to excite LAOs is by using close triggering, i.e., jets occurring near the filament. Using a 2D magnetic configuration with dips, Luna & Moreno-Insertis (2021) triggered the reconnection using the shearing motions around a parasitic polarity producing a jet. This results in oscillations of the prominence and counterstreaming flows along the magnetic field. The oscillations are LAOs (with the amplitude above $10\,\mathrm{km\,s^{-1}}$) in the longitudinal and transverse directions. The trigger causes the mass drainage down to the chromosphere along the magnetic field in some field lines. This is the first time that LAOs are excited self-consistently with a nonartificial perturbation in simulations. The numerical results by Luna & Moreno-Insertis (2021) are in agreement with the observations by Luna et al. (2014) and Zhang et al. (2017).

1.7 Why study LAOs in solar prominences: prominence seismology

Solar prominences are objects in the solar atmosphere with a complex magnetic field and plasma structure. The characteristics of the prominence plasma and magnetic field are hard to obtain from the direct measurements. The LAOs give a powerful tool for the diagnostics of different parameters of the prominences. As mentioned before, LAOs are prominence motions that have a global nature. This fact was successfully used in prominence seismology. The main idea of prominence seismology is based on finding the relations between the oscillatory properties and the characteristics of the prominence structure by means of theoretical modeling.

Models of the transverse LAOs have been widely used to estimate the magnetic field strength in prominences. The first work where this approach was used is the one by Hyder (1966). In his work, the author applied the prominence model of Kippenhahn & Schlüter (1957) to the observations of the winking filaments by Ramsey & Smith (1966). This simple model allowed the author to estimate the magnetic field strength to be around $2-30$ G, which was in agreement with the previous estimates. This example showed the power of oscillations as a diagnostic tool, and this approach was then widely used in the following decades.

Vršnak et al. (2007) assumed that longitudinal prominence oscillations were exited by a poloidal magnetic flux inserted by the magnetic reconnection at one of the prominence legs. The authors used a model of a simple harmonic oscillator and derived the poloidal and axial magnetic field components. The strength of the axial magnetic field component was found to vary between $10-30$ G, in agreement with the direct magnetic field measurements. Isobe & Tripathi (2006) used an equation for the oscillation period as a function of the magnetic field strength, length of the prominence thread, and the prominence density obtained by Kleczek & Kuperus (1969) from the model of a harmonic oscillator. By using the measured period of the transverse oscillations, and the length of the prominence threads, and assuming typical prominence density, Isobe & Tripathi (2006) estimated the magnetic field strength to be of 9.8 G. Gilbert et al. (2008) and Gosain & Foullon (2012) provided more examples of the use of the Kleczek-Kuperus model for prominence seismology and obtained values of the magnetic field strength of 30 G and 25 G, respectively. More authors considered the transverse LAOs in terms of the global kink mode and used the analytical expression for the period of this model to derive the magnetic field strength (see more, e.g., Hershaw et al. 2011; Liu et al. 2012; Xue et al. 2014).

In the pendulum model proposed by Luna & Karpen (2012) the main restoring force is the projection of gravity on the magnetic field, and the oscillation period depends only on the radius of curvature of the field lines. Thus, a simple expression can be used to derive the radius curvature of the magnetic field. Following this model, Luna et al. (2014) and Zhang et al. (2017) obtained the radii of curvature in the range of $43-66$ Mm and $70-134$ Mm, respectively. Similarly, by use of the pendulum model and assuming that the magnetic tension to be the cause of the prominence support, Li & Zhang (2012b), Luna et al. (2014), Bi et al. (2014), and Zhang et al. (2017) estimated the minimum value of the magnetic field strength needed to compensate for the gravity force acting on the prominence mass located in the dips. Luna et al. (2014), Bi et al. (2014), and Zhang et al. (2017) obtained similar values of the minimum magnetic field around 15 G, while Li & Zhang (2012b) derived a slightly stronger magnetic field in the range of $28-55$ G.

The observed damping time and possible damping mechanisms give additional information about the prominence plasma and magnetic conditions. From this point of view, it is necessary to mention the work by Hyder (1966), who used a model with a damped harmonic oscillator, where the attenuation was due to magnetic diffusivity. The author provided a first estimate of the magnetic diffusivity in solar prominences. Kleczek & Kuperus (1969) considered acoustic radiation as a damping mechanism for the horizontal prominence oscillations. This study provided important information on the possible acoustic wave generation in the solar corona by prominence oscillations. By considering the damping of LAOs due to the accretion of the mass, Luna et al. (2016a) computed the accretion rate needed to explain the observed damping time.

Several observations (Isobe & Tripathi 2006; Isobe et al. 2007; Chen et al. 2008; Pintér et al. 2008; Bocchialini et al. 2011; Li & Zhang 2012b; Bi et al. 2014; Joshi et al. 2016; Zheng et al. 2017) suggest that LAOs are present in the prominence during the pre-eruptive phase or during the slow rise stage. These oscillations can give important information on the stability of the prominence and on the evolution of the eruption. The variation of the period and amplitude with time can shed light on the evolution of the magnetic field and prominence plasma during the eruption.

The above examples show that the LAOs periods, damping times, and amplitudes allow us to derive important characteristics of the magnetic field and prominence plasma, which could be difficult to obtain from the direct measurements. Therefore, it is crucial to understand the restoring forces of the different types of LAOs and provide a theory that would be able to explain the periods and damping time dependencies on the characteristics of the prominences structure.

1.8 Aims of this thesis

Despite the progress in the observational and numerical studies of LAOs in solar prominences, there is no unique explanation for the dependence of the oscillatory characteristics on the properties of the prominence structure. The strong LAOs attenuation and the triggering mechanism also remain unclear. The thesis aims to investigate these aspects of the physics of LAOs by using the 2D and 2.5D numerical simulations in order to advance our knowledge about prominence dynamics.

Our first goal is to study the normal modes of LAOs by using a 2.5D flux rope prominence model with different parameters of the structure, such as the initial magnetic field shear angle and the prominence density contrast. These experiments will allow us to understand whether the period and damping time of the longitudinal or transverse LAOs depend on these parameters. Additionally, by using a perturbation located outside of the prominence flux rope, we aim to reproduce the scenario of the LAOs triggered by an external perturbation. We aim to identify which polarizations are excited by such a driver by analyzing the prominence dynamics.

Our second goal is to investigate the damping mechanism of LALOs by using a simple 2D magnetic configuration with a dipped region and by gradually improving the spatial resolution of simulations from 240 km down to 30 km. This convergence experiment is designed to understand if the damping time in different prominence regions saturates with improving the resolution, revealing a possible physical mechanism for the damping of oscillations. Our study aims to underline the importance of the high-resolution simulations for studying the oscillation periods, their comparison to the pendulum model, as well as other important physical aspects of LALOs.

Our last goal is to study the problem of the external triggering of LAOs. Firstly, we will use a 2.5D numerical model with two neighboring flux ropes. In this model, one flux rope remains stable and contains the prominence mass, and the other flux rope is eruptive and acts as an oscillation trigger. We aim to understand how an eruptive event in the vicinity can affect the prominence mass of the other flux rope and how the eruptive event and the flux rope prominence interact. Additionally, we want to study which oscillatory modes are excited by such perturbation in the prominence. In a different model, we aim to study the excitation of oscillations by an external artificial perturbation in the same flux ropes when both of them contain the prominence mass. Finally, we study the excitation of oscillations by a similar artificial external perturbation but using a 2D model of the dipped arcade hosting the prominence material.

1.9 Thesis organization

In the following Chapter 2, we explain the main tool used in this thesis, the MANCHA code, and the equations solved by the code. We also describe the employed numerical techniques, including spatial and temporal discretization, artificial diffusivity. Additionally, we explain the methods needed to analyze the bulk prominence motions and describe the widely-used models for prominence formation.

In Chapter 3, we describe the analysis and the main results obtained from the different configurations of the flux rope prominence model and the results extracted from the analysis of the experiment of the external LAOs triggering.

Chapter 4 presents the analysis and comparison of a set of simulations of prominence LALOs with different spatial resolutions in a 2D magnetic configuration with dips. This chapter describes how the oscillatory properties such as damping time or period depend on the spatial resolution. Additionally, we explain the possible mechanism of the LALOs attenuation and amplification.

In Chapter 5, we describe the interaction of the perturbation represented by the eruptive event with the flux rope solar prominence. This chapter also explains the types of oscillations excited by an external artificial perturbation in the two flux rope prominences and the prominence in the dipped arcade configuration.

Finally, we summarize the main results extracted from this thesis and the future prospects in Chapter 6.

2

Methodology

This chapter explains the theoretical concepts used in this thesis. We introduce the assumptions and equations of an ideal MHD and explain the concept of the linear force-free magnetic field configuration using, as an example, a sheared arcade model. Additionally, we derive the dispersion relations and the main properties of the MHD waves in the case of a homogenous atmosphere permeated by the uniform magnetic field. We then proceed by describing the main tool used in thesis work, the MHD code MANCHA3D, including the equations, numerical scheme, and boundary conditions. At the end of the chapter, we explain the methods for analyzing the numerical simulations performed with the MANCHA3D code. These methods include the analysis of plasma motions associated with different magnetic field lines and tracking fluid elements.

2.1 Theoretical concepts

The Sun consists of plasma, i.e., a highly ionized electrically conducting fluid that interacts with the solar magnetic field. Solar plasma can be described in terms of Magnetohydrodynamics (MHD). In this thesis, we study the plasma in terms of an ideal MHD approximation. This implies important assumptions that will be taken into account when deriving the main equations.

To consider a gas of charged particles to behave collectively as a plasma, the following conditions must be fulfilled:

- Plasma is considered to be electrically neutral. This condition is satisfied when the length scales at which we consider the system are much larger than the Debye length, λ_D.
- The length and time scales should greatly exceed the Larmor radii and frequency, $L \gg r_{li}$, r_{le} and $\tau \gg \Omega_{li}^{-1}$, Ω_{le}^{-1}, that are characteristics of cyclotron motions of particles around magnetic field.
- Plasma is assumed to be in thermodynamic equilibrium with Maxwellian distribution implying that $T_e = T_i$. This assumption is justified when the length scale is larger than the mean free path of the particles, and plasma is considered to be dominated by the collisions implying that the time scales of the considered processes are much longer than the collision time.

In this thesis, we consider a fully-ionized plasma. While this condition is expected to be well satisfied in the solar corona with temperatures of 10^6 K, the prominence plasma with temperatures around 10^4 K is only partially ionized. The effects of partial ionization play an important role when studying the prominence support or different types of instabilities. In this

thesis, we do not aim to study these aspects of prominence physics. Regarding the properties of oscillatory motions, the effects of partial ionization can be potentially important for the damping mechanisms of oscillations. However, according to Soler et al. (2009, 2010), the effects of partial ionization give the damping rates for the realistic wavelengths under the prominence conditions to be much longer than the observed damping rates. Consequently, the ideal MHD and fully-ionized plasma can be considered as reasonably good assumptions for models studying the global prominence dynamics, as those considered in this thesis.

2.1.1 MHD equations

In MHD, the collective behavior of plasma is governed by a simplified form of Maxwell's equations, together with Ohm's Law, a gas law, and the equations of mass continuity, motion, and energy. We begin with Maxwell's equations:

$$\nabla \times \mathbf{B} = \mu_0 \left(\mathbf{j} + \epsilon_0 \frac{\partial \mathbf{E}}{\partial t} \right), \tag{2.1}$$

$$\nabla \times \mathbf{E} = -\frac{\partial \mathbf{B}}{\partial t}, \tag{2.2}$$

$$\nabla \cdot \mathbf{E} = \frac{\rho^*}{\epsilon_0}, \tag{2.3}$$

$$\nabla \cdot \mathbf{B} = 0, \tag{2.4}$$

where $\mathbf{E}$ is the electric field, $\mathbf{B}$ is the magnetic field, $\mathbf{j}$ is the current density, ρ^* is the charge density, μ_0 is the magnetic permeability, and ϵ_0 is the permittivity of free space. Plasma is assumed to be non-relativistic. This allows us to simplify the Equation (2.1). The characteristic velocity:

$$V = \frac{L}{T}, \tag{2.5}$$

and it has to satisfy

$$V \ll c, \tag{2.6}$$

where c is the speed of light.

The order of magnitude of the spatial variations of the electric field in Equation (2.2) can be estimated as

$$\frac{E}{L} \sim \frac{B}{T} \Rightarrow E \sim B\frac{L}{T}. \tag{2.7}$$

Comparing the displacement current term with the curl of the magnetic field term, we obtain

$$\frac{|\mu_0 \epsilon_0 \frac{\partial \mathbf{E}}{\partial t}|}{|\nabla \times \mathbf{B}|} \sim \frac{\frac{1}{c^2}\frac{\mathbf{E}}{T}}{\frac{\mathbf{B}}{L}} = \frac{L^2/T^2}{c^2} = \frac{V^2}{c^2} \ll 1. \tag{2.8}$$

Neglecting the displacement current term, Equation (2.1) is simplified to

$$\nabla \times \mathbf{B} = \mu_0 \mathbf{j}. \tag{2.9}$$

The Ohm's law for the magnetized nonrelativistic plasma is defined as follows

$$\mathbf{j} = \sigma(\mathbf{E} + \mathbf{v} \times \mathbf{B}) - \frac{\sigma}{n_e e}(\mathbf{j} \times \mathbf{B}), \tag{2.10}$$

where σ is electric conductivity. The last term is the Hall term. This term can be neglected when a typical hydrodynamical frequency is smaller than the gyrofrequency, which is well satisfied in

our case. We apply the curl operator to both sides of Equation (2.10), and then substitute the expressions for current and for the electric field using Equations (2.9) and (2.2). The following induction equation is obtained:

$$\frac{\partial \mathbf{B}}{\partial t} = \nabla \times (\mathbf{v} \times \mathbf{B}) - \nabla \times (\eta \nabla \times \mathbf{B}) \,, \tag{2.11}$$

where $\eta = (\mu_0 \sigma)^{-1}$ is the magnetic diffusivity. The first term at the right-hand side of the induction equation is associated with the advection of the magnetic field with plasma motions. The second term is related to the diffusion of the magnetic field. The relative importance of both terms can be estimated as follows

$$R_m = \frac{|\nabla \times (\mathbf{v} \times \mathbf{B})|}{|\nabla \times (\eta \nabla \times \mathbf{B})|} \sim \frac{|\mathbf{v}||\mathbf{B}|/L}{\eta |\mathbf{B}|/L^2} = vL/\eta \,, \tag{2.12}$$

where v, L are the characteristic velocity and length, and η is the magnetic diffusivity. The relative importance of the terms in the induction equation is characterized by the magnetic Reynolds number, R_m. When $R_m \ll 1$, the temporal evolution of the magnetic field is dominated by diffusion. On the contrary, the advective term is dominant in the limit $R_m \gg 1$, and the diffusive term can be neglected. In the solar corona, the magnetic Reynolds number lies in the range of $10^8 - 10^{12}$ (Hood & Hughes 2011). These large values of the Reynolds number imply that the diffusive term can be neglected. The latter is one of the assumptions of an ideal MHD.

The magnetic Reynolds number characterizes the coupling between plasma flow and the magnetic field. The condition $R_m \ll 1$ indicates a weak coupling (the magnetic field diffuses through plasma), and on the contrary, a strong coupling is assumed when $R_m \gg 1$ (the magnetic field is frozen into plasma). In the limit of $R_m \to \infty$, which is equivalent to $\sigma \to \infty$, we have the so-called perfectly conducting plasma. In a perfectly conducting plasma, and assuming that the current has finite values, the Ohm's law takes the form:

$$\mathbf{E} + \mathbf{v} \times \mathbf{B} = 0 \,. \tag{2.13}$$

The perfectly conducting plasma case implies the Alfvén's theorem, stating that the plasma is frozen in the magnetic field and vice versa.

Equation (2.11) describes the coupling between the magnetic field and plasma flow. In the following, we introduce the equations that describe the plasma motions. We start with the mass conservation equation:

$$\frac{\partial \rho}{\partial t} + \nabla \cdot (\rho \mathbf{v}) = 0 \,, \tag{2.14}$$

where ρ is the mass density and $\mathbf{v}$ is the plasma velocity. Qualitatively, this equation shows that the temporal variations of density $\partial\rho/\partial t$ in a fluid element are due to the incoming or outcoming mass flux $\rho\mathbf{v}$ through the element boundaries.

The momentum conservation equation is defined as

$$\frac{\partial \rho \mathbf{v}}{\partial t} + \nabla \cdot (\rho \mathbf{v}\mathbf{v}) = \rho \mathbf{g} - \nabla p + \mathbf{j} \times \mathbf{B} + \nabla \cdot \bar{\tau} \,, \tag{2.15}$$

where p is gas pressure, $\mathbf{g}$ is the gravitational acceleration, and $\mathbf{vv}$ denotes the tensor product of the velocity. The last term represents the viscous force defined by the viscous stress tensor. In the case of a compressible gas, its components are:

$$\tau_{ij} = \mu\Big(\frac{\partial v_i}{\partial x_j} + \frac{\partial v_j}{\partial x_i} - \frac{2}{3}\delta_{ij}(\nabla \cdot \mathbf{v})\Big), \qquad i, j = 1, 2, 3 \tag{2.16}$$

with $\mu = \nu\rho$ being the dynamic viscosity. By equivalence with the induction equation, the relative importance of the diffusive term ($\nabla \cdot \bar{\tau}$) and the momentum flux term ($\nabla \cdot (\rho \mathbf{v}\mathbf{v})$) can be estimated using the Reynolds number as

$$R_e = \frac{\nabla \cdot \rho \mathbf{v}\mathbf{v}}{\nabla \cdot \bar{\tau}} \sim \frac{\rho V^2/L}{\mu V/L^2} = \frac{\rho V L}{\mu} = \frac{VL}{\nu}\,. \tag{2.17}$$

Estimating the Reynolds number in the solar corona gives large values of the order of 10^4 (Hood & Hughes 2011). Therefore, we then can neglect the term of viscous force in the momentum equation. This constitutes another assumption of an ideal MHD.

In the absence of heat flux, the energy conservation equation is introduced as follows

$$\begin{aligned}\frac{\partial e}{\partial t} + \nabla \cdot [\mathbf{v}(e + p + \frac{\mathbf{B}^2}{\mu_0}) - \frac{1}{\mu_0}\mathbf{B}(\mathbf{v}\cdot\mathbf{B})] = \\ = \frac{1}{\mu_0}\nabla \cdot (\mathbf{B} \times \eta(\nabla \times \mathbf{B})) + \nabla \cdot (\bar{\tau} \cdot \mathbf{v}) + \nabla \cdot (\kappa \nabla T) + \rho(\mathbf{g}\cdot\mathbf{v}) + Q_{\rm R}\,.\end{aligned} \tag{2.18}$$

where e is total energy density that consists of three contributions: kinetic $e_{\rm kin} = \rho v^2/2$, magnetic $e_{\rm mag} = B^2/(2\mu_0)$ and internal $e_{\rm int}$ energy densities. The case of an ideal gas, the internal energy density is related to the gas pressure as $e_{\rm int} = p/(\gamma - 1)$.

Temporal variations of the total energy density are caused by the flux terms at the left-hand side such as the convective transport of energy, $\nabla\cdot(\mathbf{v}e)$, the compression-expansion work $\nabla\cdot(\mathbf{v}p)$, the magnetic energy transport, $\nabla\cdot(|\mathbf{B}|^2/\mu_0)$, the magnetic pressure work, $(-\mathbf{B}(\mathbf{v}\cdot\mathbf{B})/\mu_0)$. The right-hand side terms that can change the energy balance are the magnetic diffusion term, the viscous term, the thermal conduction term, the work done by the gravity force, and the radiative losses term, $Q_{\rm R}$.

Alternatively, one can consider the equation of conservation of the internal energy which has the following form:

$$\frac{\partial e_{\rm int}}{\partial t} + \nabla \cdot (\mathbf{v} e_{\rm int}) + (\gamma - 1) e_{\rm int} \nabla \cdot \mathbf{v} = \eta \mathbf{j}^2 + \bar{\tau} : \nabla \mathbf{v} + \nabla \cdot (\kappa \nabla T) + Q_{\rm R}\,. \tag{2.19}$$

We consider an ideal gas with an adiabatic constant $\gamma = 5/3$. An ideal gas law is defined as

$$p = \frac{k_B}{m}\rho T\,, \tag{2.20}$$

where k_B is the Boltzmann constant and m represents the mean particle mass. Using the mean particle mass in the units of proton mass, $\tilde{\mu} = m/m_p$, Equation (2.20) can be written

$$p = \frac{R}{\tilde{\mu}}\rho T\,, \tag{2.21}$$

where $R = k_B/m_p$ is the gas constant. Since we consider the plasma to be fully ionized and taking into account that the mass of the electron is much smaller than the mass of protons, in this plasma, we have $\tilde{\mu} = 0.5$. However, considering that the solar plasma also consists of helium and other heavier elements, we modify this number having approximately around 0.6.

2.1.2 Force-free magnetic field

As we have seen in Section 1.2 the prominence magnetic field can be relatively well approximated by a force-free configuration. The magnetic force is dominant over the gas pressure and gravity forces. Therefore the force-free condition is satisfied, i.e., the Lorentz force is balanced by itself:

$$\mathbf{j} \times \mathbf{B} = \frac{1}{\mu_0}[[\nabla \times \mathbf{B}] \times \mathbf{B}] = 0\,. \tag{2.22}$$

The Lorentz force is zero when the currents are zero (potential field case), or the currents flow along the magnetic field

$$\mathbf{j} \parallel \mathbf{B}\,, \tag{2.23}$$

the latter condition can be written as

$$[\nabla \times \mathbf{B}] = \alpha \mathbf{B}\,, \tag{2.24}$$

where α is, generally saying, a scalar function that depends on the position and time. If α is not equal to zero, then the magnetic field is nonpotential. The magnetic field has to satisfy the divergence-free Maxwell equation $\nabla \cdot \mathbf{B} = 0$. By applying the vector identity $\nabla \cdot [\nabla \times \mathbf{B}] = 0$ it is obtained,

$$\nabla \cdot [\nabla \times \mathbf{B}] = \nabla \cdot (\alpha \mathbf{B}) = \alpha(\nabla \cdot \mathbf{B}) + \mathbf{B} \cdot \nabla \alpha = \mathbf{B} \cdot \nabla \alpha = 0\,. \tag{2.25}$$

That implies that α is constant along each field line,

$$[\nabla \times [\nabla \times \mathbf{B}]] = \nabla \times \alpha \mathbf{B} = \alpha\,[\nabla \times \mathbf{B}] = \alpha^2 \mathbf{B}\,. \tag{2.26}$$

The left-hand side of this equation also can be written by opening the double vector product:

$$[\nabla \times [\nabla \times \mathbf{B}]] = \nabla(\nabla \cdot \mathbf{B}) - \nabla^2 \mathbf{B}\,. \tag{2.27}$$

Combining Equations (2.26) and (2.27) and applying the divergence-free condition, we obtain

$$\nabla^2 \mathbf{B} + \alpha^2 \mathbf{B} = 0\,. \tag{2.28}$$

The family of solutions with $\alpha = \mathbf{const}$ are called linear force-free models.

2.1.3 Linear Force-free magnetic arcades

An example of a linear force-free model is a sheared arcade. In this case, the magnetic field is represented by a periodic function, and its strength is exponentially decreasing with height,

$$B_x = B_{x0} \cos(kx) \exp(-z/H_b)\,, \tag{2.29}$$
$$B_y = B_{y0} \cos(kx) \exp(-z/H_b)\,, \tag{2.30}$$
$$B_z = B_0 \sin(kx) \exp(-z/H_b)\,, \tag{2.31}$$

where $k = \pi/2L$ and the parameter L is related to the lateral extension, and the constant H_b determines the magnetic scale height. The three components of $\nabla \times \mathbf{B}$ are

$$(\nabla \times \mathbf{B})_x = \frac{B_{y0}}{H_b} \cos kx \exp\left(-z/H_b\right), \tag{2.32}$$
$$(\nabla \times \mathbf{B})_y = \left(-\frac{B_{x0}}{H_b} - kB_0\right) \cos kx \exp\left(-z/H_b\right), \tag{2.33}$$
$$(\nabla \times \mathbf{B})_z = -kB_{y0} \sin kx \exp\left(-z/H_b\right). \tag{2.34}$$

Applying the force-free condition $\nabla \times \mathbf{B} = \alpha \mathbf{B}$ with $\alpha = \mathbf{const}$, we obtain

$$\frac{B_{y0}}{H_b} = \alpha B_{x0}\,, \tag{2.35}$$
$$-\frac{B_{x0}}{H_b} - kB_0 = \alpha B_{y0}\,, \tag{2.36}$$
$$-kB_{y0} = \alpha B_0\,. \tag{2.37}$$

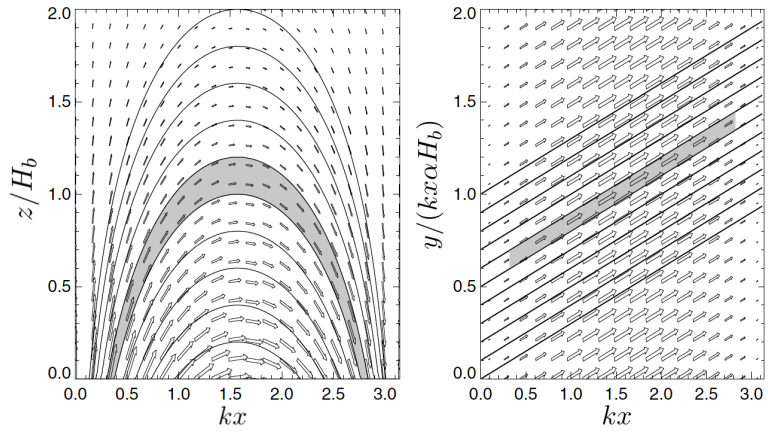

Figure 2.1: Force-free magnetic field of a sheared arcade, with the components (B_x, B_z) shown in the vertical plane (left), and the components (B_x, B_y) shown in the horizontal plane (right). The shear angle θ corresponds to the slope of the field lines at the right panel. Adapted from Aschwanden (2005).

From these equations we can derive the following conditions for the parameters of the structure:

$$B_{x0} = -\frac{B_0}{kH_b} = -\frac{2L}{\pi H_b} B_0 \,, \tag{2.38}$$

$$B_{y0} = -\sqrt{1 - \left(\frac{2L}{\pi H_b}\right)^2}\, B_0 \,, \tag{2.39}$$

$$\alpha = \sqrt{\frac{\pi^2}{4L^2} - \frac{1}{H_b^2}} \,. \tag{2.40}$$

This sheared arcade magnetic structure is shown in Figure 2.1 from the different perspectives. The shear angle correspond to the inclination in the right panel of Figure 2.1 that can be defined as

$$\tan\theta = \frac{B_y}{B_x} = \sqrt{\left(\frac{\pi H_b}{2L}\right)^2 - 1} = \alpha H_b \,. \tag{2.41}$$

This equation shows the relation between the shear angle and the nonpotential magnetic field parameters. If θ is equal to zero, this implies that α is also equal to zero, recovering a potential magnetic field case.

With all the above definitions, the magnetic field components of the sheared arcade become as follows,

$$B_x = -\frac{2LB_0}{\pi H_b} \cos(k(x - x_0)) \exp\left(-\frac{z - z_0}{H_b}\right) \,, \tag{2.42}$$

$$B_y = -\sqrt{1 - \left(\frac{2L}{\pi H_b}\right)^2}\, B_0 \cos(k(x - x_0)) \exp\left(-\frac{z - z_0}{H_b}\right) \,, \tag{2.43}$$

$$B_z = B_0 \sin(k(x - x_0)) \exp\left(-\frac{z - z_0}{H_b}\right) \,, \tag{2.44}$$

where (x_0, z_0) are the coordinates of the center of the magnetic structure.

In the numerical experiments of this thesis, we widely use the sheared arcade as an initial magnetic configuration before the formation of a flux rope (see Chapters 3, 5). In Chapter 3, we use this configuration as an initial magnetic field configuration to generate a flux rope by foot point driving. We will study oscillations of a prominence in the arcade with the two shearing angles. In Chapter 4, we use the combination of major and minor arcades as the main magnetic field configuration. In that case, the components of the magnetic field are defined as

$$B_x = B_0 \cos(k_1(x - x_0))e^{-k_1(z-z_0)} - B_0 \cos(k_2(x - x_0))e^{-k_2(z-z_0)}\,, \tag{2.45}$$

$$B_z = -B_0 \sin(k_1(x - x_0))e^{-k_1(z-z_0)} + B_0 \sin(k_2(x - x_0))e^{-k_2(z-z_0)}\,, \tag{2.46}$$

and B_y component of the magnetic field is equal to zero. In Equation 2.45, x_0, z_0 are the coordinates of the center of the magnetic structure, $k_1 = \frac{\pi}{D}$ and $k_2 = 3k_1$, and D is the half-size of the numerical domain along the x-direction. It is easy to see that the parameter α is equal to zero in this case, and we deal with the potential magnetic field.

2.1.4 MHD waves

Most of the prominence oscillations have been modeled in terms of linear MHD waves. In this section, we describe the linearization of the MHD equations, and later we proceed by discussing oscillatory modes in a uniform media.

We start from the set of MHD equations from Section 2.3. For simplicity, we consider an adiabatic approximation and neglect the gravity force, leading to the following system,

$$\frac{\partial \rho}{\partial t} + \nabla(\rho \mathbf{v}) = 0\,, \tag{2.47}$$

$$\frac{\partial \rho \mathbf{v}}{\partial t} + \nabla \cdot (\rho \mathbf{v}\mathbf{v}) = -\nabla p + \frac{1}{\mu_0}(\nabla \times \mathbf{B}) \times \mathbf{B}\,, \tag{2.48}$$

$$\frac{\partial}{\partial t}\Big(\frac{p}{\rho^\gamma}\Big) + \mathbf{v} \cdot \nabla\Big(\frac{p}{\rho^\gamma}\Big) = 0\,, \tag{2.49}$$

together with the induction equation, and the divergence-free Maxwell's condition

$$\frac{\partial \mathbf{B}}{\partial t} = \nabla \times (\mathbf{v} \times \mathbf{B})\,, \tag{2.50}$$

$$\nabla \cdot \mathbf{B} = 0\,. \tag{2.51}$$

As mentioned before, due to the large values of the Reynolds numbers in the solar atmosphere, we can neglect the viscous term in the equation of motion and the diffusive term in the induction equation. Since we consider the adiabatic process, the energy balance is represented by Equation (2.49).

The initial equilibrium is provided by the balance between the magnetic force and the gas pressure force. This condition is written as

$$0 = -\nabla p_0 + \frac{1}{\mu_0}(\nabla \times \mathbf{B}_0) \times \mathbf{B}_0\,, \tag{2.52}$$

where p_0, $\mathbf{B}_0$ are initial values of the pressure, and the magnetic field, respectively, assumed to be constant in time. The background magnetic field has to satisfy the divergence-free condition:

$$\nabla \cdot \mathbf{B}_0 = 0\,. \tag{2.53}$$

The density, pressure, and magnetic field are split into the equilibrium values and the small perturbations. The initial velocities are assumed to be zero. This way, all the variables can be represented as

$$\begin{aligned} \rho &= \rho_0 + \rho_1 \,, \\ p &= p_0 + p_1 \,, \\ \mathbf{B} &= \mathbf{B}_0 + \mathbf{B}_1 \,, \\ \mathbf{v} &= \mathbf{v}_1 \,. \end{aligned} \tag{2.54}$$

We then substitute the density, pressure and magnetic field and velocity variables in Equations (2.47)-(2.51). Neglecting the second-order terms formed by the product of perturbations and using Equation (2.52), we obtain a set of linearized equations for the perturbed quantities:

$$\frac{\partial \rho_1}{\partial t} + (\mathbf{v}_1 \cdot \nabla)\rho_0 + \rho_0(\nabla \cdot \mathbf{v}_1) = 0 \,, \tag{2.55}$$

$$\rho_0 \frac{\partial \mathbf{v}_1}{\partial t} = -\nabla p_1 + \frac{1}{\mu_0}(\nabla \times \mathbf{B}_1) \times \mathbf{B}_0 \,, \tag{2.56}$$

$$\frac{\partial p_1}{\partial t} + (\mathbf{v}_1 \cdot \nabla)p_0 - c_S^2 \Big(\frac{\partial \rho_1}{\partial t} + (\mathbf{v}_1 \cdot \nabla)\rho_0 \Big) = 0 \,, \tag{2.57}$$

$$\frac{\partial \mathbf{B}_1}{\partial t} = \nabla \times (\mathbf{v}_1 \times \mathbf{B}_0) \,, \tag{2.58}$$

$$\nabla \cdot \mathbf{B}_1 = 0 \,, \tag{2.59}$$

where the sound speed, $cs = \sqrt{\gamma p_0/\rho_0}$ is defined by the equilibrium values of the density and pressure and is constant in space assuming spatially-constant temperature and molecular weight. We then take time derivative of Equation (2.56) and substitute $\partial\rho/\partial t$, $\partial p/\partial t$ and $\partial \mathbf{B}/\partial t$ from Equations (2.55), (2.57) and (2.58), respectively. This way a single equation for the velocity perturbation is obtained:

$$\frac{\partial^2 \mathbf{v}_1}{\partial t^2} = c_S^2 \nabla(\nabla \cdot \mathbf{v}_1) + [\nabla \times (\nabla \times (\mathbf{v}_1 \times \mathbf{B}_0)] \times \frac{\mathbf{B}_0}{\mu_0 \rho_0} \,. \tag{2.60}$$

This equation allows for solutions in the form of a plane wave that propagates in the direction of $\mathbf{k}$ having an angular frequency ω:

$$\mathbf{v}_1(\mathbf{r}, t) = \mathbf{V}\, e^{i(\mathbf{k}\cdot\mathbf{r} - \omega t)} \,. \tag{2.61}$$

Introducing $\mathbf{v}_1$ in Equation (2.60) and replacing $\partial/\partial t$ and ∇ with $-i\omega$ and $i\mathbf{k}$, respectively, we obtain the following expression:

$$\omega^2 \mathbf{v}_1 = c_S^2 \mathbf{k}(\mathbf{k} \cdot \mathbf{v}_1) + \Big[\mathbf{k} \times (\mathbf{k} \times (\mathbf{v}_1 \times \mathbf{B}_0))\Big] \times \frac{\mathbf{B}_0}{\mu_0 \rho_0} \,. \tag{2.62}$$

The vector Alfvén speed can be defined as

$$\mathbf{v}_A = \frac{\mathbf{B}_0}{(\mu_0 \rho_0)^{1/2}} \,. \tag{2.63}$$

Together with the sound speed, this speed is an important characteristic of the medium where the waves propagate. Using the definition of the Alfvén speed, and expanding the vector product, Equation 2.62 reduces to the expression:

$$\omega^2\mathbf{v}_1 = (c_S^2 + v_A^2)(\mathbf{k}\cdot\mathbf{v}_1)\mathbf{k} + (\mathbf{v}_A\cdot\mathbf{k})\Big[(\mathbf{v}_A\cdot\mathbf{k})\mathbf{v}_1 - (\mathbf{v}_1\cdot\mathbf{k})\mathbf{v}_A - (\mathbf{v}_A\cdot\mathbf{v}_1)\mathbf{k}\Big]\,. \tag{2.64}$$

We now assume that the waves propagate only in the XZ-plane, implying that $\mathbf{k} = (k_x, 0, k_z)$, and that the initial magnetic field $\mathbf{B_0}$ is uniform and directed along z-axis, i. e., $\mathbf{B}_0 = (0, 0, B_0)$. Under these conditions, the three components of Equation (2.64) become,

$$\Big[\omega^2 - v_A^2k^2 - c_S^2k_x^2\Big]v_{1x} = c_S^2k_xk_zv_{1z}\,, \tag{2.65}$$

$$\omega^2 v_{1y} = v_A^2k_z^2v_{1y}\,, \tag{2.66}$$

$$c_S^2k_xk_zv_{1x} = (\omega^2 - c_S^2k_z^2)v_{1z}\,. \tag{2.67}$$

Firstly, we consider Equation (2.66) which is independent of the other two equations. Considering an angle θ_B formed by the magnetic field and the direction of propagation, the vertical projection of the vector $\mathbf{k}$ is $k_z = k\cos\theta_B$. Then, Equation (2.66) can be written as

$$\omega = kv_A\cos\theta_B = \pm\mathbf{v}_A\cdot\mathbf{k}\,. \tag{2.68}$$

This expression is the dispersion relation for the Alfvén waves, and it defines the frequency as a function of the wave number. The phase speed, that is, $v_{ph} = \omega/k = v_A\cos\theta_B$, depends on the direction of propagation. It is maximum when $\theta_B = 0$ (propagation along the magnetic field), and there is no propagation when $\theta_B = \pi/2$. Since the vector $\mathbf{k}$ lies in the XZ-plane and the velocity perturbation is along the Y-direction, these vectors are perpendicular, and the Alfvén wave is a transverse wave. The group velocity gives the direction of the energy propagation and it is equal to $\mathbf{v_g} = \partial\omega/\partial\mathbf{k} = \pm\mathbf{v_a}$ for the Alfvén wave. This expression shows that the Alfvén waves only transport energy along the magnetic field lines.

Using Equation (2.58) and introducing the perturbation of the magnetic field in the form of the plane wave, we obtain

$$-\omega\mathbf{B}_1 = \mathbf{k}\times(\mathbf{v}_1\times\mathbf{B}_0)\,, \tag{2.69}$$

that is equivalent to

$$-\omega\mathbf{B}_1 = (\mathbf{k}\cdot\mathbf{B_0})\mathbf{v}_1 - (\mathbf{k}\cdot\mathbf{v}_1)\mathbf{B}_0\,. \tag{2.70}$$

For the Alfvén waves $\mathbf{k}\cdot\mathbf{v}_1 = 0$ and $\omega = kv_A\cos\theta_B$, so Equation (2.70) simplifies to

$$\frac{\mathbf{v}_1}{v_A} = -\frac{\mathbf{B}_1}{B_0}\,, \tag{2.71}$$

indicating that the perturbation of the magnetic field and velocity are aligned. Since $\mathbf{v}_1\cdot\mathbf{B}_0 = 0$, then we automatically obtain

$$\mathbf{B}_0\cdot\mathbf{B}_1 = 0, \tag{2.72}$$

meaning that the perturbation of the magnetic field is perpendicular to the unperturbed magnetic field. The divergence-free condition for the perturbed magnetic field is $\mathbf{k}\cdot\mathbf{B}_1 = 0$.

The linearized Lorentz force is written as

$$\mathbf{j}_1\times\mathbf{B}_0 = i(\mathbf{k}\times\mathbf{B}_1)\times\mathbf{B}_0/\mu_0 = i(\mathbf{k}\cdot\mathbf{B}_0)\mathbf{B}_1/\mu_0 - i(\mathbf{B}_0\cdot\mathbf{B}_1)\mathbf{k}/\mu_0\,, \tag{2.73}$$

where the first term represents the magnetic tension and the second term is magnetic pressure. As $\mathbf{B_0}\cdot\mathbf{B_1} = 0$, the second term vanishes, and only the first term remains. Thus, given by Equation (2.73), the restoring force for the Alfvén waves is the magnetic tension.

We then combine two remaining Equations (2.65) and (2.67) to obtain the following dispersion relation:

$$\omega^4 - \omega^2 k^2 (c_S^2 + v_A^2) + c_S^2 v_A^2 k^4 \cos^2\theta_B = 0\,, \tag{2.74}$$

that allows obtaining the phase speed as

$$v_{ph}^2 = \left(\frac{\omega}{k}\right)^2 = \frac{1}{2}(v_A^2 + c_S^2) \pm \frac{1}{2}\sqrt{(v_A^2 + c_S^2)^2 - 4 v_A^2 c_S^2 \cos^2\theta_B}\,. \tag{2.75}$$

In this equation, the positive sign before the square root corresponds to the fast magnetoacoustic wave, and the negative sign gives the phase speed of the slow magnetoacoustic wave. Assuming propagation along the magnetic field, $\theta_B = 0$, we obtain that the phase speeds for the slow or fast waves are equal to either v_A or c_s, and for transverse propagation ($\theta_B = \pi/2$), the fast magnetoacoustic wave has a speed $\sqrt{v_A^2 + c_s^2}$ and the slow magnetoacoustic wave vanishes having a zero-frequency. The fast magnetoacoustic wave can propagate in any direction having its maximum phase speed equal to $\sqrt{v_A^2 + c_s^2}$ in the direction of $\theta_B = \pi/2$, and its minimum phase speed of either v_A or c_s for $\theta_B = 0$. The slow magnetoacoustic wave reaches its maximum phase speed of either v_A or c_s along the magnetic field ($\theta_B = 0$), and the phase speed decreases with increasing the angle becoming zero for $\theta_B = \pi/2$.

In the solar corona, the plasma is characterized by the low values of β-parameter equivalent to the condition $v_A \gg c_s$. In this limit, the values for the frequencies of the different modes become,

$$\omega_{\rm fast} = k v_A\,, \tag{2.76}$$

$$\omega_{\rm slow} = k c_s \cos\theta_B\,. \tag{2.77}$$

The group velocity suggests that the fast wave transports the energy in the direction of the wave propagation, while the slow mode transports the energy along the magnetic field lines.

2.2 The pendulum model

Luna et al. (2012a) proposed the so-called pendulum model to explain the prominence oscillations along the magnetic field. The thread moves along the curved magnetic flux tube, oscillating around the bottom of the dip. These oscillations resemble a pendulum with a length equivalent to an average radius of curvature of the dip. For this type of oscillation, the main restoring force is the gravity projected along the magnetic field of the dip. The gravity force projection is directed toward the bottom of the dip. The relative importance of the gas pressure modes and the gravity-driven modes in the longitudinal oscillations of the threads was studied in Luna et al. (2012c). In that work, the pendulum model was generalized. It was assumed that the plasma is low-β and is located in a static magnetic flux tube as shown in Figure 2.2. In such a situation, it is convenient to project the MHD equations along the direction s of the field lines. Luna et al. (2012c) assumed the system to be adiabatic, with no heating or radiation, and the tubes to have a uniform width. By linearizing the set of MHD equations from Karpen et al. (2005), Luna et al. (2012c) obtained the following system,

$$\frac{\partial \rho_1}{\partial t} + v_1 \frac{\partial \rho_0}{\partial s} + \rho_0 \frac{\partial v_1}{\partial s} = 0\,, \tag{2.78}$$

$$\rho_0 \frac{\partial v_1}{\partial t} + \frac{\partial p_1}{\partial s} - \rho_1 g_\parallel = 0\,, \tag{2.79}$$

$$\frac{\partial p_1}{\partial t} + v_1 \frac{\partial p_0}{\partial s} + \gamma p_0 \frac{\partial v_1}{\partial s} = 0\,. \tag{2.80}$$

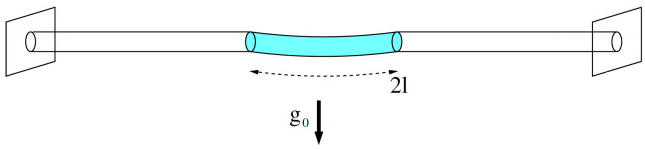

Figure 2.2: Illustration of one of the thread and the hot coronal regions configuration considered in the study of the pendulum oscillations by Luna et al. (2012c). The length of the flux tube is $2L$, the length of the thread is $2l$.

The thread is assumed to be in hydrostatic equilibrium:

$$\frac{\partial p_0}{\partial s} = \rho_0 g_{\parallel} \,. \tag{2.81}$$

Combining Equations (2.78)-(2.80) and using the expression for the hydrostatic equilibrium, it is obtained,

$$\frac{\partial^2 v_1}{\partial t^2} - c_S^2 \frac{\partial^2 v_1}{\partial s^2} = \gamma g_{\parallel} \frac{\partial v_1}{\partial s} + v_1 \frac{\partial g_{\parallel}}{\partial s} \,. \tag{2.82}$$

The blue thread segment shown in Figure 2.2 has a constant radius of curvature R_c. The radius of curvature is positive for concave-up and negative for concave-down tubes. With this consideration, the equation on each segment of the tube is modified as

$$\frac{\partial^2 v_1}{\partial t^2} - c_S^2 \frac{\partial^2 v_1}{\partial s^2} = -\gamma g_0 \sin\theta \frac{\partial v_1}{\partial s} - v_1 \frac{g_0 \cos\theta}{R_c} \,, \tag{2.83}$$

where was used $1/R_c = \partial\theta/\partial s$, defining an angle $\theta = s/R_c$. In the following, it is assumed that the radius of curvature R_c is sufficiently large to fulfill the condition $|s/R_c| \ll 1$, and, consequently, the angle θ is small. Thus, one can approximate $\sin\theta \approx \theta$ and $\cos\theta \approx 1$ and simplify Equation (2.83) as follows

$$\frac{\partial^2 v_1}{\partial t^2} - c_S^2 \frac{\partial^2 v_1}{\partial s^2} + \frac{\gamma g_0 s}{R_c} \frac{\partial v_1}{\partial s} + v_1 \frac{g_0}{R_c} = 0 \,. \tag{2.84}$$

It is easy to see from this equation that if the curvature of the field line is negligible, i.e., $R_c \to \infty$, one obtains the equation for the acoustic waves. Assuming a harmonic perturbation in the form $v(s)e^{-i\omega t}$ an equation is obtained,

$$c_S^2 \frac{\partial^2 v_1}{\partial s^2} - \frac{\gamma g_0 s}{R_c} \frac{\partial v_1}{\partial s} + v_1(\omega^2 - \frac{g_0}{R_c}) = 0 \,, \tag{2.85}$$

which describes oscillatory motions of the plasma inside the flux tube with a constant radius of curvature. Luna et al. (2012c) obtained an approximate expression for the fundamental mode of these oscillatory motions:

$$\omega_{\rm fund}^2 = \frac{g_0}{R_c} + \frac{c_{sc}^2}{l(L-l)\chi} \,, \tag{2.86}$$

where c_{sc} is the value of the coronal sound speed, l, and L are half-length of the thread and the magnetic field lines, respectively, and χ is the density contrast of the thread with respect to the surrounding corona. The fundamental mode has two contributions associated with the

gravity-driven and pressure-driven modes, whose frequencies are defined as

$$\begin{aligned} \omega_g^2 &= \frac{g_0}{R_c}\,, \\ \omega_p^2 &= \frac{c_{sc}^2}{l(L-l)\chi}\,. \end{aligned} \tag{2.87}$$

Thus, the frequency of the fundamental mode of the thread oscillations can be written as

$$\omega_{\rm fund}^2 = \omega_g^2 + \omega_p^2\,. \tag{2.88}$$

The relative importance of these two contributions can be evaluated from the ratio of R_c/R_{lim}, where R_{lim} is defined as

$$R_{lim} = \frac{l(L-l)\chi g_0}{c_{sc}^2}\,. \tag{2.89}$$

The restoring force of the LALOs is mainly the solar gravity when R_c/R_{lim} ratio is small, which is equivalent to the limit $R_c \ll R_{lim}$. On the contrary, the oscillations are pressure-driven for a large value of the ratio or $R_c \gg R_{lim}$. The length of the threads and the density contrast vary significantly in different measurements. However, under typical prominence conditions, the radius of curvature is much smaller than the critical radius, and the pendulum mode is the dominant one. In such a case, the period of the oscillations is given by the pendulum period:

$$P = 2\pi\sqrt{\frac{R_c}{g_0}}\,. \tag{2.90}$$

2.3 The MHD code

In this thesis, we use MANCHA3D code. MANCHA3D is a state-of-the-art code that solves the 3D MHD equations in a Cartesian grid with the hyperdiffusion algorithms, and it is written in Fortran 90. The code is fully MPI-parallelized using the distributed memory concept and allowing full arbitrary 3D domain decomposition.[1] The code has been developed by Khomenko & Collados (2006); Khomenko et al. (2008) and extended by Felipe et al. (2010) and later works.

Generally, the code can solve the nonideal MHD equations that include effects due to partial ionization of the plasma. In this thesis, we consider ideal MHD processes, so the following set of equations is solved:

$$\frac{\partial \rho}{\partial t} + \nabla \cdot (\rho \mathbf{v}) = \left(\frac{\partial \rho}{\partial t}\right)_{\rm diff}, \tag{2.91}$$

$$\frac{\partial \rho \mathbf{v}}{\partial t} + \nabla \cdot \left[\rho \mathbf{v}\mathbf{v} + \left(p + \frac{\mathbf{B}^2}{2\mu_0}\right)\mathbf{I} - \frac{\mathbf{B}\mathbf{B}}{\mu_0}\right] = \rho \mathbf{g} + \mathbf{S}(t) + \left(\frac{\partial \rho \mathbf{v}}{\partial t}\right)_{\rm diff}, \tag{2.92}$$

$$\frac{\partial e}{\partial t} + \nabla \cdot \left[\mathbf{v}\left(e + p + \frac{|\mathbf{B}|^2}{2\mu_0}\right) - \frac{\mathbf{B}(\mathbf{v}\cdot\mathbf{B})}{\mu_0}\right] = (\rho \mathbf{g} + \mathbf{S}(t)) \cdot \mathbf{v} + Q_{\rm R} + \left(\frac{\partial e}{\partial t}\right)_{\rm diff}, \tag{2.93}$$

$$\frac{\partial \mathbf{B}}{\partial t} = \nabla \times [\mathbf{v} \times \mathbf{B}] + \left(\frac{\partial \mathbf{B}}{\partial t}\right)_{\rm diff}, \tag{2.94}$$

where ρ is the density, p is the gas pressure, $\mathbf{B}$ is the magnetic field, $\mathbf{g}$ is the solar gravitational acceleration, and $\mathbf{v}$ is velocity, $\mathbf{I}$ is identity tensor, $\mathbf{S(t)}$ is an external force, and $Q_{\rm R}$ denotes radiative energy exchange term. We can see that each of the equations has a term associated with numerical diffusion. These terms have their physical counterparts in the MHD equations associated with the magnetic diffusivity, viscosity, or thermal conductivity, except for the continuity equation. Considering that the magnetic Reynolds number has large values in the solar atmosphere, the physical diffusivity term in the induction equation is negligible compared to the advection term. The same applies to the viscous force in the momentum equation since the Reynolds number is large. However, the induction equation and the equation of motion include the numerical counterparts of these terms. The numerical diffusion terms are used to provide stability for the numerical solution. More detailed treatment of these terms in the code is deferred to Section 2.3.2.

In Equation (2.94) the total energy per unit volume e consists of three contributions:

$$e = \frac{1}{2}\rho \mathbf{v}^2 + e_{\rm int} + \frac{\mathbf{B}^2}{2\mu_0}. \tag{2.95}$$

Alternatively, the MANCHA3D code can solve the equation of conservation of the internal energy instead of the total energy. The internal energy equation is written as

$$\frac{\partial e_{\rm int}}{\partial t} + \nabla \cdot (\mathbf{v} e_{\rm int}) + (\gamma - 1) e_{\rm int} \nabla \cdot \mathbf{v} = Q_{\rm R} + \left(\frac{\partial e_{\rm int}}{\partial t}\right)_{\rm diff} \tag{2.96}$$

The variables in the code are split into equilibrium values and nonlinear perturbations:

$$\rho = \rho_0 + \rho_1; \;\; p = p_0 + p_1; \;\; \mathbf{B} = \mathbf{B_0} + \mathbf{B}_1; \;\; \mathbf{v} = \mathbf{v}_1. \tag{2.97}$$

where index '0' corresponds to the equilibrium value of the magnetic field, pressure, and density. The index index '1' represents nonlinear perturbation. The initial velocity is assumed to be zero, therefore the total velocity is equal to the perturbed value $\mathbf{v_1}$.

[1] A more detailed description of the code can be found in the latest update of the MANCHA3D manual.

The code assumes that the initial atmosphere of the numerical experiment is in magnetohydrostatic equilibrium. This implies that the temporal derivatives of the unperturbed variables are zero. The equilibrium is defined as follows

$$\nabla \cdot \Big[\Big(p_0 + \frac{{\mathbf{B}_0}^2}{2\mu_0}\Big)\mathbf{I} - \frac{\mathbf{B_0}\mathbf{B_0}}{\mu_0}\Big] = \rho_0 \mathbf{g}\,. \tag{2.98}$$

Substituting the split variables into Equation (2.91) and taking into account the equation for magnetohydrostatic equilibrium (Equation (2.98)), we obtain the system of nonlinear equations for perturbations in a conservative form:

$$\frac{\partial \rho_1}{\partial t} + \nabla\Big[(\rho_0+\rho_1)\mathbf{v}_1\Big] = \Big(\frac{\partial \rho_1}{\partial t}\Big)_{\text{diff}}\,, \tag{2.99}$$

$$\begin{aligned}\frac{\partial[(\rho_0+\rho_1)\mathbf{v}_1]}{\partial t} + \nabla\cdot\Big[(\rho_0+\rho_1)\mathbf{v}_1\mathbf{v}_1 + \Big(p_1 + \frac{\mathbf{B}_1^2}{2\mu_0} + \frac{\mathbf{B}_1\cdot\mathbf{B}_0}{\mu_0}\Big)\mathbf{I} - \\ -\frac{1}{\mu_0}(\mathbf{B}_0\mathbf{B}_1 + \mathbf{B}_1\mathbf{B}_0 + \mathbf{B}_1\mathbf{B}_1)\Big] = \rho_1\mathbf{g} + \Big(\frac{\partial[(\rho_0+\rho_1)\mathbf{v}_1]}{\partial t}\Big)_{\text{diff}} + \mathbf{S}(\mathbf{t})\,,\end{aligned} \tag{2.100}$$

$$\begin{aligned}\frac{\partial e_1}{\partial t} + \nabla\cdot\Big[\mathbf{v_1}\Big((e_0+e_1) + (p_0+p_1) + \frac{|\mathbf{B}_0+\mathbf{B}_1|^2}{2\mu_0}\Big) - \\ -\frac{1}{\mu_0}(\mathbf{B}_0+\mathbf{B}_1)\Big(\mathbf{v}_1\cdot(\mathbf{B}_0+\mathbf{B}_1)\Big)\Big] = (\rho_0+\rho_1)(\mathbf{g}\cdot\mathbf{v_1}) + Q_{\text{R}} + \Big(\frac{\partial e_1}{\partial t}\Big)_{\text{diff}}\,,\end{aligned} \tag{2.101}$$

$$\frac{\partial \mathbf{B}_1}{\partial t} = \nabla\times[\mathbf{v}_1\times(\mathbf{B}_0+\mathbf{B}_1)] + \Big(\frac{\partial \mathbf{B}_1}{\partial t}\Big)_{\text{diff}}\,. \tag{2.102}$$

MANCHA3D code deals with split variables and solves the equations for perturbations. This approach gives several advantages for the numerical performance. On the one hand, the perturbed values can exceed by orders of magnitude the initial values, leading to the numerical precision problems. This can be avoided by solving the equations for perturbation. On the other hand, the finite precision when computing derivatives can lead to undesirable changes of the equilibrium in the case of solving the full-variable equations. This can also be avoided by using the split variable approach when the equilibrium values of the variables remain preserved in time. Finally, it is much easier to define the boundary conditions for the perturbation rather than for full-variable.

In terms of the Cartesian coordinates, the continuity equation is written as

$$\frac{\partial \rho_1}{\partial t} + \frac{\partial}{\partial x}[(\rho_0+\rho_1)v_{1x}] + \frac{\partial}{\partial y}[(\rho_0+\rho_1)v_{1y}] + \frac{\partial}{\partial z}[(\rho_0+\rho_1)v_{1z}] = \Big(\frac{\partial \rho_1}{\partial t}\Big)_{\text{diff}}\,. \tag{2.103}$$

The following are the three projections of the momentum equation, assuming the external force $\mathbf{S}(\mathbf{t}) = 0$. Each projection includes the corresponding diffusivity term:

$$\begin{aligned}&\frac{\partial}{\partial t}[(\rho_0+\rho_1)v_{1x}] + \\ &+\frac{\partial}{\partial x}\Big\{(\rho_0+\rho_1)v_{1x}^2 + p_1 + \frac{1}{\mu_0}[B_{y0}B_{y1} + B_{z0}B_{z1} - B_{x0}B_{x1} + \frac{1}{2}(B_{y1}^2 + B_{z1}^2 - B_{x1}^2)]\Big\} + \\ &+\frac{\partial}{\partial y}\Big\{(\rho_0+\rho_1)v_{1x}v_{1y} - \frac{1}{\mu_0}[B_{x1}B_{y0} + B_{x0}B_{y1} + B_{x1}B_{y1})]\Big\} + \\ &+\frac{\partial}{\partial z}\Big\{(\rho_0+\rho_1)v_{1x}v_{1z} - \frac{1}{\mu_0}[B_{x1}B_{z0} + B_{x0}B_{z1} + B_{x1}B_{z1})]\Big\} = \Big(\frac{\partial(\rho_0+\rho_1)v_{1x}}{\partial t}\Big)_{\text{diff}}\,,\end{aligned} \tag{2.104}$$

$$\frac{\partial}{\partial t}[(\rho_0+\rho_1)v_{1y}]+ \\ +\frac{\partial}{\partial x}\Big\{(\rho_0+\rho_1)v_{1y}v_{1x}-\frac{1}{\mu_0}[B_{y1}B_{x0}+B_{y0}B_{x1}+B_{y1}B_{x1}]\Big\}+ \\ +\frac{\partial}{\partial y}\Big\{(\rho_0+\rho_1)v_{1y}^2+p_1+\frac{1}{\mu_0}[B_{x0}B_{x1}+B_{z0}B_{z1}-B_{y0}B_{y1}+\frac{1}{2}(B_{x1}^2+B_{z1}^2-B_{y1}^2]\Big\}+ \\ +\frac{\partial}{\partial z}\Big\{(\rho_0+\rho_1)v_{1y}v_{1z}-\frac{1}{\mu_0}[B_{y1}B_{z0}+B_{y0}B_{z1}+B_{y1}B_{z1}]\Big\}=\Big(\frac{\partial(\rho_0+\rho_1)v_{1y}}{\partial t}\Big)_{\text{diff}}, \quad (2.105)$$

$$\frac{\partial}{\partial t}[(\rho_0+\rho_1)v_{1z}]+ \\ +\frac{\partial}{\partial x}\Big\{(\rho_0+\rho_1)v_{1z}v_{1x}-\frac{1}{\mu_0}[B_{z1}B_{x0}+B_{z0}B_{x1}+B_{z1}B_{x1}]\Big\}+ \\ +\frac{\partial}{\partial y}\Big\{(\rho_0+\rho_1)v_{1z}v_{1y}-\frac{1}{\mu_0}[B_{z1}B_{y0}+B_{z0}B_{y1}+B_{z1}B_{y1}]\Big\}+ \\ +\frac{\partial}{\partial z}\Big\{(\rho_0+\rho_1)v_{1z}^2+p_1+\frac{1}{\mu_0}[B_{x0}B_{x1}+B_{y0}B_{y1}-B_{z0}B_{z1}+\frac{1}{2}(B_{x1}^2+B_{y1}^2-B_{z1}^2]\Big\}= \\ =-\rho_1 g+\Big(\frac{\partial(\rho_0+\rho_1)v_{1z}}{\partial t}\Big)_{\text{diff}}. \quad (2.106)$$

Three projections of the induction equations are written as follows

$$\frac{\partial B_{x1}}{\partial t}=\frac{\partial}{\partial y}[v_{1x}(B_{y0}+B_{y1})-v_{1y}(B_{x0}+B_{x1})]- \\ -\frac{\partial}{\partial z}[v_{1z}(B_{x0}+B_{x1})-v_{1x}(B_{z0}+B_{z1})]+\Big(\frac{\partial B_{x1}}{\partial t}\Big)_{\text{diff}}, \quad (2.107)$$

$$\frac{\partial B_{y1}}{\partial t}=\frac{\partial}{\partial z}[v_{1y}(B_{z0}+B_{z1})-v_{1z}(B_{y0}+B_{y1})]- \\ -\frac{\partial}{\partial x}[v_{1x}(B_{y0}+B_{y1})-v_{1y}(B_{x0}+B_{x1})]+\Big(\frac{\partial B_{y1}}{\partial t}\Big)_{\text{diff}}, \quad (2.108)$$

$$\frac{\partial B_{z1}}{\partial t}=\frac{\partial}{\partial x}[v_{1z}(B_{x0}+B_{x1})-v_{1x}(B_{z0}+B_{z1})]- \\ -\frac{\partial}{\partial y}[v_{1y}(B_{z0}+B_{z1})-v_{1z}(B_{y0}+B_{y1})]+\Big(\frac{\partial B_{z1}}{\partial t}\Big)_{\text{diff}}. \quad (2.109)$$

Finally, the equation for the perturbation of the total energy is defined as

$$\frac{\partial e_1}{\partial t}+\frac{\partial}{\partial x}\Big\{v_{1x}\Big((e_0+e_1)+(p_0+p_1)+\frac{(\mathbf{B}_0+\mathbf{B}_1)^2}{2\mu_0}\Big)-\frac{1}{\mu_0}(B_{x0}+B_{x1})\Big(\mathbf{v}_1\cdot(\mathbf{B}_0+\mathbf{B}_1)\Big)\Big\}+ \\ +\frac{\partial}{\partial y}\Big\{v_{1y}\Big((e_0+e_1)+(p_0+p_1)+\frac{(\mathbf{B}_0+\mathbf{B}_1)^2}{2\mu_0}\Big)-\frac{1}{\mu_0}(B_{y0}+B_{y1})\Big(\mathbf{v}_1\cdot(\mathbf{B}_0+\mathbf{B}_1)\Big)\Big\}+ \\ +\frac{\partial}{\partial z}\Big\{v_{1z}\Big((e_0+e_1)+(p_0+p_1)+\frac{(\mathbf{B}_0+\mathbf{B}_1)^2}{2\mu_0}\Big)-\frac{1}{\mu_0}(B_{z0}+B_{z1})\Big(\mathbf{v}_1\cdot(\mathbf{B}_0+\mathbf{B}_1)\Big)\Big\}= \\ =-(\rho_0+\rho_1)gv_{1z}+Q_{\text{R}}+\Big(\frac{\partial e_1}{\partial t}\Big)_{\text{diff}}. \quad (2.110)$$

The perturbed internal energy equation is defined as

$$\frac{\partial e_{\rm int1}}{\partial t}+\frac{\partial}{\partial x}\Big(v_{1x}(e_{\rm int1}+e_{\rm int0})\Big)+\frac{\partial}{\partial y}\Big(v_{1y}(e_{\rm int1}+e_{\rm int0})\Big)+\frac{\partial}{\partial z}\Big(v_{1z}(e_{\rm int1}+e_{\rm int0})\Big)+ \\ +(\gamma-1)(e_{\rm int1}+e_{\rm int0})\Big\{\frac{\partial v_{1x}}{\partial x}+\frac{\partial v_{1y}}{\partial y}+\frac{\partial v_{1x}}{\partial x}\Big\}=Q_{\rm R}+\left(\frac{\partial e_{\rm int1}}{\partial t}\right)_{\rm diff}, \tag{2.111}$$

As mentioned above, the $Q_{\rm R}$ term represents radiative losses. Computation of this term for the low solar atmosphere in the code is rather complex and includes the full solution of the Radiative Transfer Equation in the approximation of the Local Thermodynamic Equilibrium. For this thesis, we use a simpler approximation. Given that solar corona can be considered as an optically thin medium, we define radiative energy losses through Newton's cooling law:

$$Q_{\rm R}=-\rho_0 c_v\frac{T_1}{\tau_R}\,. \tag{2.112}$$

In this equation, τ_R is radiative relaxation time, a free parameter of the simulations. This radiative losses term is used only in the experiments with the flux rope prominence model, where it is important to avoid the strong heating inside the flux rope appearing in the absence of radiative losses (see more, e.g., Kaneko & Yokoyama 2015).

2.3.1 Numerical scheme

This section explains the numerical scheme employed by the code, including spatial and temporal discretization. The system of equations solved by the code can be written in the conservative form as

$$\frac{\partial \mathbf{u}}{\partial t}=\mathcal{R}(\mathbf{u})=-\nabla\mathbf{F}(\mathbf{u})+\mathbf{S}(\mathbf{u})\,, \tag{2.113}$$

where $\mathbf{u}$ represents variables in the equations:$[\rho_1,(\rho_1+\rho_0)\mathbf{v_1},e_1,\mathbf{B_1}]$. $\mathbf{R}(\mathbf{u})$ is the operator that includes the spatial derivatives of fluxes, $\mathbf{F}(\mathbf{u})$, and the source terms, $\mathbf{S}(\mathbf{u})$.

The solution is advanced in time using fourth-order Runge-Kutta written in compact form as

$$\mathbf{u}^{(k)}=\mathbf{u}^{(n)}+\alpha_k\Delta t\mathcal{R}\left(\mathbf{u}^{(k-1)}\right),\qquad k=1,\ldots,m,\;\;\mathbf{u}^{(n+1)}=\mathbf{u}^{(m)}\,, \tag{2.114}$$

where $\mathbf{u}^{(n+1)}$ corresponds to the solution at $t_{n+1}=t_n+\Delta t$, with Δt given by the Courant, Friedrichs, and Lewy (CFL) condition, m corresponds to the order of RK scheme, and the corresponding coefficients α_k can be computed as

$$\alpha_k=\frac{1}{m+1-k}\,. \tag{2.115}$$

The four steps are done in order to obtain the solution of an equation in the next time moment:

$$\begin{aligned}\mathbf{u}^{(1/4)}&=\mathbf{u}^{0}+\frac{\Delta t}{4}\mathcal{R}(\mathbf{u}^{(0)})\,,\\ \mathbf{u}^{(1/3)}&=\mathbf{u}^{(0)}+\frac{\Delta t}{3}\mathcal{R}(\mathbf{u}^{(1/4)})\,,\\ \mathbf{u}^{(1/2)}&=\mathbf{u}^{(0)}+\frac{\Delta t}{2}\mathcal{R}(\mathbf{u}^{(1/3)})\,,\\ \mathbf{u}^{(1)}&=\mathbf{u}^{(0)}+\Delta t\mathcal{R}(\mathbf{u}^{(1/2)})\,.\end{aligned} \tag{2.116}$$

The computational domain is discretized with a constant step in each of the three Cartesian directions. The spatial derivatives are approximately computed using a centered six-order

numerical scheme. For these purposes, the code needs the values of variables in 11 points in total. The first step corresponds to interpolations of the values in the mid-points (Nordlund & Galsgaard 1995) as follows

$$\mathbf{F}(\mathbf{u})_{i+1/2} = a_1\Big(\mathbf{F}(\mathbf{u})_i + \mathbf{F}(\mathbf{u})_{i+1}\Big) + b_1\Big(\mathbf{F}(\mathbf{u})_{i-1} + \mathbf{F}(\mathbf{u})_{i+2}\Big) + c_1\Big(\mathbf{F}(\mathbf{u})_{i-2} + \mathbf{F}(\mathbf{u})_{i+3}\Big)\,. \quad (2.117)$$

For computing the derivatives in the grid-point with index i, it is necessary to obtain the interpolated values of the variables in the grid-points with indexes $i+1/2,\ i-1/2,\ i+3/2,\ i-3/2,\ i+5/2,\ i-5/2$. The second step is computing the derivatives in the grid-point with index i using all needed interpolated values:

$$\Big(\frac{\partial \mathbf{F}(\mathbf{u})}{\partial s}\Big)_i = \frac{a_2}{\Delta s}\Big(\mathbf{F}(\mathbf{u})_{i-1/2} - \mathbf{F}(\mathbf{u})_{i+1/2}\Big) + \\ + \frac{b_2}{\Delta s}\Big(\mathbf{F}(\mathbf{u})_{i-3/2} - \mathbf{F}(\mathbf{u})_{i+3/2}\Big) + \frac{c_2}{\Delta s}\Big(\mathbf{F}(\mathbf{u})_{i+5/2} - \mathbf{F}(\mathbf{u})_{i+5/2}\Big)\,, \quad (2.118)$$

were the coefficients are equal to

$$c_1 = \frac{3}{256};\ \ b_1 = -\frac{1}{16} - 3c_1;\ \ a_1 = \frac{1}{2} - b_1 - c_1\,, \quad (2.119)$$

$$c_2 = -\frac{3}{640};\ \ b_2 = \frac{1}{24} - 5c_2;\ \ a_2 = -1 - 3b_2 - 5c_2\,. \quad (2.120)$$

2.3.2 Artificial diffusivity

In order to avoid the exponential growth of the perturbations on the unresolved scales, the MANCHA3D code uses artificial diffusivities. As mentioned before, the diffusivity terms in the equation of motion, induction equation, and energy equation are equivalent to the physical terms of viscosity, magnetic diffusivity, and thermal conduction, respectively. In the continuity equation, the diffusivity term is entirely artificial. This philosophy resembles the one described in Caunt & Korpi (2001) and Vögler et al. (2005). In the code, each of the artificial diffusivity coefficients consist of three terms: time-constant diffusivity ($\nu^{\rm cte}$), variable (hyper) diffusivity ($\nu^{\rm hyp}$) and shock diffusivity ($\nu^{\rm shk}$).

Considering index i corresponds to any spatial dimension, the time-constant diffusivity is defined as follows

$$\nu_i^{\rm cte}(\mathbf{u}) = c^{\rm cte}(\mathbf{u})\,(c_{\rm S0} + v_{\rm A0})\Delta x_i F^{\rm cte}(x,y,z)\,, \quad (2.121)$$

where $c^{\rm cte}$ is coefficient that is defined in the control file for each of the variables, Δx_i is the spatial step in the i-direction, $F^{\rm cte}(x,y,z)$ is a function that defines the spatial profile for the constant diffusion. If no such function is defined by the user, the code assumes $F^{\rm cte}(x,y,z) = 1$ in the whole numerical domain. The definition of the constant diffusivities also includes the sum of the sound and Alfvén speeds of the background (initial) atmosphere.

The hyper diffusivity coefficient is defined as

$$\nu_i^{\rm hyp}(\mathbf{u}) = c^{\rm hyp}(\mathbf{u})\,(v + c_{\rm S} + v_{\rm A})\Delta x_i\,\frac{\max_3 \Delta_i^3 \mathbf{u}}{\max_3 \Delta_i^1 \mathbf{u}}\,, \quad (2.122)$$

where, the third and the first derivatives, Δ_i^3 and Δ_i^1 at the grid point h in the direction i are defined as:

$$\Delta_i^3 \mathbf{u} = |3(\mathbf{u}_{h+1} - \mathbf{u}_h) - (\mathbf{u}_{h+2} - \mathbf{u}_{h-1})|\,, \quad (2.123)$$

and

$$\Delta_i^1 \mathbf{u} = |\mathbf{u}_{h+1} - \mathbf{u}_h| \tag{2.124}$$

The $\max_3$ denotes the maximum value of the corresponding differences over three nearby points. The ratio $\frac{\max_3 \Delta_i^3 \mathbf{u}}{\max_3 \Delta_i^1 \mathbf{u}}$ is limited in the code to vary from zero to unity. The hyper diffusion coefficient is therefore defined to have the largest values at locations where large amplitude variations of a given parameter develop at small scales. The amplitude parameter $c^{\rm hyp}(\mathbf{u})$ is provided by the user through the control file separately for each of the variables. The hyper diffusion coefficient scales with the sum of the flow velocity, the sound, and Alfvén speeds and is proportional to the spatial resolution of the corresponding dimension.

Finally, the shock diffusion is written as

$$\begin{aligned} \nu_i^{\rm shk}(\mathbf{u}) &= c^{\rm shk}(\mathbf{u})(\Delta x_i)^2 |\nabla \cdot \mathbf{v_1}| \qquad \nabla \cdot \mathbf{v_1} < 0\,, \\ \nu_i^{\rm shk}(\mathbf{u}) &= 0 \qquad\qquad\qquad\qquad\quad \nabla \cdot \mathbf{v_1} \geq 0\,. \end{aligned} \tag{2.125}$$

The parameter $c^{\rm shk}(\mathbf{u})$ is the amplitude coefficient set through the control file, and it has the same value for each of the variables $\mathbf{u}$. The shock diffusion acts only where the velocity divergence is negative. This allows the smoothing of strong converging flows in the domain.

After the numerical diffusivity coefficients are defined, it is necessary to introduce the complete diffusivity terms in the set of the equations. As mentioned before, these terms mimic the physical terms of viscosity, magnetic diffusivity, and thermal conduction. According to this philosophy, the diffusivity term in the equation of motion is defined as follows

$$\left(\frac{\partial(\rho_1+\rho_0)\mathbf{v_1}}{\partial t}\right)_{\rm diff} = \nabla \cdot \bar{\tau}\,, \tag{2.126}$$

where $\bar{\tau}$ is viscous stress tensor with the components:

$$\tau_{ij} = \frac{1}{2}(\rho_1+\rho_0)\left(\nu_j(v_{1i})\frac{\partial v_{1i}}{\partial x_j} + \nu_i(v_{1j})\frac{\partial v_{1j}}{\partial x_i}\right). \tag{2.127}$$

For the direction i, the diffusivity term in the equation of motion is written as

$$\left(\frac{\partial(\rho_1+\rho_0)v_{1i}}{\partial t}\right)_{\rm diff} = \frac{\partial \tau_{ix}}{\partial x} + \frac{\partial \tau_{iy}}{\partial y} + \frac{\partial \tau_{iz}}{\partial z}\,. \tag{2.128}$$

Similarly, the diffusivity term in the induction equation is introduced:

$$\left(\frac{\partial \mathbf{B_1}}{\partial t}\right)_{\rm diff} = -\nabla \times \vec{\varepsilon} \tag{2.129}$$

where $\vec{\varepsilon}$ is a vector which components are defined as

$$\begin{aligned} \varepsilon_x &= \left(\nu_y(B_{1z})\frac{\partial B_{1z}}{\partial y} - \nu_z(B_{1y})\frac{\partial B_{1y}}{\partial z}\right), \\ \varepsilon_y &= \left(\nu_z(B_{1x})\frac{\partial B_{1x}}{\partial z} - \nu_x(B_{1z})\frac{\partial B_{1z}}{\partial x}\right), \\ \varepsilon_z &= \left(\nu_x(B_{1y})\frac{\partial B_{1y}}{\partial x} - \nu_y(B_{1x})\frac{\partial B_{1x}}{\partial y}\right). \end{aligned} \tag{2.130}$$

As mentioned before, the diffusivity term in the continuity equation does not correspond to a physical term. Nevertheless, it is defined following the same strategy as in the equations above:

$$\left(\frac{\partial \rho_1}{\partial t}\right)_{\rm diff} = \sum_i \frac{\partial}{\partial x_i}\left[\nu_i(\rho_1)\frac{\partial \rho_1}{\partial x_i}\right]. \tag{2.131}$$

The diffusivity term in the total energy equation consists of the terms analogous to thermal conduction, Ohmic, and viscous heating. The thermal conduction term is introduced as

$$\left(\frac{\partial e_1}{\partial t}\right)_{\text{cond}} = \sum_i \frac{\partial}{\partial x_i}\left((\rho_1+\rho_0)\nu_i(T_1)\frac{\partial c_P T_1}{\partial x_i}\right). \tag{2.132}$$

The term of the Ohmic heating is defined as

$$\left(\frac{\partial e_1}{\partial t}\right)_{\text{Ohm}} = \nabla\cdot((\mathbf{B_1}+\mathbf{B_0})\times\vec{\varepsilon}). \tag{2.133}$$

that can be expanded as

$$\begin{aligned}\left(\frac{\partial e_1}{\partial t}\right)_{\text{Ohm}} &= \frac{\partial}{\partial x}\left((B_{y1}+B_{y0})\varepsilon_z-(B_{z1}+B_{z0})\varepsilon_y\right)+\\ &+\frac{\partial}{\partial y}\left((B_{z1}+B_{z0})\varepsilon_x-(B_{x1}+B_{x0})\varepsilon_z\right)+\frac{\partial}{\partial z}\left((B_{x1}+B_{x0})\varepsilon_y-(B_{y1}+B_{y0})\varepsilon_x\right)\end{aligned} \tag{2.134}$$

Finally, the viscous heating is represented as follows

$$\left(\frac{\partial e_1}{\partial t}\right)_{\text{visc}} = \nabla\cdot(\mathbf{v_1}\cdot\bar{\tau}). \tag{2.135}$$

Regarding the internal energy equation, the artificial diffusivity is composed of heat conduction, Ohmic, and viscous terms,

$$\left(\frac{\partial e_{\text{int}}}{\partial t}\right)_{\text{cond}} = \sum_i \frac{\partial}{\partial x_i}\left((\rho_1+\rho_0)\nu_i(T_1)\frac{\partial c_P T_1}{\partial x_i}\right), \tag{2.136}$$

$$\left(\frac{\partial e_{\text{int}}}{\partial t}\right)_{\text{Ohm}} = \sum_i \varepsilon_i J_i. \tag{2.137}$$

$$\left(\frac{\partial e_{\text{int}}}{\partial t}\right)_{\text{visc}} = \sum_i\sum_j \bar{\tau}_{ij}\frac{\partial v_i}{\partial x_j}. \tag{2.138}$$

The first term is the same as for the total energy equation. The second term contains the electric current components, computed as

$$\mathbf{J} = \frac{1}{\mu_0}\nabla\times\mathbf{B_1}. \tag{2.139}$$

The diffusivity terms include the second derivatives that are computed from the first derivatives following Equations (2.117) and (2.118).

2.3.3 Time step

The CFL (Courant–Friedrichs–Lewy) condition limits the integration time step, which ensures that the physical dependence domain is inside the numerical dependence domain. In practice, this means that the mesh width must be larger than the distance traveled by the information in a single time step due to mass flow, wave propagation, or diffusion transport. According to this, the time step has to be smaller than the characteristic times imposed by the advection and diffusion:

$$\Delta t \leq \min(\Delta t_{\text{v}}, \Delta t_{\text{diff}}). \tag{2.140}$$

In this expression, $\Delta t_{\rm v}$ is the time step imposed by a modified CFL condition, approximately valid for the MHD equations,

$$\Delta t_{\rm v} = c_{\rm v}\left[\frac{1}{1/\Delta x^2 + 1/\Delta y^2 + 1/\Delta z^2}\right]^{1/2}\frac{1}{v_{\rm max}}\,, \tag{2.141}$$

where $v_{\rm max}$ is the maximum value of the sound and Alfvén speeds. The time step imposed by diffusion, $\Delta t_{\rm diff}$, corresponds to the minimum of the diffusion time across the three dimensions,

$$\Delta t_{\rm diff} = c_{\rm diff}\,\min\left(\frac{\Delta x^2}{\nu_x}, \frac{\Delta y^2}{\nu_y}, \frac{\Delta z^2}{\nu_z}\right). \tag{2.142}$$

The constant coefficients $c_{\rm v}$ and $c_{\rm diff}$ are set to 0.5 by default to ensure the stability of the solution. The diffusion coefficients $\nu_{x,y,z}$ are those defined in Section 2.3.2.

2.3.4 Filtering

IIn the numerical simulations of solar prominences, the high diffusivity is not desirable since it can potentially reduce a prominence density contrast, damp prominence oscillations, or decelerate eruptive events. Therefore, in most of the experiments, we aim to minimize the numerical diffusivities. At the same time, low diffusion cannot always prevent the development of high-frequency noise. In such cases, we perform additional filtering of small wavelengths. Following Parchevsky & Kosovichev (2007), MANCHA3D uses a sixth-order digital filter to eliminate unresolved short-wavelength components:

$$u_{\rm filt} = u(x) - \sum_{m=-3}^{3} d_{\rm m} u(x + m\Delta x)\,, \tag{2.143}$$

where u is a variable before the filtering, and $u_{\rm filt}$ is the variable after the filtering. The filter is applied in the three spatial coordinates independently. The coefficients $d_{\rm m}$ have been chosen to construct the filtering function:

$$G(k\Delta x) = 1 - \sum_{m=-3}^{3} d_m e^{imk\Delta x} = 1 - \sin^6\left(\frac{k\Delta x}{2}\right). \tag{2.144}$$

The frequency of application of the filter depends on the simulation, but it is usually applied every 10 seconds. Due to the relatively small time step in our experiments, we use the filtering more frequently, every 1.5 seconds.

2.3.5 Boundary conditions

The code allows using different boundary conditions such as periodic, closed, gradient-free. In our numerical simulations, we use different types of boundary conditions at the different sides of the numerical domain. As we choose the magnetic configurations to be periodic at the side boundaries in each experiment, we are allowed to use the periodic boundary conditions.

At the top boundary, it is convenient to use the symmetric and antisymmetric conditions for the different variables. We assume v_{1x}, v_{1y}, and B_{1z} to be symmetric. MANCHA3D has a peculiarity that the guard cells in the vertical direction are located inside the domain. Therefore

the symmetric BCs are defined as,

$$\begin{aligned} u_{n_z} &= u_{n_z-9}, \\ u_{n_z-1} &= u_{n_z-8}, \\ u_{n_z-2} &= u_{n_z-7}, \\ u_{n_z-3} &= u_{n_z-6}, \\ u_{n_z-4} &= u_{n_z-5}. \end{aligned} \tag{2.145}$$

For the thermodynamic variables as density, gas pressure, temperature, we also apply symmetric conditions.

v_{1z}, B_{1x}, and B_{1y} are assumed to be antisymmetric:

$$\begin{aligned} u_{n_z} &= -u_{n_z-9}, \\ u_{n_z-1} &= -u_{n_z-8}, \\ u_{n_z-2} &= -u_{n_z-7}, \\ u_{n_z-3} &= -u_{n_z-6}, \\ u_{n_z-4} &= -u_{n_z-5}, \end{aligned} \tag{2.146}$$

where u is a corresponding variable and n_z is the number of points in the vertical direction.

At the bottom boundary, the magnetic field components are calculated from the induction equation following the velocity settings. In some cases, we use the line-tying condition imposing zero-velocity at the bottom. In the other cases, we apply the shearing or converging motions at the foot points. For the rest of the variables at the bottom boundary, we assume the symmetric conditions defined as

$$\begin{aligned} u_1 &= u_{10}, \\ u_2 &= u_9, \\ u_3 &= u_8, \\ u_4 &= u_7, \\ u_5 &= u_6. \end{aligned} \tag{2.147}$$

2.3.6 Parallelization

The code has been parallelized using MPI (Message Passing Interface) following distributed memory concept. This means that all the data used by a processor belong to its memory partition and only this processor has access to it. All the data are divided among a certain number of processors using a domain decomposition scheme. The communication between the processors is provided by exchanging the information between the five layers of the "ghost" cells located at each subdomain boundary. If the subdomain is located next to the boundary, the values in the "ghost" cells are imposed by the boundary condition.

2.4 Analysis of the numerical data

In this section, we describe the methods used for the analysis of the prominence motions. We aim to study the plasma motions in the different prominence regions and to study different polarizations of plasma oscillations. To this end, we used two approaches. The first one is to trace the field lines and compute the rest of the magnitudes along these field lines. The second approach is to advect the velocity field following the fluid elements. As the frozen-in condition is fulfilled, both approaches are similar, but the convenience of each one depends on the problem considered. The first approach is more convenient when studying the plasma motions in a quasi-static magnetic field, which implies the slow temporal evolution of the magnetic field. In this case, choosing the initial coordinates for the integration of the field lines, we can advect the motions in the same field lines at every time iteration. However, this approach cannot be used when the prominence moves in a strongly evolving magnetic field. We then use the analysis of the trajectories of the fluid elements by computing the magnitudes along the traces of the particles.

2.4.1 Motions in the different prominence regions

The first approach implies the computation of the magnitudes along the magnetic field lines. The first step of this approach is to integrate these lines and select good initial coordinates for the integration. It is important to choose the initial position where the magnetic field remains almost unperturbed. In Chapter 3 we use a flux rope magnetic configuration. The field lines of the flux rope are ellipses in the 2D projection. The upper parts of these ellipses remain mostly unperturbed, making this upper region the most convenient to start integrating the field lines. The initial positions are chosen in such a way that the field lines permeate the whole prominence body. In Chapter 4, we use a dipped arcade configuration with foot points anchored in the dense chromosphere. This implies that the magnetic field integration can be initiated from the bottom region, as we assume that the field lines are line-tied in the dense chromosphere.

After choosing the initial positions, we start the field lines integration. In order to have good accuracy when integrating the field lines, we use a fourth-order RK method. The integration of the field lines is done following the expression:

$$\mathbf{p_{i+1}} = \mathbf{p_i} + \frac{1}{6}\Delta s(\mathbf{k_1} + 2\mathbf{k_2} + 3\mathbf{k_3} + \mathbf{k_4}), \tag{2.148}$$

where $\mathbf{p_{i+1}}$ and $\mathbf{p_i}$ are the corresponding vectors at moment of time i and $i+1$, s is the coordinate along the field line and Δs is the corresponding integration step. A smaller Δs step produced smaller integration errors. The k-vectors are defined as follows

$$\begin{aligned} \mathbf{k_1} &= \mathbf{b_i}, \\ \mathbf{k_2} &= \mathbf{b^1_{i+1}}, \\ \mathbf{k_3} &= \mathbf{b^2_{i+1}}, \\ \mathbf{k_4} &= \mathbf{b^3_{i+1}}, \end{aligned} \tag{2.149}$$

where $\mathbf{b} = \mathbf{B}/B$, and vectors $\mathbf{b^1_{i+1}}$, $\mathbf{b^2_{i+1}}$, $\mathbf{b^3_{i+1}}$ corresponds to the points $\mathbf{p_i} + 1/2\mathbf{k_1}$, $\mathbf{p_i} + 1/2\mathbf{k_2}$, $\mathbf{p_i} + \mathbf{k_3}$, respectively. As a result, we obtain the integrated magnetic field lines to be used in our analysis. The vectors $\mathbf{p_0}$ contain the coordinates of the initial positions of the integration.

As mentioned before, we aim to study the different polarizations of oscillations, which are motions along the magnetic field and transverse to the magnetic field. First, we compute the

corresponding velocities in the grid-points of the domain as follows

$$\mathbf{v}_{\parallel} = \frac{(\mathbf{v}\cdot\mathbf{B})\mathbf{B}}{B^2}, \tag{2.150}$$

$$\mathbf{v}_{\perp} = \mathbf{v} - \frac{(\mathbf{v}\cdot\mathbf{B})\mathbf{B}}{B^2}. \tag{2.151}$$

Second, we express these projected velocities in the coordinates of the field lines obtained from the integration. Additionally, we interpolate the density along the same field lines. From the interpolation, we obtain the arrays for the velocities and density as functions of time and position along the field lines, $\mathbf{v}_{\parallel} = \mathbf{v}_{\parallel}(s,t)$, $\mathbf{v}_{\perp} = \mathbf{v}_{\perp}(s,t)$, $\rho = \rho(s,t)$. Finally, we compute the center-of-mass velocities using the integrals:

$$v_{i\parallel}(t) = \frac{\int v_{\parallel}(s_i,t)\rho(s_i,t)ds}{\int \rho(s_i,t)ds}, \tag{2.152}$$

$$v_{i\perp}(t) = \frac{\int v_{\perp}(s_i,t)\rho(s_i,t)ds}{\int \rho(s_i,t)ds}. \tag{2.153}$$

When it is hard to advect the same magnetic field lines at each moment, we use the other approach based on the analysis of the motions of the corks (i.e., fluid elements). Many authors used this method to investigate the prominence motions following the trajectories of several fluid elements (see, e.g., Schmieder et al. 2014). The collective behavior of the corks can help to explain some properties of prominence motions. We follow the individual fluid elements by integrating the velocity field at each time moment. The initial coordinates of the fluid elements are chosen in the correposndence with the prominence location. The trajectories of the fluid elements in the velocity field are computed similarly to the magnetic field lines. Thus, we again used the fourth-order RK method applying it to the velocity field. The k-vectors in Equation (2.148) are defined using the corresponding velocity vectors $\mathbf{v_i}$, $\mathbf{v^1_{i+1}}$, $\mathbf{v^2_{i+1}}$, $\mathbf{v^3_{i+1}}$. Having the trajectories of the fluid elements, we can compute the interpolated values of the different magnitudes along the trajectories.

We then study the periods of oscillatory signals in different velocity components, which are obtained either from field line or cork analysis. Having the signals, we then obtain periodograms following the modified Lomb-Scargle algorithm (Lomb 1976; Carbonell & Ballester 1991) that is based on the least-squares frequency analysis. We use this algorithm in order to estimate the power of the signal at the given frequency.

2.4.2 Curvature of the magnetic field lines and pendulum period

As mentioned in Section 1.6, the pendulum model is important for an understanding of the longitudinal prominence oscillations. It is necessary to compute the theoretical pendulum period and compare it with the periods obtained from the numerical experiments. In the pendulum model, it is assumed that the main restoring force for the longitudinal oscillations is the gravity projected along the magnetic field, and the period is defined by Equation (2.90). The only parameter that is needed is the radius of curvature of the magnetic field lines. For that, we first compute the curvature value at the grid-points as follows:

$$\boldsymbol{\kappa} = (\mathbf{b}\cdot\nabla)\mathbf{b}, \tag{2.154}$$

where $\mathbf{b} = \mathbf{B}/B$. Then, the absolute value of the curvature is interpolated along the magnetic field lines, similar to what is explained in Section 2.4.1. After that, the curvature is averaged around the current position of the magnetic dips. As the curvature of the magnetic field lines slightly evolves due to the plasma motions, we additionally average the curvature in time. The radius of curvature can be computed as $R_c = 1/\kappa$.

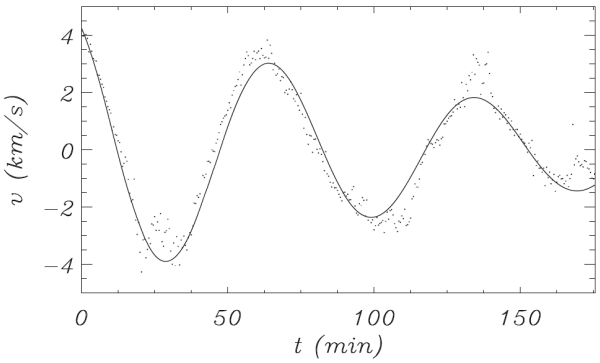

Figure 2.3: Observed Doppler velocity (dots) of the prominence oscillation and fitted function (continuous line) versus time. The fitting is done with a damped sinusoidal function (Equation (2.155)). The period obtained from the fit is of 70 minutes; the damping time is of 140 minutes. Adapted from Molowny-Horas et al. (1999).

2.4.3 Study of damping times

Most of the LAO and SAO observations reveal that the amplitude of the prominence motions tends to decrease with time and the periodic signal disappears after several oscillatory periods. This means that the oscillations are damped and, apart from the oscillation period, one can define another quantity that characterizes the oscillations, i.e., the attenuation time τ. For the analysis of LAOs obtained from simulations, we fitted the signal to a damped sinusoidal function.

In the past, the fitting with the damped harmonic function was widely used for SAOs by many authors. An example of such a fitting is shown in (Figure 2.3). In this example, the fit was used for the Doppler velocity time series taken from certain prominence regions. This fitting function is defined as follows

$$v = v_0 e^{-t/\tau} \sin(2\pi t/P + \phi), \tag{2.155}$$

where v_0 and P are the amplitude and the period of the signal, ϕ is the phase shift. Later this approach was widely also used to determine the characteristics of the observed LAOs (see, e.g., Jing et al. 2003, 2006; Vršnak et al. 2007; Hershaw et al. 2011; Shen et al. 2014a). The characteristic time τ can be positive or negative depending on whether the signal shows attenuating or amplifying behavior. By analogy it has been also used to define the damping times of LAOs in numerical experiments (see, e.g., Zhou et al. 2018; Zhang et al. 2019; Adrover-González & Terradas 2020; Fan 2020).

3

Numerical simulations of large-amplitude oscillations in flux rope solar prominences

Large-amplitude oscillations (LAOs) of solar prominences are a very spectacular, but poorly understood, phenomena. These motions have amplitudes larger than $10\,\mathrm{km\,s^{-1}}$ and can be triggered by the external perturbations such as Moreton or EIT waves. In this work, we aim to understand LAOs in a realistic prominence structure and how the properties of these LAOs depend on different parameters of the structure (i.e., density contrast and shear angle). Additionally, we study how an external disturbance excites different modes of oscillation of the structure. We performed time-dependent numerical simulations of LAOs using a magnetic flux rope model with the two values of shear angle and density contrast. We studied the oscillatory modes of the prominence using horizontal and vertical triggering. In addition, we used a perturbation that arrives from outside to understand how such external disturbance can produce LAOs. This Chapter is organized as follows: in Section 3.1, an initial numerical configuration is described. In Section 3.2, we explain how the prominence was perturbed and how the plasma and magnetic field respond to the internal (horizontal and vertical) and external perturbations. In Section 3.4, the main results are summarized. This chapter corresponds to the already published paper *"Numerical simulations of large-amplitude oscillations in flux rope solar prominences"* (Liakh et al. 2020, A&A, 637, A75).

3.1 Numerical model

Our objective is to study the oscillatory properties of the prominence models triggered by internal and external perturbations. We numerically solve the equations of ideal MHD described in Section 2.3 using the MANCHA3D code (Khomenko et al. 2008, 2014; Felipe et al. 2010; Khomenko & Collados 2012). We used the 2.5D approximation in which all the vectors have three spatial components, but the perturbation is only allowed to propagate in two dimensions. The governing equations and the corresponding source terms are described by Felipe et al. (2010). In this section, the numerical setup is outlined. We form the prominence structure from a force-free arcade using the cancelation process. Once the flux rope is formed, we load the cool prominence mass. The initial configuration and the processes of the flux rope formation, mass loading, and relaxation are explained below in Sections 3.1.1, 3.1.2, and 3.1.3, respectively. The numerical domain consists of 800×600 grid points, which corresponds to the physical size of $192\,\mathrm{Mm} \times 144\,\mathrm{Mm}$ (a spatial resolution of $0.24\,\mathrm{Mm}$), except for one case in which we use a resolution that is four times higher. The Cartesian coordinate system is used with z- and x-axes

defining the vertical and horizontal directions, respectively.

3.1.1 Initial equilibrium

The initial configuration consists of an isothermal atmosphere with a temperature of $T = 2$ MK gravitationally stratified along the vertical direction with a density at the bottom of the numerical domain of $\rho = 1.31 \times 10^{-12}$ kg m^{-3}. We used an initial temperature larger than the typical value of the low corona of 1 MK. The reason for this selection is to have a large pressure scale height. This allowed us to have smoother stratification, avoiding huge Alfvén speeds at the top of the domain. The thermal conduction is not taken into account, but we included the radiative losses during the stage of the flux rope formation later on. We considered a monoatomic gas with an adiabatic constant, $\gamma = 5/3$.

The initial force-free magnetic field is a periodic sheared arcade (see Section 2.1.3) defined as

$$B_x = -\frac{2LB_0}{\pi H_b}\cos(k(x-x_0))\exp\left(-\frac{z-z_0}{H_b}\right), \tag{3.1}$$

$$B_y = -\sqrt{1-\left(\frac{2L}{\pi H_b}\right)^2}\,B_0\cos(k(x-x_0))\exp\left(-\frac{z-z_0}{H_b}\right), \tag{3.2}$$

$$B_z = B_0\sin(k(x-x_0))\exp\left(-\frac{z-z_0}{H_b}\right), \tag{3.3}$$

where $(x_0, z_0) = (0, 1)$ Mm are the coordinates of the center of the magnetic structure. The polarity inversion line (PIL), in this case, coincides with the line $x = 0$. The parameter L is related to the lateral extension $k = \pi/2L$, and the constant H_b determines the magnetic scale height. In our experiments, we considered $L = 48$ Mm and $B_0 = 20$ G.

It is useful to define an initial shear angle, θ, as

$$\tan\theta = \frac{B_y}{B_x} = \sqrt{\left(\frac{\pi H_b}{2L}\right)^2 - 1}\,, \tag{3.4}$$

that is, the angle between the arcade field and the line perpendicular to the PIL. A large angle θ involves large magnetic shear. From Equation (3.4), we see that there is a relation between the shear, θ, and the magnetic stratification, H_b. We considered the models with two initial shear angles, $\theta = 60°,\ 45°$. The corresponding parameters of the structure have values of $H_b = 61,\ 43$ Mm, respectively. The initial magnetic field in the 2D projection is shown in Figure 3.1(a). In all the initial configurations considered the maximum Alfvén speed is $v_A = B/\sqrt{\mu_0\rho_0} = 1594$ km s^{-1} and the plasma-β less than one everywhere in the domain.

3.1.2 Flux rope formation

Observations show that cool and dense prominence plasma is usually located in the dipped part of the curved magnetic field (see, e.g., reviews by Mackay et al. 2010 and Vial & Engvold 2015). The dense prominence plasma is supported against gravity by the Lorentz magnetic force (Kippenhahn & Schlüter 1957; Kuperus & Raadu 1974). Several models have been proposed for the magnetic structure of prominences, but the flux rope structure is the most plausible. In this work, we consider the formation of the flux rope from the initial sheared arcade using the van Ballegooijen & Martens (1989) mechanism. This approach is similar to Kaneko & Yokoyama (2015). We only applied the converging motions at the bottom boundary in the direction toward

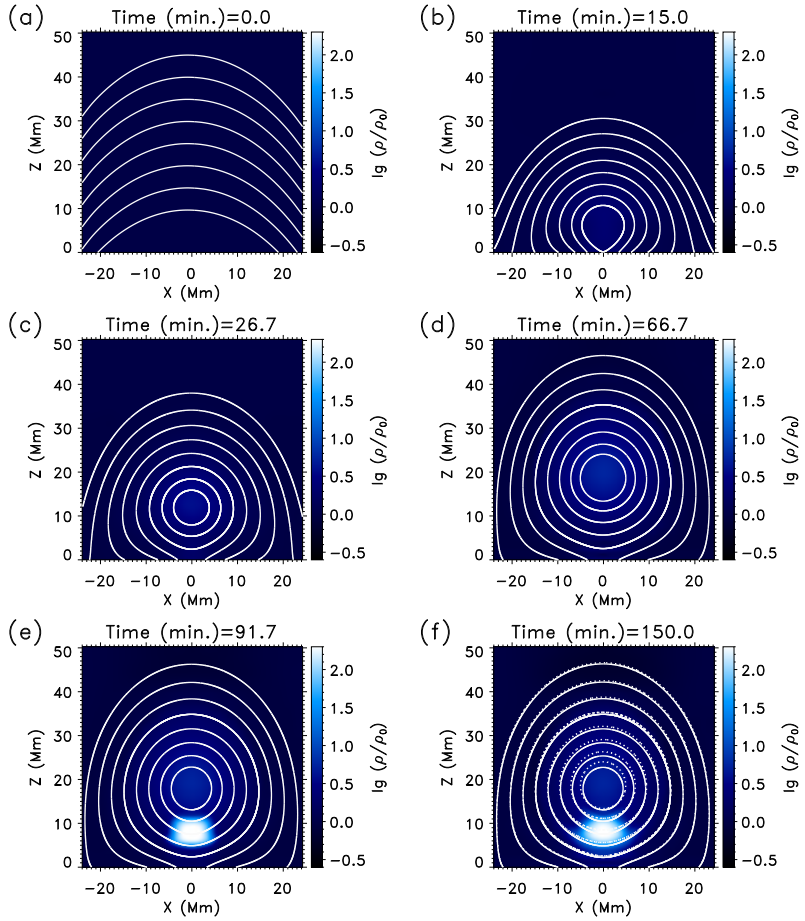

Figure 3.1: Magnetic field lines and density distribution in the central part of the computational domain during the prominence formation. Panel (a): The initial atmosphere and the magnetic field. Panels (b)-(d): The processes of the convergence and the reconnection. Panel (e) and (f): The initial and final stages of the mass loading. In panel (f), the dashed line indicates the magnetic field lines just before the mass loading process. The color bar scale indicates the logarithm of the density contrast.

the PIL. The horizontal velocity imposed at the base is written as

$$V_x(x,t) = -V_0(t)\sin\left[\frac{2\pi(x-x_0)}{L}\right]\exp\left[-\frac{(x-x_0)^2}{2\sigma^2}\right], \tag{3.5}$$

where parameter $L = 189.6\,\mathrm{Mm}$ is the double width of the arcade, $x_0 = 0\,\mathrm{Mm}$ is the position of PIL, and $\sigma = 13.6\,\mathrm{Mm}$ is related to the half-size of the converging region. We additionally set the V_y and V_z velocity components to zero at the bottom of the domain. We activated and

disactivated the cancelation process smoothly with a function $V_0(t)$ defined as

$$V_0(t) = V_{00}\left\{0.5\left[\mathrm{erf}\left(\frac{t-2\lambda-t_1}{\lambda}\right)+1\right] -0.5\left[\mathrm{erf}\left(\frac{t-2\lambda-t_2}{\lambda}\right)+1\right]\right\}, \tag{3.6}$$

where $V_{00} = 3V_{max}$. The parameter $V_{max} = 38\,\mathrm{km\,s^{-1}}$ is the maximum converging velocity. Since we are interested in the final result of the flux rope formation, and not in the process, we used this high-velocity value to achieve the final stage quickly. The parameters $t_1 = 100$ seconds and $t_2 = 3100$ seconds determine the initiation and termination of the formation process. The parameter $\lambda = 150$ seconds determines the duration of the transition, and consequently, it is responsible for the smoothness of the cancelation process. The cancelation process produces a heating of the plasma of the flux rope. Consequently, the gas pressure inside of the rope and plasma-β also increase to values higher than desirable in a prominence (see, e.g., Hillier et al. 2012). This effect was already described by Kaneko & Yokoyama (2015). Following these authors, we include a radiative loss term in our energy equation (Equation (2.110)). We use the Newton's radiation law (Equation (2.112))

$$Q_{\mathrm{R}} = -c_v \rho_0 \frac{T_1}{\tau_{\mathrm{R}}}, \tag{3.7}$$

where T_1 is the perturbation of the temperature with respect to the initial 2 MK, ρ_0 is the background density, τ_{R} is the radiative relaxation time, and c_v is the specific heat at constant volume. This Q_{R} is only used during the flux rope formation process. We used a spatially constant and very small $\tau_{\mathrm{R}} = 3$ seconds to keep the temperature near 2 MK. At the end of the cancelation, the temperature is 2 MK, and then we deactivated the Q_{R} term. In Figures 3.1(a)-3.1(d) different stages of the formation are shown. Figure 3.1(a) shows the initial field of the magnetic arcade, described by Equations (3.1)-(3.3). Figure 3.1(b) shows how the foot points of the field lines move toward the $x = 0$ axis following Equation (3.5). When the field lines approach each other, they reconnect near the origin of the coordinates, forming a twisted magnetic structure (Figure 3.1(c)). The flux rope slowly evolves through a series of stable equilibria and rises to the higher heights. The continuation of the converging process at the bottom could eventually lead the system to lose equilibrium and erupt. However, in the present work, we do not study the stability and eruption of the prominences. This problem can be addressed in future work. To avoid the eruption and to have a stable prominence, we stopped the convergence at $t = 55$ min. The resulting flux rope (see Figure 3.1(d)) has its center at the height of 18.24 Mm. The magnetic field strength in the dipped part is about of 14 G. The characteristics of the flux rope are comparable to those observed in the solar prominences.

We used symmetric (for V_x, V_y, B_z) or antisymmetric (for V_z, B_x, B_y) boundary conditions at the top boundary. The thermodynamic variables are fixed by assuming gradient-free condition. The periodic boundary conditions are assumed at the left and right boundaries. At the bottom, we let the magnetic field evolve according to the velocity field. During the flux rope formation process, the magnetic field is computed from the induction equation using the converging velocity. Later on, the line-tied conditions are applied using zero-velocities. For the rest of the variables, zero-derivative conditions are assumed.

3.1.3 Mass loading and relaxation

In this work we do not consider the mechanisms of the prominence mass formation (see, e.g., Xia et al. 2011, 2012a; Luna et al. 2012c; Xia & Keppens 2016). Instead of this, we placed the

prominence mass artificially in the dip of the flux rope, adding a source term in the continuity equation, as in Terradas et al. (2013). Thereby, in a defined region of the domain, the density increases in comparison to the surrounding corona while the temperature decreases, keeping the gas pressure constant. The continuity equation is written as

$$\frac{\partial \rho}{\partial t} + \nabla \cdot (\rho \mathbf{v}) = \left(\frac{\partial \rho}{\partial t}\right)_{\text{diff}} + S_\rho \,, \tag{3.8}$$

that is an equivalent expression to Equation (2.91) plus the source term S_ρ. The corresponding source for the continuity equation is determined as follows:

$$S_\rho = \frac{\chi \rho_0}{t_{\text{load}}} \exp\left(-\frac{(x-x_p)^4}{\sigma_x^4} - \frac{(z-z_p)^4}{\sigma_z^4}\right) , \tag{3.9}$$

where ρ_0 and χ are the background density and density contrast, respectively. The time parameter $t_{\text{load}} = t_4 - t_3 = 500\,$seconds is associated with the loading rate, where $t_3 = 5000\,$seconds and $t_4 = 5500\,$seconds determine the initial and final stages of the mass loading process. The spatial parameters $x_p = 0\,$Mm, $z_p = 8.4\,$Mm are coordinates of the prominence center and $\sigma_x = 3.6\,$Mm, $\sigma_z = 2.4\,$Mm are related to the half-size of the mass distribution region. In this study we considered light and heavy prominences with $\chi = 100$ and $\chi = 200$.

The cancelation and the mass loading produce non-negligible vertical oscillations of the prominence structure. These oscillations are not desirable for our study. We defined a relaxation process that removes these oscillations. During the relaxation process, the velocities in the domain are decreased owing to artificial damping. At each iteration, the equations are updated with the new values of the velocities and total energy. It is necessary to let this system evolve and relax for a long time (4000 seconds in our case).

Figure 3.1(e) shows the density distribution at the beginning of the mass loading process. The flux rope center drops down to find a new equilibrium position. The dense mass modifies the magnetic field lines making them more elongated downward (see Figure 3.1(e)). The magnetic forces increase as a result of lines stretching at the top and compression at the bottom. This way, magnetic forces compensate for the gravity increased due to the dense prominence mass. In the final stage of the relaxation, the prominence is close to equilibrium with velocities less than $2\,\text{km}\,\text{s}^{-1}$. In the investigation of the prominence equilibrium in the 2.5D models, Hillier & van Ballegooijen (2013) showed that in the case of the absence of X-point, in the situation similar to ours, the prominence mass is supported by a combination of the magnetic tension force, magnetic pressure gradient, and gas pressure gradient.

In the final stage of the relaxation process, the prominence is located at a height of 7.4 Mm. The mass loading process produces a reconfiguration of the magnetic field and the plasma that produces a slight increase of the plasma-β in the dipped part of the flux rope. However, this increase is small, and the low-β situation is maintained.

3.2 Oscillations from internal perturbations

After flux rope formation, mass loading, and relaxation process, we obtained a prominence close to a static equilibrium at $t = 150.0\,$minutes, as we described in Section 3.1. We first excited the system with internal perturbations to investigate the possible normal modes of different polarizations. This approach has already been used in several works (see, e.g., Terradas et al. 2013; Luna et al. 2016b; Zhou et al. 2018) but for different configurations. We considered four prominence configurations corresponding to a combination of the two shear angles, $\theta = 45°, 60°$, and the two maximum density contrasts, $\chi = 100, 200$. Each system is perturbed in both vertical and horizontal directions. The perturbations can be produced by introducing a

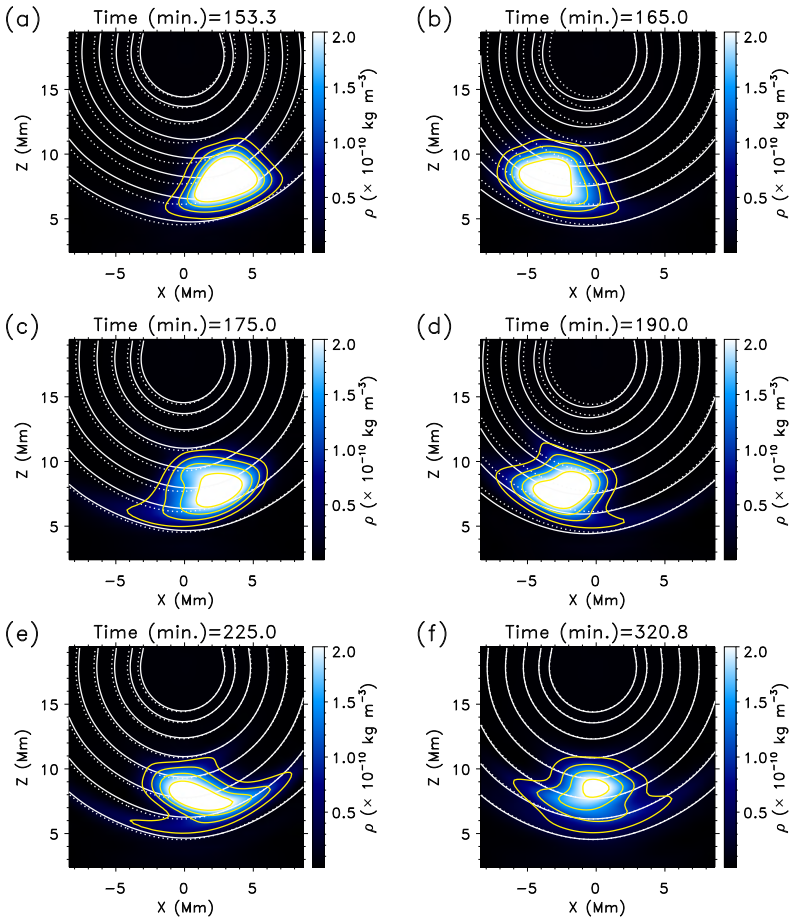

Figure 3.2: Evolution of the density and magnetic field after the horizontal perturbation. The figure shows the dipped part of the flux rope. Panel (a) demonstrates the motion of the prominence just after the perturbation; panels (b), (c) show the lagging of the bottom part from the rest of the prominence body, and panels (d), (e) demonstrate the zigzag shape of the motions. Panel (f) shows the state of the prominence in the final stage of simulation. The dashed lines indicate the magnetic field lines before the perturbation. The yellow lines represent the density isocontours.

pulse in some of the quantities. For example, Terradas et al. (2013), Luna et al. (2016b), and Zhou et al. (2018) imposed a perturbation exclusively in the velocity field and the rest of the magnitudes remain unchanged. These kinds of perturbations are unphysical because the rest of the magnitudes should also be modified to fulfill the governing equations. However, the system rapidly accommodates these perturbations in a few time steps. In some situations, if the initial perturbation is large, the numerical simulation crashes. We adopted an alternative approach

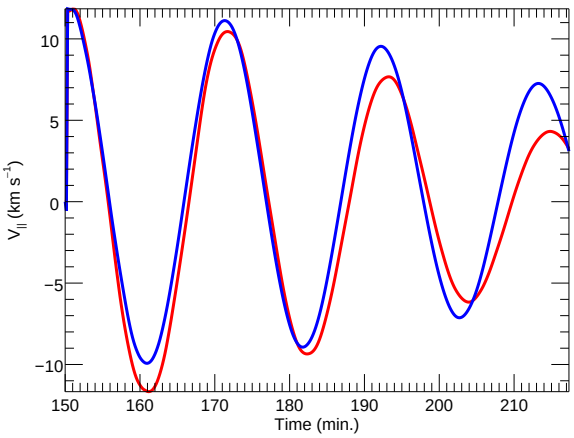

Figure 3.3: Longitudinal velocity variations at the position of the center of mass of the prominence for the simulations with different resolutions. The red and blue lines indicate the resolution of 240 km and 60 km, respectively.

to perturb the system. We incorporated a source term for each of the MHD equations in the MANCHA3D code (Equations (2.91)), similar to what we did for the mass loading (Section 3.1.3). The source term in the momentum equation represents an external force (see Equation (2.93)). This way, we produced self-consistent solutions. All the variables adjust to the source term following the MHD equations. The equation of motion is defined as

$$\frac{\partial \rho \mathbf{v}}{\partial t} + \nabla \cdot \left[\rho \mathbf{v}\mathbf{v} + \left(p + \frac{\mathbf{B}^2}{2\mu_0} \right) \mathbf{I} - \frac{\mathbf{B}\mathbf{B}}{\mu_0} \right] = \rho \mathbf{g} + \left(\frac{\partial \rho \mathbf{v}}{\partial t} \right)_{\text{diff}} + \mathbf{S_m} \,. \tag{3.10}$$

The system is perturbed in either vertical or horizontal directions by the source terms in the z- or x-projection of Equation (3.10), correspondingly. The source has the following form:

$$S_m = \frac{\rho v_{\text{pert}}}{t_{\text{pert}}} \exp\left(-\frac{(x - x_{\text{pert}})^4}{\sigma_x^4} - \frac{(z - z_{\text{pert}})^4}{\sigma_z^4} \right) , \tag{3.11}$$

where $t_{\text{pert}} = 10\,\text{seconds}$ is the duration of the initial perturbation, $\sigma_x = \sigma_z = 12\,\text{Mm}$, $x_{\text{pert}} = 0\,\text{Mm}$ and $z_{\text{pert}} = 7.4\,\text{Mm}$ set the half-size and the x- and z-coordinates of the center of the perturbation, respectively. The maximum velocity of the perturbation, $v_{\text{pert}} = 20\,\text{km}\,\text{s}^{-1}$, is in the range of the observed amplitudes.

3.2.1 Horizontal perturbation

Figure 3.2 shows the time sequence of the density and magnetic field evolution owing to the horizontal perturbation for the case $(\theta, \chi) = (45°, 200)$. The three remaining cases are not shown because the temporal evolution is qualitatively similar. The solid lines represent the magnetic field, while the dashed lines indicate the magnetic field lines just before the perturbation at $t = 150.0\,\text{minutes}$ (at the end of the relaxation). The figure shows that the field lines change

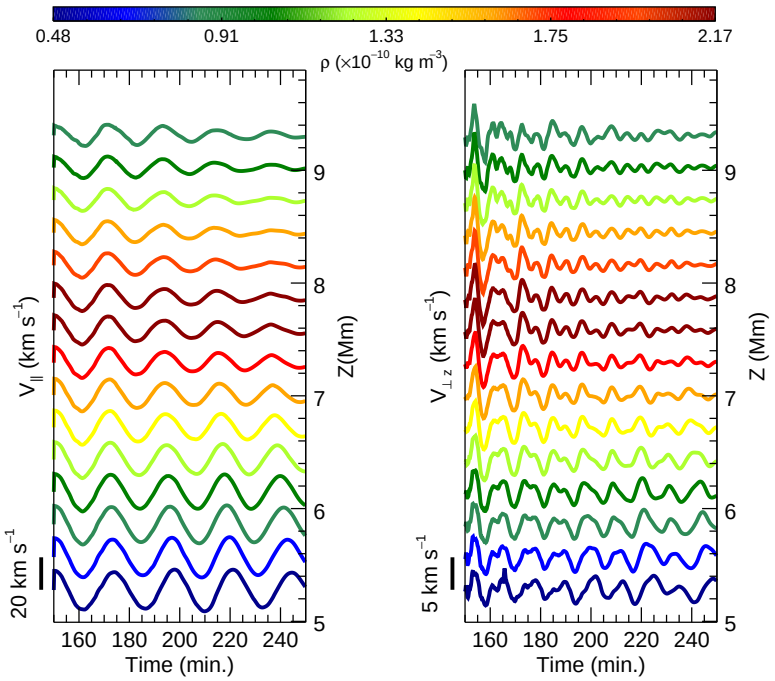

Figure 3.4: Temporal evolution of the longitudinal velocity (left panel) and vertical component of the transverse velocity (right panel) after the horizontal perturbation. The prominence model used has a shear angle of $\theta = 45°$ and a density contrast of $\chi = 200$. Colored lines indicate velocity variations at the center of mass of different field lines. The colors denote the maximum initial density at the field lines according to the color bar scale. The right vertical axis indicates the height of the magnetic dips; the left vertical axis represents the scale of the maximum initial amplitude.

following the motion of the mass. However, the time-dependent changes in the shape of the magnetic field seem small. At the beginning, the prominence moves to the right and reaches its maximum displacement 3 minutes after the perturbation (Figure 3.2(a)). In this initial stage, the prominence moves mainly as a whole (Figures 3.2(b) and 3.2(c)). However, the bottom part is slightly delayed from the rest of the prominence. Later, the oscillations become less synchronized, the phase difference increases, resulting in a zigzag shape of the prominence (Figures 3.2(d), 3.2(e)). In the recent work by Luna et al. (2016b), the zigzag appearance of LALOs is related to the differences in the period between the neighboring field lines. These phase shifts can make an impression of the vertical wave propagation. Such apparent wave motion has been called super-slow mode (Kaneko et al. 2015; Raes et al. 2017; Zapiór et al. 2019).

From Figure 3.2(f), we see that the longitudinal oscillations are damped. This damping could be associated with the numerical dissipation. To test the convergence of our simulations and verify to which extent the damping is caused by the numerical reasons, we performed the simulations with a higher resolution (60 km). Figure 3.3 shows the velocity of the center of

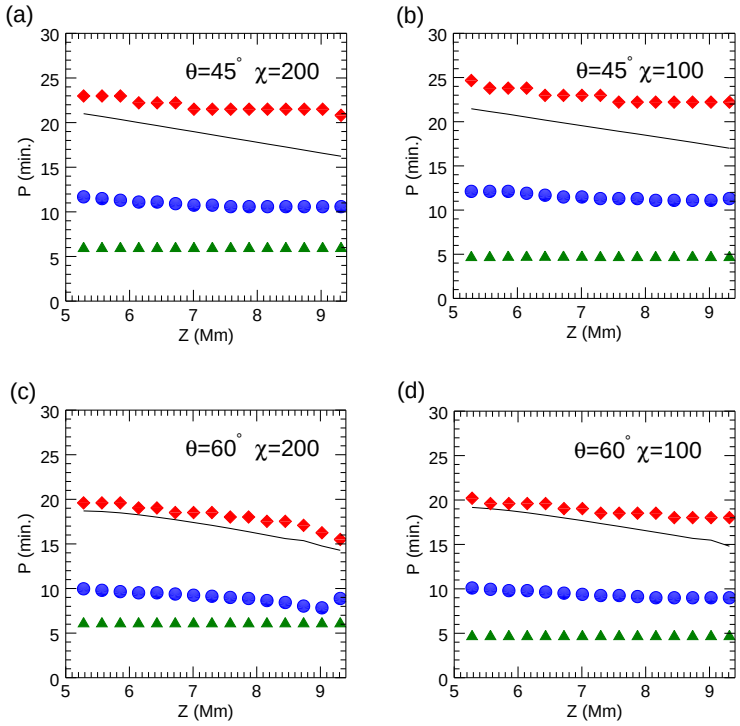

Figure 3.5: Oscillation periods as a function of height of the magnetic dips. The top panels correspond to the models with $\theta = 45°$ and the bottom panels correspond to the models with $\theta = 60°$. The left and right panels show the periods of the heavy and light prominence models, respectively. Red diamonds: longitudinal period; blue circles: vertical period due to the horizontal perturbation; green triangles: vertical period due to the vertical perturbation; and solid line: period from the theoretical pendulum model.

Table 3.1: Radii of curvature, the longitudinal and transverse vertical periods of the configurations with the different shear angle, θ, and the density contrast, χ.

	X-perturbation		Z-perturbation		External perturbation	
(θ,χ)	R_c (Mm)	$P_\parallel$ (min.)	$P_\parallel$ (min.)	P_v (min.)	$P_\parallel$ (min.)	P_v (min.)
$(45°, 200)$	$6.6 - 11.0$	$20.8 - 23.0$	$12.8 - 13.9$	5.9	$18.5 - 23.8$	5.9
$(45°, 100)$	$7.2 - 11.5$	$22.2 - 24.7$	$10.8 - 11.9$	4.7	-	-
$(60°, 200)$	$5.1 - 8.7$	$15.5 - 19.6$	$14.8 - 16.3$	6.1	-	-
$(60°, 100)$	$5.5 - 9.2$	$18.0 - 20.2$	$12.1 - 12.3$	4.7	-	-

mass of the prominence projected along the magnetic field for the simulations with 240 km and 60 km resolution. This test shows that the damping in higher resolution simulation is weaker, indicating that the damping has a numerical contribution. It would be necessary to perform a dedicated study to understand this damping further by considering consecutively higher spatial resolutions. This can be a subject of future work. For both resolutions considered in this work, the periodicity is similar. We then conclude that the system has converged. An additional effect of the numerical diffusivity is a slight reduction of the prominence density with time. The high-resolution simulation shows a smaller reduction of the density. However, this density reduction does not seem to affect the prominence dynamics. Taking these results into account, for our purposes it is enough to consider a spatial resolution of 240 km.

As we see in Figure 3.2, different parts of the structure oscillate differently, with different periods and phases. In addition, these motions are essentially nonlinear, and the plasma is a subject to important advection. The frozen-in condition applies in our fluid because we consider it to be perfectly conducting. Thus, it is necessary to advect every field line considered to catch the longitudinal and transverse motions of the plasma. We are interested in the cold plasma of the prominence, where the xz-projections of the field lines are more or less ellipses (Figure 3.1(f)). We realized that the top part of these ellipses is approximately unperturbed. Thus, any field line starting at the top of the flux rope follows the plasma motion, simplifying the study of the oscillations. Following Luna et al. (2016b), we calculated the longitudinal and transverse velocities at the positions of the center of mass of each field line. More detailed description of the analysis can be found in Section 2.4. We selected 15 field lines of the flux rope with dips located at heights between 5 Mm to 10 Mm.

The temporal evolution of the longitudinal velocity for each of the selected field lines is shown in the left panel of Figure 3.4. The velocity amplitude of these oscillations depends on the field line considered because of the shape of the triggering (Equation (3.11)). The initial velocity is around $20\,\mathrm{km\,s^{-1}}$ for the field lines centered at the cold plasma around $z = 7.5$ Mm and is lower for the rest. For the field lines with $z > 6$ Mm, the oscillations show damping that depends on the height. However, for the field lines with $z < 6$ Mm, the amplitude is constant, or it slightly amplifies at the half time shown in the figure. From the edge of the flux rope to its center, the magnetic field lines become more twisted. Thus, we conclude that oscillations are strongly damped at places in which the lines have large curvature. In contrast to Luna et al. (2016b), the phase differences between the lines are small. However, the combination of these small phase shifts and the different damping of the different layers produces the zigzag appearance.

The horizontal perturbation excites not only the longitudinal oscillations but also the transverse oscillations, as we see in the right panel of Figure 3.4. This figure shows that the initial vertical velocity is zero at all the height of the structure. However, immediately, the system starts to oscillate with the amplitudes of approximately $5\,\mathrm{km\,s^{-1}}$. Similarly to the longitudinal oscillations, for heights $z > 6$ Mm, the motions are clearly damped, whereas for $z < 6$ Mm, the plasma keeps oscillating.

We repeated the previous analysis for all four cases obtaining the temporal evolution at the different layers of the different prominence configurations. We analyzed the periods of oscillations at every field line considered as well as in the two polarization directions. The results for all four (θ, χ) configurations are plotted in Figure 3.5. The red diamond symbols show the period of the longitudinal oscillations as a function of the height of the dips. In all four cases, we can see that the period tends to decrease with height. The difference between the minimum and the maximum value is $2 - 3$ minutes (see Table 3.1). The longitudinal period slightly changes for different field lines. As a result, the prominence is shaped in the form of a zigzag after several cycles of oscillations (Figure 3.2(e)). The vertical period due to the horizontal perturbation is plotted with the blue circle symbols in Figure 3.5. The vertical oscillations have periods that are

half of the longitudinal periods. The behavior with height is identical to that of the longitudinal oscillation. This result indicates that the vertical motion is the back-reaction to the longitudinal oscillations, as shown in Figure 3.4. For example, when the prominence mass passes through the dip, it pushes the structure downward. This happens twice for each period explaining why the vertical oscillations have half of the period of the longitudinal oscillation.

We computed the radii of curvature averaged around the bottom of the dip to compare our results with the pendulum model. The magnetic field evolves as a consequence of the motion of the prominence plasma. Because of that, we used the time-averaged values of the radii of curvature, R_c. This allowed us to calculate the theoretical period of the longitudinal oscillations. We obtained the pendulum period shown as a solid line in Figure 3.5 by using equation, $P = 2\pi\sqrt{R_c/g}$, from Luna et al. (2012a), where $g = 273.94$ m s^{-2} is the solar gravitational acceleration. For $\theta = 45°$ the periods obtained in the numerical experiment show a good agreement with the theoretical period for $z < 7.5$ Mm and larger discrepancy for larger heights. In contrast, for $\theta = 60°$ the agreement is much better in all the spatial domain. We conclude that, for this type of oscillation, the restoring force is the projected solar gravity. The remaining difference between the numerical experiment and the theory of about $7\% - 15\%$ can be related to the local deformation of the magnetic field lines due to the motion of the heavy mass. Zhang et al. (2019) and Zhou et al. (2018) show using 2D and 3D simulations, respectively, that the pendulum model might lead to a large error in determining the radius of curvature using longitudinal periods when the gravity to Lorentz force ratio is close to unity. The authors define a dimensionless parameter to quantify this ratio as $\delta = 2gL_p/v_A^2$ being $L_p \cong 10$ Mm a typical dimension of the prominence and the local Alfvén speed, $v_A \cong 100\,\mathrm{km\,s^{-1}}$, in the case of $\chi = 200$. In our situation, this parameter is close to $\delta = 0.6$, indicating that the deformation of the field lines by the gravity could have some moderate effect on the longitudinal oscillations.

A comparison between the different simulations in Figure 3.5 shows that a change of the shear angle or the density contrast does not lead to a large difference in the longitudinal period. Comparing the heavy and light prominence models in Figure 3.5, we can see that the longitudinal period is only $1 - 2$ minutes longer in the case of the lower density contrast, $\chi = 100$. Since we concluded that the projected solar gravity is the main restoring force, the period should essentially depend only on the radius of curvature. This means that the radii of curvature are slightly larger, where prominence is less massive. As mentioned before, the loaded cold mass deforms the magnetic field lines decreasing the radius of curvature (Figure 3.1(f)). It is expected that heavier mass affects the shape of the field lines more, as a consequence, decreasing the longitudinal period.

The top and bottom panels of Figure 3.5 compare oscillations for the models with $\theta = 45°$ and $\theta = 60°$. The longitudinal period does not show a large difference in these two cases. The difference of $3 - 4$ minutes can be related to the projection effect. The more sheared structure has a smaller radius of curvature in the 2D projection (Table 3.1). As a result, the longitudinal period is also slightly shorter.

In order to estimate the damping time, the signal of the longitudinal velocity at the position of the center of mass of the prominence is fitted by the decayed sinusoidal function $v = v_0 e^{-t/\tau_D} \sin(2\pi t/P + \phi)$ as described in Section 2.4.3. We computed the damping time for the case shown in Figure 3.4. For the lines at the bottom of the prominence, the damping time $\tau_D = 100$ minutes, while at the top, the damping time is only 60 minutes. Thus, the damping time shows a decrease with height, in agreement with the visual impression from the left panel of Figure 3.4. We repeated the analysis for each of the models and obtained a similar behavior of damping with height.

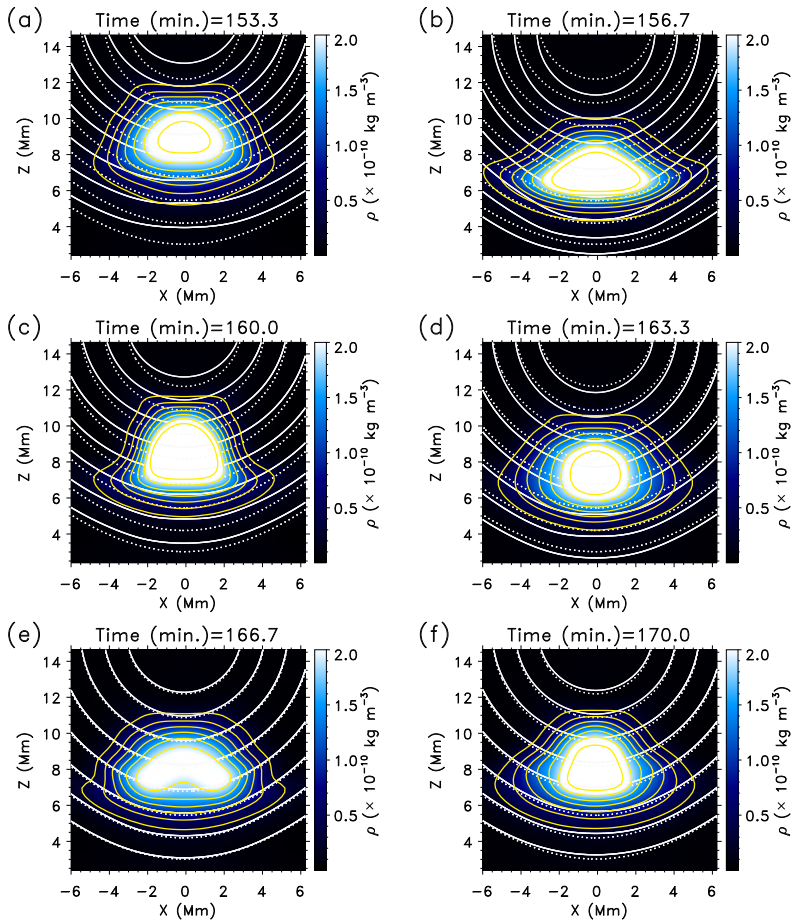

Figure 3.6: Evolution of the density and magnetic field after the vertical perturbation. The panels (b)-(f) demonstrate the longitudinal motions at the bottom of the prominence due to compression and rarefaction. The dashed lines denote the magnetic field lines before the perturbation. The yellow lines represent the density isocontours.

3.2.2 Vertical perturbation

We perturb the prominence along the vertical direction by applying the source term (Equation (3.11)) to the z-component of the equation of motion. The temporal evolution of the prominence mass just after the vertical perturbation is shown in Figure 3.6. Figure 3.6(a) shows the vertical upward motion of the prominence right after the perturbation. We see how the field follows the plasma motion due to the frozen-in condition and the dips flatten. In Figure 3.6(b), the direction of the motion has changed. The motion is downward and the magnetic field is bent in comparison to the initial configuration. In addition to the vertical motion, the prominence is a subject to the longitudinal motions. These longitudinal motions are due to the compression and rarefaction

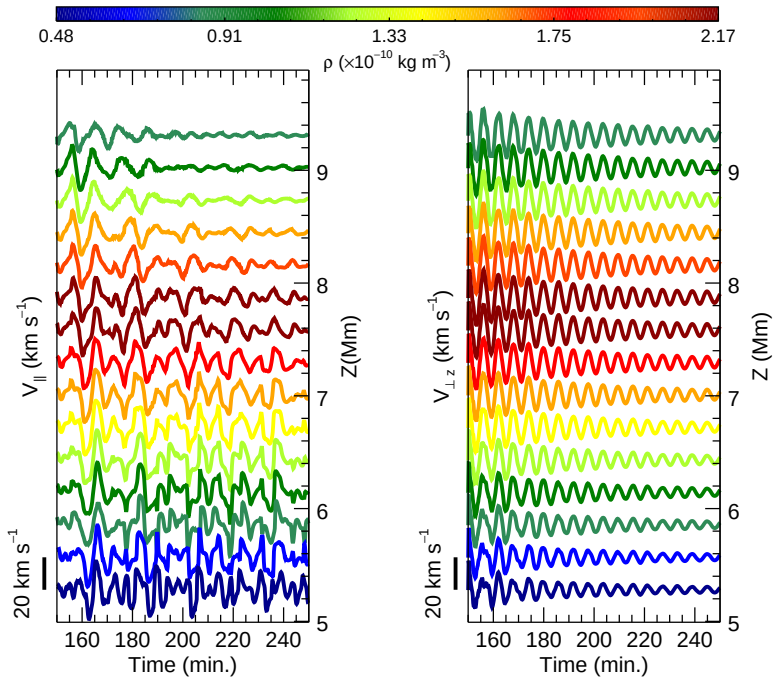

Figure 3.7: Temporal evolution of the longitudinal velocity (left panel) and vertical component of the transverse velocity (right panel) after the vertical perturbation. The prominence model used has a shear angle of $\theta = 45\,^{\circ}$ and a density contrast of $\chi = 200$. The colored lines indicate velocity variations at the center of mass (right) or the certain distance from the center of mass (left) at each field line. The colors indicate the maximum initial density at the field line according to the color bar scale. The right vertical axis indicates the height of the magnetic dips; the left vertical axis represents the scale of the maximum initial amplitude.

of the plasma. In Figure 3.6(b), we can see clearly how the prominence expands symmetrically with respect to the $x = 0$ axis along the field lines. In Figures 3.6(d) and 3.6(f), prominence shows symmetric longitudinal motions. This motion is more noticeable as the difference between the behavior at the bottom and at the upper prominence layer. In Figure 3.6(f), it is seen that the bottom part is more expanded than the upper part.

The behavior of the different components of the velocity at several prominence layers is shown in Figure 3.7. The right panel of Figure 3.7 shows the vertical oscillations at the center of mass of each field line, as in Section 3.2.1. However, owing to the symmetry of the vertical oscillations, the longitudinal velocity is zero at the center of mass of each line. For this reason, we measured the longitudinal velocity outside of the center close to the position of the maximum velocity. Figure 3.7(left) shows the temporal evolution of the longitudinal velocity at the selected field lines. We can see that the initial amplitude is zero, but the longitudinal oscillations start rapidly. Figure 3.6(b) shows the expansion of the prominence body when it moves downward. The amplitudes increase, reaching the value of $20\,\mathrm{km\,s^{-1}}$ at some lines. A very interesting feature

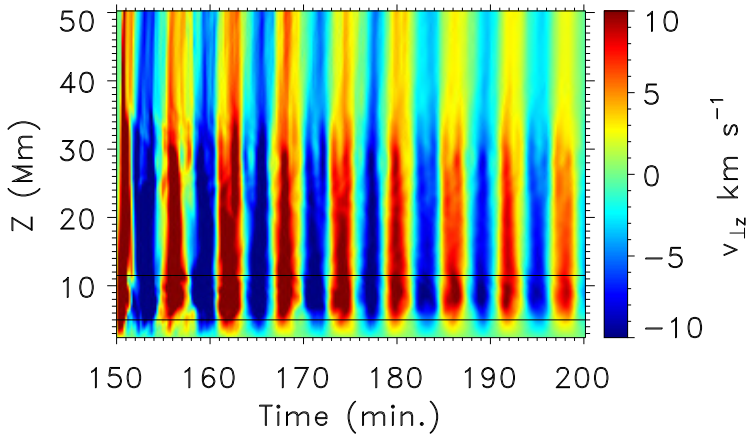

Figure 3.8: Time-distance diagram of the vertical component of the transverse velocity along z - axis at $x = 0$, in the model with the shear angle of $\theta = 45\,^{\circ}$ and the density contrast of $\chi = 200$. Black lines denote a region where the prominence mass is located.

of this numerical experiment that a vertical perturbation also produces an important horizontal oscillation of the cool plasma. It is unclear if, in the first stages of the oscillation, there is a mode coupling between vertical and horizontal polarization modes or, in contrast, it is just the transition phase of the establishment of modes, where the oscillation is composed of vertical and horizontal compression and rarefaction movements. Generally, the energy transfer could be related to the fast-to-slow mode conversion in the region where plasma-β is close to unity (Schunker & Cally 2006; Chen et al. 2016) or to the resonant absorption in the Alfvén continuum at the prominence-corona transition region (PCTR) (Goossens et al. 2014; Antolin et al. 2015). Since we have plasma-β lower than unity everywhere in the numerical domain, the mechanism of the fast-to-slow mode conversion is not taking place. The resonant absorption could still be responsible for the energy transfer and the damping of the global prominence modes. If this mechanism is in action, the global mode of the prominence is transferred to the local modes in the magnetic surfaces of the PCTR. We studied the distribution of the kinetic energy with time and we have not detected any transfer of energy to magnetic surfaces of the structure. Unlike our case, the energy of transverse oscillations was shown to be transferred to a thin region at the PCTR in 3D MHD simulations by Terradas et al. (2016). The nonexistence of this phenomenon in our case could be associated with limitations of the 2.5D modeling. The resonant absorption in 3D flux rope structures will be the subject of a future study.

After two minutes, the longitudinal motions seem to be established. However, the oscillations are very irregular with a complex pattern. These longitudinal motions are associated with compression and rarefaction, as shown in Figures 3.6(a)-3.6(f), rather than related to the projected solar gravity. The periods of these longitudinal modes (see Table 3.1) are shorter than those of the pendulum-like motions of Section 3.2.1. Also, these periods are not identical or the double of the vertical periods indicating that the longitudinal modes are not related to

the vertical modes. Altogether, this may indicate that the vertical perturbation also excites overtones of the structure with antisymmetric velocity profiles, as studied in Joarder & Roberts (1992b), Oliver et al. (1993), and Luna et al. (2012b). The temporal evolution of the vertical velocity is shown in the right panel of Figure 3.7. The vertical oscillations in the different layers of the structure show a very coherent motion with oscillations almost in phase at all heights. The periods are very uniform with values shown in Table 3.1 and in Figure 3.5. Also, in all the field lines, the attenuation is moderate and very uniform along the vertical direction. As we explained previously, there is no resonant absorption or fast-to-slow mode conversion, and these can be discarded as possible damping mechanisms. However, this attenuation can be explained by numerical diffusivity or by the wave leakage. Figure 3.8 shows a time-distance diagram of the vertical velocity along a vertical cut at the center of the structure. The red and blue colors correspond to the upward and downward motions, respectively. The prominence is located between 5 Mm to 10 Mm. As we can see from this figure, strong vertical motion appears after the perturbation at heights above the prominence and it extends even higher. The vertical bands have a slight inclination. This inclination reveals that there is a propagation of the velocity perturbations in the form of waves. The inclination is consistent with a velocity of $1000\,\mathrm{km\,s^{-1}}$. This means that some energy leaves the system during this time owing to the wave leakage. Taking the attenuation into account shown in the right panel of Figure 3.7, we conclude that this wave leakage contributes to the damping of the vertical oscillations. We calculated the damping time, as described in Section 3.2.1. The damping time is about of 60 minutes in almost all the lines and is slightly shorter at the bottom (about of 50 minutes).

In several works (Hyder 1966; Kleczek & Kuperus 1969; Luna et al. 2016b; Zhou et al. 2018), the authors have concluded that the restoring force for the transverse oscillations has a magnetic origin. We calculated the magnetic forces and their relative variations as done by Zhou et al. (2018). The variations of the magnetic pressure gradient exceed the variations of the magnetic tension force for all considered configurations. This indicates that in our model, the magnetic pressure gradient is the main restoring force for the vertical oscillations.

We obtained the period of the vertical oscillations as in Section 3.2.1(Table 3.1). The vertical period is plotted with green triangles as a function of the height of the dips in Figure 4.4. The oscillatory period remains constant at different layers of the prominence for all models. This indicates that the vertical motion is associated with global normal mode (Terradas et al. 2013; Luna et al. 2016b). From Figure 4.4, we see that the transverse periods are much shorter than longitudinal periods, similar to as revealed by observations (see review Tripathi et al. 2009, Table 1). Same as the longitudinal period, the vertical period does not change much for different models with an average difference of around 1 minute (see Table 3.1). Part of the variation of the vertical period for different density contrast can be due to the inertia effect. For the more massive prominence, with the density contrast $\chi = 200$, the vertical period is slightly longer (Figures 4.4(a) and 4.4(c)). Comparing the top and bottom panels of Figure 4.4, we can see that the vertical period seems to be almost insensitive to the shear angle variation.

3.3 Oscillations from external perturbation

Usually, LAOs are triggered by external perturbations such as Moreton or EIT waves. It is crucial to understand how external perturbation interacts with the flux rope structure and produces oscillations of the cold prominence. We modeled this scenario using the perturbation that arrives from outside. In order to produce strong perturbation comparable to the realistic energetic events, we used the source term of the total energy equation written as

$$\frac{\partial e}{\partial t} + \nabla \cdot \left[\mathbf{v}\left(e + p + \frac{|\mathbf{B}|^2}{2\mu_0}\right) - \frac{\mathbf{B}(\mathbf{v}\cdot\mathbf{B})}{\mu_0} \right] = \rho \mathbf{g}\cdot\mathbf{v} + Q_{\mathrm{R}} + \left(\frac{\partial e}{\partial t}\right)_{\mathrm{diff}} + S_e\,. \tag{3.12}$$

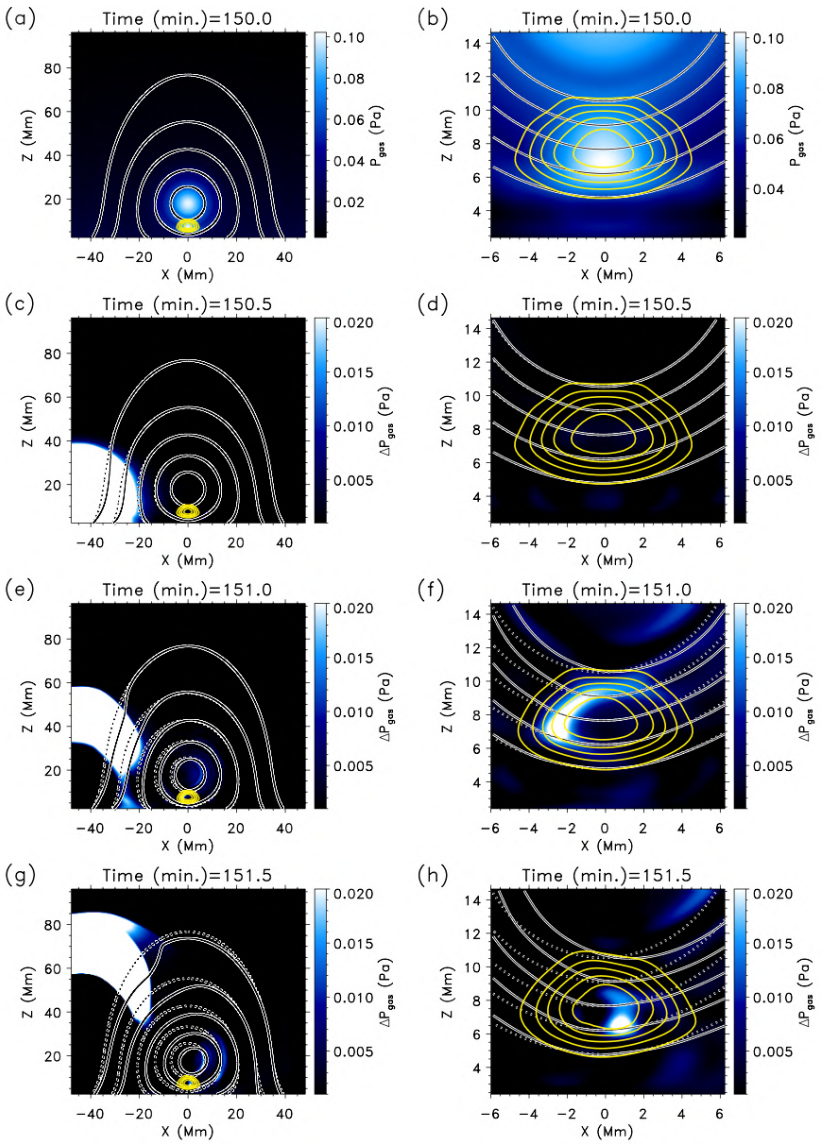

Figure 3.9: Evolution of the magnetic field and gas pressure during the wave front propagation. Panels (a), (b): The initial gas pressure distribution; panels (c)-(h): the running difference of the two consecutive snapshots. The left-hand panels show the same as the right-hand panels but focused at the location around the prominence. The dashed lines indicate the magnetic field lines before the perturbation. The yellow lines represent the density isocontours.

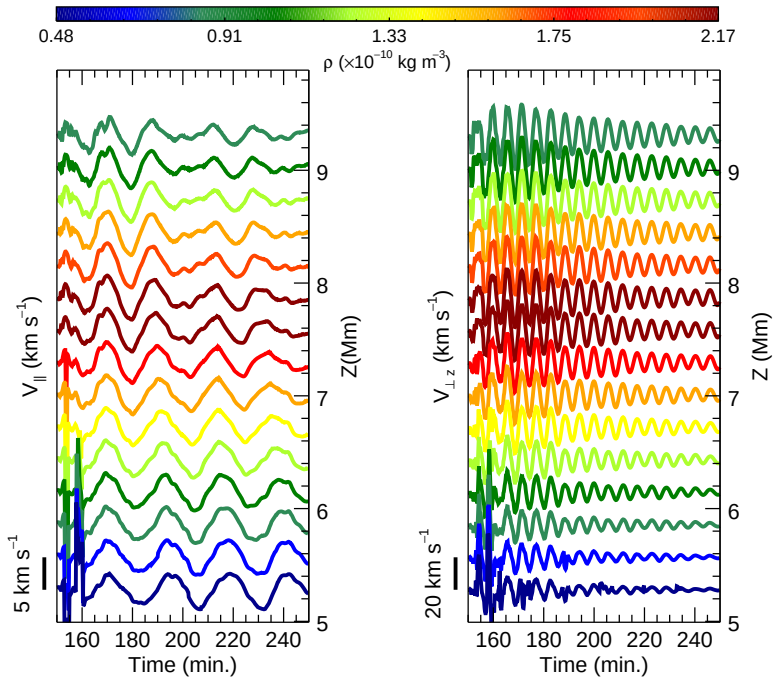

Figure 3.10: Temporal evolution of the longitudinal velocity (left panel) and vertical component of the transverse velocity (right panel) after the wave front propagation. The prominence model used has a shear angle of $\theta = 45°$ and a density contrast of $\chi = 200$. The colored lines indicate velocity variations at the center of mass of different field lines. The colors indicate the maximum initial density at the field lines according to the color bar scale. The right vertical axis indicates the height of the magnetic dips; the left vertical axis represents the scale of the maximum initial amplitude.

In this case, we add energy to the system, all variables are adjusted following the MHD equations, and we have a self-consistent perturbation (see the discussion on Section 3.2.1). We placed the perturbation at some distance from the prominence center as follows:

$$S_e = \frac{\alpha}{t_{\rm pert}} \exp\left(-\frac{(x - x_{\rm pert})^2}{\sigma_x^2} - \frac{(z - z_{\rm pert})^2}{\sigma_z^2}\right), \tag{3.13}$$

where the parameter $\alpha = 2$ J m^{-3}. In solar flares temperature and density can be up to 10^7 - 10^8 K and 10^{16} m^{-3} that corresponds to the parameter α from 2 J m^{-3} to 20 J m^{-3}. With this parameter, we produce an initial corresponding velocity around of 360 km s^{-1}. This value is typical for EIT waves that are usually associated with flares or coronal mass ejections (Moses et al. 1997; Thompson et al. 1998). In turn, $t_{\rm pert} = 50$ seconds, $x_{\rm pert} = -45.6$ Mm, $z_{\rm pert} = 12$ Mm, $\sigma_x = \sigma_z = 12$ Mm are the same parameters as in Equation (3.11).

Our aim is to study how the wave front propagates and interacts with the flux rope. The source of the wave should be placed at a certain distance from the flux rope. We consider a

periodic system, virtually composed of an infinite number of arcades separated by a region of the vertical field. In our domain, we not only have the main arcade but also the neighboring arcades. If the perturbation were located far (in the area of the neighboring arcade), the wave front would propagate along the field lines to the boundary, and most energy would remain trapped in the neighboring arcade with only a small part of the energy reaching the prominence. To avoid this behavior, we choose the initial position of the perturbation between the arcades, where the magnetic field is predominantly vertical. The temporal evolution of the system is shown in Figure 3.9 (left panels). The right-hand panels show the same, but with a more detailed view around the cold prominence. Figures 3.9(a) and 3.9(b) show the initial distribution of the gas pressure. We can see high pressure inside the flux rope in comparison with the environment. In this region, pressure increases during the flux rope formation process. In order to visualize the propagation of the perturbation, we compute the running differences by subtracting two consecutive snapshots separated by 30 seconds (Figures 3.9(c)-3.9(h)). As shown in Figures 3.9(c) and 3.9(d), just after the source term activation, the external perturbation propagates mainly vertically, producing significant changes in the magnetic field. The field lines are displaced to the right with respect to the equilibrium structure (dashed lines). The external gas pressure perturbation is unable to cross the flux rope and does not reach the internal region of the prominence. However, the compression of the lines creates a gas pressure excess inside the flux rope near the cold prominence plasma (Figures 3.9(e) and 3.9(f)). From Figures 3.9(e) and 3.9(f), we see that pressure perturbation inside the flux rope propagates crossing the cold prominence, but the prominence is not deformed or displaced by this perturbation. Figure 3.9(g) shows that the external wave front continues propagating along the arcade field lines producing significant perturbations of the magnetic field. In Figure 3.9(h), we see that the internal gas pressure pulse has crossed the prominence, slightly deforming it. After this transient, an oscillation is established. From this temporal evolution, we see that the magnetic field is responsible for the movement of the prominence. The external perturbation produces an Alfvénic disturbance that displaces the flux rope, and then the cold prominence mass moves. In this sense, the motion of the prominence is secondary because the perturbation firstly perturbs the flux rope.

Chen et al. (2016) studied the interaction between the fast-mode shock wave and the arcade magnetic field structure using 2D MHD simulations of the periodic arcade magnetic field. The system did not include the prominence mass. The authors concluded that if a wave vector is parallel to the magnetic field and the wave propagates in the region where plasma-β is close to unity, the fast-to-slow mode conversion happens (see Chen et al. 2016, Figure 7). In the present case, the shock wave propagates in the low-β environment and we do not observe the fast-to-slow mode conversion.

As in the previous sections, we obtain the longitudinal and vertical velocities at the field lines center of mass between $z = 5$ Mm to 10 Mm. From both panels of Figure 3.10, we can see a complex dynamical behavior. In the longitudinal velocity, there are no clear signatures of oscillations in the first ten minutes after the perturbation. In the bottom part of the structure, there are strong peaks associated with the external disturbance that propagates along the circular magnetic field lines of the flux rope. After some time, it reaches the bottom part of the flux rope, producing these spikes. The oscillations have an initial amplitude of about $5\,\mathrm{km\,s^{-1}}$. The period of the longitudinal oscillation slightly decreases with height that resembles the behavior of the period with height shown in the left panel of Figure 3.4. The vertical oscillations are established after the first five minutes of the perturbation (see Figure 3.10 right panel). The amplitude of the vertical oscillations is around $20\,\mathrm{km\,s^{-1}}$. We can see that the signal reaches the maximum amplitude after several cycles of oscillations. The motions are coherent in the different prominence layers. The damping of the signal is similar to the situation shown in the right panel of Figure 3.7. Therefore, as in the case of the vertical perturbation, this attenuation

can be associated with the wave leakage (see Section 3.2.2). The periods of oscillations shown in Table 3.1 are in agreement with oscillatory modes. From this numerical experiment, we conclude that external perturbation can excite both longitudinal and vertical oscillations. Even if the vertical oscillations are excited with larger amplitudes, they are also damped faster than the longitudinal modes. In this situation, the oscillation is mainly vertical just after the triggering, but the final phase contains mainly longitudinal oscillations.

3.4 Summary and conclusions

To study the physics of the LAOs, we performed 2.5D numerical simulations using the mechanism of van Ballegooijen & Martens (1989) for the flux rope formation. Once the flux rope was formed, the cold mass is artificially loaded in the dipped part of the magnetic structure. After the relaxation process, we applied the horizontal and vertical perturbations at the prominence position and studied oscillatory modes of different polarizations. We also considered the case of the external LAOs triggering using the disturbance placed out of the flux rope.

The horizontal perturbation triggers both longitudinal and transverse vertical oscillations. The period of the longitudinal oscillations, obtained numerically, shows a good agreement with the pendulum period. This confirms that, under the prominence conditions, gravity is the dominant restoring force for the longitudinal oscillations. The damping of the longitudinal motions is mostly related to the numerical dissipation. The vertical oscillations are associated with the back-reaction of the magnetic field to the longitudinal motions.

The vertical perturbation drives vertical motions together with the longitudinal component, associated with compression and rarefaction. The period of the vertical oscillations remains constant with height. This indicates that the vertical disturbance triggers global normal mode of the structure. The oscillations show attenuation. We found indications that the wave leakage could be responsible for the damping of the vertical oscillations.

We considered oscillations of different polarizations using models with the two values of shear angle and density contrast. We compared the periods of the different prominence configurations. The periods of longitudinal and vertical oscillations show a weak dependence on these parameters of the prominence structure. In the case of the longitudinal period, the small difference in the period is related to the variations of the radius of curvature. In contrast, the vertical periods are slightly different for the heavy and light prominences due to the inertia effect.

We investigated the triggering mechanism by external disturbance, choosing the location of the source at a certain distance from the flux rope. The external perturbation reaches the flux rope displacing and deforming the magnetic field lines. The flux rope displacement creates perturbation inside the prominence and, as a consequence, the prominence is also displaced from the equilibrium position. The signal analysis related to the different field lines has shown that the plasma motions have a complex character and external disturbance drives both longitudinal and transverse vertical LAOs.

Using the time-dependent numerical simulations, we demonstrated that the period of the longitudinal oscillations is in a good agreement with the pendulum model, and the period of the vertical oscillations only slightly depends on the prominence density and the shear angle of the magnetic field. We also proposed a model of the external LAOs excitation. This simulation shows that the external disturbance excites the normal prominence modes of the different polarizations.

In the future, it will be necessary to investigate the oscillatory properties, using 3D prominence models. Firstly, in a 3D model, the flux rope can be anchored at the foot points, which allows the magnetic tension to make a significant contribution to the restoring force. Therefore, including the perpendicular direction can significantly change the oscillatory properties of this model. Secondly, 3D simulations can allow us to study external triggering in more detail. It

is possible to reproduce the scenario when a wave arrives from different directions with respect to the prominence spine. For future work, it is essential to consider more realistic external disturbances such as an energy release due to the magnetic reconnection or the energetic wave associated with the prominence eruption.

4

Large-amplitude longitudinal oscillations in solar prominences simulated with different resolutions

Large-amplitude longitudinal oscillations (LALOs) in solar prominences have been widely studied in recent decades. However, their damping and amplification mechanisms are not well understood. In this study, we investigate the attenuation and amplification of LALOs using high-resolution numerical simulations with progressively increasing spatial resolutions.

Observations have shown that the period of the LALOs is around 1 hour, and the damping time is usually less than two periods, indicating strong attenuation of the motions. Luna et al. (2018) cataloged the filament oscillations using several months of the Global Oscillation Network Group (GONG) Hα data near the maximum of solar cycle 24. The catalog provides a large sample of the LALOs and statistics of the periods and damping times. On average, these latter authors found that the ratio of damping time to period is equal to 1.25, in agreement with the earlier observations. An intriguing phenomenon in the prominence oscillations is the amplification of motions. Contrary to the damping caused by energy loss, oscillations somehow acquire additional energy and increase their amplitudes in time. The first amplification event was reported by Molowny-Horas et al. (1999) from time-series of Hβ filtergrams of a polar crown prominence. These authors measured a periodic Doppler signal and found clear oscillations with periods of between 60 and 95 minutes and damping times between 119 and 377 minutes at six locations of the prominence. At one of the locations, they also found an oscillation with a period of 28 minutes and a growing amplitude with a characteristic time of 140 minutes. More recently, Zhang et al. (2017) reported the observation of LALOs in which the oscillatory amplitude remains constant or increases with time in some regions of the prominence. This unusual behavior of the LALO amplitude has also been found in the GONG catalog by Luna et al. (2018; see, e.g., Figure 25).

In order to explain both the damping and the amplification of prominence oscillations, Ballester et al. (2016) derived an expression for the temporal variation of the background temperature, taking into account the radiative losses and thermal conduction. The authors concluded that using some combination of the characteristic times of the different mechanisms and increasing or decreasing the background temperature could lead to damping or amplification of the oscillations. Zhang et al. (2017) proposed an alternative mechanism to explain the amplification: the threads located at the different dips of the same flux tube interchange their energy. Using 1D numerical simulations, Zhou et al. (2017) studied the different combinations

of the active–passive threads and demonstrated that the energy exchange significantly affects the damping or amplification time of the LALOs. However, this mechanism cannot explain the amplification of the threads that belong to the different field lines.

All the studies of LALOs in 2D and 3D have been done using numerical simulations (see Section 1.6). In these numerical experiments, dissipation is unavoidable. Terradas et al. (2016) investigated the influence of the numerical dissipation on the prominence oscillations in the 3D model, increasing spatial resolution up to 300 km. These latter authors concluded that the energy losses associated with the numerical dissipation are significantly reduced in the high-resolution experiments. In more recent 3D simulations, Adrover-González & Terradas (2020) and Fan (2020) pointed out that the reduction in numerical dissipation is crucial when studying the damping of LALOs. Terradas et al. (2013), Luna et al. (2016b), and Zhang et al. (2019) performed 2D numerical experiments of the prominence oscillation with spatial resolution up to 125 and 156 km, respectively. These numerical simulations showed significant damping which might be partly contributed by numerical diffusivity. In Chapter 3, we studied the convergence of a 2.5D experiment of LALOs excited in a magnetic flux rope, performing an experiment with a spatial resolution of 60 km and comparing it to a similar experiment with a spatial resolution of 240 km. We have seen that the periods of LALOs are consistent in the two experiments, although the damping time becomes longer in the higher resolution experiment. Therefore, we have concluded that in these experiments, the attenuation of LALOs is associated mainly with numerical dissipation.

In this work, we aim to understand the physical origin of the LALO damping and the other processes usually hidden by the artificial dissipation in numerical experiments. To this end, we performed 2D convergence experiments with progressively increasing spatial resolutions up to the highest value of 30 km. High-resolution experiments can be crucial when studying the periods and the damping mechanism of LALOs. Furthermore, the numerical diffusion in simulations with insufficient spatial resolution can hide important physical mechanisms.

This Chapter is organized as follows: In Section 4.1, the numerical model is described. In Sections 4.2 and 4.3, we explain the temporal evolution of the plasma under the disturbance directed along the field and compare the oscillatory parameters in the experiments with the different spatial resolution and the different prominence layers. In Section 4.4, we summarize the main results. This chapter corresponds to the already published paper *"Large-amplitude longitudinal oscillations in solar prominences simulated with different resolutions"* (Liakh et al. 2021, A&A, 654, A145).

4.1 Initial configuration

We assume a 2D prominence model as shown in Figure 4.1. The model is defined in the Cartesian coordinate system in the XZ-plane, where z-axis corresponds to the vertical direction. The initial magnetic field is a potential configuration which contains a dipped part suitable to support a prominence (see also Section 2.1.3). The magnetic configuration is composed of periodic arcades defined as

$$\frac{B_x}{B_0} = \cos(k_1(x-x_0))e^{-k_1(z-z_0)} - \cos(k_2(x-x_0))e^{-k_2(z-z_0)}, \tag{4.1}$$

$$\frac{B_z}{B_0} = -\sin(k_1(x-x_0))e^{-k_1(z-z_0)} + \sin(k_2(x-x_0))e^{-k_2(z-z_0)}, \tag{4.2}$$

where $B_0 = 33$ G, $x_0 = 0$ Mm, and $z_0 = -2$ Mm. We also set $k_1 = \frac{\pi}{D}$ and $k_2 = 3k_1$ where $D = 191.4$ Mm, that is the half-size of the numerical domain along the x-direction. The superposition of the major and minor arcades form the magnetic field structure shown in Figure 4.1 with the

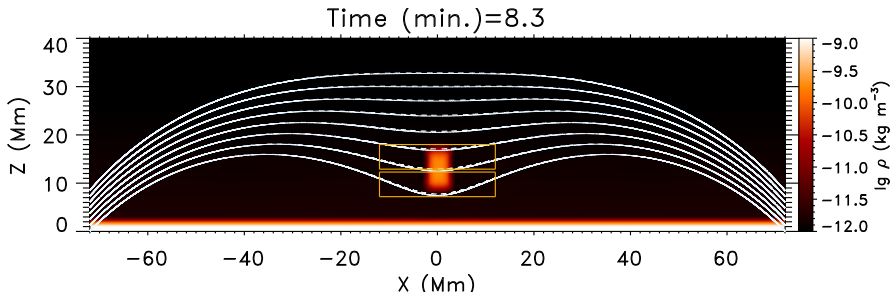

Figure 4.1: Density distribution and magnetic field lines at the central part of the computational domain after the mass loading and relaxation processes. The dashed lines denote the initial magnetic field prior to the mass loading.

dipped part centered at $x = 0$ Mm and between $z = 0$ and 25 Mm. As shown in the figure, the curvature of the magnetic field lines decreases with height. For $z > 27$ Mm, the magnetic field lines change from concave-up to concave-down, becoming ordinary loops. A detailed description of this magnetic configuration is given by Terradas et al. (2013) and Luna et al. (2016b). The magnetic field strength varies between 9.0 and 12.5 G from the bottom to the top of the dipped region ($z = 8 - 25$ Mm). The magnetic field strength lies in the range of the values obtained from the magnetic field measurements in the solar prominences (Leroy et al. 1983, 1984).

We assume an initial atmosphere consisting of a stratified plasma in hydrostatic equilibrium, including the chromosphere, transition region (TR), and corona. The temperature profile is given by

$$T(z) = T_0 + \frac{1}{2}(T_c - T_0)\left[1 + \tanh\left(\frac{z - z_c}{W_z}\right)\right]. \quad (4.3)$$

We choose $T_c = 10^6$ K, $T_0 = 10^4$ K, $W_z = 0.4$ Mm, and $z_c = 3.6$ Mm. In this profile the temperature ranges from $T_{ch} = 10^4$ K at the base of the chromosphere to $T_c = 10^6$ K in the corona. As the plasma is stratified in the vertical direction, the density changes from $\rho = 9 \times 10^{-9}$ kg m^{-3} in the chromosphere to $\rho = 1.69 \times 10^{-12}$ kg m^{-3} at the base of the corona at the height $z_c = 3.6$ Mm.

We numerically solve ideal MHD equations using the MANCHA3D code (Khomenko et al. 2008; Felipe et al. 2010; Khomenko & Collados 2012). The governing equations of mass, momentum, internal energy, induction equation are described in Section 2.3 and the corresponding source terms are described in Felipe et al. (2010). The computation domain consists of a box of 384 × 108 Mm in size. In order to study the influence of the numerical diffusivity on the prominence oscillations, we use four spatial resolutions with $\Delta = 240$, 120, 60 and 30 km from the coarse to the fine grids. We assume a periodic condition at the left and right boundaries. At the bottom boundary, we apply the current-free condition for the magnetic field (see, e.g., Luna et al. 2016b) and a symmetric condition for the temperature and pressure. At the bottom boundary, the density is fixed. At the top boundary, the zero-gradient condition is applied to all the variables except for B_x. We impose that B_x is antisymmetric.

In order to add the prominence mass to the dipped region of the magnetic field, we use artificial mass loading, as described by Liakh et al. (2020)(see also Chapter 3). We use the source term in the continuity equation to increase the density in the dipped region of the magnetic field. The density source term distribution is a Gaussian function (see Equation (9) from Liakh et al. (2020) work) centered at $(x, z) = (0, 11.8)$ Mm. The mass loading starts at $t = 0$ seconds and

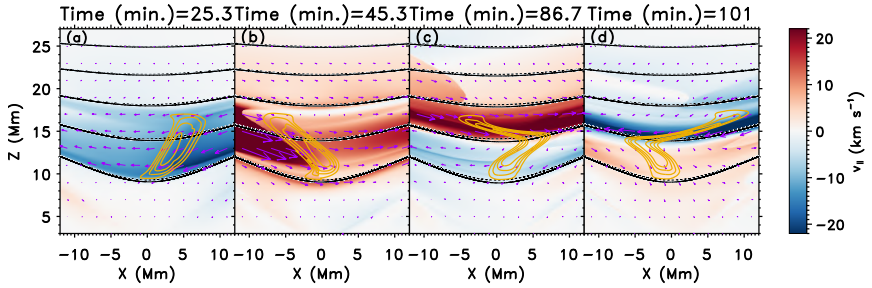

Figure 4.2: Temporal evolution of $v_{\parallel}$, magnetic field, and the prominence mass after the perturbation. Dashed black lines denote unperturbed magnetic field lines; solid black lines are the actual magnetic field lines at a given moment; orange lines are density isocontours, and purple arrows are the velocity field. Spatial resolution: $\Delta = 30$ km.

ends at $t = 100$ seconds. The resulting prominence has a density of 110 times the density of the initial corona with dimensions of 5 and 9 Mm in the horizontal and vertical directions, respectively.

During the first 8.3 minutes, we use intensive artificial damping in order to minimize the undesirable motions caused by the response of the magnetic field to the mass-loading process. Figure 4.1 shows the prominence after this relaxation phase. The dashed lines denote the initial magnetic field. As we can see, the magnetic field lines are slightly elongated downwards due to the heavy prominence mass. The prominence itself also has some deformation, becoming more compressed toward the center of the dip, and slightly drops down with respect to the initial height. At the end of the relaxation process, the system is close to static equilibrium.

Similarly to our previous work (Liakh et al. 2020), we trigger oscillation after the relaxation phase by applying an external force over the prominence. This force is incorporated as a source term in the momentum equations as

$$S_{mx} = \frac{\rho v_{\rm pert} B_x}{t_{\rm pert} B} \exp\left(-\frac{(x-x_{\rm pert})^4}{\sigma_x^4} - \frac{(z-z_{\rm pert})^4}{\sigma_z^4}\right), \tag{4.4}$$

$$S_{mz} = \frac{\rho v_{\rm pert} B_z}{t_{\rm pert} B} \exp\left(-\frac{(x-x_{\rm pert})^4}{\sigma_x^4} - \frac{(z-z_{\rm pert})^4}{\sigma_z^4}\right), \tag{4.5}$$

where $t_{\rm pert} = 10$ seconds is the duration of the disturbance that starts at $t = 8.3$ minutes. The parameters $\sigma_x = \sigma_z = 12$ Mm are the half-sizes of the perturbed region in the horizontal and vertical directions centered at $(x_{\rm pert}, z_{\rm pert}) = (0, 12)$ Mm. The force given by Equations (4.4) and (4.5) is directed along the local magnetic field in contrast to our previous work (Liakh et al. 2020) where the perturbation is purely horizontal or vertical. The maximum velocity of the perturbation is $v_{\rm pert} = 22\,{\rm km\,s^{-1}}$, which is in the range of the observed amplitudes of LAOs (see review by Arregui et al. 2018). In order to study the long-term evolution of prominence motions, we run the experiments for 275 minutes of physical time. In the case of the lowest spatial resolution (i.e., 240 and 120 km), it took for the code 2 and 4 hours using 288 and 1152 processors, respectively, to complete the numerical experiment. Completing the experiments with spatial resolution 60 and 30 km took more time, namely 32 and 256 hours, also using 1152 processors.

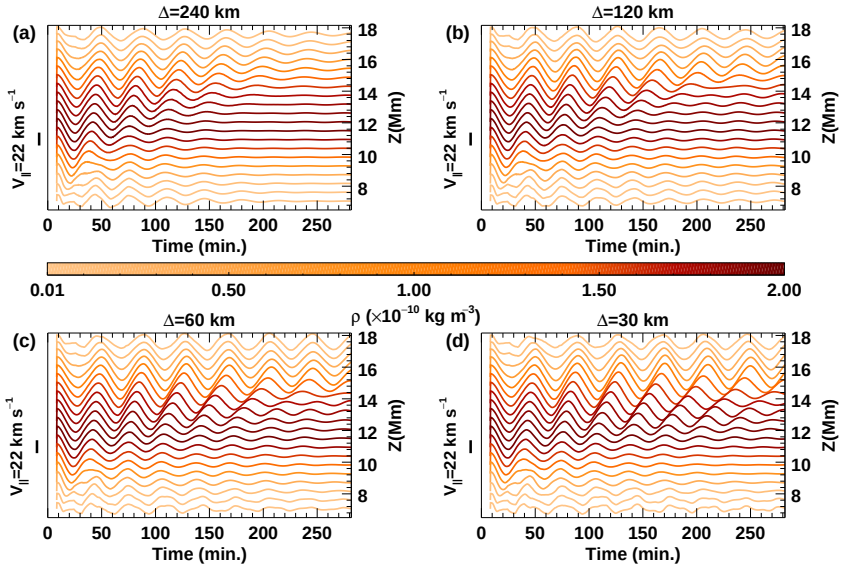

Figure 4.3: Temporal evolution of $v_{\parallel}$ at the center of mass at the selected field lines. The color bar denotes the maximum initial density at each field line. The left vertical axis indicates the velocity amplitude scale. The right vertical axis denotes the vertical location of the dips of selected magnetic field lines.

4.2 Influence of spatial resolution on prominence dynamics

In this work, we study the influence of the numerical diffusivity in the LAOs by progressively increasing the spatial resolution as described above. Figure 4.2 shows an example of the temporal evolution after the perturbation for $\Delta = 30$ km. This kind of evolution is representative of all our numerical experiments. After the initial disturbance at $t = 8.3$ minutes, the prominence moves to the right along the magnetic field and reaches its maximum initial displacement at approximately $t = 17$ minutes (Figure 4.2(a)). We see that the maximum horizontal displacement is large at the upper prominence part, whereas the bottom part is only slightly displaced from the equilibrium position. The reason is that, as the initial perturbation launches the prominence mass along the field lines with similar velocities, the plasma reaches different horizontal locations as the field lines have different curvatures. Figure 4.2(b) shows the prominence at $t = 45.3$ minutes. At this time, the prominence has reached its maximum displacement on the left side and begins to move again toward the right. The top part of the prominence slightly delays from the rest of the prominence body, suggesting a longer oscillation period. Figures 4.2(c) and 4.2(d) show the prominence evolution after several cycles of oscillations. From the velocity field displayed by the purple arrows, we can see that the prominence layers oscillate out of phase producing counterstreaming flows. Such counterstreaming flows are commonly observed in the filaments (Schmieder et al. 1991; Zirker et al. 1998; Lin et al. 2005a). Chen et al. (2014) claimed that these counterstreaming motions are associated with oscillations. The oscillation period depends

on the physical conditions of the magnetic field line where the prominence plasma resides. This means that the period can vary slightly for the neighboring field lines. This explains a phase difference between the motions of the prominence layers, shown in Figure 4.2(c). In addition, these alternate motions can be associated with processes of evaporation and condensation in prominences (Zhou et al. 2020) or shock downstreams produced by jets (Luna & Moreno-Insertis 2021).

In order to study the prominence plasma oscillations, we analyze the bulk motions of the plasma in the two possible polarizations: transverse and longitudinal to the magnetic field. Following method described in Section 2.4 we compute the velocities of the center of mass of independent field lines using Equations (5) and (6) from Luna et al. (2016b). The parameters $v_{\parallel}$ and $v_{\perp}$ are the longitudinal and transverse velocities of the center of mass of each field line. First, we select 20 equally spaced field lines that permeate the prominence body at the height from 7.2 Mm up to 17.6 Mm. We then start integrating the field lines in the chromosphere, where the magnetic field remains unchanged according to the line-tying condition. As our fluid is perfectly conducting, the frozen-in condition is fulfilled. This allows us to advect the motions in the same field line at any moment in time. We selected an identical set of field lines for each numerical experiment in order to compare the resulting velocities.

Figure 4.3 shows the temporal evolution of $v_{\parallel}$ for the four numerical experiments with different spatial resolutions. The global behavior of the prominence is similar in each of the experiments. After the initial perturbation at $t = 8.3$ minutes, the longitudinal velocity increases in all the lines. The longitudinal velocity reaches the highest value, $v_{\parallel} = 22\,\mathrm{km\,s^{-1}}$, in the densest prominence part at a height of $z = 11.8$ Mm. At $t = 15 - 35$ minutes, we see a certain shift in the signal. This phase shift is related to the different periods associated with the different field lines. On the one hand, we see that the oscillations are less attenuated with increasing spatial resolution, although the difference between the cases $\Delta = 60$ and 30 km is less pronounced. On the other hand, the behavior of the damping changes with height. This is in agreement with the visual impression from Figure 4.2, discussed above. Oscillations at the bottom and in the central part are strongly damped in all the experiments. At the height of $13 - 17$ Mm, the oscillations with weaker attenuation last for a longer time. In the highest-resolution simulation, the upper prominence part keeps oscillating with a significant amplitude even at the final stage of the numerical experiment.

4.2.1 Influence of spatial resolution on the period

Figure 4.4 shows the periods of the longitudinal oscillations for each of the 20 selected field lines and each numerical experiment with different spatial resolutions. The period is more or less uniform under 10.2 Mm and above 16.1 Mm. In contrast, for heights $z = 10.2 - 16.1$ Mm, we see an increase in period with the height of the magnetic dip. These heights correspond to the prominence region with the highest density contrast. One can observe in this figure that the slope of the curves depends on the spatial resolution. The steepest slope corresponds to the experiment with the highest spatial resolution ($\Delta = 30$ km). In contrast, for $\Delta = 240$ km, the period is more uniform with a smoother variation with height.

Under prominence conditions, the main restoring force of these oscillations is the solar gravity projected along the magnetic field (see e.g., Luna & Karpen 2012; Luna et al. 2012a, 2016b; Zhou et al. 2018; Liakh et al. 2020; Fan 2020). Luna & Karpen (2012) suggested that the period of the longitudinal oscillations depends only on the radius of curvature of the magnetic dip, R_c, as

$$P = 2\pi\sqrt{\frac{R_c}{g}}\,, \tag{4.6}$$

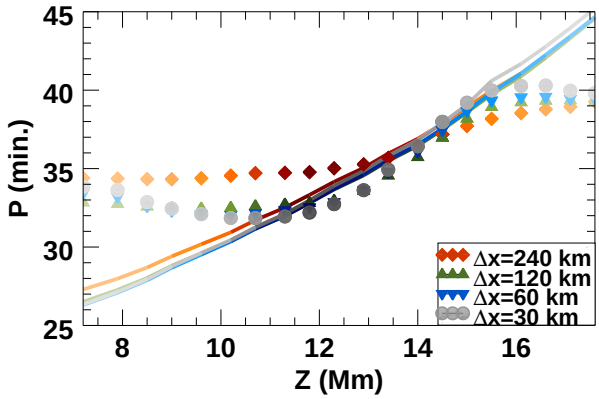

Figure 4.4: Periods as a function of height of the magnetic dips. The symbols denote the longitudinal period obtained from the numerical experiments, and the solid lines are the periods predicted by the pendulum model. Different colors and symbols correspond to the experiments with different spatial resolutions. The color gradation from dark to light corresponds to a decrease in the density contrast.

where $g = 274\,\mathrm{m\,s^{-2}}$ is the solar gravitational acceleration. In our magnetic configuration, the curvature of the magnetic field lines in the prominence area decreases with height. This implies that the period of the different field lines increases with height in agreement with Figure 4.3. The radius of curvature of the dips of the field lines changes with time in response to plasma motion. In order to compare the results of the simulations with the pendulum model, we compute the time-averaged radius of curvature. The values obtained are $R_c = 17.3 - 51.1\,\mathrm{Mm}$ for the selected field lines from the bottom to the top of the dipped region. With Equation (4.6) we computed the theoretical period shown in Figure 4.4 as a solid line. From the figure, we see that for the experiments with $\Delta = 30, 60$, and 120 km, we see good agreement between the numerical results and the pendulum model at heights $z = 10.2 - 16.1\,\mathrm{Mm}$, where the body of the prominence is located. We also observe that even though all three resolutions show good agreement with the pendulum model, the agreement is slightly better for the finest resolution. In contrast, in the coarse case with $\Delta = 240$ km, there is only agreement at the central part of the prominence. This indicates a strong influence of the numerical diffusivity on the period of oscillations and shows that a certain spatial resolution is necessary to reach agreement with the pendulum model. Using 3D numerical simulations, Zhou et al. (2018) and Fan (2020) concluded that in their experiments the disagreement with the pendulum model is of the order of 10 %. We suggest that high-resolution experiments can reduce this discrepancy.

Figure 4.4 shows a clear deviation from the pendulum model below the prominence, $z < 10.2\,\mathrm{Mm}$, and above it, $z > 16\,\mathrm{Mm}$, even for high spatial resolution. This behavior suggests the existence of a physical reason for the deviation. Previous works (such as Zhou et al. 2018; Zhang et al. 2019; Liakh et al. 2020; Fan 2020) have also found discrepancies with the pendulum model. Zhou et al. (2018) and Zhang et al. (2019) found that if the gravity-to-Lorentz-force ratio is close to unity, the heavy prominence plasma can significantly deform the magnetic field lines. They defined the dimensionless parameter as the ratio between the weight of the thread

and the magnetic pressure, as

$$\delta = \frac{2\rho g l}{B^2/2\,\mu_0}\,, \tag{4.7}$$

where l is the half-length of the prominence thread. The authors argued that if the parameter δ is close to unity, the weight of the prominence changes the field geometry dynamically. In this situation, the actual trajectory of the plasma does not coincide with the field lines, and the trajectory of the plasma has a larger radius of curvature than the one corresponding to an unperturbed magnetic field line (see Figure 9 from Zhang et al. 2019). Thus, the resulting period of LALOs can be longer than predicted by the pendulum model. In our model, the magnetic field at the dipped part increases with z, from 9 G at the base of the prominence up to 12 G at its top. Using the parameters of our model, we obtain that the maximum value $\delta = 0.7$ reached at around $z = 11.8$ Mm, which is around the densest region of the prominence. In that region, we obtain good agreement with the pendulum model. For the regions below and above the prominence, δ is much smaller. We conclude that the weakness of the magnetic field cannot explain the discrepancies between the pendulum model and our simulations. However, we find that the interaction between the longitudinal motion of the prominence and the magnetic structure is not negligible. When the prominence moves, the magnetic field structure changes considerably. These perturbations of the magnetic field could be transmitted to the rest of the field structure. This contributes to the damping of the LALOs due to wave leakage, as we discuss below in Section 4.3.

As discussed in Chapter 1, Luna et al. (2012a) showed that the restoring force of LALOs is a combination of the gravity projected along the magnetic field and the gas pressure gradient. The relative importance of both restoring forces depends on the radius of curvature of the field lines with respect to a characteristic radius R_{lim}. In a situation where $R_c \ll R_{lim}$, the gravity dominates, and the pendulum model is valid. In contrast, for $R_c \gtrsim R_{lim}$ the gas pressure term dominates. The radius R_{lim} depends on several parameters of the structure

$$R_{lim} = \frac{l(L-l)\chi g}{c_{sc}^2}\,, \tag{4.8}$$

where c_{sc} is coronal sound speed, L is half-length of the field line, and χ is the density contrast between the prominence and the ambient corona. In our situation, below the prominence ($z < 10.2$ Mm), the ratio $R_c/R_{lim} > 0.2$, and it increases for smaller values of z. The main reason is that the density contrast χ is close to 1 in that region. This indicates that the contribution of the gas pressure to the restoring force is important, and the pendulum model is no longer valid. Similarly, for $z \geq 16.1$ Mm, both the curvature of the field lines and the density contrast decrease with height. Thus R_c/R_{lim} increases in these field lines from 0.4 up to 5.9 for higher values of z. This explains why the period of the longitudinal oscillations deviates from the pendulum period for locations below and above the prominence. In turn, in the central region, $z = 10.2 - 16.1$ Mm, the ratio is around 0.1.

The prominence is also subject to transverse oscillations. Similarly to the longitudinal velocity, we obtained the temporal evolution of $v_\perp$ using Equation (6) from Luna et al. (2016b) for each selected field line. Figure 4.5 shows the temporal evolution for the $\Delta = 30$ km case. We only show the case with the finest spatial resolution because all experiments have a very similar temporal evolution of the transverse velocity. From the figure, we see that the transverse motions are synchronized in all the field lines with the same oscillatory period, $P = 4$ minutes. This uniformity of the oscillations shows that the motion is related to a global normal mode of the field structure. The oscillation in $v_\perp$ is not harmonic, and the amplitude is modulated every approximately 30 minutes. This modulation is also synchronized in all the field lines shown in the figure. The amplitude of the transverse oscillations is equal to $5\,\mathrm{km\,s^{-1}}$,which is much

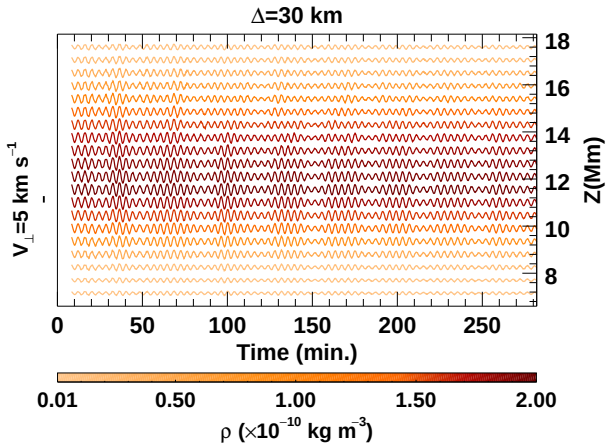

Figure 4.5: Temporal evolution of $v_\perp$ at the center of mass of the selected field lines. The color bar denotes the maximum initial density at each field line. The left vertical axis indicates the velocity amplitude scale. The right axis denotes the height of the dips of the field lines.

smaller than for the longitudinal motions. This modulation of the amplitude is probably related to the motion of the prominence mass. The global motion of the plasma periodically changes the characteristics of the magnetic structure, resulting in a modulation of the oscillation. The signal modulation of the transverse velocity can also indicate the longitudinal to transverse mode conversion. This could be the subject of future work. During the simulation time, the transverse oscillations show nearly no significant damping in the four numerical experiments with different Δ, indicating that numerical dissipation does not affect this kind of motion.

4.2.2 Influence of spatial resolution on the damping

In order to study in detail the damping in the experiments with different Δ, we consider longitudinal velocity in two field lines with dips at $z = 11.8$ Mm (central part of the prominence) and $z = 16.1$ Mm (top part). The $v_\parallel$ in the central and top field lines are shown in Figure 4.6. The upper panel of Figure 4.6 shows that the attenuation is strongest in the experiment with the coarsest resolution ($\Delta = 240$ km). The oscillation signal is almost completely damped after 150 minutes. In contrast, the experiment with $\Delta = 30$ km is where we observe the weakest attenuation. Comparing all the cases, we see that the damping time increases for increasing spatial resolution (i.e., decreasing Δ). The curves for $\Delta = 60$ and 30 km are relatively close to each other. This indicates that the damping time is close to the saturation and that the high-resolution experiment shows indications of physical damping not associated with numerical diffusivity. In order to quantify the damping time, we fit the signal of $v_\parallel$ with a decaying sinusoidal function such as $v_\parallel = V_0 e^{-t/\tau_d} \sin(2\pi t/P + \phi)$ (Section 2.4.3). The values of τ_d obtained from the best fit to $v_\parallel$ are shown in Figure 4.7 (top panel) as a function of spatial resolution, Δ. We observe that the damping time increases when Δ decreases for experiments with $\Delta = 240, 120$, and 60 km. In these three experiments, the damping time shows a quadratic dependence on Δ denoted by the solid line in the top panel of Figure 4.7. The trend marked by the solid line seems to indicate the damping time of about $\tau_d = 110$ minutes as Δ approaches zero.

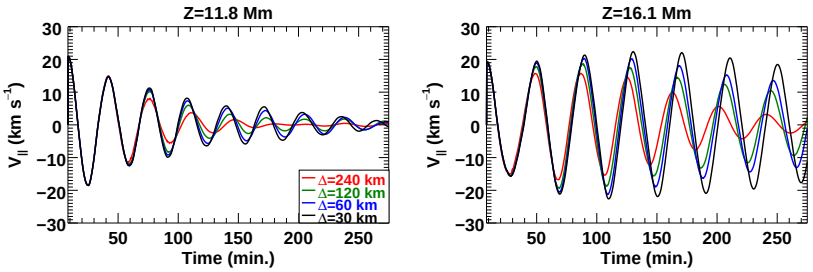

Figure 4.6: Temporal evolution of $v_\parallel$ at the center of mass of the selected field lines. Top: Field line close to the prominence center. Bottom: Field line at the top part of the prominence. The different colors distinguish the experiments with different spatial resolutions.

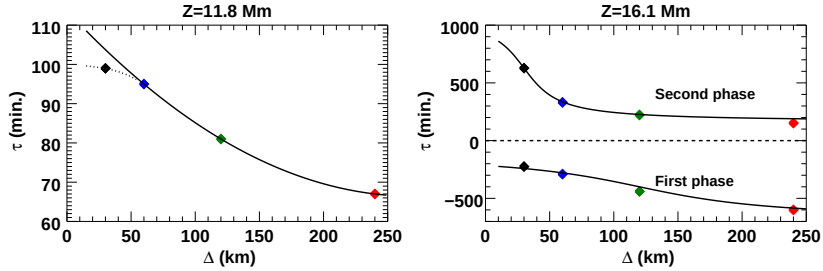

Figure 4.7: Top: Damping time of oscillations at a height of 11.8 Mm as a function of the spatial resolution Δ. The solid line denotes the quadratic dependence, and the dashed line shows fitting with an arctangent function. Bottom: Same for the height 16.1 Mm. The solid lines denote fitting with an arctangent function.

However, the damping time in the experiment with $\Delta = 30$ km deviates from this quadratic trend and has a similar value to the one in the $\Delta = 60$ km experiment. We fitted an arctangent function to all four values of τ_d, including the one in $\Delta = 30$ km experiment. This new fit is shown as a dashed line at the top panel of Figure 4.7. The trend, including the highest resolution case, deviates from the quadratic trend as the curve becomes flatter. This suggests that τ_d may saturate for decreasing values of Δ showing the non-numerical (i.e., physical) origin of this damping. According to the dashed line, $\tau_d \to 100$ minutes as Δ approaches zero.

We repeated the same analysis for the magnetic field line located at $z = 16.1$ Mm, which is at the top of the prominence. The results are shown in the bottom panel of Figure 4.6. The temporal evolution of the longitudinal velocity differs significantly from the one at $z = 11.8$ Mm. We can clearly distinguish two stages in temporal evolution. In the first stage, the velocity is amplified after the initial perturbation. The amplification is more significant and extended in time in the simulations with higher spatial resolution. For the case of $\Delta = 30$ km, the amplitude increases from $v_\parallel = 19.5\,\mathrm{km\,s^{-1}}$ up to $23\,\mathrm{km\,s^{-1}}$ over 130 minutes. This amplification can be clearly traced in the snapshots of temporal evolution shown in Figure 4.2(d) above. The oscillations are attenuated in the bottom and central parts of the prominence. However, at heights $z > 15$ Mm, the displacement is not only comparable to but is even larger than the initial displacement shown in Figure 4.2(a). During the second stage, the oscillations begin to decay

slowly. At the end of the simulated time ($t = 275$ minutes), the motions are almost completely damped for the experiments with $\Delta = 240, 120$ km. In the higher resolution simulations, $\Delta = 30$ and 60 km, the upper prominence part oscillates undamped for a longer time. In order to quantify the damping time for these complex oscillations, we split the velocity signal into two parts associated with the amplification and damping. We then fit $v_{\parallel}$ with the decaying and amplifying sinusoidal functions. For the amplification stage, we assume the characteristic time, τ_A, to be negative, and for the decaying stage, we assume the damping time, τ_D, to be positive. From the best fit to the longitudinal velocity, we obtain values of τ_A in the range $[-600, -225]$ minutes, and values of τ_D in the range of $[152, 628]$ minutes. The higher values of both parameters correspond to better resolutions. The results of this analysis are shown in the bottom panel of Figure 4.7. The characteristic time of the amplification, τ_A, differs significantly between the high- and low-resolution experiments. We observe that, in the experiment with $\Delta = 30$ km, $\tau_A = -225$ minutes, which is the most significant amplification. In addition, the bottom panel of Figure 4.6 shows that this amplification stage is more extended in time for the finer spatial resolutions. The damping time in the second phase reaches a value of $\tau_D = 628$ minutes for the simulation with $\Delta = 30$ km, indicating the weakest damping. The amplification stage is not as relevant for the experiment with $\Delta = 240$ km. For this experiment, the amplification time $\tau_A = -600$ minutes is the longest, and the oscillations have an almost constant amplitude during the first 67.8 minutes. We performed a fit to both τ_A and τ_D using an arctangent function, allowing us to find the trend for both parameters (Figure 4.7, solid lines at the bottom panel). With these trends, we can roughly estimate that the real physical amplification for our system would have a characteristic time of -200 minutes, whereas the damping time would be longer than 900 minutes. These results may indicate that our highest-resolution experiment is about to resolve a physical mechanism for these effects.

4.3 Physical reasons for the amplification and damping of oscillations

As we have shown in Section 4.2.2 above, oscillations at the bottom part of the prominence damp quickly, and those at the top part are initially amplified and damped later. We have also seen that these phenomena may have a physical origin and are not related to numerical dissipation. In this section, we perform a detailed analysis to shed light on the possible physical mechanisms that produce these effects.

First, we study the contributions of the different forces to the energy balance in two regions of the prominence defined by the orange rectangles in Figure 4.1. Equations (4.9–4.11) show the temporal derivatives of the work done by the different forces in the region, which we denote Σ. In addition, Equation (4.12) gives the kinetic energy flow along the boundaries of the region, $\partial\Sigma$. These equations are:

$$\dot{W}_g = \iint_{\Sigma} \rho\, \mathbf{g}\cdot\mathbf{v}\, d\sigma\,, \tag{4.9}$$

$$\dot{W}_p = -\iint_{\Sigma} \mathbf{v}\cdot\nabla p\, d\sigma\,, \tag{4.10}$$

$$\dot{W}_B = \iint_{\Sigma} \frac{1}{\mu_0}(\nabla\times\mathbf{B})\times\mathbf{B} d\sigma\,, \tag{4.11}$$

$$\dot{\Pi}_K = -\oint_{\partial\Sigma} \frac{1}{2}\rho v^2 \mathbf{v}\cdot\mathbf{n}\; dl\;, \tag{4.12}$$

where $\mathbf{n}$ is the vector normal to the region boundaries. The combination of the four terms is equal to the temporal derivative of the kinetic energy integrated in the region Σ, $\dot{E}_K$. Figure 4.8 shows the temporal evolution of the terms given by Equations (4.9–4.12). All these magnitudes

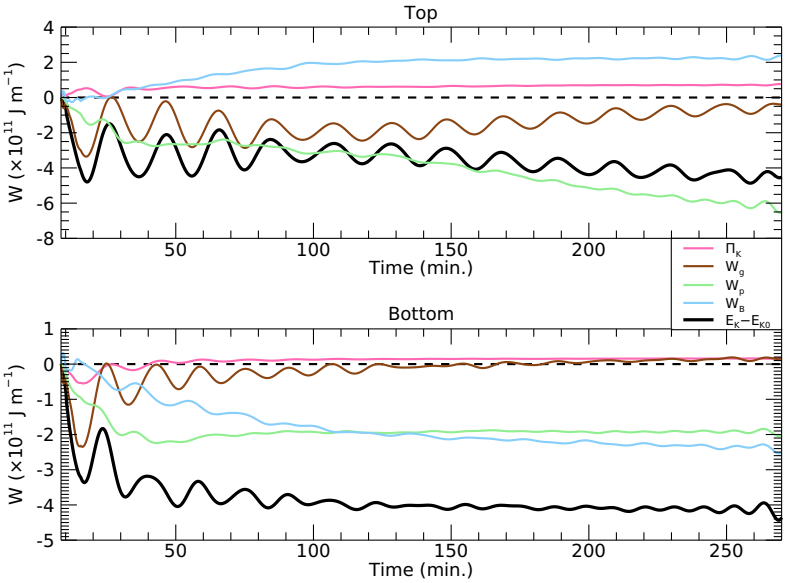

Figure 4.8: Work done by the gravity force (brown line), by the gas pressure force (light green line), by the Lorentz force (light blue line), and the kinetic energy flow (pink line) integrated in two rectangles shown by the orange lines in Figure 4.1. The black lines denote a total kinetic energy variation with respect to its value at $t = 8.5$ minutes.

are shown with respect to their values at $t = 8.5$ minutes. The top and bottom panels of the figure show the quantities computed in the top and bottom regions shown in Figure 4.1, respectively.

Figure 4.8 shows a clear difference in the evolution of the plasma in both regions of the prominence. At the top of the structure, the kinetic energy decreases rapidly immediately after the initial perturbation. The curve oscillates around an average value that seems to increase slightly from approximately 30 to 100 minutes. The amplification of the oscillations at the upper part of the prominence does not result in a significant increase in the kinetic energy because the region of integration is larger than the prominence size and includes the nonamplified regions. After $t = 100$ minutes, the kinetic energy decreases. Figure 4.8 (top panel) shows that the gas pressure work is negative and that it makes the largest contribution to the kinetic energy losses after $t = 100$ minutes. In contrast, the work done by the Lorentz force in the first 100 minutes is positive, indicating that it accelerates the prominence plasma. In turn, the kinetic energy inflow through the boundaries is relatively small compared to the other terms.

At the bottom part of the prominence (Figure 4.8, bottom panel), the black line shows a substantial decrease in the first 100 minutes coinciding with the significant attenuation of the oscillations in this region. The bottom panel shows that the main contribution to the kinetic energy losses is associated with the work of the gas pressure and the Lorentz force. This may indicate the generation of fast MHD waves, which are emitted from the prominence region. This mechanism can contribute to the damping of the oscillations, as already suggested by Zhang et al. (2019). These fast waves are associated with the gas pressure and the Lorentz forces.

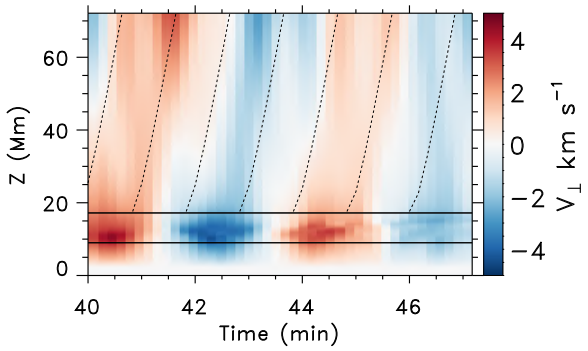

Figure 4.9: Time–distance diagram of the transverse velocity, $v_\perp$, along the vertical direction at the horizontal position $x = 0$ Mm. Black horizontal lines denote the position of the prominence. Dashed lines denote the position of a hypothetical wave front propagating at a local Alfvén speed.

Additional evidence for the wave leakage is shown in Figure 4.9, which shows the time–distance diagram of the transverse velocity, $v_\perp$, along the axis, $x = 0$ Mm, over 10 minutes. The fast MHD waves produce perturbations of the $v_\perp$ field. The figure shows the waves that travel upwards with a pattern of alternating positive and negative values of $v_\perp$. The inclination of the ridges is indicative of the speed of the waves. As we performed the experiments in the low-β regime, the speed of the fast waves is approximately the Alfvén speed, v_A. The dashed lines represent locations of a wave front that would propagate at a local Alfvén speed. We can see that the waves emitted from the prominence propagate with speed similar to the Alfvén speed. Figures 4.8 and 4.9 indicate that an important portion of the energy of the prominence oscillation is emitted in the form of fast MHD waves.

Figure 4.8 demonstrates that the increase in W_B at the top may be related to its decrease at the bottom part of the structure. Therefore, not all the energy losses at the bottom of the prominence are emitted in the form of waves. Instead, a part of this energy is transferred to the top of the structure. This transfer can explain the amplification of the oscillations at the upper part of the prominence.

We computed the incoming Poynting flux into two regions shown by the orange lines in Figure 4.1 as

$$\dot{\Pi}_{mag} = -\oint_{\partial\Sigma} \left(\frac{B^2 \mathbf{v}}{\mu_0} - \frac{(\mathbf{B}\cdot\mathbf{v})\mathbf{B}}{\mu_0} \right) \cdot \mathbf{n}\, dl \ . \tag{4.13}$$

Figure 4.10 shows the time integral of the incoming Poynting flux in both regions. We can see that during the time interval $65-150$ minutes, the incoming Poynting flux at the prominence top dominates over the outcoming flux. This indicates that the magnetic energy increases at the upper prominence region. The opposite situation occurs at the bottom region. The magnetic energy leaves the region, and the time integral of the Poynting flux has a negative sign. In addition, the shapes of both curves are similar but are of opposite phase with respect to each other, indicating that the top part gains a significant part of the energy lost by the bottom part. Apart from this energy transfer, the flux at the bottom part also shows the leakage of energy emitted to the ambient atmosphere in the form of fast waves. Overall, Figure 4.10 indicates that magnetic energy seems to be partially transferred from the bottom to the top of the prominence.

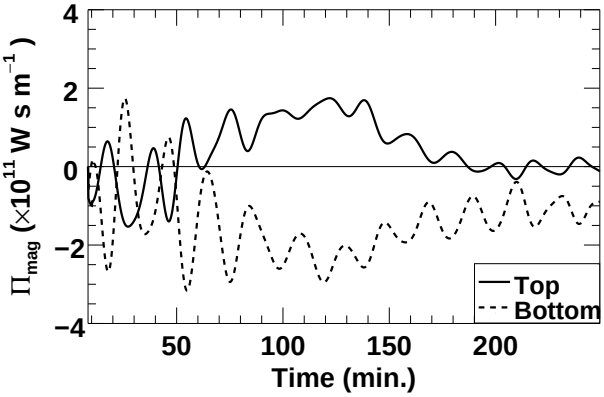

Figure 4.10: Time-integrated magnetic energy inflow through the boundaries of the domains indicated by orange lines in Figure 4.1. The short-period component has been filtered out.

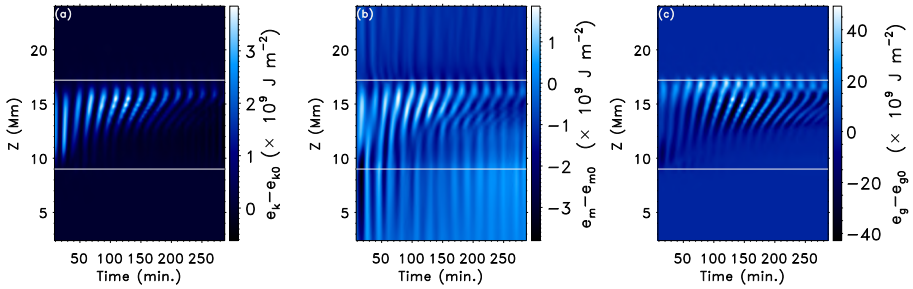

Figure 4.11: The time–distance diagram of the energy variations with respect to their values immediately before the perturbation, $e - e_0$, integrated in the region from $x = -12$ Mm to $x = 12$ Mm. The white lines denote the heights where the prominence is located. (a) Kinetic energy density, $e_k = \rho v^2/2$; (b) magnetic energy density, $e_B = B^2/2\mu_0$; (c) gravitational energy density, $e_g = \rho g z$.

In order to understand the physical reason for the transfer of the energy from the bottom to the upper layers of the prominence, we computed the time–distance diagrams of the different contributions to the total energy along the vertical direction integrated in the region from $x = -12$ Mm to $x = 12$ Mm. The result of this calculation is shown in Figure 4.11. The three panels show the kinetic energy density, $e_k = \rho v^2/2$ (Figure 4.11(a)), the magnetic energy density, $e_B = B^2/2\mu_0$ (Figure 4.11(b)), and the gravitational energy density, $e_g = \rho g z$ (Figure 4.11(c)), at times immediately after the perturbation. We are interested in the variation of these energies after the mass loading. Therefore, Figure 4.11 shows the difference with respect to the values of each of the energies at $t = 8.3$ minutes. The light and dark fringes reflect the plasma motions and velocity variations. The figure clearly shows the phase shift between the oscillations at different heights inside the prominence. In addition, it can be observed that the kinetic energy increases at $t = 60-130$ minutes and at heights $z > 13$ Mm. A similar increase can

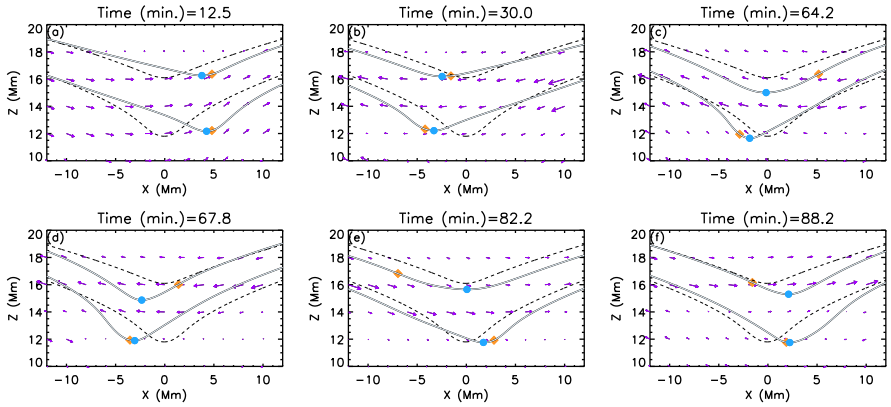

Figure 4.12: Temporal evolution of the fluid elements and the magnetic field lines after the perturbation. The orange diamonds denote the positions of the fluid elements, and the blue circles correspond to the locations of the center of each dip. The purple arrows denote the velocity field. Dotted lines are unperturbed magnetic field lines; solid lines are actual magnetic field lines at a given moment. We note that the magnetic field perturbation is multiplied by a factor of ten for better visibility.

be seen for the magnetic and gravitational energies in Figures 4.11(b) and 4.11(c). The magnetic energy increase is associated with the energy exchange between the bottom and top parts of the prominence, as was already shown in Figure 4.10. The gravitational energy increases during the same period of time which is related to the amplification of the oscillation velocities at the top of the prominence. As plasma is accelerated, it can reach greater heights along the magnetic field. As a result, the total gravitational energy increases. At the bottom, in the region of strong attenuation, we can see the energy losses in all the panels. As mentioned before, some fraction of the energy is taken away by the fast MHD waves, and some other fraction is transferred to upper prominence layers.

The results above seem to indicate that the amplification of the oscillations is related to the energy transfer from the bottom to the top parts of the structure. The magnetic field structure changes with time thanks to the oscillations, and the actual trajectory of the plasma motions is no longer along the unperturbed magnetic field lines. In a situation with a rigid magnetic field, the trajectory coincides with the field line, and the Lorentz force has no projection along the trajectory of the plasma. However, in our situation, the trajectory does not coincide with the unperturbed field lines. In such a case, the forces along the trajectory can become different from the forces projected along the magnetic field lines. In order to understand the detailed mechanism for the amplification and damping, we study the motion of the individual fluid elements by integrating the velocity field at each moment in time. We selected two plasma elements with the initial coordinates $(x, z) = (0, 16.1)$ and $(0, 11.8)$ Mm which correspond to the particles at the top and the central part of the prominence.

In order to highlight the modifications of the magnetic field lines due to the plasma motions, we multiply the magnetic field perturbation by a factor of ten. This magnetic field is defined as $\mathbf{B'} = \mathbf{10}(\mathbf{B} - \mathbf{B_0}) + \mathbf{B_0}$, where $\mathbf{B}$ is the actual magnetic field at time t and $\mathbf{B_0}$ is the magnetic field at $t = 0$ minutes. Similarly, the displacement of the fluid elements is also multiplied by the same factor in order to fulfill the frozen-in condition. Figure 4.12 shows the positions of the

fluid elements (orange diamonds) and centers of the dips (blue circles) of the magnetic field lines at the different moments in time. Figure 4.12(a) shows the maximum displacement of the fluid elements immediately after the perturbation. We see that the field lines hosting the particles change, and the positions of the dips follow the motion of the particles. In Figure 4.12(b), the fluid elements move to the left of the structure. The dip at the lower line continues following the particle motion. In contrast, at the upper line, the dip is located ahead of the particle. In this situation, the upper particle reaches the dip in a position that is displaced to the left of the original dip. Thus, the upper particle has gained an increment in velocity during this first half period of oscillation. This process is repeated during the following period. In Figure 4.12(c), we observe that the particle has gained energy and that the amplitude of the oscillation is larger. In Figure 4.12(d), the dip has moved away from the particle again, leading to an increase in the amplitude. The same process is also produced in the reverse direction, as can be observed in Figures 4.12(e) and 4.12(f). The motion of the upper dip follows the motion of the dip at the bottom line. The reason for this is that the magnetic structure reacts to the bulk motion of the prominence. In this sense, the changes in the magnetic configuration at the bottom part of the structure affect the top part of the structure.

The situation is exactly the opposite at the bottom of the structure. The plasma motions also modify the field lines, but the dip approaches the particle in this case. In this way, the oscillatory amplitude is reduced in each oscillation period. In Figures 4.12(c) and 4.12(d), we observe the following situation: the motion of the fluid element at the bottom causes displacement of the corresponding magnetic dip. As we can see from Figures 4.12(e) and 4.12(f), the dip at the bottom continues following the fluid element in the next period of oscillations. Thus, the particle continues losing energy in each period, and the oscillations damp quickly.

In order to study the oscillation amplification phenomena in more detail and check how the motions at the upper and lower part of the prominence affect each other, we performed an alternative experiment described below. We used the same prominence model, but the height of the maximum of the perturbation was shifted down to $z = 9\,\mathrm{Mm}$, and the characteristic vertical size of the perturbed region was reduced to $\sigma_z = 4.8\,\mathrm{Mm}$. Using this numerical setup, we excited the prominence oscillations only at the bottom, while the upper part of the prominence remained unperturbed. We then repeated the calculations of $v_\parallel$, as was done in Section 4.2. Figure 4.13 shows $v_\parallel$ at the selected field lines. We observe that the motions of the plasma at heights of $7.2 - 10.2\,\mathrm{Mm}$ are produced directly by the perturbation. These oscillations are significantly attenuated during the time interval shown in Figure 4.13. No perturbation has been applied for the field lines with $z > 10.2\,\mathrm{Mm}$, and therefore $v_\parallel$ at those field lines is initially zero. However, after 20 minutes of evolution, we observe a signature of oscillations with a small amplitude at the upper part. After 20 minutes, the oscillation fronts reach the top of the prominence, and their amplitude increases. At the time $100-150$ minutes, we can clearly see oscillation at $z > 10.2\,\mathrm{Mm}$. We also observe the phase shift of the signal between different heights, which resembles Figure 4.3. We additionally performed the opposite experiment perturbing the top region and leaving the bottom and central part without initial perturbation. The analysis of motions revealed a similar result, namely that the oscillations at the top drive the oscillations at the bottom layers of the prominence. This experiment seems to indicate that the transfer of energy could be symmetric. However, in the regular experiments where all the layers are excited simultaneously, the bottom part of the prominence drives the motion producing the amplification of the top part. The coupling of the oscillations of the different regions of prominence is a very interesting subject for future research.

In order to check if oscillation amplification is a common phenomenon of LALOs, we performed yet another experiment. Here, we did not use any external perturbation but instead loaded the prominence mass at some distance from the center of the magnetic dips. As the mass

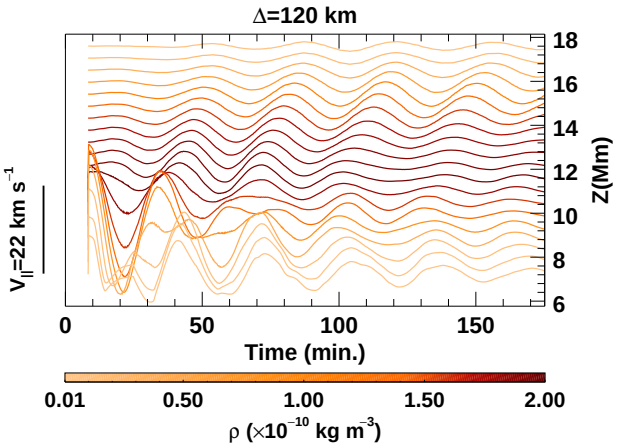

Figure 4.13: Temporal evolution of $v_{\parallel}$ at the center of mass of the selected field lines in the experiment with the perturbation at the bottom. The color bar denotes the maximum initial density at each field line. The left vertical axis indicates the velocity amplitude scale. The right vertical axis denotes the height of the dips of the field lines.

is not in equilibrium, it starts to move under the action of gravity in the direction toward the center of the dips. Thus, the plasma starts to oscillate around the equilibrium position, and the LALOs are established without any disturbance. We find that the resulting oscillations in this experiment are similar to those obtained in the previous experiments. Namely, we observe that the velocity at the top of the prominence increases while at the bottom of the prominence, it rapidly decreases. After several cycles of oscillations, the velocity of the plasma at the upper prominence region becomes high enough to allow plasma to leave the shallow dips. Consequently, the acceleration of the plasma at the top leads to mass drainage from the upper prominence region.

Summarizing all of above, we conclude that the effect of amplification of the plasma at the prominence top takes place in several alternative experiments, such as experiments where we perturb only the bottom part of the prominence or do not apply perturbation but place prominence in a nonequilibrium position. This means that the effect of amplification is a frequent ingredient of LALOs and deserves further investigation in the future.

4.4 Summary and Conclusions

We studied the properties of LALOs, including their periods and damping mechanism, based on 2D numerical simulations. We used a simple magnetic field configuration that includes a dipped region. After the mass loading in the dips, we applied a perturbation to the prominence. This perturbation was directed along the magnetic field. Our main goal was to investigate the physical mechanism of attenuation of the LALOs covered by the numerical diffusion. Therefore, we studied the oscillations in the same numerical model while gradually increasing spatial resolution, Δ.

We analyzed the prominence motions and computed the periods in the different prominence regions. The period of the oscillations shows an increase with height. We also find that the period

depends on Δ. In the higher resolution simulations, the period shows a strong dependence on height, while in the lower resolution experiments, this dependence is less pronounced. The period shows good agreement with the pendulum model in our simulations with the highest resolution, namely of 30 km.

We studied the damping of oscillations in different experiments and at different prominence regions. In all the experiments, the bottom part of the prominence is characterized by strong attenuation of oscillations. This attenuation is present even in the highest resolution experiments. The experiments with the finest resolution, $\Delta = 60$ and 30 km, demonstrated that further improvement of the spatial resolution does not significantly affect the damping time. This means that our experiments reached the resolution where the damping of oscillations is no longer associated with the numerical dissipation but is rather caused by some physical mechanism. In a real situation, additional effects such as thermal conduction and radiative losses also contribute to the damping. It is necessary to include these additional effects in order to understand which mechanism dominates in damping of the LALOs. This will be the subject of future research.

Our experiments revealed that oscillations at the prominence top are amplified during the first 130 minutes of simulations and are later slowly attenuated. The amplification appears to be more efficient and extended in time in the high-resolution experiments.

In order to explain the strong attenuation of oscillations at the prominence bottom and their simultaneous amplification at the prominence top, we analyzed the evolution of different types of energies in the corresponding regions. This analysis revealed that the damping of the oscillations is partially due to the collective work done by the gas pressure and Lorentz force. The energy is emitted in the form of fast magnetoacoustic waves. This result is in agreement with the findings of Zhang et al. (2019). Furthermore, we see that the damping of the oscillations is related to the strength of the magnetic field. The motion of the prominence plasma produces periodic changes in the magnetic field. We find that this effect leads to the generation of fast MHD waves. The time–distance diagram of the transverse velocity provides another piece of evidence for the wave leakage. The inclination of the wave front ridges found in the time–distance diagram is in agreement with the inclination predicted by the Alfvén speed. Yet another conclusion from our analysis is that the Lorentz force plays an important role in the damping and amplification of LALOs. While at the bottom, it contributes to the kinetic energy losses and acts to decelerate plasma, at the top of the prominence the work done by the Lorentz force is positive and provides the gain in energy needed for amplification of oscillations. The analysis of the Poynting flux revealed that a significant portion of the energy leaving the bottom part is transferred to the top. These results suggest that the energy losses in the lower region of the prominence are caused by both wave leakage and energy and momentum transfer to the upper prominence region.

Our study of LALOs based on 2D numerical simulations shows that high spatial resolution is crucial for investigating the periods of LALOs. The period agrees with the pendulum model only when the spatial resolution is sufficiently high. High spatial resolution is also important for understanding the damping of LALOs. On the other hand, the numerical dissipation can hide important physical mechanisms such as amplification of LALOs.

In the future, it will be useful to study the attenuation and amplification mechanisms further using high-resolution experiments with more complex 3D setups, which would allow us to take the mechanism of resonant absorption into consideration. Furthermore, it is also desirable to include nonadiabatic effects. This could allow us to study the relative importance of the mechanisms described in this paper with respect to the resonant absorption and nonadiabatic effects. On the other hand, more observations are needed to further study the phenomena of the amplified prominence oscillations.

5

Large-amplitude oscillations in solar prominences triggered by external perturbations

Several energetic disturbances have been identified as triggers of the large-amplitude oscillations (LAOs) in prominences (Section 1.3). Observations show that Moreton or EIT waves excite prominence oscillations of the longitudinal, transverse, or even mixed polarities (see Section 1.5). However, the mechanisms for the LAOs excitation by these waves are not well understood. These waves are usually associated with CMEs or eruptions (Biesecker et al. 2002; Chen 2006, 2011). It is widely accepted that the Moreton wave is a fast-mode wave that propagates in the chromosphere and the low corona. Initially, EIT waves were explained as a coronal counterpart of the Moreton waves (Thompson et al. 1998; Wang 2000). However, this interpretation contradicted the observed velocities of these waves. EIT waves usually have velocities approximately three times smaller than the velocities of the Moreton waves. More importantly, it has been found in observations that the EIT fronts can be stationary, implying that the fronts can be trapped in the magnetic arcades slowing down there and finally stopping close to quasi-separatrix layers (QSL) (Delannée & Aulanier 1999; DeVore & Antiochos 2000). It suggests that these EIT waves have a different physical interpretation because the fast-mode is expected to propagate through separatrix. Since then, different explanations have been proposed for the EIT waves, such as magnetic field line stretching model (Chen et al. 2002, 2005), successive reconnection model (Attrill et al. 2007), the slow-mode wave model (Wills-Davey et al. 2007), and the current shell model (Delannée et al. 2008). Interesting events were observed when EIT waves interact with different magnetic objects in the corona, such as streamers, cavities, coronal holes, or loops (Srivastava et al. 2016; Zong & Dai 2017; Shen et al. 2018a,b; Liu et al. 2019; Zheng et al. 2019; Shen et al. 2019; Fulara et al. 2019; Hu et al. 2019; Chandra et al. 2021). Previously, in Section 1.5, we described several observations of coronal waves interacting with prominences and, in some of them, exciting oscillatory motions. From the theoretical point of view, the interaction of the coronal waves with the magnetic features has also been studied in the numerical simulations (Piantschitsch et al. 2017; Afanasyev & Zhukov 2018; Xie et al. 2019; Mei et al. 2020). However, none of the numerical studies can yet explain all the aspects of the interaction of the coronal waves with the prominence structures. It also remains unclear how the modes of different polarizations can be excited by such interaction.

In this chapter, we describe our preliminary results from three experiments associated with the triggering of prominence oscillation by external perturbations. In numerical experiments,

the energetic disturbances can be generated self-consistently or artificially. Recently, Luna & Moreno-Insertis (2021) provided the numerical experiment of an energy release process in a magnetic structure, resulting in the excitation of the large-amplitude longitudinal oscillations (LALOs). In contrast to this work, Liakh et al. (2020) employed the triggering by an artificial perturbation placed at some region of the numerical domain in order to mimic a real energetic disturbance, such as a distant flare. In Section 5.1, we describe the experiments where the external perturbation is self-consistent caused by an eruption of a nearby flux rope. After that, in Section 5.2, we show the experiment where an energetic wave is produced artificially and impacts on two flux rope prominences that are placed at different distances from the perturbation location. Finally, in Section 5.3, we describe the interaction of a distant artificial disturbance with a dipped arcade magnetic field and the prominence located in the magnetic dips.

5.1 Self-consistent perturbation associated with an erupting flux rope

We study the triggering of the prominence oscillations by the neighboring eruption by means of 2.5D numerical simulations using the MANCHA3D code. The 2.5D approximation implies that all the vectors have three spatial components, but the perturbation is only allowed to propagate in the XZ-plane. In this section, we explain the numerical setup that is similar to the one we used in Chapter 3. We form the flux rope structures from the sheared arcades using the converging motions alone or combining them with the shearing motions. In these numerical experiments, we first form a prominence-hosting flux rope using only the converging motions at the foot points. Once the flux rope is formed, we load the prominence mass in the dipped region. We then start to form an erupting flux rope using both the converging and shearing motions until this flux rope becomes unstable and erupts. The eruption in this numerical setup is based on the standard solar flare model, whose main ingredients are the flux rope and magnetic reconnection underneath it. A detailed description of the standard solar flare model can be found in Martens & Kuin (1989).

5.1.1 Numerical model

The numerical domain consists of 2400×3200 grid points, corresponding to the physical size of $576\,\mathrm{Mm} \times 768\,\mathrm{Mm}$ (a spatial resolution of $0.24\,\mathrm{Mm}$). As in all the previous numerical experiments, we used the Cartesian coordinate system with z- and x-axes corresponding to the vertical and horizontal directions, respectively. The numerical domain is shown in Figure 5.1. The flux rope that hosts the prominence (FR1) is formed at $x = -96\,\mathrm{Mm}$, and the erupting flux rope (FR2) is formed at $x = 0\,\mathrm{Mm}$.

Initial equilibrium

The initial atmosphere is an isothermal corona with a temperature of $T = 1.5$ MK, gravitationally stratified along the vertical direction with a density at the bottom of the numerical domain of $\rho = 2.12 \times 10^{-12}$ kg m^{-3}. The thermal conduction is not taken into account, but we included the radiative losses during the stage of the FR1 formation.

The initial atmosphere is permeated by a force-free magnetic field represented by a periodic sheared arcade. The components of the magnetic field are defined in Section 2.1.3. We consider the lateral extension $L = 48\,\mathrm{Mm}$, the magnetic scale height $H_b = 118\,\mathrm{Mm}$ and the magnetic field strength at the bottom, $B_0 = 10$ G. Using these parameters in Equation (2.41), we obtain the shear angle $\theta = 75\,^\circ$, which is the angle between the arcade field and x-axis. The initial magnetic field in the 2D projection is shown in Figure 5.1. As we can see, several identical magnetic arcades

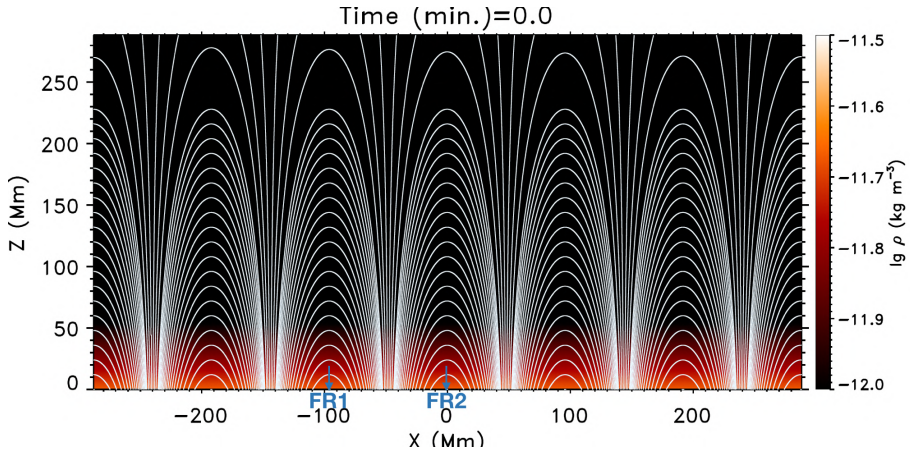

Figure 5.1: Density distribution and magnetic field configuration in the initial atmosphere. The blue arrows mark the positions where the flux ropes are formed.

are nested in the numerical domain. As we use the periodic system, we increase the horizontal extension of the domain in order to reduce the perturbation coming from the side boundaries.

Flux rope formation

The dense prominence plasma is supported against the gravity by the Lorentz magnetic force of the concave-up magnetic field (i.e., the dips; Kippenhahn & Schlüter 1957; Kuperus & Raadu 1974). Initially, we have the magnetic field that does not contain the dipped region (see Figure 5.2(a)). We then use the van Ballegooijen & Martens (1989) mechanism for the flux ropes formation from the sheared arcades as applied, for example, in the numerical experiments by Kaneko & Yokoyama (2015). For the FR1, we only used the converging motions at the foot points in the direction along the PIL (see purple arrows in Figure 5.2). The horizontal velocity imposed at the base is given by

$$V_x(x,t) = -V_0(t)\sin\left[\frac{2\pi(x-x_1)}{W}\right]\exp\left[-\frac{(x-x_1)^2}{2\sigma^2}\right], \tag{5.1}$$

where $W = 576.0\,\mathrm{Mm}$ defines the horizontal extension of the domain, $x_1 = -96\,\mathrm{Mm}$ is the central position of the function that is centered at the PIL and $\sigma = 13.6\,\mathrm{Mm}$ is the half-width of the converging region. We additionally set the V_y and V_z velocity components to zero at the bottom of the domain. The activation and deactivation of the convergence are controlled by a function $V_0(t)$:

$$V_0(t) = V_{conv}\left\{0.5\left[\mathrm{erf}\left(\frac{t-2\lambda-t_1}{\lambda}\right)+1\right] - 0.5\left[\mathrm{erf}\left(\frac{t-2\lambda-t_2}{\lambda}\right)+1\right]\right\}, \tag{5.2}$$

where $V_{conv} = 12\,\mathrm{km\,s^{-1}}$ is the maximum converging velocity. The flux rope is formed during the time defined by the parameters $t_1 = 100\,\mathrm{seconds}$ and $t_2 = 4000\,\mathrm{seconds}$. The parameter

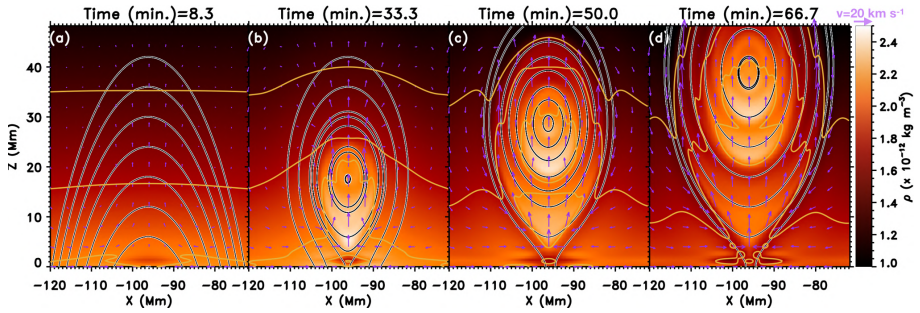

Figure 5.2: Evolution of the density and the magnetic field lines during the FR1 formation. The yellow lines denote the density isocontours. The purple arrows show the velocity field. Note that field lines in the different panels are not the same field lines carrying the same plasma. They are drawn to reflect the topological structure of the magnetic field at a given time moment.

$\lambda = 150$ seconds is responsible for the smoothness in time of activation and desactivation of the converging process. As explained in Chapter 3, due to the converging process, the temperature starts to increase inside the flux rope. This leads to an increase in the gas pressure and, consequently, of the plasma-β. In order to avoid this heating of the plasma in the prominence-hosting FR1, we use the Newton's cooling law given by

$$Q_{\rm R} = -c_v \rho_0 \frac{T_1}{\tau_{\rm R}}, \tag{5.3}$$

where T_1 is the perturbation of the temperature, ρ_0 is the initial density, $\tau_{\rm R}$ is the radiative relaxation time that is equal to 3 seconds everywhere in the domain, and c_v is the specific heat at constant volume. We use radiative cooling only during the formation of the FR1 up to time $t = 4000$ seconds. These radiative losses allow us to maintain the temperature equal to the initial one, i.e., 1.5 MK, everywhere in the domain.

In Figure 5.2 different stages of the formation are shown. Figure 5.2(a) shows the initial field of the magnetic arcade. Figure 5.2(b) shows how the foot points of the field lines move toward $x = -96$ Mm following Equation (5.1). When the field lines approach each other, they reconnect, forming a twisted flux rope. As we continue the converging process, the flux rope slowly rises to the higher positions (Figures 5.2(c) and 5.2(d)). In order to prevent the eruption of the FR1, we stopped the convergence at $t = 66.7$ min, when the center of the flux rope is located at the height of 39 Mm, approximately (see Figure 5.2(d)). The magnetic field strength in the dipped region ranges between $7 - 9$ G. In Figures 5.2(b)-5.2(d), we can see that the rising flux rope has a slightly increased density inside the dipped region which implies that the flux rope lifts some plasma from the lower atmosphere. In the recent 2.5D numerical study, Jenkins & Keppens (2021) showed in more detail the process of the prominence formation in the levitation-condensation models, as the one considered here. Unlike our case, their model included a portion of the chromosphere in the simulation domain. This can explain a larger density contrast of the lifted plasma in work by Jenkins & Keppens (2021) compared to our model.

As mentioned before, the eruption of the FR2 plays the role of the main trigger in this experiment. As we aim to produce an energetic eruption, we included the shearing motions in addition to the converging ones. This allows us to increase the shear angle and, consequently, the axial component of the magnetic field B_y. Now, the V_x and V_y components of the velocity

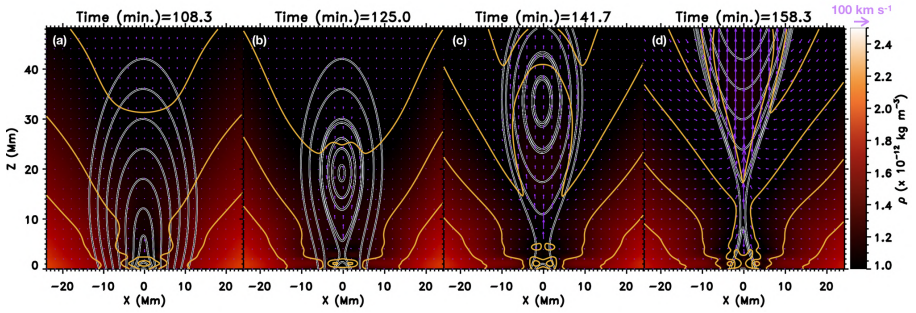

Figure 5.3: Evolution of the density and the magnetic field lines during the FR2 formation due to the converging and shearing motions at the base. The yellow lines denote the density isocontours. The purple arrows show the velocity field. Note that field lines in the different panels are not the same field lines carrying the same plasma. They are drawn to reflect the topological structure of the magnetic field at a given time moment.

at the bottom of the domain are defined as follows

$$V_x(x,t) = - V_0(t)\sin\left[\frac{2\pi(x-x_2)}{W}\right]\exp\left[-\frac{(x-x_2)^2}{2\sigma^2}\right], \tag{5.4}$$

$$V_y(x,t) = V_0(t)\sin\left[\frac{2\pi(x-x_2)}{W}\right]\exp\left[-\frac{(x-x_2)^2}{2\sigma^2}\right], \tag{5.5}$$

where $W = 576\,\mathrm{Mm}$, and $x_2 = 0\,\mathrm{Mm}$ is the central position located at the PIL and $\sigma = 13.6\,\mathrm{Mm}$ is the half-size of the converging and shearing regions. The vertical V_z velocity component remains zero at the bottom of the domain. The temporal evolution is defined by the following expression:

$$V_0(t) = V_{max}\left\{0.5\left[\mathrm{erf}\left(\frac{t-2\lambda-t_3}{\lambda}\right)+1\right] - 0.5\left[\mathrm{erf}\left(\frac{t-2\lambda-t_4}{\lambda}\right)+1\right]\right\}, \tag{5.6}$$

where V_{max} is either the maximum converging velocity $V_{conv} = 4\,\mathrm{km\,s^{-1}}$, or maximum shearing velocity, $V_{shear} = 18\,\mathrm{km\,s^{-1}}$. The rest of the parameters are $t_3 = 4000$ seconds, $t_4 = 10000$ seconds, and $\lambda = 150$ seconds. The FR2 is formed in absence of radiative losses.

Figure 5.3 shows the formation process of the FR2 after the formation of the FR1. It can be noted that the evolution slightly differs from the evolution of the FR1. Since we use the shearing motions together with the converging ones, the shear angle of the magnetic structure increases. Figure 5.3(b) shows that the FR2 has more elliptical magnetic field lines than in the case of the FR1 in the 2D projection that is related to the increased axial magnetic field. From Figure 5.3(d), we can see the onset of the flux rope eruption at around $t = 158$ minutes. The velocity field shows a large upward velocity in the flux rope associated with its rise.

We used symmetric (for $V_x, V_y, B_z, p, \rho, T, e_{int}, e$) or antisymmetric (for V_z, B_x, B_y) boundary conditions at the top boundary. The system is assumed to be periodic at the side boundaries. At the bottom, the magnetic field evolves according to the velocity field during the flux ropes formation process. Later on, the line-tied conditions are applied using zero velocities. The rest of the variables are assumed to be symmetric at the bottom boundary.

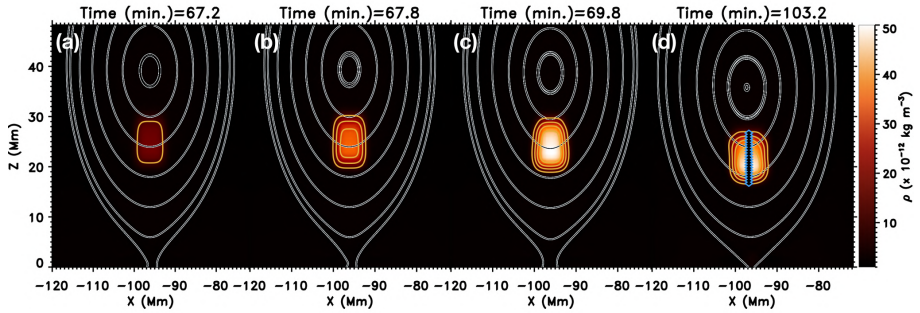

Figure 5.4: Evolution of the density and the magnetic field lines during and after the mass loading process. The yellow lines denote the density isocontours. In panel (d), the sequence of the blue diamonds shows the positions of the fluid elements used for the analysis of motions. Note that field lines in the different panels are not the same field lines carrying the same plasma. They are drawn to reflect the topological structure of the magnetic field at a given time moment.

Mass loading and relaxation

After the formation of the FR1, we load a prominence in the dips of the flux rope as in Section 3, adding a source term in the continuity equation as:

$$S_\rho = \frac{\chi\rho_0}{t_{\rm load}} \exp\left(-\frac{(x-x_p)^4}{\sigma_x^4} - \frac{(z-z_p)^4}{\sigma_z^4}\right). \tag{5.7}$$

The ρ_0 and χ parameters are the background density and the density contrast, respectively. The mass is loaded during the time $t_3 = 4000$ seconds and $t_4 = 4100$ seconds and the time parameter $t_{load} = t_4 - t_3 = 100$ seconds is associated with the loading rate. The spatial parameters $x_p = -96$ Mm, $z_p = 25.4$ Mm are coordinates of the center of the distribution and $\sigma_x = 3.6$ Mm, $\sigma_z = 4.8$ Mm are related to the half-size of the mass distribution region. In this study, we consider the density contrast, $\chi = 30$.

Figures 5.4(a)-5.4(c) show that during the mass loading process, the flux rope center drops down by a few Mm to find a new equilibrium position. The magnetic configuration accommodates the heavy mass against the gravity in the dipped region. After the mass loading, the system evolves for 16.7 minutes freely. During this time, the system relaxes and settles in a quasi-equilibrium (Figure 5.4(d)) with small vertical oscillations. This relaxation time is necessary in order to avoid a possible influence of the mass loading process in the posterior dynamics of the system.

5.1.2 Evolution of the eruption

When we stop the shearing and converging motions around $x = 0$ Mm at $t = 166.7$ minutes, the FR2 has already reached the critical height where its loss of equilibrium and eruption are unavoidable. Therefore, the FR2 continues moving upwards even if we deactivate the velocities at the foot points. Figure 5.5 shows the rising flux rope at the different times. Comparing the velocity fields in Figures 5.5(a)- 5.5(c), we can see that the flux rope is strongly accelerated during its rise. At the time 186.7 minutes, the velocity of the eruption is around 300 km s^{-1}. From Figure 5.5(d), we can see that the flux rope has slightly decelerated in comparison to

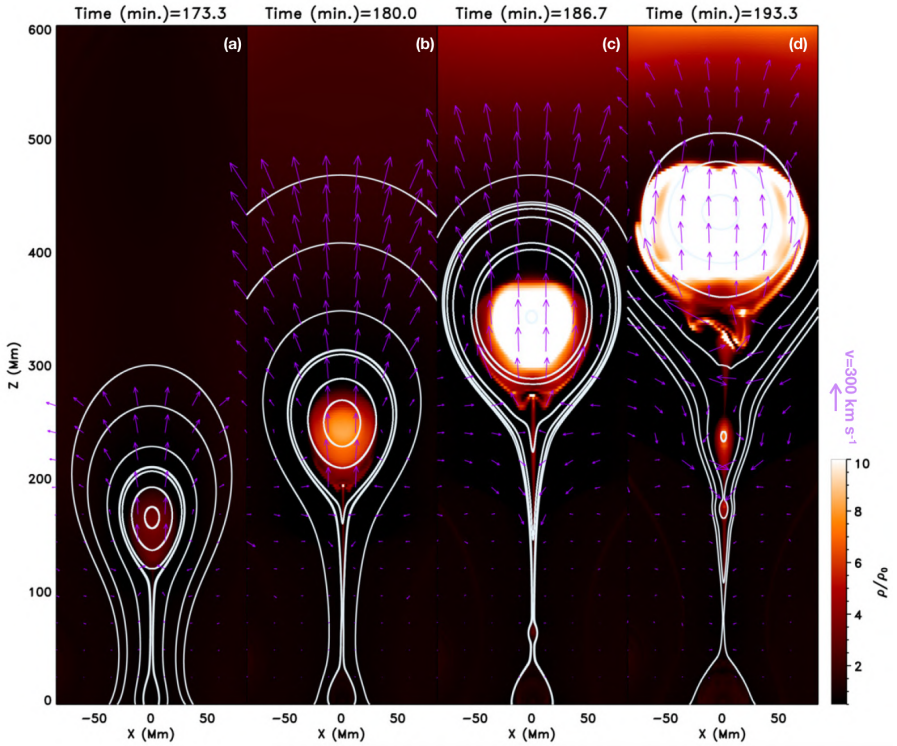

Figure 5.5: Evolution of the density contrast and the magnetic field lines during the eruption of the FR2. The purple arrows denote the velocity field. Note that field lines in the different panels are not the same field lines carrying the same plasma. They are drawn to reflect the topological structure of the magnetic field at a given time moment.

5.5(c). The density contrast shows that the flux rope carries inside the denser plasma than the surrounding plasma. Above the flux rope, we can see a reduced density region, the so-called dimming region (Moses et al. 1997; Thompson et al. 1998). On the contrary, slightly above the dimming region, we can see the area of the enhanced density that is formed when the flux rope rises, pushing the plasma above it. By comparing this behavior with the previous numerical simulations, we know that this region of enhanced density is associated with the propagation of the EIT front (see, e.g., Chen et al. 2002).

In Figure 5.5, the white lines show the magnetic field that strongly evolves during the rise of the FR2. The width of the flux rope grows, and its field lines become less elliptical. Below the flux rope, a vertical current sheet is formed, and its size increases while the eruption develops. Underneath the vertical current sheet, the loops are formed as a consequence of the reconnection of the field lines. In Figures 5.5(b)-5.5(d), we see that during the process, more field lines are reconnected, and the region of the post-reconnection loops expands at both sides of the PIL. Figures 5.5(c) and 5.5(d) show that the current sheet is fragmented due to the development of the magnetic islands, the so-called plasmoids. As seen from this figure, these plasmoids are mini

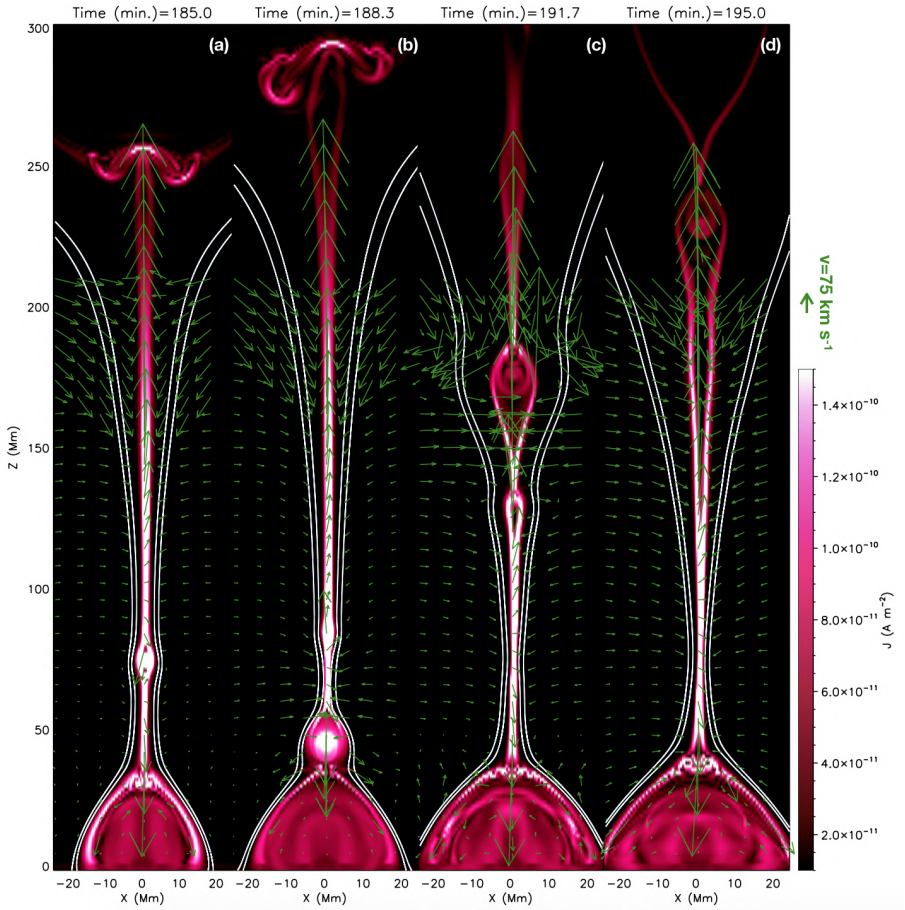

Figure 5.6: Current density distribution and magnetic field lines underneath the erupting FR2. The green arrows denote the velocity field.

flux ropes and have an increased density contrast. We can compare our study with the work by Zhao et al. (2017, 2019), who studied the properties of the standard solar flare model using 2.5D numerical simulations. It was shown that the plasmoids formation leads to a decrease in the density of the current sheet, suggesting that the plasmoids transport dense material upwards and downwards along the current sheet.

Figure 5.6 represents a closer look at the current sheet during the flux rope rise. The current sheet becomes fragmented due to the appearance of the plasmoids at the time 185 minutes. The first plasmoid forms at the height of $60 - 70$ Mm and starts to propagate downwards in the direction to the post-reconnection loops (Figures 5.6(a) and 5.6(b)). Figures 5.6(c) and 5.6(d) show the propagation of the plasmoids in the opposite direction to that of the flux rope. Later on, the magnetic islands are chaotically formed and propagate both upwards and downwards, in the

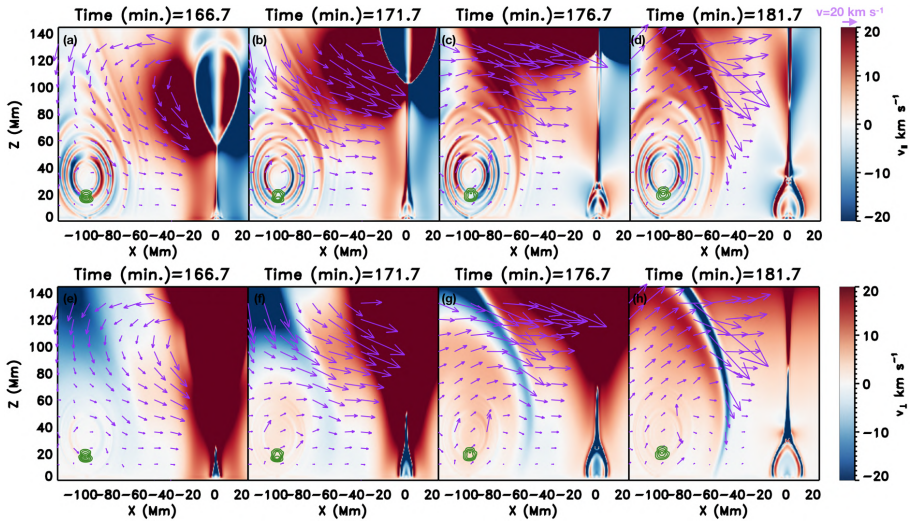

Figure 5.7: Evolution of $v_{\parallel}$ (top panel) and $v_{\perp}$ (bottom panel) in the region of the FR1 during the FR2 eruption. The purple arrows denote the velocity field. The green lines show the density isocountours.

direction of the flux rope or the post-reconnection loops, respectively. The velocity field shows the perturbations associated with the motion of the plasmoids. In Figure 5.6(b), we see that the plasmoid approaches the loops at the bottom with a large velocity. This plasmoid merges with the post-reconnection loop structure producing an important perturbation. In this way, the plasmoids can produce additional disturbances that can affect the surroundings, including the nearby flux rope prominence. From this figure, we can also observe that the surrounding plasma is driven inwards towards the current sheet.

In this experiment, our aim was to excite oscillations in the FR1 by the nearby activity produced either by the eruption of the FR2 itself or by the motions of the plasmoids in the current sheet. In the following subsection, we will explore the mechanisms that caused the excitation of oscillations in the FR1. As described above, the flux rope erupts at time 166.7 minutes. It propagates quickly upwards, reaching greater heights. Thus, this front cannot directly affect the FR1 and its prominence. This front, which we initially anticipated as a possible candidate to excite oscillations, develops at higher heights and does not affect the prominence. In contrast, once the vertical current sheet is formed at $t > 185$ minutes, the magnetic islands are produced, and the FR1 can be disturbed by these plasmoids starting from this time. In the following, we describe how the prominence mass responds to each of these disturbances.

5.1.3 Perturbation caused by eruption

Figures 5.7(a)-5.7(d) show the evolution of velocity component along the magnetic field, $v_{\parallel}$, defined by Equation (2.151), in a region that includes both flux ropes. The time sequence is taken during the onset of the eruption. Figure 5.7(a) shows the moment when the center of the flux rope reached the height of 100 Mm, approximately. In this figure, we can see that the eruption produces velocity disturbances around it. Above the FR2, we see the diverging flow,

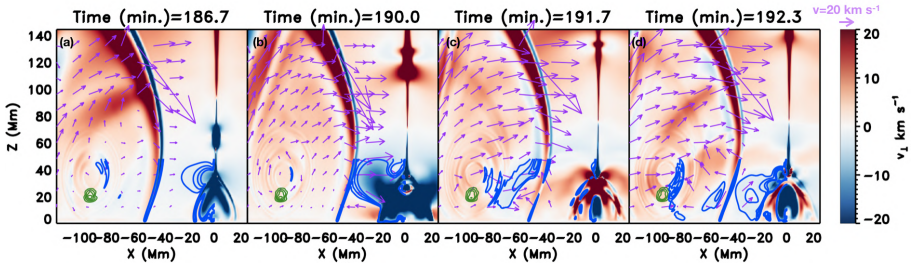

Figure 5.8: Evolution of $v_\perp$ in the region of the FR1 during the magnetic islands formation in the current sheet of the FR2. The purple arrows denote the velocity field. The green lines show the density isocountours.

implying the rarefaction of the plasma above the erupting flux rope (Figures 5.5(c) and 5.5(d)). Right below the FR2, the situation is the opposite. Instead of diverging flow, we see the strong converging motions in direction to $x = 0$ Mm. The diverging flow above and the converging flow below the FR2 lead to the counterclockwise flow at the left side of the flux rope, as is shown by the purple arrows. However, FR2 reaches higher positions and the influence of the flows around the FR2 decreases (Figure 5.7(b)-5.7(d)). However, a converging flow remains directed to the current sheet associated with the reconnection process (Figure 5.7). Comparing the position of the FR1 in panel (a) and panel (d), we can see that the flux rope is inclined in the direction of the current sheet due to the influence of the converging flow. The inclination of the rope displaces the bottom of the dips to the right, also moving the prominence plasma.

Figures 5.7(e)-5.7(h) show the transverse velocity, $v_\perp$, defined by Equation (2.151), during the propagation of the eruption. The panels of this figure show the motion of the FR2 in the transverse direction with respect to the overlaying magnetic arcades. The dark-red region corresponds to the largest velocity of the upward propagation of the FR2. In these panels, we do not see any wave-like front propagation perpendicularly to the magnetic field as expected for the fast-mode perturbation. The fast-mode wave can still be present in our experiment, but perhaps due to its low intensity with respect to the other disturbances, we cannot observe it in this figure.

5.1.4 Perturbations caused by plasmoids

At $t = 185$ minutes, the first magnetic islands start to form in the current sheet. In this section, we aim to understand the perturbations created by the plasmoids when they reach the region of the post-reconnection loops. Another interesting question is whether these plasmoids create the disturbances able to propagate across the magnetic field, reaching another magnetic flux region such as the FR1. Figure 5.8(a) shows a recently formed plasmoid that starts to move downwards. When it approaches the loops at the bottom, it creates a perturbation clearly seen in Figure 5.8(c). In order to follow the wave front created by this perturbation, we added the velocity isocontours to the figure (see blue lines). We can observe in Figures 5.8(c) and 5.8(d) that the left part of the wave front moves toward the FR1 and the prominence mass. Figure 5.8(c) shows that this front from the disturbance enters the region of the FR1. At $t = 192.3$ minutes, this wave front also reaches the prominence mass as seen in Figure 5.8(d). This affects the prominence mass and may some motions in it. This figure only illustrates the behavior of a single plasmoid that moves downwards. However, multiple disturbances can be produced at the

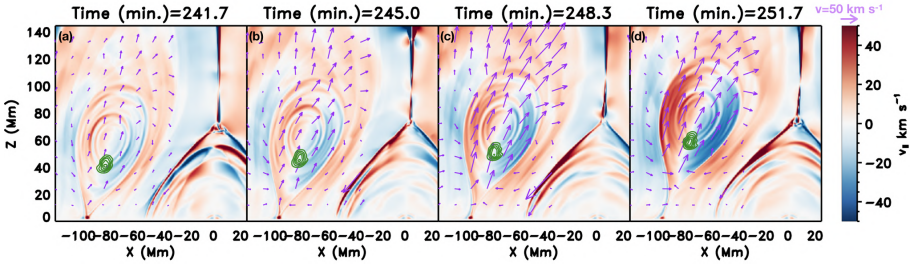

Figure 5.9: Evolution of $v_{\parallel}$ during the eruption of the FR1. The purple arrows denote the velocity field. The green lines show the density isocountours.

stage of the chaotic formation of the magnetic islands. Anther plasmoid located higher in the current sheet is shown in Figures 5.8(b)-5.8(d). This plasmoid propagates upwards, and it seems that its motion does not affect the FR1.

5.1.5 Eruption of the prominence-hosting flux rope

As shown by the velocity field in Figure 5.7, the converging flow in the direction to the current sheet is continuously affecting the FR1. This disturbance pulls the FR1 up and to the right. At the time 241.7 minutes, the FR1 becomes unstable and starts to rise in the direction of the current sheet. In Figures 5.9(a)-5.9(d), we can see the evolution of the longitudinal velocity. These panels show the converging flow below the flux rope and diverging flow above it. This resembles the onset of the eruption of the FR2, although due to the inclination of the FR1, the diverging region is not so symmetric with respect to the flux rope axis. Later on, the FR1 continues moving upward and to the right. Figure 5.9(d) shows that the current sheet starts to form below the FR1. During the time-interval shown in this figure, the FR1 is greatly accelerated upwards, and its center reaches the height of around 80 Mm.

5.1.6 Prominence oscillations

As shown before, the FR1 is significantly influenced by the dynamics of the FR2. These dynamics create significant changes in its magnetic field structure. In a situation with a stable magnetic field, we could analyze motions of the center of mass of the different field lines. In contrast, in our situation it is more convenient to use an approach associated with the analysis of corks (Section 2.4.1). We study the motion of the selected fluid elements by integrating the velocity field at each time iteration. The initial positions of the corresponding corks are shown in Figure 5.4(d). The plasma elements have the initial coordinates from $(x, z) = (-96, 16.8)$ to $(-96, 26.8)$ Mm. We start to follow the fluid elements when the FR2 erupts at $t = 166.7$ minutes.

Figure 5.10 shows the evolution of the longitudinal and transverse velocities up to the time of the eruption of the FR1. Considering the first phase of the temporal evolution up to 185 minutes, we see only a small variation of the velocity around $1 - 2\,\mathrm{km\,s^{-1}}$ in the denser part of the prominence. The longitudinal velocity indicates that the plasma moves from the equilibrium position along the magnetic field (top left panel). The transverse velocity shows a small increase at all of the field lines (bottom left panel). These variations of both longitudinal and transverse velocity occur due to the inclination of the FR1 shown in the panels of Figure 5.7. As mentioned before, the converging flows below the erupting flux rope and around the current sheet significantly affect the FR1 producing its inclination towards the $x = 0$ Mm axis.

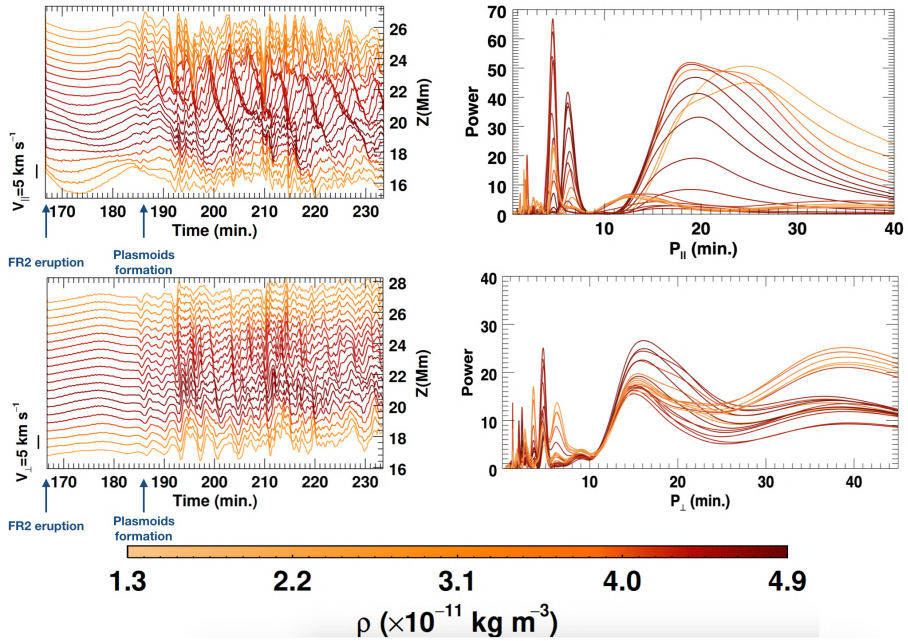

Figure 5.10: Left panels: temporal evolution of $v_{\parallel}$ (top) and $v_{\perp}$ (bottom) of the fluid elements shown with blue diamonds in Figure 5.4(d) after the eruption of the FR2. Right panels: the periodograms of the $v_{\parallel}$ (top) and $v_{\perp}$ (bottom) in time-interval 187-233 minutes. The color bar denotes the density of the fluid elements. The left vertical axis indicates the velocity amplitude scale. The right vertical axis denotes the initial vertical positions of the fluid elements.

After time $t = 185$ minutes, the multiple peaks can be seen at the top left and bottom left panels of Figure 5.10. This coincides in time with the development of the instability in the current sheet and the formation of the magnetic islands. It is noticeable that the plasmoids produce more significant perturbation of the prominence than the eruption of the FR2 itself. However, both panels show that these prominence motions are small-amplitude oscillations (SAOs) rather than LAOs. The $v_{\parallel}$ shows the complex dynamics (upper left panel) with motions that combine the different oscillatory modes. The upper right panel shows the periodogram obtained for $v_{\parallel}$ using the Lomb-Scargle algorithm (Lomb 1976; Carbonell & Ballester 1991) for the time-interval 187-233 minutes when the plasmoids appear. We can observe that the longitudinal oscillations are dominated by the short-period modes with periods in the range of $2 - 6.5$ minutes. We can also see the peaks in the periodogram that correspond to the long-period oscillations. The period ranges between $12.5 - 24$ minutes. It can be noted that a certain shift of the long-period peaks is present for the different field lines. This reflects the shift of the signal of $v_{\parallel}$ at the different field lines seen in the upper left panel.

The bottom left panel of Figure 5.10 illustrates $v_{\perp}$, and it can be observed that the vertical SAOs are present at every field line. We can see that the dynamics are very complex, with several different periodicities. It is noticeable that the transverse oscillations are more coherent with height than the longitudinal oscillations. The corresponding periodogram also shows a variety of

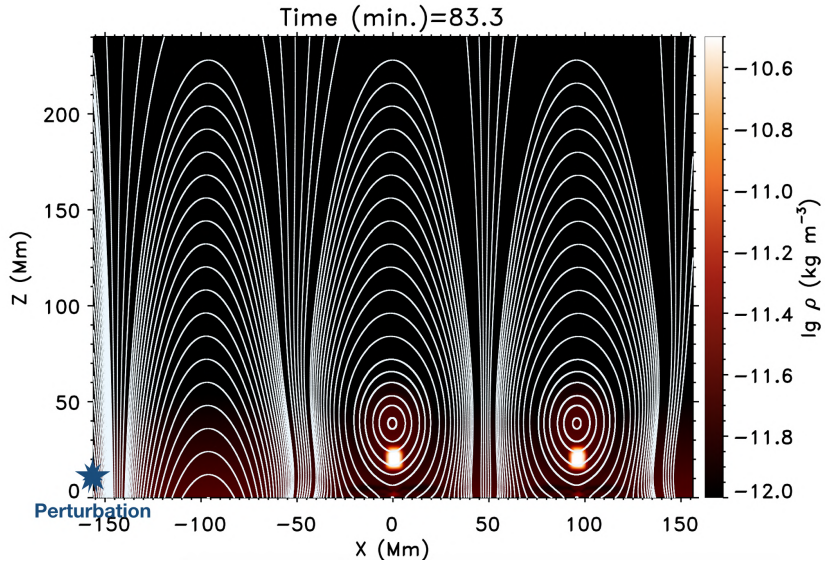

Figure 5.11: Density distribution at the central part of the numerical domain immediately before applying the external disturbance. The white lines show the magnetic field lines. The position of the external disturbance is also shown at the bottom left.

the periods that are present in the signals. The dominant period has a value of 16 minutes for all the field lines. While this periodicity is not very evident directly from the $v_\perp$ plot (bottom left), it can be masked by the other signals. Another important peak in the periodogram corresponds to the short-period oscillations with a period of 5 minutes.

5.2 Impact of external perturbation on distant prominences

The motivation of this section comes from the interesting observations of Shen et al. (2014a). The authors reported the oscillations of the sequence of the filaments excited by the same wave coming from a flare. Therefore, we aim to understand how such a perturbation propagates in the magnetic environment reaching two filaments located at a different distance from the flare. Additionally, we aim to study the polarization of the oscillations which can be excited in this way. For this, we use the numerical model based on the one described in the previous section, except for two differences. First, both flux ropes are formed with only the converging motions at $x = 0$ and $x = 96\,\mathrm{Mm}$, and they both host prominences. Second, instead of producing an eruptive event to perturb the prominences, we used the source term in the energy equation as described in Section 3.3. We then study how the disturbance propagates in the magnetic environment and can excite the prominence motions in the closer and further flux ropes. In this experiment, the source term in the energy equation is defined by the expression:

$$S_e = \frac{\alpha}{t_{\mathrm{pert}}} \exp\left(-\frac{(x - x_{\mathrm{pert}})^2}{\sigma_x^2} - \frac{(z - z_{\mathrm{pert}})^2}{\sigma_z^2}\right), \tag{5.8}$$

where the parameter $\alpha = 2\ \mathrm{J\ m^{-3}}$, and the rest of parameters $t_{\mathrm{pert}} = 50\,\mathrm{seconds}$, $x_{\mathrm{pert}} = -151.2\,\mathrm{Mm}$, $z_{\mathrm{pert}} = 12\,\mathrm{Mm}$, $\sigma_x = \sigma_z = 12\,\mathrm{Mm}$ correspond to the half-size and the x- and

z-coordinates of the center of the perturbation, respectively. The positions of the prominence-hosting flux ropes and the location of the perturbation are shown in Figure 5.11. The numerical domain extends from $x = -288$ to $x = 288$ Mm. On the one hand, this allows us to choose the perturbation position at the significant distances from the flux ropes to mimic a distant flare (see Figure 5.11). On the other hand, the source of the disturbance is located far enough from the boundaries. As we use a periodic system, when the perturbation reaches the left boundary, the undesirable perturbation appears on the other side of the domain. Thus, by choosing the current position, the disturbance is located at the optimal position with respect to the flux ropes and the left boundary.

5.2.1 Propagation of the perturbation

It is expected that the external perturbation will produce a complex pattern of interacting wave modes. Furthermore, the energy release causes a nonlinear perturbation so that the situation can be even more complex. One of the ways to separate the modes was proposed by Cally (2017) and Khomenko et al. (2018); Khomenko & Cally (2019) and it is based on the construction of the following quantities:

$$f_{\rm long} = \mathbf{e}_\parallel \cdot \nabla v_\parallel \,, \tag{5.9}$$

$$f_{\rm fast} = \nabla \times \mathbf{v}_\perp \,, \tag{5.10}$$

$$f_{\rm alf} = \mathbf{e}_\parallel \cdot \nabla \times \mathbf{v} \,, \tag{5.11}$$

where, $\mathbf{e}_\parallel = \mathbf{B}/B$ is a unit-vector directed along the magnetic field, $v_\parallel$ and $v_\perp$ are the longitudinal and transverse velocities defined by Equations (2.151). This decompostion allows to separate incompressible perturbation along the magnetic field lines using Equation (5.11). As we consider low-β plasma, the decomposition allows us also to distinguish the slow and fast modes due to anisotropy in the propagation direction.

Figures 5.12 and 5.13 show $f_{\rm long}$ normalized to $\sqrt{\rho_0 c_s}$ (left column) and $f_{\rm fast}, f_{\rm alf}$ normalized to $\sqrt{\rho_0 v_A}$ (right column and Figure 5.13, respectively), where ρ_0, c_s, and v_A are the density, the sound and Alfvén speed of the initial atmosphere. Figure 5.12(a) shows the initiation of the disturbance. The source in the energy equation causes the disturbance that propagates in all directions, as is shown by the purple arrows. Panels (b)-(d) show the propagation of the slow-mode wave. After the initiation, the wave front starts to move along the vertical magnetic field. In Figure 5.12(b), the wave front reaches the height of 60 Mm, approximately. In panels (c) and (d), we observe the corresponding wave front as a very thin structure at the height of 160 Mm and 210 Mm, respectively. The comparison between these panels allows us to estimate the velocity of propagation of this front, which comes to be around 575 km s^{-1}. This value significantly exceeds the value of the local sound speed of 180 km s^{-1}. Therefore, this disturbance is significantly supersonic, and we can observe the formation of the shock front in panels (c) and (d).

Figures 5.12(e) and 5.12((f) show the initial propagation of the fast-mode wave from the perturbation region. We can observe how the wave front moves across the magnetic field of the nearby arcades in panel (f). Figure 5.12(g) shows the moment when the fast-mode wave passes the flux rope at $x = 0$ Mm. This closer flux rope appears to be pushed down and slightly inclined to the left by the front. As can be noticed, this front affects the magnetic field considerably. Due to its propagation, the vertical magnetic field lines at $x = -48$ Mm and the magnetic arcades around the flux rope at $x = 0$ Mm are strongly deformed. At the same time, we do not observe any significant displacement of the prominences mass. This can suggest that the wave front does not move the prominence mass directly. However, it significantly affects the hosting magnetic field. Due to the frozen-in condition, we can expect the prominence motions as the secondary effect of the perturbation. In Figures 5.12(h), one can observe that the front reaches the second

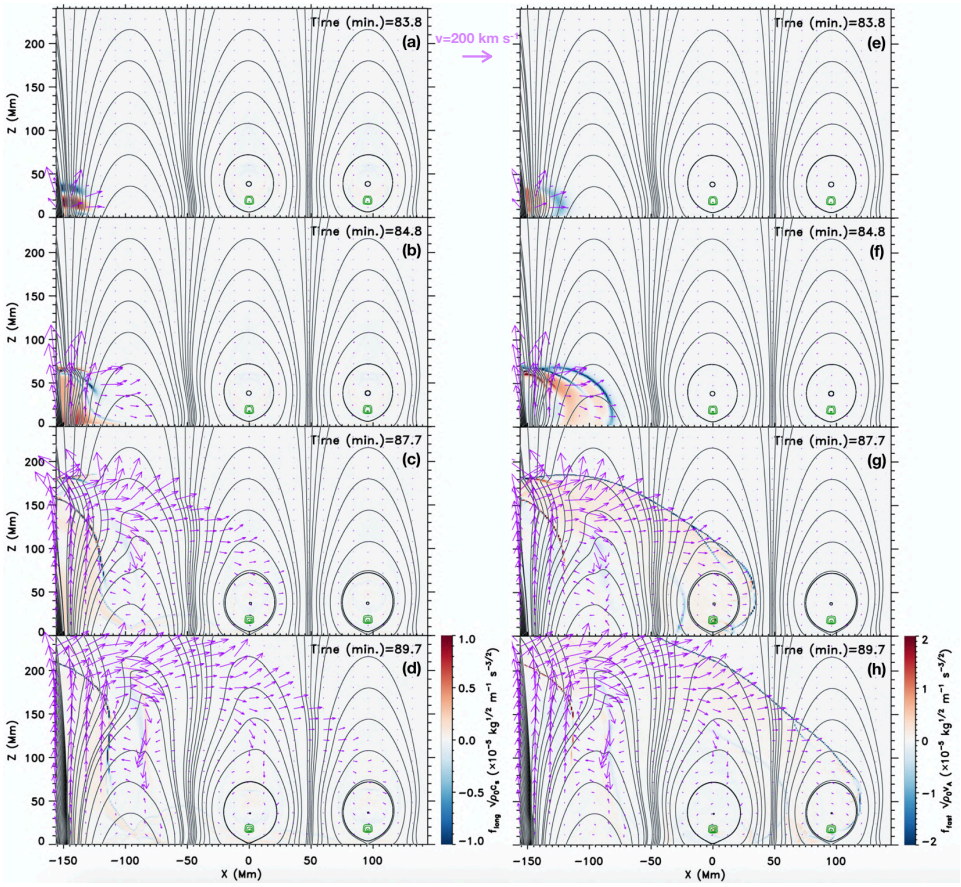

Figure 5.12: Temporal evolution of the wave field after the initiation of the perturbation. Left panels: $f_{\rm long}\sqrt{\rho_0}c_s$; right panels: $f_{\rm fast}\sqrt{\rho_0}v_A$. The black lines denote the magnetic field. The green lines show the density isocountrours. The purple arrows show the velocity field.

flux rope located at $x = 96$ Mm. The wave front produces a disturbance that pushes down and inclines this flux rope, similar to the first one. Comparing panels (g) and (h), we can see that the wave front reaches the closer and further flux ropes at $t = 87$ and 89 minutes, respectively. This time delay corresponds to the finite velocity of the perturbing wave front. From this delay, we obtained the velocity of the wave front propagation to be as large as $\sim 800\,{\rm km\,s^{-1}}$. From Figures 5.12(f)-5.12(h), we conclude that the fast-mode shock wave causes the main perturbation to the flux ropes in this experiment. It is interesting to compare the properties of oscillations in the closer and further flux ropes and study the possibility of the excitation of the different modes of LAOs by the same front. We discuss this in Section 5.2.2.

As we consider the 2.5D approximation, we can expect that using the source term in the energy equation, we produce also perturbation of the velocity component perpendicular to the

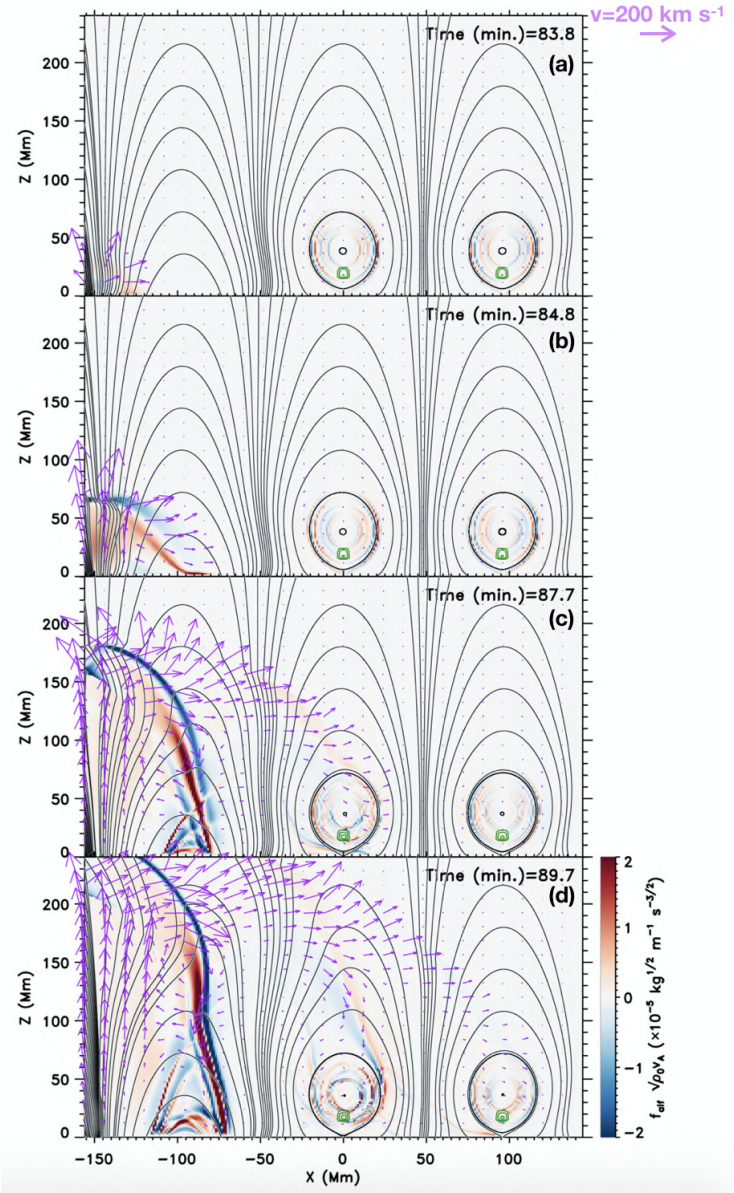

Figure 5.13: Temporal evolution of $f_{\rm alf}\sqrt{\rho_0 v_A}$ after the initiation of the perturbation. The black lines denote the magnetic field. The green lines show the density isocountrours. The purple arrows show the velocity field.

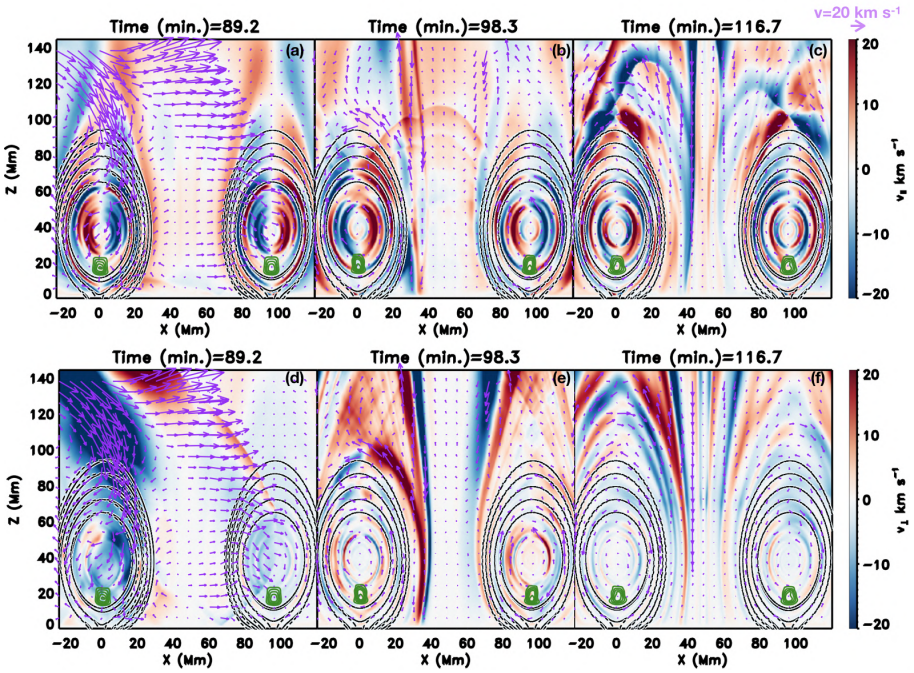

Figure 5.14: Evolution of $v_{\parallel}$ (left panel) and $v_{\perp}$ (right panel) in the flux rope prominences after the wave propagation. The purple arrows denote the velocity field. The green lines show the density isocountours.The dashed lines denote the flux ropes magnetic field just before perturbation.

XZ-plane. Figure 5.13 shows the evolution of the incompressible perturbation associated with the Alfvén wave. After the initiation of the perturbation shown in Figure 5.13(a), the wave front starts to propagate along the magnetic arcade closest to the perturbed region (Figure 5.13(b)). Panels (c) and (d) show the posterior evolution of this wave front. One can observe that the front moves along the magnetic arcades causing strong deformations of the field lines. When this perturbation reaches the bottom boundary, it is reflected and moves in the opposite direction. As a result, we can see a counterstreaming pattern in the low-lying arcades in Figure 5.13(d). Thus, the Alfvén front is trapped by the nearby arcades and does not produce any perturbations of the distant flux ropes.

Figures 5.14(a) and 5.14(d) show a closer look at the flux ropes and prominences when the fast-mode wave approaches the further flux rope. After the wave front propagation, the closer flux rope is pushed down and slightly inclined to the right. It is also seen that the prominence inside the closer flux rope remains almost unperturbed and does not look deformed or displaced by the proper action of the wave front. However, in the rest of the panels of this figure, we can see that the prominence starts to move slightly. Figures 5.14(c) and 5.14(f) show that some motions are still present in both prominences 27.5 minutes after it is hit by the wave front. It is interesting to note that the magnetic flux ropes at that time almost entirely recovered their initial positions. This indicates that the magnetic field quickly returns to the initial state while

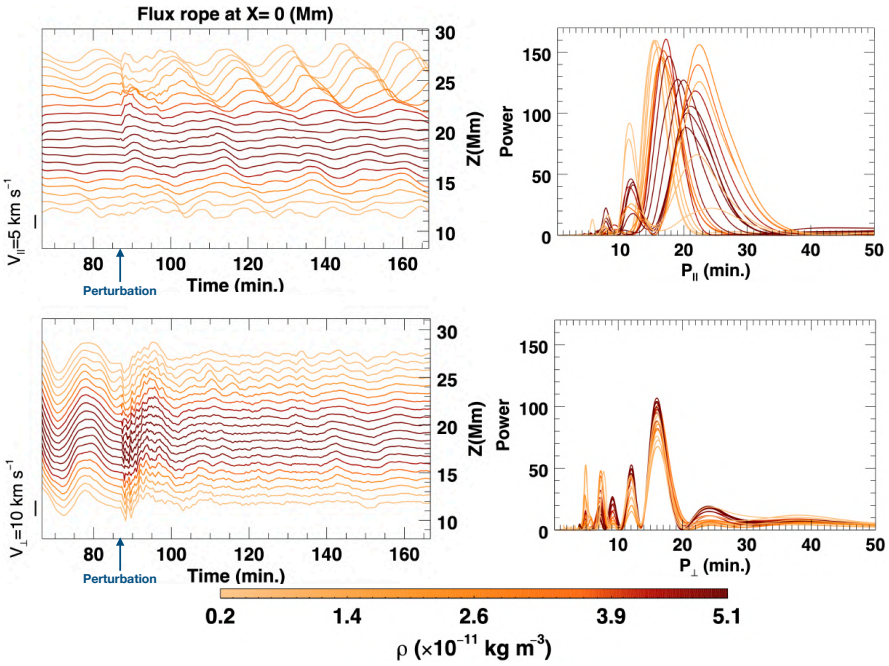

Figure 5.15: Left panels: temporal evolution of $v_{\parallel}$ (top) and $v_{\perp}$ (bottom) at the center of mass at the selected field lines of the flux rope at $x = 0$ Mm. Right panels: the periodograms of the $v_{\parallel}$ (top) and $v_{\perp}$ (bottom) in time-interval 83-167 minutes. The color bar denotes the maximum initial density at each field line. The left vertical axis indicates the velocity amplitude scale. The right vertical axis denotes the vertical location of the dips of the selected magnetic field lines.

the prominence mass continues moving due to the inertia. In panels (b),(c) and panels (e), (f), the density isocountours show the complex prominences dynamics inside both flux ropes.

5.2.2 Prominence oscillations

It is important to study which polarizations of the motions were triggered by this perturbation. As before, we analyze the longitudinal and transverse velocities at the center of mass of the selected field lines. For this analysis, we used some 20 field lines that belong to each flux rope.

First, we study the motions associated with a prominence at $x = 0$ Mm. Figure 5.15 shows the temporal evolution of the longitudinal and transverse velocities. We obtained periodograms using the signals in time-interval 83-167 minutes from these velocities. The top panels show the analysis for $v_{\parallel}$. The perturbation reaches the prominence at $x = 0$ Mm at the time 87 minutes approximately. Before that moment, the velocities at the field lines are below $2\,\mathrm{km\,s^{-1}}$. The arrival of the perturbation results in a small increase of the velocity of about $2-3\,\mathrm{km\,s^{-1}}$. Later on, the longitudinal oscillations develop, and they are more prominent at the field lines located at the height of $23-28$ Mm. We can see that the amplitude of oscillations increases with time.

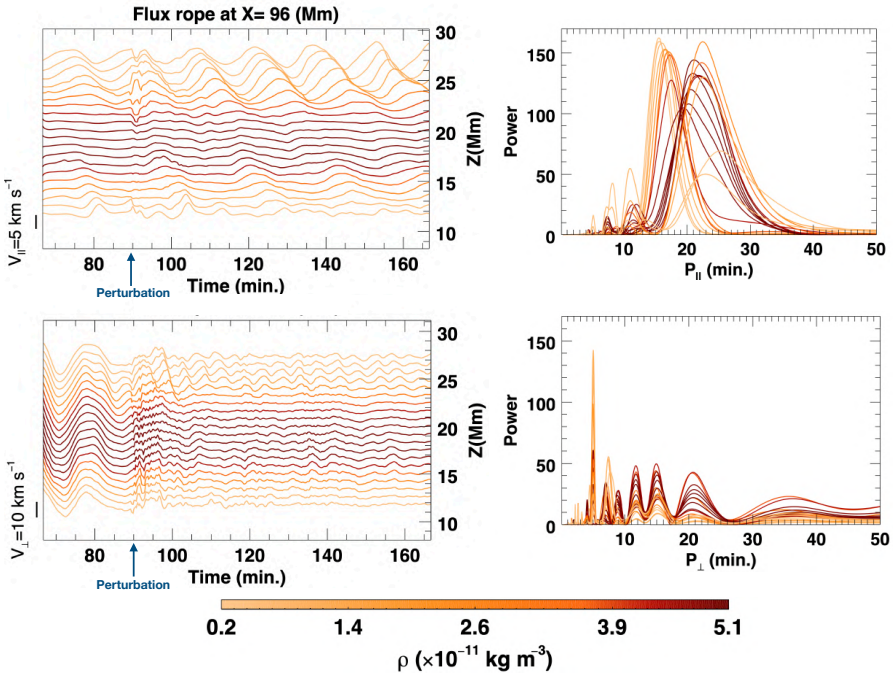

Figure 5.16: Left panels: temporal evolution of $v_{\parallel}$ (top) and $v_{\perp}$ (bottom) at the center of mass at the selected field lines of the flux rope at $x = 96$ Mm. Right panels: the periodograms of the $v_{\parallel}$ (top) and $v_{\perp}$ (bottom) in time-interval 83-167 minutes. The color bar denotes the maximum initial density at each field line. The left vertical axis indicates the velocity amplitude scale. The right vertical axis denotes the vertical location of the dips of the selected magnetic field lines.

Initially, when the wave front reaches the prominence, we observe only a small increase in the signal. However, as mentioned before, the wave front significantly affects the magnetic field of the flux ropes, inclining and deforming it. As the plasma is considered to be frozen in the magnetic field, the prominence mass follows the motions of the magnetic field. This way, the magnetic field transfers the perturbation to the prominence plasma. This is why we see the amplitude of the longitudinal oscillations gradually increasing later on, after the action of the main disturbance. The top right panel of Figure 5.15 shows the periodogram of the $v_{\parallel}$ at the different field lines. The periodogram demonstrates that the period changes from 22.5 minutes to 15.5 minutes, reflecting the decrease of the period with height seen in the top left panel. This change of the period can be associated with the decrease of the radius of curvature of the magnetic field lines with height in the flux rope model.

The bottom panels of Figure 5.15 show the analysis of $v_{\perp}$ in the same prominence. During the first minutes after the mass loading, the prominence shows the vertical oscillations. These oscillations have a very long damping time and are prominent in the signal up to $t = 87$ minutes. When the wave front approaches the prominence ($t = 87$ minutes), it causes the velocity perturbation of approximately 10 km s^{-1}. Thanks to this perturbation, the transverse

oscillations are established. The motions are complex and consist of short-period and long-period components. The motions at all the field lines are similar with no significant shift as observed for $v_{\parallel}$. One can observe at the right panel that the power peaks for all the considered field lines seem to be located at the same periods, suggesting more coherent motions. This result suggests that the transverse prominence oscillations in this experiment have a global character, implying that the whole prominence body oscillates with the same periods.

The top panels of Figure 5.16 shows $v_{\parallel}$ in the set of field lines of the distant flux rope. Comparing the temporal evolution and the periodogram of the longitudinal velocity at the different field lines with the ones of the closer flux rope (Figure 5.15), we can see that motions have very similar periods and amplitudes. Furthermore, we can observe the same amplification of oscillations of the field lines at the heights of $23 - 28$ Mm. Similarly, the period decreases with height. We obtain similar period values of $15.5 - 22.5$ minutes from the periodograms. This implies that the distant perturbation can excite similar kinds of longitudinal oscillations at the flux rope prominences located at different distances.

We obtain a slightly different results for the transverse oscillations shown at the bottom panels of Figure 5.16 compared to those shown in Figure 5.15. In both cases, we observe coherent transverse oscillations at the different field lines. After the arrival of the perturbation, one can see that the short-period mode is excited. However, the amplitudes are slightly smaller for the further flux rope. The periodogram shows that nearly the same modes of the transverse polarization were excited in both flux ropes. However, the power of the modes differs between the two flux ropes. In the case of the second flux rope (at $x = 96$ Mm), the dominant mode corresponds to the motions with a short period of 5 minutes. This mode is not so prominent in the case of the first flux rope(at $x = 0$ Mm). The rest of the oscillation modes have periods varying between $7 - 21$ minutes. This result indicates that the distance from the disturbance source determines the excitation of different transverse modes in the flux ropes prominences.

5.3 Impact of external perturbation on a dipped arcade prominence

The numerical experiment described in this section was motivated by the suggestion from Shen et al. (2014b) to explain the excitation of the different modes in sheared arcade model depending on the direction of arrival of the shock wave with respect to the filament spine (see Figure 1.11). In particular, it was suggested that the longitudinal oscillations of the prominence located at the dipped arcade could be excited when the direction of the normal vector of the wave front is parallel to the filament spine. Luna & Moreno-Insertis (2021) studied the excitation of the LALOs in the dipped arcade when the source of the perturbation was an energetic jet that had a magnetic connection with the main prominence field. The authors found that the LALOs are excited by the direct influence of the mass flow injected by the jet. In contrast, in this study, we aim to investigate a possibility to trigger LALOs when the source of the perturbation is located far enough and is not magnetically connected to the prominence magnetic field.

5.3.1 Numerical model

The numerical model for this study is similar to the case studied in Chapter 4. We briefly recall its properties in this section. The 2D prominence model is shown in Figure 5.17. It is defined in the Cartesian coordinate system in the XZ-plane, where z-axis corresponds to the vertical direction. The computation domain consists of a box of 384×240 Mm in size (spatial resolution 240 km). The initial magnetic field is a potential configuration that consists of a superposition of the major and minor arcades and contains a dipped part at the central region (see also Section 2.1.3). We choose the following parameters of the magnetic field structure: $B_0 = 10$

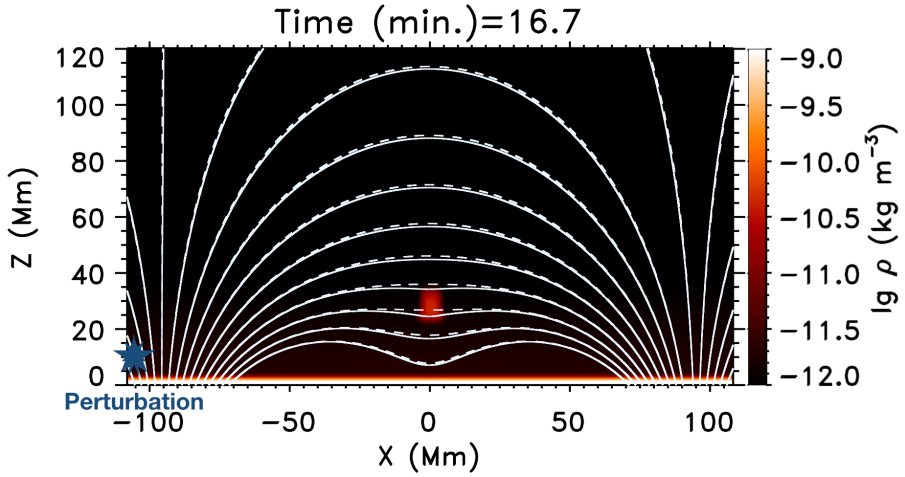

Figure 5.17: Density distribution and magnetic field lines at the central part of the computational domain after the mass loading. The dashed lines denote the initial magnetic field before the mass loading. The position of the external distrubance is also shown at the bottom left.

G, $x_0 = 0\,\mathrm{Mm}$, $z_0 = -2\,\mathrm{Mm}$ are coordinates of the center of the structure, $k_1 = \frac{\pi}{D}$, $k_2 = 3k_1$ are the lateral extensions of the arcades, and $D = 191.4\,\mathrm{Mm}$ is the half-size of the numerical domain along the x-direction. A more detailed description of this magnetic configuration was provided in Sections 2.1.3 and 4.1. The magnetic field strength varies between 3.0 and 4.0 G from the bottom to the top of the dipped region. Similarly to Chapter 4, the initial atmosphere is a stratified plasma in hydrostatic equilibrium. The initial atmosphere includes the upper chromosphere, transition region (TR), and corona. The corresponding temperature profile is written as

$$T(z) = T_0 + \frac{1}{2}\left(T_\mathrm{c} - T_0\right)\left[1 + \tanh\left(\frac{z - z_c}{W_z}\right)\right]. \tag{5.12}$$

We choose $T_\mathrm{c} = 10^6$ K, $T_0 = 10^4$ K, $W_z = 0.7\,\mathrm{Mm}$, and $z_c = 4.8\,\mathrm{Mm}$. This profile provides the temperature ranging from $T_{ch} = 10^4$ K at the base of the chromosphere to $T_c = 10^6$ K in the corona. As the plasma is stratified in the vertical direction, the density changes from $\rho = 9 \times 10^{-9}$ kg m^{-3} in the chromosphere to $\rho = 1.98 \times 10^{-12}$ kg m^{-3} at the base of the corona at the height $z_c = 4.8\,\mathrm{Mm}$.

The boundary conditions are identical to what we used in Chapter 4 implying the periodic condition at the side boundaries, and the current-free condition for the magnetic field together with the symmetric condition for the temperature and pressure, and fixed density at the bottom. At the top boundary, we use the symmetric boundary condition for all the variables except for B_x, which is antisymmetric.

In order to increase the density in the dipped region of the magnetic field, we use the source term in the continuity equation defined by a Gaussian distribution centered at $(x, z) = (0, 30)\,\mathrm{Mm}$. The mass loading starts at $t = 0$ seconds and ends at $t = 100$ seconds. The resulting prominence has a density of 30 times larger than in corona, and prominence dimensions are 7 and 10 Mm in horizontal and vertical directions.

During the first 16.7 minutes, we let the magnetic configuration with prominence evolve,

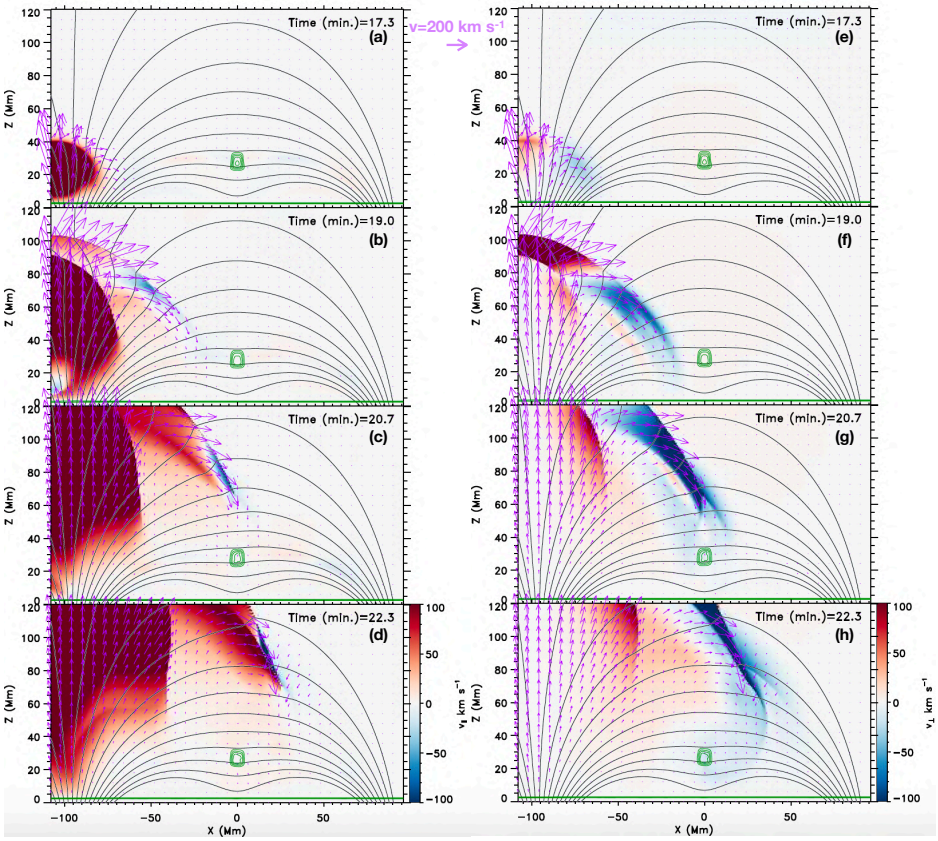

Figure 5.18: Evolution of $v_{\parallel}$ (left panel) and $v_{\perp}$ (right panel) during the wave propagation. The black lines denote the magnetic field. The green lines show the density isocountours. The purple arrows denote the velocity field.

reaching an equilibrium state. The dashed lines in Figure 5.17 illustrate the initial magnetic field. As we can see, the magnetic field is slightly deformed due to the presence of a heavy mass.

5.3.2 Perturbation

In the numerical experiment performed in this section, the external perturbation is caused by the source term in the energy equation, similar to the previous section. The source term is defined by Equation 5.8. We used a following set of the the parameters: $\alpha = 2$ J m^{-3}, $t_{\rm pert} = 50$ seconds, $x_{\rm pert} = -105.6$ Mm, $z_{\rm pert} = 12$ Mm, $\sigma_x = \sigma_z = 12$ Mm. The approximate position of the perturbation is shown by the blue star in Figure 5.17. We choose the position of the perturbation at the optimal distance from the prominence position and the left boundary. As we deal with a periodic system, the perturbation cannot be placed further, because in this

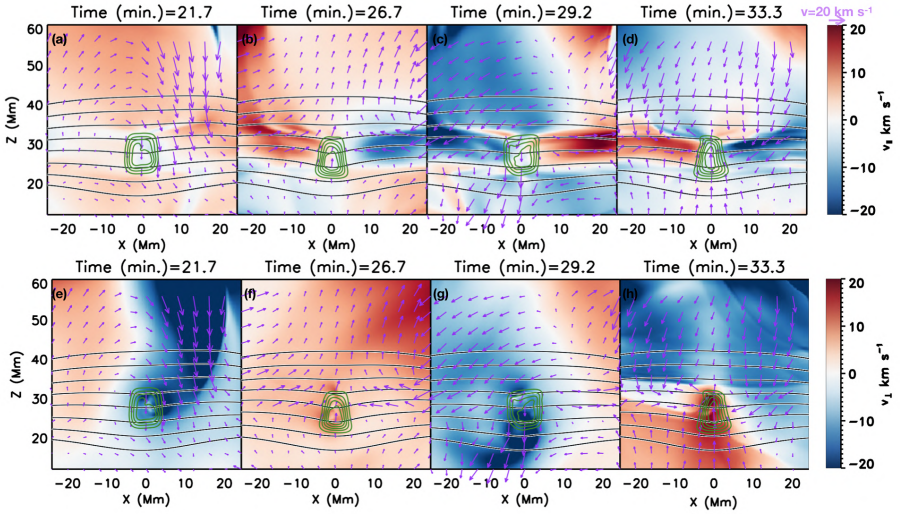

Figure 5.19: Evolution of $v_{\parallel}$ (left panel) and $v_{\perp}$ (right panel) during the wave propagation. The black lines denote the magnetic field. The green lines show the density isocountours. The purple arrows denote the velocity field.

case, most of the disturbance would propagate in the direction to the left boundary and, later on, it would appear from the other side of the numerical domain. In order to avoid that, we placed the perturbation at a location just behind the region of the vertical magnetic field (Figure 5.17). Such a location also allows having a perturbation not magnetically connected with the prominence cool mass mimicking a distant flare.

Figure 5.18 shows the time evolution of the transverse and longitudinal velocities. Panels (a) and (e) represent the moment when the perturbation is applied. One can observe from the velocity field shown by purple arrows that the perturbation starts to propagate in all directions. The following panels (b) and (f) show the later stages of the propagation of the disturbance. In the left column, we can see that the perturbation of the longitudinal velocity continues moving along the vertical magnetic field. The right column shows the transverse velocity distribution. We can see a fast-wave front that is ahead of the one observed in the distribution of the longitudinal velocity. The magnetic field lines that correspond to the location of this front appeared to be strongly deformed. In panels (c) and (g), we can observe that the fast wave propagates in the magnetic arcades. The skirt of its front also reaches the prominence body (the location of the prominence mass is shown by the green lines). The wave pushes the prominence down, displacing it from the equilibrium position. According to the density isocontours, the prominence body is slightly deformed due to the wave propagation. The rest of the disturbance moves slower along the vertical magnetic field and in the overlying magnetic arcades.

Figures 5.19(a) and 5.19(e) give a closer look at the moment of the arrival of the wave when the prominence is pushed downward. The following panels to the right show that the prominence starts moving upwards, trying to recover its initial position. Alongside, panel (b) shows the motions along the magnetic field around the prominence plasma, which results in compression of the prominence body. This is evident from the deformation of the green lines in

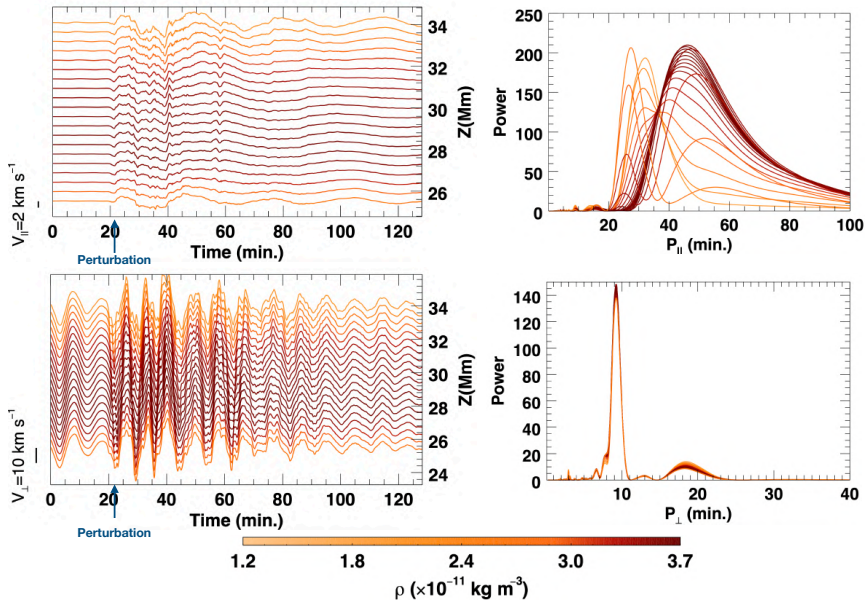

Figure 5.20: Left panels: temporal evolution of $v_{\parallel}$ (top) and $v_{\perp}$ (bottom) at the center of mass at the selected field lines of the dipped arcade. Right panels: the periodograms of the $v_{\parallel}$ (top) and $v_{\perp}$ (bottom) in time-interval 22-127 minutes. The color bar denotes the maximum initial density at each field line. The left vertical axis indicates the velocity amplitude scale. The right vertical axis denotes the vertical location of the dips of the selected magnetic field lines.

this figure. The situation is the opposite in panels (c) and (g). There, the velocity field is such that the prominence moves down. One can observe from the distribution of the longitudinal velocity that the prominence body experiences a rarefaction. This rarefaction is evident from the density isocontours. Namely, the density isocontours appear to be elongated along the magnetic field. Panels (d) and (h) reveal an upward motion accompanied by the simultaneous compression of the prominence body. Overall, we conclude that in this experiment, the vertical prominence motions interchange with the motions due to the compression and rarefaction.

5.3.3 Prominence oscillations

Next, we analyzed the longitudinal and transverse motions associated with the different field lines that permeate the prominence body. The integration of the field lines started from the positions where the magnetic field lines are unperturbed, i.e., at the base of the magnetic arcades anchored in the dense chromosphere. The results of the analysis of $v_{\parallel}$ are shown in the top panels of Figure 5.20. Previously, we have concluded by analyzing Figure 5.19 that the prominence moves along the field lines, as a consequence due to, mainly, compression and rarefaction. It is noticeable that these motions are symmetric with respect to the vertical prominence axis.

Thus, taking the signal of $v_{\parallel}$ at the center of mass of the field lines, we automatically exclude the motions due to the compression and rarefaction from the consideration. The longitudinal velocity shows that, after the arrival of the perturbation at $t = 21.7$ minutes, no LALOs in this prominence are excited. We can only detect oscillations with a small amplitude below $2\,\mathrm{km\,s^{-1}}$. The periodogram gives the oscillation period of 41 minutes in the densest prominence region. Before the arrival of the disturbance, the left bottom panel shows some vertical motions after the mass loading process. The amplitude of these oscillations decreases significantly when the prominence structure evolves. The moment $t = 21.7$ minutes corresponds to the arrival of the wave. We can see that the amplitude rapidly increases in all the field lines. In the next time moments, we observe that the vertical oscillations are established. From the visual impression, these oscillations seem to be synchronized in the different field lines. The bottom right panel of Figure 5.20 shows the periodogram for the vertical oscillations. We can see that the dominant period in all the lines has the same value equal to 9 minutes approximately. The vertical period remains constant with height, indicating a global normal mode.

5.4 Discussion and conclusions

In this chapter, we studied the triggering mechanisms associated with the external disturbances and their interaction with flux rope and dipped arcade prominences. In the first experiment, we studied the excitation of oscillations in the flux rope prominence by the eruption of the nearby flux rope. The second experiment involved two flux rope prominences located at different distances from the energetic release introduced by the source term in the energy equation. In the third experiment, we also used the energy release as a distant perturbation, but the dipped arcade hosting the prominence mass model was used instead of the magnetic flux rope model.

In this chapter, we studied the triggering mechanisms associated with the external disturbances and their interaction with flux rope and dipped arcade prominences. In the first experiment, we studied the excitation of oscillations in the flux rope prominence by the eruption of the nearby flux rope. The second experiment involved two flux rope prominences located at different distances from the energetic release introduced by the source term in the energy equation. In the third experiment, we also used the energy release as a distant perturbation, but the dipped arcade hosting the prominence mass model was used instead of the magnetic flux rope model.

In the first experiment, which involved an eruptive event, we found two stages of the interaction of the erupting rope with the prominence. The first stage is associated with the eruption of the flux rope structure, producing an inflow motion on its wake and forcing the inclination of the prominence-hosting flux rope. However, this process does not excite LAOs in the prominence. Eruptive events are considered as the main sources of the Moreton and EIT waves production (Biesecker et al. 2002; Chen 2006, 2011). These waves can propagate over large distances in the solar atmosphere and are proposed to be responsible for excitation of LAOs (see, e.g., Shen et al. 2017). In our numerical experiment, we have not found clear evidence of the Moreton wave reaching the prominence. Perhaps, in our case, this wave was too faint and not powerful enough to perturb the prominence. In contrast, we have found an important perturbation at the front of the erupting flux rope moving laterally and upwards as the density enhancement followed by the dimming. In principle, such a front can be identified as an EIT wave (Chen et al. 2002). However, in our case, this EIT wave moves mostly above the prominence and never reaches it. Our model can be improved in several ways in order to perturb LAOs in the prominence, such as increasing the magnetic field strength (i.e., its energy) of the initial configuration. Another possibility is to include a null point above the erupting flux rope, trying to reproduce the so-called break-out current sheet model (Karpen et al. 2012). We have also seen that the EIT wave propagates from the top of the erupting rope above the prominence. Thus

by increasing the distance between the erupting flux rope and the prominence, one can possibly produce an EIT wave propagating laterally and reaching prominence. Additionally, by reducing the size of the erupting flux rope, one can increase the probability that the EIT wave reaches prominence. All these points regarding possible ways of interaction of a large-amplitude wave with the prominence can be addressed in future studies.

In the eruption experiment, the largest perturbations in the prominence are produced by the plasmoids formed in the current sheet rather than by the flux rope eruption itself. In this work, we paid more attention to the perturbations caused by the activity of plasmoids rather than the mechanism and the properties of their formation. The physical aspects of the magnetic islands in the current sheet in 2.5D flux rope models were described in more detail by Zhao et al. (2017, 2019). The plasmoids formed in the current sheet move downwards to the post-reconnection loops or upwards following the erupting flux rope. The latter ones do not significantly affect the nearby filament. In contrast, the magnetic islands that propagate downward reach the small post-reconnection loops. The interaction of the plasmoids with these loops produces the perturbation of the velocity field. These disturbances can propagate and reach the flux rope prominence producing the mixed longitudinal and transverse small-amplitude oscillations.

It has been known from the numerical experiments that tearing instability can develop in the current sheet. As a result, the plasmoids can be formed. The activity of the plasmoids is considered as a candidate for the periodic perturbation for the generation of quasi-periodic pulsations (QPP). In this scenario, the disturbances are generated by the precipitation of the plasmoids at the foot points. Bárta et al. (2008) showed that the interaction of the plasmoids with post-reconnection loops at the bottom could cause loops oscillations. In our numerical experiment, we have shown that the plasmoids perturb the post-reconnection loops and generate velocity disturbances that can propagate at a significant distance. In our work, these disturbances were observed to be responsible for the excitation of the SAOs in the nearby prominence.

The motivation for the second experiment comes from the observations by Shen et al. (2014a) of the chain of the winking filaments triggered by the same wave from the flare. The observational time-sequence of these three prominences demonstrated the presence of LAOs, whose excitation temporally coincides with the arrival of the wave. We intended to reproduce a similar scenario assuming a model of the magnetic flux ropes hosting the prominence mass. We found the fast-mode wave propagating across the magnetic field and entering the magnetic flux regions, and displacing both flux ropes from the initial position. This action does not directly affect the prominence mass but significantly perturbs the magnetic field. Due to the displacement and deformation of the magnetic environment, the prominence is displaced from its equilibrium. We found the transverse oscillations in both flux ropes with similar dominant periods. The analysis revealed that these motions are coherent at different heights suggesting a global mode. Additionally, in both flux ropes, we obtained the longitudinal SAOs with similar oscillatory properties. In both prominences, the period of longitudinal oscillations changes with height. We suggest that this variation of the period can be related to the different curvatures of the lines.

The last experiment is associated with a scenario of the triggering of LALOs in the dipped arcade prominence model given by Shen et al. (2014b). The authors suggested that a shock can excite LALOs when the shock propagates along the filament spine. In our numerical experiment, we have found that a distant source, not magnetically connected with prominence, reaches the filament. Its propagation strongly affects the magnetic field of the arcades. When the disturbance reaches the prominence, it strongly pushes down the dipped region with the prominence mass inside. This way, the transverse oscillations are established. The analysis revealed that these motions have a large amplitude that exceeds $10\,\mathrm{km\,s^{-1}}$. Additionally, the prominence evolution shows evidence of the motions along the magnetic field due to the compression and rarefaction. Notably, we do not observe excitation of the LALOs either in the prominence evo-

lution or from the analysis of motions. The analysis reveals that only transverse LAOs, together with the motions due to compression and rarefaction, are excited in this numerical experiment.

From all the experiments described above, we conclude that investigating the triggering mechanism of LAOs is crucial for our understanding of the physical nature of prominences and the propagation and interaction of the energetic waves with different magnetic configurations. We have studied the triggering of LAOs by an eruptive event and by the artificial energy release on the flux rope and dipped magnetic arcade configurations. We conclude that the external triggering of prominence oscillations is a complex process that excites longitudinal, transverse or a mix of both types of motions with small or large amplitudes.

6

Conclusions and future prospects

In this thesis, we have investigated the properties of the large-amplitude oscillations (LAOs) in solar prominences using numerical simulations. The numerical experiments allow testing the different scenarios in order to study prominence dynamics, including LAOs. This investigation is focused on three main aspects of LAOs physics: the relation of these LAOs to the prominence structure, damping or amplifying mechanism of the longitudinal LAOs (LALOs), and the triggering mechanism of the different polarizations of LAOs. From the analysis, we retrieve the important results for the prominence of seismology. We can shed light on the attenuation and amplification of LALOs and infer the mechanism of excitation of the longitudinal or transverse polarizations by the external energetic event reproducing some observational aspects of LAOs. In what follows, the key findings obtained during this thesis are summarized.

6.1 Oscillatory properties of LAOs in flux-rope prominence models

We have performed a 2.5D numerical experiment using the model based on the sheared arcade magnetic configuration. The sheared arcade is used to form a twisted flux rope by applying the converging motions at its footpoints. The prominence mass is loaded to the magnetic dips of the flux rope. We aim to study the normal modes of the configurations with different shear angles and plasma density contrasts. Additionally, we have studied the oscillatory modes that are excited by the perturbation placed out of the flux-rope configuration. The key findings of this work can be summarized as follows.

- Horizontal perturbation excites LALOs with period decreasing with height, in agreement with the pendulum model. It also triggers the vertical oscillations related to the back-reaction of the magnetic field to the longitudinal motions.
- Vertical perturbation triggers the vertical oscillations, which period remains constant with height. These oscillations are accompanied by the motions along the magnetic field due to compression and rarefaction of the prominence plasma.
- The period of LALOs decreases with height in agreement with the pendulum model. In contrast, the period of vertical LAOs remains constant with height suggesting the global nature of oscillations.
- The periods of LAOs do not show a significant difference in the models with the different shear angles of the magnetic field or the prominence density contrasts. For the longitudinal oscillations, the period decreases in the models with more sheared magnetic configuration,

which is associated with a small variation of the radii curvature in the 2D perspective. The period of vertical LAOs is slightly longer in the case of larger density contrast.

- An external trigger can excite oscillations in the flux rope prominence by perturbing and deforming the hosting magnetic field rather than directly affecting the prominence. The excited motions can be classified as the vertical LAOs and the longitudinal small-amplitude oscillations (SAOs). Their properties (i.e., periods and damping times) agree with those excited by the horizontal and vertical perturbations suggesting that the external wave triggers the normal modes of prominence.

6.2 LALOs in the dipped arcade model simulated with different resolutions

We have studied the damping and amplifying mechanisms of LALOs in the 2D prominence model that involves a dipped arcade as the main magnetic configuration suitable for mass support. The prominence is perturbed along the magnetic field. We have considered the same numerical setup increasing the spatial resolution and comparing the oscillatory properties in each experiment. The results of this research are:

- The period of LALOs agrees with the period predicted by the pendulum model for the highest spatial resolutions. The periods depend on the spatial resolution of the numerical experiment. By increasing the resolution of the simulations, the periods fit progressively better the analytical pendulum model.
- Experiments with better spatial resolution show significant improvement of the damping time at the bottom and central regions of the prominence. However, the two experiments with the highest resolution show only a small difference in the damping time. This saturation of the damping time with the resolution suggests that we have reached a limit in which the attenuation of LALOs is associated with a physical mechanism rather than the numerical dissipation.
- We have found a very interesting behavior of the oscillations at the top region of the prominence. Namely, we observed that during the first 130 minutes, the amplitude of the longitudinal velocity increases. This effect appears to be almost irrelevant for the low-resolution experiments because the amplitude remains almost constant. However, with the improvement of the spatial resolution, this amplification becomes very important. After the amplification phase, the LALOs amplitude shows slow damping.
- The analysis of the different energy contributions shows that the kinetic energy losses are mainly caused by the collective work done by the gas pressure gradient and Lorentz forces. It indicates that the damping of the oscillations is due to the loss of energy in the form of emitted magneto-acoustic waves. The time-distance diagram along the vertical axis confirms this result showing that the waves propagate upward.
- The analysis of the energies shows that, in contrast to the bottom and central part of the prominence, at its top, the Lorentz force contributes positively to the kinetic energy. This indicates that the Lorentz force can accelerate the plasma in the upper prominence region.
- The analysis of the Poynting flux shows that a large part of the energy from the bottom part goes to the top part. This demonstrates that the amplification phenomenon at the top part of the prominence is due to an energy transfer from the bottom part. In addition, the strong damping of the bottom part is also partially due to the transfer from the bottom to the top.

- This energy transfer is due to the deformation of the magnetic field lines by the motions of the heavy prominence mass. The bottom part deforms the magnetic field producing deformations of the field at the top of the prominence. These deformations of the magnetic field at the top result in the dips moving in front of the cool plasma, producing an amplification of the motion.

6.3 Oscillations triggered by external perturbations

This study is dedicated to investigating the triggering mechanisms of prominence oscillations by external disturbances in 2D and 2.5D models. In the first experiment, the flux rope prominence is perturbed self-consistently by an eruption of a neighboring flux rope. In the second experiment, two adjacent flux rope prominences are excited by an energetic event produced artificially. In the third experiment, an artificial perturbation is used to perturb the oscillations in a dipped-arcade prominence model. The preliminary results from these experiments can be summarized as follows:

- The nearby eruption does not excite the LAOs in the flux-rope prominence. The converging motion behind the eruptive flux rope and around the current sheet inclines the prominence structure but does not drive oscillations.
- The longitudinal and transverse SAOs in the prominence are produced by the plasmoids formed in the current sheet. Those plasmoids that move downward and interact with the post-reconnection loops cause the perturbations that reach prominence and excite SAOs.
- In the experiment with two adjacent prominences, the distant energetic event produces a fast-mode wave that propagates in the magnetic environment and reaches both flux ropes. This wave produces important perturbation of both ropes. These motions are finally transmitted to the prominence plasma producing their oscillations.
- The analysis reveals the excitation of both longitudinal and transverse oscillations in both flux ropes. Furthermore, the properties of oscillations of the different polarizations, such as periods and damping behavior, are similar for both flux rope prominences.
- The experiment with the external driver perturbing the distant dipped arcade model shows that the wave reaches the prominence mass and pushes it down. This process triggers the vertical LAOs that, similarly to our first work, is accompanied by the motions due to compression and rarefaction. In this experiment, we have found that the wave from the energetic event does not excite the LALOs in contrast to what has been suggested by some authors.

6.4 Outlook

The simulation results suggest that the LAOs are complex manifestations of the prominence dynamics involving various excitation and attenuation mechanisms. In this thesis, we have extended the knowledge of the nature of LAOs and advanced the current modeling of these structures by performing multi-dimensional numerical simulations. We have studied the longitudinal and transverse LAOs from three different points of view. First, we have investigated the relation of the period to the parameters of the global prominence structure that brings important knowledge to prominence seismology. Second, we have performed the convergence test when studying the damping mechanism of LALOs and found that numerical dissipation in

low-resolution simulation hides the important amplification of LALOs. Finally, we have performed important experiments proposing several scenarios to explain the triggering of purely longitudinal and transverse or even mixed polarizations of LAOs involving the nearby eruption event or the energetic event mimicking a distant solar flare. These numerical experiments can serve as a basis for further investigation of the triggering mechanism of LAOs and propagation and interaction of the coronal perturbations with the magnetic structures such as prominences.

6.5 Future prospects

There are several open questions related to the nature of LAOs that deserve to be studied in the future. In the following, we outline several outstanding issues:

- The external triggering mechanism should be investigated in 3D models. This would allow us to investigate in more detail which polarizations are excited when the perturbation comes from a different direction with respect to the axis of the prominence spine. The models using the different driving conditions are also desirable, such as the different distances to the source of the perturbation.
- The numerical model of the interaction of the erupting flux rope with a prominence should be improved in order to increase the perturbations and exited LAOs in the prominence. Several scenarios can be proposed as increasing the distance between both objects or reducing the size of the erupting rope. This would further allow us to investigate the generation of Moreton and EIT waves and the interaction with a distant filament.
- It remains unclear the role of plasmoids in the triggering of the LAOs due to nearby eruption. In this work, we have obtained that they can excite only SAOs. However, the improvement of the magnetic field model with a simultaneous increase of the spatial resolution may shed light on this aspect of LAOs driving.
- We should investigate the damping mechanism of the longitudinal and transverse LAOs in the 3D prominence configurations using high-resolution simulations. As shown in this thesis work, high-resolution simulations are crucial for studying the properties of LAOs. In order to have more realistic prominence models in the high-resolution simulations, it makes sense to include the effects of partial ionization.
- The coupling of the longitudinal and transverse LAOs obtained in most of the numerical experiments of this thesis should be further investigated because it could play an important role in the damping and amplification of LAOs.
- We aim to study further the mechanisms of the damping and amplification of LALOs in the different prominence regions. The effectivity of this mechanism should be tested in a more realistic model, including the non-adiabatic effects. The results should be compared with the already observed amplifications.
- Models with prominence fine structure have to be considered. In such models, the prominence is considered as a bundle of threads rather than a continuous structure. Using these models, one could study the influence of the fine structure on the interaction of an external perturbation with the prominence, oscillation, and damping or amplification mechanisms. Alongside, the oscillations of the multiple threads could be used to investigate the influence of the line-of-sight (LOS) effect in the observations, which could lead to overestimating the damping of LALOs.

- In this work, we have not considered the realistic models of the prominence formations such as injection, levitation, or evaporation-condensation models. We form prominences with an artificial mechanism. Using the realistic models of mass loading to the magnetic dips may play an important role in the onset of the prominence oscillations and their attenuation. In order to reproduce realistic prominence formation, it is necessary to implement thermal conduction and a more realistic model for coronal radiative losses in MANCHA3D.

Bibliography

Adrover-González, A., & Terradas, J. 2020, A&A, 633, A113

Afanasyev, A. N., & Zhukov, A. N. 2018, A&A, 614, A139

Antiochos, S. K., Dahlburg, R. B., & Klimchuk, J. A. 1994, ApJ, 420, L41

Antiochos, S. K., MacNeice, P. J., & Spicer, D. S. 2000, ApJ, 536, 494

Antiochos, S. K., MacNeice, P. J., Spicer, D. S., & Klimchuk, J. A. 1999, ApJ, 512, 985

Antolin, P., Okamoto, T. J., De Pontieu, B., et al. 2015, ApJ, 809, 72

Archontis, V. 2008, Journal of Geophysical Research (Space Physics), 113, A03S04

Archontis, V., Moreno-Insertis, F., Galsgaard, K., Hood, A., & O'Shea, E. 2004, A&A, 426, 1047

Archontis, V., & Török, T. 2008, A&A, 492, L35

Arregui, I., Oliver, R., & Ballester, J. L. 2018, Living Reviews in Solar Physics, 15, 3

Asai, A., Ishii, T. T., Isobe, H., et al. 2012, ApJ, 745, L18

Aschwanden, M. J. 2005, XXII, 908

Aschwanden, M. J., Schrijver, C. J., & Alexander, D. 2001, ApJ, 550, 1036

Attrill, G. D. R., Harra, L. K., van Driel-Gesztelyi, L., Démoulin, P., & Wülser, J. P. 2007, Astronomische Nachrichten, 328, 760

Aulanier, G., & Demoulin, P. 1998, A&A, 329, 1125

Aulanier, G., & Schmieder, B. 2002, A&A, 386, 1106

Babcock, H. W., & Babcock, H. D. 1955, ApJ, 121, 349

Ballester, J. L., Carbonell, M., Soler, R., & Terradas, J. 2016, A&A, 591, A109

Bárta, M., Vršnak, B., & Karlický, M. 2008, A&A, 477, 649

Bi, Y., Jiang, Y., Yang, J., et al. 2014, ApJ, 790, 100

Biesecker, D. A., Myers, D. C., Thompson, B. J., Hammer, D. M., & Vourlidas, A. 2002, The Astrophysical Journal, 569, 1009

Bocchialini, K., Baudin, F., Koutchmy, S., Pouget, G., & Solomon, J. 2011, A&A, 533, A96

Bruzek, A. 1951, Zeitschrift für Astrophysik, 28, 277

Cally, P. S. 2017, MNRAS, 466, 413

Canou, A., Amari, T., Bommier, V., et al. 2009, ApJ, 693, L27

Carbonell, M., & Ballester, J. L. 1991, A&A, 249, 295

Casini, R., López Ariste, A., Tomczyk, S., & Lites, B. W. 2003, The Astrophysical Journal, 598, L67

Caunt, S. E., & Korpi, M. J. 2001, A&A, 369, 706

Chae, J. 2001, ApJ, 560, L95

Chae, J., Moon, Y.-J., & Park, Y.-D. 2005, ApJ, 626, 574

Chae, J., Wang, H., Qiu, J., et al. 2001, ApJ, 560, 476

Chandra, R., Chen, P. F., Devi, P., et al. 2021, ApJ, 919, 9

Chen, J., Xie, W., Zhou, Y., et al. 2017, Ap&SS, 362, 165

Chen, P. F. 2006, The Astrophysical Journal, 641, L153

Chen, P. F. 2011, Living Reviews in Solar Physics, 8, 1

Chen, P. F., Fang, C., Chandra, R., & Srivastava, A. K. 2016, Sol. Phys., 291, 3195

Chen, P. F., Fang, C., & Shibata, K. 2005, ApJ, 622, 1202

Chen, P. F., Harra, L. K., & Fang, C. 2014, ApJ, 784, 50

Chen, P. F., Innes, D. E., & Solanki, S. K. 2008, A&A, 484, 487

Chen, P. F., Wu, S. T., Shibata, K., & Fang, C. 2002, ApJ, 572, L99

Collados, M., Trujillo Bueno, J., & Asensio Ramos, A. 2003, in Astronomical Society of the Pacific Conference Series, Vol. 307, Solar Polarization, ed. J. Trujillo-Bueno & J. Sanchez Almeida, 468

D'Azambuja, L., & D'Azambuja, M. 1948, Annales de l'Observatoire de Paris, Tome VI

De Pontieu, B., McIntosh, S. W., Carlsson, M., et al. 2007, Science, 318, 1574

Delannée, C., & Aulanier, G. 1999, Sol. Phys., 190, 107

Delannée, C., Török, T., Aulanier, G., & Hochedez, J. F. 2008, Sol. Phys., 247, 123

DeVore, C. R., & Antiochos, S. K. 2000, ApJ, 539, 954

DeVore, C. R., Antiochos, S. K., & Aulanier, G. 2005, ApJ, 629, 1122

Díaz, A. J., Oliver, R., Erdélyi, R., & Ballester, J. L. 2001, Astronomy and Astrophysics, v.379, p.1083-1097 (2001), 379, 1083

Dodson, H. W. 1949, Astrophysical Journal, 110, 382

Dyson, F. 1930, Monthly Motices Roy. Astron. Soc., 91, 239

Eto, S., Isobe, H., Narukage, N., et al. 2002, PASJ, 54, 481

Fan, Y. 2001, ApJ, 554, L111

—. 2009, ApJ, 697, 1529

—. 2020, ApJ, 898, 34

Felipe, T., Khomenko, E., & Collados, M. 2010, ApJ, 719, 357

Foukal, P. 1971a, Sol. Phys., 20, 298

—. 1971b, Sol. Phys., 19, 59

Fulara, A., Chandra, R., Chen, P. F., et al. 2019, Sol. Phys., 294, 56

Gaizauskas, V., Mackay, D. H., & Harvey, K. L. 2001, ApJ, 558, 888

Gaizauskas, V., Zirker, J. B., Sweetland, C., & Kovacs, A. 1997, ApJ, 479, 448

Galsgaard, K., Archontis, V., Moreno-Insertis, F., & Hood, A. W. 2007, ApJ, 666, 516

Galsgaard, K., & Longbottom, A. W. 1999, ApJ, 510, 444

Gibson, S. E., & Fan, Y. 2006, Journal of Geophysical Research (Space Physics), 111, A12103

Gilbert, H. R., Daou, A. G., Young, D., Tripathi, D., & Alexander, D. 2008, ApJ, 685, 629

Goossens, M., Soler, R., Terradas, J., Van Doorsselaere, T., & Verth, G. 2014, ApJ, 788, 9

Gosain, S., & Foullon, C. 2012, ApJ, 761, 103

Guo, Y., Schmieder, B., Démoulin, P., et al. 2010, ApJ, 714, 343

Hale, G., & Ellerman, F. 1903, Publ. Yerkes Obs., 3(I), 3

Hanaoka, Y., & Sakurai, T. 2017, ApJ, 851, 130

Harvey, J. W. 1969, Thesis (PH.D.)–UNIVERSITY OF COLORADO AT BOULDER

Hershaw, J., Foullon, C., Nakariakov, V. M., & Verwichte, E. 2011, A&A, 531, A53

Hillier, A., Hillier, R., & Tripathi, D. 2012, ApJ, 761, 106

Hillier, A., & van Ballegooijen, A. 2013, ApJ, 766, 126

Hindman, B. W., Haber, D. A., & Toomre, J. 2006, ApJ, 653, 725

Hirayama, T. 1985, Sol. Phys., 100, 415

Hood, A. W., & Hughes, D. W. 2011, Physics of the Earth and Planetary Interiors, 187, 78

Hu, H., Liu, Y. D., Zhu, B., et al. 2019, ApJ, 878, 106

Hyder, C. L. 1966, ZAp, 63, 78

Isobe, H., & Tripathi, D. 2006, A&A, 449, L17

Isobe, H., Tripathi, D., Asai, A., & Jain, R. 2007, Sol. Phys., 246, 89

Janssen, P. 1868, Compt. Rend. Acad. Sci., 67, 838

Jelínek, P., Karlický, M., Smirnova, V. V., & Solov'ev, A. A. 2020, A&A, 637, A42

Jenkins, J. M., & Keppens, R. 2021, Astronomy & Astrophysics, 646, A134

Jing, J., Lee, J., Spirock, T. J., & Wang, H. 2006, Sol. Phys., 236, 97

Jing, J., Lee, J., Spirock, T. J., et al. 2003, ApJ, 584, L103

Joarder, P. S., & Roberts, B. 1992a, A&A, 256, 264

—. 1992b, Astronomy and Astrophysics (ISSN 0004-6361), 261, 625

Joshi, A. D., Hanaoka, Y., Suematsu, Y., et al. 2016, ApJ, 833, 243

Kaneko, T., Goossens, M., Soler, R., et al. 2015, ApJ, 812, 121

Kaneko, T., & Yokoyama, T. 2015, ApJ, 806, 115

Karpen, J. T., & Antiochos, S. K. 2008, ApJ, 676, 658

Karpen, J. T., Antiochos, S. K., & DeVore, C. R. 2012, ApJ, 760, 81

Karpen, J. T., Antiochos, S. K., Hohensee, M., Klimchuk, J. A., & MacNeice, P. J. 2001, ApJ, 553, L85

Karpen, J. T., Antiochos, S. K., & Klimchuk, J. A. 2006, ApJ, 637, 531

Karpen, J. T., Antiochos, S. K., Klimchuk, J. A., & MacNeice, P. J. 2003, ApJ, 593, 1187

Karpen, J. T., Tanner, S. E. M., Antiochos, S. K., & DeVore, C. R. 2005, ApJ, 635, 1319

Khomenko, E., & Cally, P. S. 2019, ApJ, 883, 179

Khomenko, E., & Collados, M. 2006, ApJ, 653, 739

—. 2012, ApJ, 747, 87

Khomenko, E., Collados, M., & Felipe, T. 2008, Sol. Phys., 251, 589

Khomenko, E., Díaz, A., de Vicente, A., Collados, M., & Luna, M. 2014, A&A, 565, A45

Khomenko, E., Vitas, N., Collados, M., & de Vicente, A. 2018, A&A, 618, A87

Kippenhahn, R., & Schlüter, A. 1957, ZAp, 43, 36

Kleczek, J., & Kuperus, M. 1969, Sol. Phys., 6, 72

Kolotkov, D. Y., Nisticò, G., & Nakariakov, V. M. 2016, A&A, 590, A120

Kolotkov, D. Y., Nisticò, G., Rowlands, G., & Nakariakov, V. M. 2018, Journal of Atmospheric and Solar-Terrestrial Physics, 172, 40

Kuckein, C., Centeno, R., Martínez Pillet, V., et al. 2009, A&A, 501, 1113

Kuperus, M., & Raadu, M. A. 1974, A&A, 31, 189

Labrosse, N., Heinzel, P., Vial, J. C., et al. 2010, Space Sci. Rev., 151, 243

Leroy, J. L. 1989, Observation of prominence magnetic fields, ed. E. R. Priest, Vol. 150, 77–113

Leroy, J. L., Bommier, V., & Sahal-Brechot, S. 1983, Sol. Phys., 83, 135

—. 1984, A&A, 131, 33

Leroy, J. L., Ratier, G., & Bommier, V. 1977, A&A, 54, 811

Li, T., & Zhang, J. 2012a, ApJ, 760, L10

—. 2012b, ApJ, 760, L10

Liakh, V., Luna, M., & Khomenko, E. 2020, A&A, 637, A75

—. 2021, A&A, 654, A145

Lin, Y., Engvold, O., Rouppe van der Voort, L., Wiik, J. E., & Berger, T. E. 2005a, Sol. Phys., 226, 239

Lin, Y., Martin, S. F., & Engvold, O. 2008a, in Astronomical Society of the Pacific Conference Series, Vol. 383, Subsurface and Atmospheric Influences on Solar Activity, ed. R. Howe, R. W. Komm, K. S. Balasubramaniam, & G. J. D. Petrie, 235

Lin, Y., Martin, S. F., Engvold, O., Rouppe van der Voort, L. H. M., & van Noort, M. 2008b, Advances in Space Research, 42, 803

Lin, Y., Wiik, J. E., Engvold, O., Rouppe van der Voort, L., & Frank, Z. A. 2005b, Sol. Phys., 227, 283

Lites, B. W. 2005, ApJ, 622, 1275

Lites, B. W., & Low, B. C. 1997, Sol. Phys., 174, 91

Litvinenko, Y. E. 2000, Sol. Phys., 196, 369

Litvinenko, Y. E., & Martin, S. F. 1999, Sol. Phys., 190, 45

Litvinenko, Y. E., & Wheatland, M. S. 2005, ApJ, 630, 587

Liu, R., Liu, C., Xu, Y., et al. 2013, ApJ, 773, 166

Liu, R., Wang, Y., Lee, J., & Shen, C. 2019, ApJ, 870, 15

Liu, W., Ofman, L., Nitta, N. V., et al. 2012, ApJ, 753, 52

Lockyer, J. N. 1868, Compt. Rend. Acad. Sci., 67, 836

Lomb, N. R. 1976, Ap&SS, 39, 447

Luna, M., Díaz, A. J., & Karpen, J. 2012a, ApJ, 757, 98

Luna, M., Díaz, A. J., & Karpen, J. 2012b, ApJ, 757, 98

Luna, M., Díaz, A. J., Oliver, R., Terradas, J., & Karpen, J. 2016a, A&A, 593, A64

Luna, M., & Karpen, J. 2012, ApJ, 750, L1

Luna, M., Karpen, J., Ballester, J. L., et al. 2018, ApJS, 236, 35

Luna, M., Karpen, J. T., & Devore, C. R. 2012c, The Astrophysical Journal, 746, 30

Luna, M., Knizhnik, K., Muglach, K., et al. 2014, ApJ, 785, 79

Luna, M., & Moreno-Insertis, F. 2021, ApJ, 912, 75

Luna, M., Su, Y., Schmieder, B., Chandra, R., & Kucera, T. A. 2017, ApJ, 850, 143

Luna, M., Terradas, J., Khomenko, E., Collados, M., & de Vicente, A. 2016b, ApJ, 817, 157

Lyot, B. 1936, Compt. Rend. Acad. Sci., 202, 392

Mackay, D. H., Karpen, J. T., Ballester, J. L., Schmieder, B., & Aulanier, G. 2010, Space Science Reviews, 151, 333

Mackay, D. H., & van Ballegooijen, A. A. 2006, ApJ, 641, 577

Magara, T. 2006, ApJ, 653, 1499

Manchester, W., I., Gombosi, T., DeZeeuw, D., & Fan, Y. 2004, ApJ, 610, 588

Martens, P. C., & Zwaan, C. 2001, ApJ, 558, 872

Martens, P. C. H., & Kuin, N. P. M. 1989, Sol. Phys., 122, 263

Martin, S. F., Marquette, W. H., & Bilimoria, R. 1992, in Astronomical Society of the Pacific Conference Series, Vol. 27, The Solar Cycle, ed. K. L. Harvey, 53

Mazumder, R., Pant, V., Luna, M., & Banerjee, D. 2020, A&A, 633, A12

Mei, Z. X., Keppens, R., Cai, Q. W., et al. 2020, MNRAS, 493, 4816

Molowny-Horas, R., Wiehr, E., Balthasar, H., Oliver, R., & Ballester, J. L. 1999, in JOSO Annu. Rep., 1998, 126–127

Moreno-Insertis, F. 2004, Ap&SS, 292, 587

Moreton, G. E., & Ramsey, H. E. 1960, PASP, 72, 357

Moreton, G. E., & Ramsey, H. E. 1960, Publications of the Astronomical Society of the Pacific, 72, 357

Moses, D., Clette, F., Delaboudinière, J. P., et al. 1997, Sol. Phys., 175, 571

Müller, D. A. N., De Groof, A., Hansteen, V. H., & Peter, H. 2005, A&A, 436, 1067

Müller, D. A. N., Hansteen, V. H., & Peter, H. 2003, A&A, 411, 605

Murray, M. J., Hood, A. W., Moreno-Insertis, F., Galsgaard, K., & Archontis, V. 2006, A&A, 460, 909

Newton, H. W. 1935, Monthly Motices Roy. Astron. Soc., 95, 650

Nordlund, A., & Galsgaard, K. 1995, A 3D MHD code for Parallel Computers (NBIfAFG, Astronomical Observatory)

Okamoto, T. J., Nakai, H., Keiyama, A., et al. 2004, ApJ, 608, 1124

Okamoto, T. J., Tsuneta, S., Lites, B. W., et al. 2009, ApJ, 697, 913

Oliver, R. 1999, in ESA Special Publication, Vol. 9, Magnetic Fields and Solar Processes, ed. A. Wilson & et al., 425

Oliver, R., & Ballester, J. L. 2002, Sol. Phys., 206, 45

Oliver, R., Ballester, J. L., Hood, A. W., & Priest, E. R. 1993, The Astrophysical Journal, 409, 809

Oliver, R., Čadež , V. M., Carbonell, M., & Ballester, J. L. 1999, A&A, 351, 733

Paletou, F., & Aulanier, G. 2003, in Astronomical Society of the Pacific Conference Series, Vol. 307, Solar Polarization, ed. J. Trujillo-Bueno & J. Sanchez Almeida, 458

Paletou, F., López Ariste, A., Bommier, V., & Semel, M. 2001, A&A, 375, L39

Palmieri, L. 1881, Rend. R. Acad. Sci. Fis. Mat, Serie. I, 20, 150

Pant, V., Mazumder, R., Yuan, D., et al. 2016, Sol. Phys., 291, 3303

Pant, V., Srivastava, A. K., Banerjee, D., et al. 2015, Research in Astronomy and Astrophysics, 15, 1713

Parchevsky, K. V., & Kosovichev, A. G. 2007, ApJ, 666, 547

Parenti, S., Lemaire, P., & Vial, J. C. 2005, A&A, 443, 685

Parenti, S., & Vial, J. C. 2007, A&A, 469, 1109

Piantschitsch, I., Vršnak, B., Hanslmeier, A., et al. 2017, ApJ, 850, 88

Pintér, B., Jain, R., Tripathi, D., & Isobe, H. 2008, ApJ, 680, 1560

Pneuman, G. W. 1983, Sol. Phys., 88, 219

Priest, E. R., Hood, A. W., & Anzer, U. 1989, ApJ, 344, 1010

Priest, E. R., van Ballegooijen, A. A., & Mackay, D. H. 1996, ApJ, 460, 530

Raes, J. O., Van Doorsselaere, T., Baes, M., & Wright, A. N. 2017, A&A, 602, A75

Ramsay, W. 1895, Proc. Roy. Soc., 58, 81

Ramsey, H., & Smith, S. F. 1965, AJ, 70, 688

Ramsey, H. E., & Smith, S. F. 1966, AJ, 71, 197

Régnier, S., & Amari, T. 2004, A&A, 425, 345

Régnier, S., Amari, T., & Kersalé, E. 2002, A&A, 392, 1119

Régnier, S., & Canfield, R. C. 2006, A&A, 451, 319

Régnier, S., & Priest, E. R. 2007, A&A, 468, 701

Ruderman, M. S., & Luna, M. 2016, A&A, 591, A131

Rust, D. M., & Kumar, A. 1994, Sol. Phys., 155, 69

Sahal-Brechot, S., Bommier, V., & Leroy, J. L. 1977, A&A, 59, 223

Saito, K., & Hyder, C. L. 1968, Sol. Phys., 5, 61

Saito, K., & Tandberg-Hanssen, E. 1973, Sol. Phys., 31, 105

Schmieder, B., Raadu, M. A., & Wiik, J. E. 1991, A&A, 252, 353

Schmieder, B., Roudier, T., Mein, N., et al. 2014, A&A, 564, A104

Schunker, H., & Cally, P. S. 2006, MNRAS, 372, 551

Schutgens, N. A. J., & Tóth, G. 1999, A&A, 345, 1038

Secchi, A. 1875, Le Soleil

Shen, Y., Chen, P. F., Liu, Y. D., et al. 2019, ApJ, 873, 22

Shen, Y., Ichimoto, K., Ishii, T. T., et al. 2014a, ApJ, 786, 151

Shen, Y., Liu, Y., Liu, Y. D., et al. 2018a, ApJ, 861, 105

Shen, Y., Liu, Y., Tian, Z., & Qu, Z. 2017, ApJ, 851, 101

Shen, Y., Liu, Y. D., Chen, P. F., & Ichimoto, K. 2014b, ApJ, 795, 130

Shen, Y., Tang, Z., Miao, Y., Su, J., & Liu, Y. 2018b, ApJ, 860, L8

Soler, R., Oliver, R., & Ballester, J. L. 2009, The Astrophysical Journal, 699, 1553

—. 2010, The Astrophysical Journal, 726, 102

Srivastava, A. K., Singh, T., Ofman, L., & Dwivedi, B. N. 2016, MNRAS, 463, 1409

Stellmacher, G., Wiehr, E., & Dammasch, I. E. 2003, Sol. Phys., 217, 133

Su, Y., van Ballegooijen, A., Lites, B. W., et al. 2009, ApJ, 691, 105

Takahashi, T., Asai, A., & Shibata, K. 2015, ApJ, 801, 37

Tandberg-Hanssen, E. 1995, The nature of solar prominences, Vol. 199

Terradas, J., Soler, R., Díaz, A. J., Oliver, R., & Ballester, J. L. 2013, ApJ, 778, 49

Terradas, J., Soler, R., Luna, M., et al. 2016, ApJ, 820, 125

Thompson, B. J., Plunkett, S. P., Gurman, J. B., et al. 1998, Geophys. Res. Lett., 25, 2465

Titov, V. S., & Démoulin, P. 1999, A&A, 351, 707

Tripathi, D., Isobe, H., & Jain, R. 2009, Space Sci. Rev., 149, 283

Tsubaki, T. 1988, in Observations of periodic oscillations or waves in the solar corona and prominences, 140–149

van Ballegooijen, A. A. 2004, ApJ, 612, 519

van Ballegooijen, A. A., & Martens, P. C. H. 1989, ApJ, 343, 971

Vassenius, B. 1773, Philosophical Transactions of the Royal Society of London, 38, 134

Vial, J.-C., & Engvold, O. 2015, Solar Prominences, Vol. 415, doi:10.1007/978-3-319-10416-4

Vögler, A., Shelyag, S., Schüssler, M., et al. 2005, A&A, 429, 335

Vrsnak, B. 1993, Hvar Observatory Bulletin, 17, 23

Vršnak, B., Veronig, A. M., Thalmann, J. K., & Žic, T. 2007, A&A, 471, 295

Vršnak, B., Žic, T., Lulić, S., Temmer, M., & Veronig, A. M. 2016, Sol. Phys., 291, 89

Wang, B., Chen, Y., Fu, J., et al. 2016, ApJ, 827, L33

Wang, Y. M. 1999, ApJ, 520, L71

Wang, Y.-M. 2000, The Astrophysical Journal, 543, L89

Wang, Y. M. 2001, ApJ, 560, 456

Wang, Y. M., & Muglach, K. 2007, ApJ, 666, 1284

Welsch, B. T., DeVore, C. R., & Antiochos, S. K. 2005, ApJ, 634, 1395

Wills-Davey, M. J., DeForest, C. E., & Stenflo, J. O. 2007, The Astrophysical Journal, 664, 556

Winebarger, A. R., Warren, H., van Ballegooijen, A., DeLuca, E. E., & Golub, L. 2002, ApJ, 567, L89

Xia, C., Chen, P. F., & Keppens, R. 2012a, ApJ, 748, L26

—. 2012b, ApJ, 748, L26

Xia, C., Chen, P. F., Keppens, R., & van Marle, A. J. 2011, ApJ, 737, 27

Xia, C., & Keppens, R. 2016, ApJ, 823, 22

Xie, X., Mei, Z., Huang, M., et al. 2019, MNRAS, 490, 2918

Xue, Z. K., Yan, X. L., Qu, Z. Q., & Zhao, L. 2014, in Astronomical Society of the Pacific Conference Series, Vol. 489, Solar Polarization 7, ed. K. N. Nagendra, J. O. Stenflo, Z. Q. Qu, & M. Sampoorna, 53

Zapiór, M., Schmieder, B., Mein, P., et al. 2019, A&A, 623, A144

Zhang, L. Y., Fang, C., & Chen, P. F. 2019, ApJ, 884, 74

Zhang, Q. M. 2020, A&A, 642, A159

Zhang, Q. M., Chen, P. F., Xia, C., & Keppens, R. 2012, A&A, 542, A52

Zhang, Q. M., Chen, P. F., Xia, C., Keppens, R., & Ji, H. S. 2013, A&A, 554, A124

Zhang, Q. M., Guo, J. H., Tam, K. V., & Xu, A. A. 2020, A&A, 635, A132

Zhang, Q. M., & Ji, H. S. 2018, ApJ, 860, 113

Zhang, Q. M., Li, T., Zheng, R. S., Su, Y. N., & Ji, H. S. 2017, ApJ, 842, 27

Zhao, X., Xia, C., Keppens, R., & Gan, W. 2017, ApJ, 841, 106

Zhao, X., Xia, C., Van Doorsselaere, T., Keppens, R., & Gan, W. 2019, ApJ, 872, 190

Zheng, R., Xue, Z., Chen, Y., Wang, B., & Song, H. 2019, ApJ, 871, 232

Zheng, R., Zhang, Q., Chen, Y., et al. 2017, ApJ, 836, 160

Zhou, Y. H., Chen, P. F., Hong, J., & Fang, C. 2020, Nature Astronomy, 4, 994

Zhou, Y.-H., Xia, C., Keppens, R., Fang, C., & Chen, P. F. 2018, ApJ, 856, 179

Zhou, Y.-H., Zhang, L.-Y., Ouyang, Y., Chen, P. F., & Fang, C. 2017, ApJ, 839, 9

Zirin, H., & Severny, A. 1961, The Observatory, 81, 155

Zirker, J. B., Engvold, O., & Martin, S. F. 1998, Nature, 396, 440

Zong, W., & Dai, Y. 2017, ApJ, 834, L15

A

Appendix: Contributions during this thesis

A.1 Publications during this thesis

1. *Numerical simulations of large-amplitude oscillations in flux rope solar prominences*; Liakh, V., Luna, M., Khomenko, E.; 2020, A&A, 637, A75

2. *Large-amplitude longitudinal oscillations in solar prominences simulated with different resolutions*; Liakh, V., Luna, M., Khomenko, E.; 2020, A&A, 654, A145

A.2 Conference proceedings

1. *Numerical simulations of large-amplitude oscillations in flux rope solar prominences*; Liakh, V., Luna, M., Khomenko, E.; Contributions to the XIV.0 Scientific Meeting (virtual) of the Spanish Astronomical Society, held 13-15 July 2020

A.3 Oral contributions

1. **Contributed talk.** Liakh, V., Luna, M., Khomenko, E.; *Large-amplitude oscillations in solar prominences in 2D models.* April 2018, International space science institute (ISSI) meeting,, Bern, Switzerland.

2. **Contributed talk.** Liakh, V., Luna, M., Khomenko, E.; *Large-amplitude oscillations in solar prominences in 2.5D models.* September 2018, Waves and instabilities in the solar atmosphere: Confronting the current state-of-the-art, Instituto de Astrofísica de Canarias (IAC), La Laguna, Tenerife Spain.

3. **Contributed talk.** Liakh, V., Luna, M., Khomenko, E.; *Large-amplitude oscillations in solar prominences in 2.5D models.* April 2019, Young Scientists' Conference on Astronomy and Space Physics, Taras Shevchenko National University of Kyiv, Ukraine.

4. **Contributed talk.** Liakh, V., Luna, M., Khomenko, E.; *Large-amplitude oscillations in solar prominences in 2.5D models.* May 2019, International space science institute (ISSI) meeting,, Bern, Switzerland.

5. **Seminar.** Liakh, V., Luna, M., Khomenko, E.; *Large-amplitude oscillations in solar prominences derived from high-resolution simulations.* November 2020, Universitat de les Illes Balears (UIB), Palma de Mallorca, Spain (virtual).

6. **Seminar.** Liakh, V., Luna, M., Khomenko, E.; *Large-amplitude oscillations in solar prominences derived from high-resolution simulations.* March 2021, European Solar Physics Online Seminars (ESPOS).

7. **Poster talk.** Liakh, V., Luna, M., Khomenko, E.; *Damping mechanism Of longitudinal large-amplitude ascillations In solar prominence in the high-resolution simulation.* July 2020, XIV.0 Scientific SEA Meeting of the Spanish Astronomical Society (virtual).

8. **Poster talk.** Liakh, V., Luna, M., Khomenko, E.; *Damping mechanism Of longitudinal large-amplitude ascillations In solar prominence in the high-resolution simulation.* March 2021, Advances in Observations and Modelling of Solar Magnetism and Variability (virtual).

9. **Poster talk.** Liakh, V., Luna, M., Khomenko, E.; *Large-amplitude longitudinal oscillations in solar prominences derived from high-resolution simulations.* September 2021, The 16th European Solar Physics Meeting (ESPM-16) (virtual).